BEILSTEIN JOURNAL OF NANOTECHNOLOGY

Symposium of Nanoscience and Nanomaterials 2024 (SNN 2024)

Edited by Ruben D. Cadena-Nava, Uriel Caudillo-Flores, Mario H. Farias-Sanchez, Raul Rangel-Rojo and Sergio Fuentes Moyado

Imprint

Beilstein Journal of Nanotechnology
www.bjnano.org
ISSN 2190-4286
Email: journals-support@beilstein-institut.de

The *Beilstein Journal of Nanotechnology* is published by the Beilstein-Institut zur Förderung der Chemischen Wissenschaften.

Beilstein-Institut zur Förderung der Chemischen Wissenschaften
Trakehner Straße 7–9
60487 Frankfurt am Main
Germany
www.beilstein-institut.de

BEILSTEIN JOURNAL OF NANOTECHNOLOGY

AI-assisted models to predict chemotherapy drugs modified with C_{60} fullerene derivatives

Jonathan-Siu-Loong Robles-Hernández[1], Dora Iliana Medina[2], Katerin Aguirre-Hurtado[3], Marlene Bosquez[3], Roberto Salcedo[*3] and Alan Miralrio[*1]

Full Research Paper

Open Access

Address:
[1]Tecnologico de Monterrey, Escuela de Ingeniería y Ciencias, Ave. Eugenio Garza Sada 2501, Monterrey 64849, Mexico, [2]Tecnologico de Monterrey, Institute of Advanced Materials for Sustainable Manufacturing, Monterrey 64849, Mexico and [3]Instituto de Investigaciones en Materiales, Universidad Nacional Autónoma de México, Circuito exterior s/n, Ciudad Universitaria, Coyoacán, 04510, Ciudad de México, Mexico

Email:
Roberto Salcedo[*] - salcedo@unam.mx; Alan Miralrio[*] - miralrio@tec.mx

* Corresponding author

Keywords:
breast cancer; CXCR7; drug nanocarriers; QSAR

Beilstein J. Nanotechnol. **2024,** *15,* 1170–1188.
https://doi.org/10.3762/bjnano.15.95

Received: 28 May 2024
Accepted: 30 August 2024
Published: 19 September 2024

This article is part of the thematic issue "Symposium of Nanoscience and Nanomaterials 2024 (SNN 2024)".

Guest Editor: R. D. Cadena-Nava

Abstract

Employing quantitative structure–activity relationship (QSAR)/ quantitative structure–property relationship (QSPR) models, this study explores the application of fullerene derivatives as nanocarriers for breast cancer chemotherapy drugs. Isolated drugs and two drug–fullerene complexes (i.e., drug–pristine C_{60} fullerene and drug–carboxyfullerene C_{60}–COOH) were investigated with the protein CXCR7 as the molecular docking target. The research involved over 30 drugs and employed Pearson's hard–soft acid–base theory and common QSAR/QSPR descriptors to build predictive models for the docking scores. Energetic descriptors were computed using quantum chemistry at the density functional-based tight binding DFTB3 level. The results indicate that drug–fullerene complexes interact more with CXCR7 than isolated drugs. Specific binding sites were identified, with varying locations for each drug complex. Predictive models, developed using multiple linear regression and IBM Watson artificial intelligence (AI), achieved mean absolute percentage errors below 12%, driven by AI-identified key variables. The predictive models included mainly quantitative descriptors collected from datasets as well as computed ones. In addition, a water-soluble fullerene was used to compare results obtained by DFTB3 with a conventional density functional theory approach. These findings promise to enhance breast cancer chemotherapy by leveraging fullerene-based drug nanocarriers.

Introduction

Breast cancer is the most diagnosed cancer in women and the second leading cause of cancer-related mortality in women [1,2]. Heritage is the most critical risk factor, and 15 to 20% of breast cancer is familiar [3]. One of the characteristics of breast cancer is that it can be wholly cured given an early diagnosis [4]. The mortality rate from breast cancer has been reduced by 1.9% annually from 2002 to 2011 and 1.3% from 2011 to 2020 [5]. Diagnostics and treatments have continuously improved through the years. However, the situation is different in each country considering the costs and technological advances in each country. In the United States, 300,590 cases of breast cancer had been estimated for the year 2023, with a total of 43,700 deaths [6]. Latin America has over 210,000 new cases and around 60,000 deaths yearly [7]. For the year 2020, it was estimated that about 2.3 million breast cancer cases were diagnosed in women globally, and about 685,000 died from this disease [8]. A recurrent problem with standard treatments are the side effects. Regarding the use of chemotherapeutic drugs, such issues are nephrotoxicity of cisplatin, cardiotoxicity of doxorubicin, and pulmonary fibrosis from the use of bleomycin [9-11]. Besides, in the case of radiotherapy, fibrosis, atrophy, and neuronal damage caused by irradiation can occur [12,13]. Consequently, novel treatments try to reduce the secondary effects while retaining the benefits of standard approaches.

Chemotherapy is one of the most extensively applied treatments for breast cancer, with different drug targets depending on the type of cancer. Progesterone- or estrogen-receptor-positive tumors are related to cancers with low mortality [14]. Another common target in chemotherapy is human epidermal growth factor receptor 2 (HER2). Only 15 to 20% of all tumors are HER2-positive, overexpressing Erb-B2 receptor tyrosine kinase 2 (ERBB2) in the cell membrane. HER2 tumors are usually more aggressive than other ones, but the advantage is that their treatment is very effective [15]. Another chemotherapy target is the chemokine C-X-C motif receptor 7 (CXCR7) [16,17]. This G-protein is targeted because studies show a possible positive effect on inhibiting the metastasis of cervical cancer cells [18]. However, more clinical and preclinical studies on CXCR7 and its co-player CXCR4 are required since alterations have been detected in diseases such as cancer, central nervous system and cardiac disorders, and autoimmune diseases [16].

In recent years, nanomaterials have attracted the attention of different scientific communities by providing them with new solutions for drug delivery [19,20]. These nanotechnological applications have made it possible to obtain treatments that release substances at specific sites of interest, reducing the required drug amount and side effects. Nanostructures to form these drug delivery systems can be divided into organic and inorganic [19,20], with the latter one being the less extensively studied. One option currently considered in pharmacy and medicine is carbon-based nanomaterials because of their physicochemical, mechanical, electrical, thermal, and optical properties [19,20], as well as their capacity to modify existing drugs. Fullerene derivatives have been proposed recently, particularly those obtained from fullerene C_{60} [21]. The unmodified fullerene C_{60} is known as a "free radical sponge" because its double bonds tend to accept free radicals [22]. Because of its size, surface area, and capacity to extinguish or generate reactive oxygen species, C_{60} is very promising in medicine and clinical therapy [23,24]. It is also possible to modify pristine fullerenes by adding polar functional groups (e.g., –COOH, –OH, or $–NH_2$), to improve water solubility, antioxidant properties, and even biological activity [25]. For instance, polyhydroxy fullerenes (PHFs) exhibit properties suitable for biomedical applications, such as water solubility, biodegradability, biocompatibility, and hypoallergic response. It has been shown that PHFs can inhibit cancer tumor growth and positively regulate the immune system [26]. The same is valid for carboxylated fullerenes [27]; for instance, $C_{60}[C(COOH)_2]_3$ is well known for its high biological activity in plants [28] and within mitochondrial dynamics [29].

Since the evaluation of novel drugs is a task that requires significant human and material resources, innovative strategies have been formulated as alternatives. Quantitative structure–activity and quantitative structure–property relationships (QSAR/QSPR) are a paradigm that can be useful in choosing promising molecules, considering the information on inactive and active compounds, through in silico approaches. According to the QSAR/QSPR paradigm, a given activity/property, f, can be modeled using a set of quantitative descriptors, $x_1, x_2, x_3,..., x_n$, theoretically determined or measured by experiments [30]. A relationship $f(x_1, x_2, x_3,..., x_n)$ can be defined to predict the activity or property of molecules after the evaluation of their quantitative descriptors. However, the QSAR/QSPR paradigm does not explain how to select the descriptors or how to build the mathematical function. Consequently, the following paragraphs discuss basic concepts about selecting descriptors and regression techniques implemented in this manuscript.

Lipinski's rule of five is a compendium of guidelines commonly used to determine if a molecule can be proposed as an orally delivered drug according to its physicochemical properties. According to this rule, a drug compound should have a molecular weight below 500 g/mol, a octanol–water partition coefficient (LogP) below 5, less than five hydrogen bond donor sites, and less than ten hydrogen bond acceptors sites. It is possible to add

two other conditions, namely polar surface area (PSA) ≤ 140 Å^2 and less than ten rotatable bonds [31]. Taking advantage of the readiness of these quantities in public datasets, the current study proposes some of these quantities as potentially suitable descriptors for predictive models. Besides, Pearson's hard–soft acid–base (HSAB) theory suggests other descriptors to describe and predict the interactions between chemical species, such as those between a drug molecule as a ligand and a protein [32]. These quantitative values are based on the vertical ionization energy (I) and electron affinity (A). According to Koopmans' theorem, both can be approximated by $I = -E_{HOMO}$ and $A = -E_{LUMO}$, where E_{HOMO} is the energy of the highest occupied molecular orbital (HOMO), and E_{LUMO} is the energy of the lowest unoccupied molecular orbital (LUMO). It is advantageous to combine these properties to find out if an interaction between two species will occur and to obtain new quantitative relationships. Another helpful descriptor is the global electrophilicity, calculated as $\omega = \chi^2/2\eta$ [33]. Electrophilicity is related to the energetic stabilization that a species gains by obtaining an additional electron.

Methods

First, 42 drugs related to chemotherapy treatments for breast cancer were proposed. Although the most notable fullerene derivatives for biological applications are those with several hydrophilic groups, the carboxylic acid derivative C_{60}–COOH has been studied as well. Baglayan and coworkers carried out a conformation analysis within DFT to obtain the ground state structure for C_{60}–COOH [34]. In addition, they discussed its usage as a potential drug carrier for the antimetabolic and anticancer drug 5-fluoruracil [34]. Similarly, Parlak and Alver reported a theoretical study on the interactions and stability of paracetamol complexes with C_{60}–COOH [35]. Consequently, this work proposes the interaction of C_{60}–COOH fullerene with anticancer drugs. As a complement, a water-soluble fullerene predicted as stable at the normal human body temperature was proposed to study the interactions with doxorubicin and gemcitabine [36]. The water-soluble fullerene is introduced to avoid known mutagenic reactions related to breast cancer [36]. It was also studied as a potential carrier for bedaquiline, an agent against tuberculosis [37]. The current study only considered molecules and complexes formed with up to 100 atoms to be affordable with our computational resources.

A set of descriptors was chosen to build the dataset, including molecular weight and pK_a [38]. Also, LogP was included, as a descriptor associated with the concentration of a given substance in the aqueous phase of a two-phase octanol–water mixture [39]. Similarly, LogS, related to the water solubility of a substance, was considered. Besides, PSA, as molecular surface associated with charge accumulation due to heteroatoms and polar groups, as well as polarizability (α) associated with the tendency of a given molecule to acquire an electric dipole moment in the presence of an external electric field were taken into account. The mentioned QSAR/QSPR descriptors were obtained from the Drugbank dataset (https://go.drugbank.com). Initial drug structures and connectivity were also obtained from the simplified molecular input line entry specification (SMILES) retrieved from Drugbank.

Molecular mechanics and density functional-based tight binding (DFTB) with dispersion and solvation corrections were used to obtain the optimized structures of the molecules under study and to compute E_{HOMO}, E_{LUMO}, and ω as quantitative descriptors. As an alternative to the most robust but computationally more expensive density functional theory (DFT) method, DFTB was used. A reference electron density ρ_0 represents the sum of the neutral atomic densities [40]. Within the third-order approach DFTB3, the ground state density $\rho(r)$ is obtained as the reference density ρ_0 perturbed by density fluctuations $\delta\rho$, that is,

$$E_{\mathrm{DFTB3}}\left[\rho_0+\delta\rho\right] = E_0\left[\rho_0\right] + E_1\left[\rho_0+\delta\rho\right] + E_2\left[\rho_0+\left(\delta\rho\right)^2\right] + E_3\left[\rho_0+\left(\delta\rho\right)^3\right]. \quad (1)$$

For all calculations within DFTB3, the 3OB parameter set was used [41]. To carry out the global optimization procedure, Balloon 1.8.2 [42] and DFTB+ 17.1 [40] were used for the initial conformational study by genetic algorithms and final optimization at the DFTB3 level, respectively. London dispersion forces were considered in the DFTB3 and global optimization procedures by Lennard-Jones potentials, as implemented in UFF and MMFF94 force fields, respectively. The solvent effect was included by the Born solvation model within DFTB3. The study considered the chemotherapy drugs isolated and interacting with pristine C_{60} fullerene as well as its carboxylic acid derivative C_{60}–COOH. Eight initial drug–fullerene structures were proposed to obtain their global optimization by means of DFTB3. The drugs were initially set at 1.5 Å of minimal distance from the fullerene. Once the global optimization was done, the same steps as for the isolated drugs were carried out for the molecular docking. The datasets were modified to take into account the effect of the fullerenes. Also, the validation set was reduced because of the large size of the complexes.

The atypical chemokine receptor 3, also known as CXCR7 or G-protein-coupled receptor 159 (GPR159) [16,18,43], was selected as the target protein for molecular docking. The iterative assembly refinement server (I-Tasser) was used to produce an initial structure for the CXCR7 protein by the homology approach. The sequence was extracted from the UniProtKB/

Swiss-Prot dataset. From all homology structures produced by the I-Tasser server, the one with the highest confidence coefficients was selected to produce a reliable initial structure [44]. The lowest-energy structure, as in the study of Muthiah and coworkers [45], was validated using PROCHECK [46] to check the quality of the protein structure. The PDB produced with the previous step was subsequently optimized by an energy minimization through Amber force fields using the USCF Chimera 1.14 toolkit [47]. The secondary structural features were stabilized by TMpred [48] and HMMTOP [49] during energy minimization. Last, the protein was prepared by setting atomic charges and hydrogen atoms and merging the nonpolar groups. Once the structures were optimized, molecular docking was performed with the CXCR7 protein, using Autodock Vina 1.1, to obtain the docking score, established hydrogen bonds, and the binding site (pocket). The above was done for all drugs in the dataset and an external validation set.

IBM Watson AI was used to build the models and to predict the docking score through the Extra Trees regressor algorithm [50,51]. It was also used to obtain the most significant quantum descriptors used in each model. Extra Trees, an abbreviation of "extremely randomized trees", is a mathematical method used to estimate a relationship between data and the covariates [52]. The Extra Trees algorithm creates many decision trees [52], but the sampling of each one is random. Thus, a dataset for each tree contains unique samples. The optimization of the hyperparameters associated with the decision trees obtained was performed by the derivative-free global search algorithm known as RBfOpt, which fits a radial basis function mode to accelerate the discovery of the hyperparameters [53]. All the above was used through the AutoAI tool within IBM Watson, an automatized routine to select the model with the best performance among those available in the platform. Since this method does not produce exportable mathematical models, another approach was used as detailed below [50].

Multiple linear regression (MLR) could be a tool to solve the problem in a complementary way to Extra Trees regression. MLR is a mathematical model that can be seen as an extension of linear regression. In terms of n input variables, $x_1, x_2,\ldots, x_n$, the outcome y can be expanded by the following linear expansion [54]:

$$y = \beta_0 + \beta_1 \times x_1 + \beta_2 \times x_2 + \beta_3 \times x_3 + \ldots + \beta_n \times x_n. \quad (2)$$

In Equation 2, β_k are the partial regression coefficients, and β_0 is the value of y when all variables are set to zero.

To obtain the AI and MLR models, a fivefold approach was implemented, by using 80% of the data available to obtain the predictive model as training set and the remaining 20% as testing set. Supporting Information File 1 gives the results of the cross-validation for all the models reported in the current manuscript. Once the models were built, an additional external validation set was used to obtain evaluation metrics and to determine the most accurate models between methodologies. The metrics proposed to evaluate the performance of the predictive models were mean squared error (MSE), mean absolute percentage error (MAPE), mean absolute error (MAE), and root mean squared error (RMSE). These metrics were computed as follows:

$$\mathrm{MAPE} = (1/n)\sum_{i=1}^{n}\left|(y_i - \hat{y}_i)/y_i\right| \times 100\%,$$

$$\mathrm{MAE} = (1/n)\sum_{i=1}^{n}\left|(y_i - \hat{y}_i)\right|,$$

$$\mathrm{MSE} = (1/n)\sum_{i=1}^{n}(y_i - \hat{y}_i)^2,$$

and

$$\mathrm{RMSE} = [(1/n)\sum_{i=1}^{n}(y_i - \hat{y}_i)^2]^{1/2}.$$

Here, y_i is the docking score for compound I, $\hat{y}_i$ is the estimated value of the docking score for compound I provided by the model. The workflow diagram in Figure 1 summarizes the procedure followed to obtain the models.

Results and Discussion

Table 1 presents the quantum descriptors proposed for the current study and the symbols used for them. The physical unit of each descriptor, as well as references to their usage in similar QSAR/QSPR models, were included as well.

Isolated drugs

A dataset containing all the descriptors of Table 1 for 33 drugs was created to obtain the predictive models. Also, another nine compounds were considered to build an external validation set, allowing for the comparison between methodologies (Supporting Information File 1, Table S1). In the case of the training set, the molecular weight was obtained with values between 130.08 and 915.4 g/mol. Water solubility values varied between 0.0004 mg/mL and 22.3 mg/mL. The LogP values varied between −2 and 6.54, whereas LogS ranged from −6 to −1.1. Besides, pK_a values varied between −8 and 14.55. The hydrogen acceptor count varied widely between 2 and 13, whereas the hydrogen donor count varied between 0 and 6. In addition, the polar surface area had variations between 12.47 and 221.29 Å^2. The cases of thiotepa and aldoxorubicin were not considered because they are part of the validation set. Rotatable bonds were obtained ranging from 0 to 15. The polarizability varied from 9.46 to 87.46 Å^3; everolimus was excluded as part of the

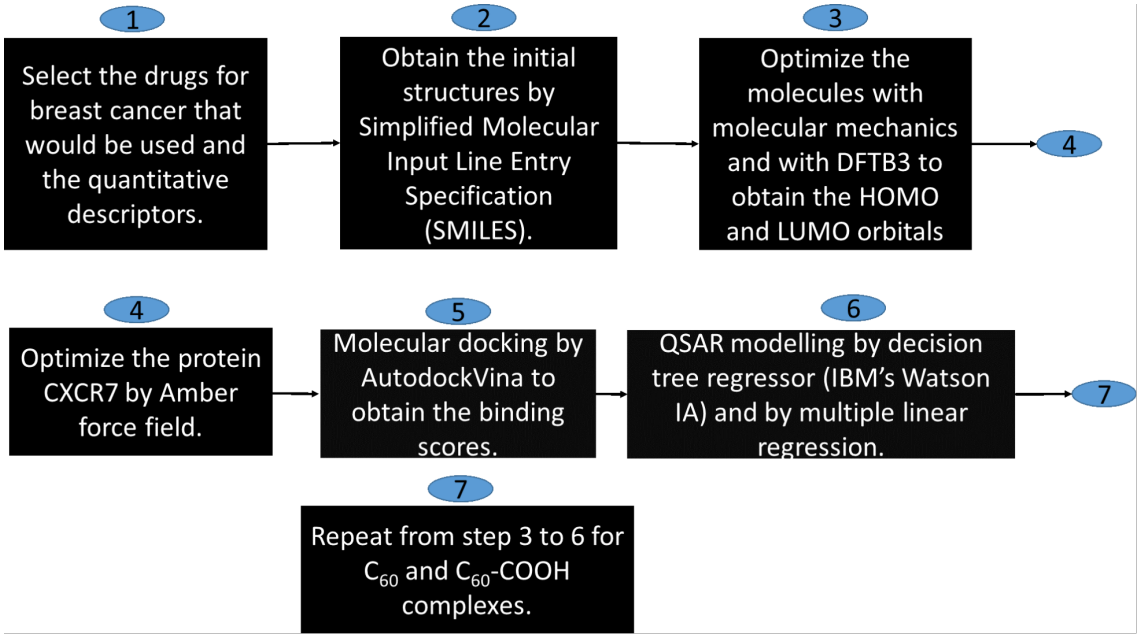

Figure 1: Workflow diagram of the stages during modeling.

Table 1: Quantitative descriptors proposed to model the docking score of the isolated drugs, as well as of those modified with fullerenes C_{60} and C_{60}–COOH, interacting with the protein CXCR7.

Variable	Descriptor	Symbol	Unit	Reference
x_1	molecular weight	MW	g/mol	[55,56]
x_2	water solubility	WS	mg/mL	[57]
x_3	octanol–water partition coefficient	LogP	—	[58,59]
x_4	solubility coefficient	LogS	—	—
x_5	acid dissociation constant	pK_a	—	[60]
x_6	hydrogen acceptor count	Ac	—	[61]
x_7	hydrogen donor count	Dn	—	[61]
x_8	polar surface area	PSA	$Å^2$	[62]
x_9	rotatable bond count	RBC	—	[63]
x_{10}	polarizability	α	$Å^3$	[64]
x_{11}	number of rings	NOR	—	[65]
x_{12}	energy of HOMO	E_{HOMO}	eV	[66,67]
x_{13}	energy of LUMO	E_{LUMO}	eV	[66,67]
x_{14}	electrophilicity	ω	eV	[66,67]

external validation set. Also, values of number of rings were obtained from 0 to 9. The energy of the HOMO was computed ranging from −7.400 to −4.392 eV, and the LUMO energy from −5.341 to −0.889 eV. Finally, the electrophilicity varied from 2.12 to 180.39 eV. Figure S1 (Supporting Information File 1) shows the correlation matrix between the ten most relevant quantum descriptors used to obtain the mathematical models. There are significant correlations between the molecular weight and the polarizability of about 0.93 and between polarizability and the number of rings of about 0.88. Also, molecular weight and number of rings, as well as WS and LogS exhibited considerable correlations, with values of 0.87 and 0.73, respectively. However, all variables showed a correlation below 0.95. Once the drugs were optimized, blind molecular docking was performed with the CXCR7 protein to obtain the docking score, number of established hydrogen bonds, and the protein residues

interacting with the ligands in a coordination sphere of 3 Å. The results obtained with Autodock Vina [47,68] for training–testing and validation sets are shown in Table 2.

The docking scores ranged from −10.1 to −4.6 kcal/mol for the training set. The molecule with the most significant bond strength, according to its docking score, was olaparib, whereas the one with the lowest bond strength was fluorouracil. The number of hydrogen bonds was computed ranging from 0 to 5. It is important to note that the number of hydrogen bonds is not directly related to the docking score since there are weak and strong hydrogen bonds. This assumption was proved by the analysis performed to obtain the predictive models, as discussed below.

According to the results of the interacting residues annotated in Table 2, two things can be highlighted. First, the analyzed isolated drugs bind inside the protein CXCR7 (Figure 2); second, the pocket is similar for several analyzed drugs. For example, the leucine residue Leu297 is shared by eleven drugs, indicating that their binding zone is close to each other. Comparing the interacting residues with those recently obtained by Muthiah et

Table 2: Docking score, number of established H-bonds, and protein–ligand interacting residue in three-letter symbol, up to 3 Å distance. Drugs marked with an asterisk were used as external validation set.

Ligand	Docking score (kcal/mol)	H-bonds	Interacting residues
doxorubicin	–8.4	5	Asp275, Phe294, Leu297, Tyr200, His298, Arg197, Ser198, Cys196, Asp179, Trp100
neratinib maleate	–8.5	2	Ile276, Leu297, Phe294, His298, Tyr 268, Gln30, Ser216, Ser198, Phe129, Asp179, Leu183, His121, Phe124
epirubicin	–8.1	2	Asp275, Leu297, Tyr200, Ser198, Arg197, Cys196, His121, Trp100, Leu104, His298, Phe294, Gln301,
lapatinib ditosylate	–8.9	1	Glu213, Ile276, Val272, Leu297, Tyr200, His298, Arg197, Ser198, Leu183, His121, Cys196,
fulvestrant	–7.9	0	Leu297, Ile276 Val272, Tyr268, Gln301, Trp100, Phe124, Cys196, Asp179, Ser198, Ser216, Arg197
dinaciclib	–8.4	1	Leu297, Gln301, Tyr268, Trp100, Cys196, Arg197, Phe124, Leu128, Ser198, Asp179, Phe129, Met212, Ser216
abemaciclib	–9.8	1	Asn108, Trp100, Trp110, Leu104, Arg197, Lys40, Asn36, Pro38, Leu43, His298
gemcitabine	–6.2	0	Asn36, Phe294, Met37, Pro38, Asn39, Leu43, Lys40, Leu104, Asn108
voruciclib	–8.8	0	Asn36, Pro38, Asn39, His298, Leu43, Lys40, Leu104, Asn108, Trp100, Ser103, Trp110, Arg197
fluorouracil	–4.6	1	Asn319, Asn321, Lys73, Ile83, His80
letrozole	–8.1	0	His298, Gln301, Arg197, Leu104, Trp100, Ser198, His121, Trp110, Leu183
olaparib	–10.1	2	Tyr268, Val272, Ile276, Glu213, Leu209, Ile205, Met212, Tyr200, Phe199, Ser198, Leu128, Phe124
paclitaxel	–9.6	0	His298, Phe294, Leu297, Tyr268, Gln301, Val272, Leu104, Trp100, Phe124, His121, Trp110, Arg197, Ser198, Leu209, Tyr200, Leu183
seliciclib	–7.6	0	Leu183, Asp179, Ser125, Phe124, Phe129, Leu128, Ser216, Tyr268, Leu297
ixabepilone	–8.2	0	Leu297, Val272, Tyr268, Trp265, Phe124, Arg197, His298, Leu128, Ser198, Leu209, Tyr200, Met212, Ser216
anastrozole	–7.7	0	Met212, Leu209, Ser216, Tyr200, Phe129, Asp179, Ser125, Ser198, Phe124, Leu183, His121
pentostatin	–6.3	3	Phe294, Lys40, Leu104, Trp100, Asn108, Trp110
alvocidib	–8.6	1	His298, Leu43, Lys40, Leu104, Trp100, Asn108, Ser103, Trp110, Arg197
methotrexate	–8.5	3	Leu104, Gln301, Tyr268, Val272, Trp100, Trp110, Cys196, Phe124, His121, Ser198, Leu183, Asp179, Phe129, Glu213, Ser216
milciclib	–9.2	0	Lys40, Phe294, Leu297, Leu104, Asn108, Tyr268, Arg197, Val272, His121
ribociclib	–9.5	1	Lys40, Leu104, Leu43, Tyr195, Cys196, Arg197, Phe124, His121, Ser198, Leu183, Asp179

Table 2: Docking score, number of established H-bonds, and protein–ligand interacting residue in three-letter symbol, up to 3 Å distance. Drugs marked with an asterisk were used as external validation set. (continued)

exemestane	−8.0	0	Phe294, Leu43, Lys40, Leu104, Trp110
tamoxifen	−7.9	1	Asn39, Pro38, Leu43, Lys40, Leu104, Trp110, Tyr195, Arg197
idarubicin	−8.8	1	Phe294, His298, Leu43, Leu104, Asn108, Ser103, Trp110, Cys196, His121
palbociclib	−8.3	1	Phe294, Asn36, Pro38, Leu43, Lys40, Leu104, Asn108, Arg197, Cys196
toremifene	−7.4	0	Leu43, Asn39, Leu104, Pro38, Lys40, Asn36, Phe294, Trp110, Tyr195, Arg197
vinblastine	−9.5	2	Leu43, Asn39, Leu104, His298, Phe294, Lys40, Asn108, Trp110, Arg197, Tyr195, Ile205, Leu209
pirarubicin	−9.4	1	Val272, Leu297, Tyr268, Gln301, Met212, Ile205, Leu209, Glu213, Arg197, Phe199, Trp110, Cys196, Phe199,
roniciclib	−8.4	1	Asn39, Met37, His298, Phe294, Pro38, Asn36, Trp100, Leu104, Lys40, Ser103, Asn108, Trp110,
capecitabine	−7.7	2	Gln301, Phe129, Phe124, Ser198, Arg197, His121, Cys196, Trp110, Leu183
sulfanilamide	−5.4	2	Tyr268, Val272, Glu213, Ser216, Leu128, Phe129, Met212, Ser125
zoledronic acid hydrate	−5.7	1	Tyr268, Glu213, Ser216, Phe129, Phe124, Ser125, Ser198, Met212, Asp179
pamidronic acid	−4.8	4	Val272, Tyr268, Trp265, Val217, Glu213, Ser216, Val215, Phe129, Met212, Val175, Phe124, Ser125, His121, Ser76, Tyr200, Asp179
docetaxel*	−9.5	2	Leu209, Glu213, Met212, Ser198, Ser216, Arg197, Leu183, Phe124, His121, Trp110, Ile276, Val272, Leu297, Tyr268, His298, Gln301, Leu104
topotecan*	−8.2	2	Tyr268, His298, Gln301, Trp100, Leu104, Trp110, Cys196, Phe124, Leu183, Ser198
tucatinib*	−10.1	1	Val272, Tyr268, Leu104, Arg197, Ser198, Trp110, His121, Phe124, Asp179, Leu183
aldoxorubicin*	−8.4	1	Ile205, Leu209, Tyr200, Ser198, Asp179, Arg197, Leu193, Asp179, His121, Phe124, Ser125, Trp110, Asn108, Leu104, His298, Gln301, Leu297, Val272, Tyr268
vinorelbine*	−9.1	0	Leu297, Tyr268, Phe294, His298, Gln301, Leu43, Leu47, Leu104, Arg197, Trp110, Ser198, Tyr200, Leu209
etoposide*	−9.3	2	Lys 40, Leu43, Asn108, Leu104, Trp100, Trp110, His121, Phe124, Leu183, Gln301
pemetrexed*	−9.1	2	Leu104, Ser103, Trp100, Trp110, Cys196, His121, Phe124, Leu183, Ser198, Tyr200, Val272, Glu213, Ser216
everolimus*	−9.2	3	Leu209, Met33, Asn36, Phe294, His298, Asn39, Leu43, Lys40, Leu104, Asn108, Tyr195, Arg197
thiotepa*	−3.9	1	Tyr268, Val272, Ser216, Phe124

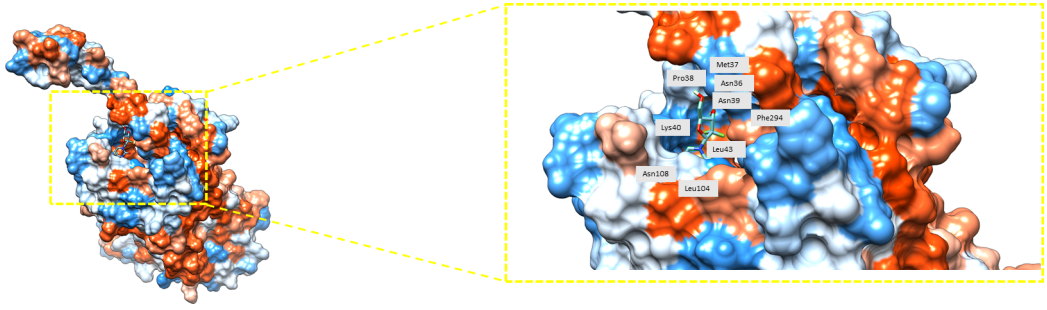

Figure 2: Gemcitabine after blind docking with the protein CXCR7. Blue color indicates the most hydrophilic sites and orange-red the most hydrophobic ones. Interacting residues are labeled as well.

al. [45], it is possible to conclude that the pockets are similar. For instance, doxorubicin was obtained in both cases with Asp179, Cys196, and Trp100 as interacting residues. Also, similar pockets could be obtained because the selected drugs are mostly designed to serve as chemotherapy agents for breast cancer. Thus, it is possible to assume that several drugs share a common mechanism of action and, subsequently, a common protein target, such as CXCR7. For instance, gemcitabine, shown in Figure 2, shares the pocket within CXCR7 with several drugs.

The quantitative descriptors included in the produced models are discussed next. Table 3 contains the used quantitative descriptors and the importance that each one has in the mathematical models. The docking score was the predicted variable in all cases. In addition, the correlation matrix (Supporting Information File 1, Figure S1) was used to build the models. Among the IBM Watson AI models, the first one was obtained using all the initially proposed quantitative descriptors (Table 1). In the second and fourth models, polarizability was not used because, as shown in the correlation matrix, it was found to be closely related to molecular weight. The third and fifth models did not consider molecular weight because of the same relationship with polarizability. Also, the descriptors pK_a, Ac, and PSA were not considered because their importance in the previous models was below 10% (Table 3). Although conceptually different, E_{HOMO} was discarded because it is related to E_{LUMO} and electrophilicity. The last model did not include α because of its relationship with MW. It is important to notice that the most important variables in the six models were NOR, polarizability, LogS, MW, and WS. The least important variables in the six models were E_{LUMO}, pK_a, PSA, E_{HOMO}, and Ac; they all had less than 10% importance in all models. Hence, the computed E_{HOMO} and E_{LUMO} values were not particularly useful in predicting the ligand–protein docking score and, subsequently, the docking score.

To compare the performance offered by the Extra Trees algorithm of Watson AI, a comparison with a family of MLR models was made. Supporting Information File 1 contains the cross-validation for all reported MLR models. Table S2 (Supporting Information File 1) shows the docking scores obtained for the validation set by using both methodologies. With these values, it is possible to appreciate the difference between the docking score obtained directly by molecular docking through Autodock Vina and the prediction of the mathematical models for the external validation set.

To clearly state the performance comparison between AI and MLR, Table 4 reports the values computed for the evaluation metrics proposed for each model. The MSE ranged from 0.30 to 1.73 kcal^2/mol^2, whereas the MAPE varied from 6.1 to 16.37%. Also, MAE values from 0.46 to 1.13 kcal/mol and RMSE values from 0.55 to 1.32 kcal/mol were obtained. The above shows that both AI and MLR approaches accurately model the protein–ligand docking score, yielding higher confidence in the case of Extra Tree regressor models. The best performance, according to the computed minimum errors, was obtained in the

Table 3: Input variables (IV) and output importance (OI) of six Extra Tree regressor models obtained from IBM Watson. Variables are annotated according to Table 1. The best model, according to the MAPE values, is highlighted in bold.

Model 1		Model 2		Model 3		Model 4		Model 5		Model 6	
IV	OI (%)	IV	OI (%)	IV	OI (%)	IV	OI (%)	IV	OI (%)	IV	OI (%)
NOR	100	WS	100	**WS**	**100**	LogS	100	NOR	100	LogS	100
α	57	NOR	97	**LogS**	**99**	MW	53	α	74	NOR	15
LogS	43	LogP	94	**α**	**56**	NOR	26	LogS	49	E_{LUMO}	7
WS	38	LogS	87	**NOR**	**39**	WS	17	WS	31	MW	6
MW	33	MW	20	**ω**	**18**	ω	12	LogP	19	ω	5
LogP	32	Dn	14	**E_{LUMO}**	**6**	E_{LUMO}	5	Dn	13	RBC	0
Ac	8	RBC	12	**E_{HOMO}**	**5**	E_{HOMO}	3	E_{LUMO}	5	Dn	0
Dn	6	E_{LUMO}	7	**PSA**	**4**	PSA	3	RBC	0	Ws	0
E_{HOMO}	2	PSA	4	**pK_a**	**1**	pK_a	1	ω	0	LogP	0
RBC	1	E_{HOMO}	3	**LogP**	**1**	RBC	0	—	—	—	—
PSA	1	pK_a	2	**RBC**	**0**	Ac	0	—	—	—	—
ω	1	Ac	1	**Dn**	**0**	Dn	0	—	—	—	—
pK_a	0	Ω	0	**Ac**	**0**	LogP	0	—	—	—	—
E_{LUMO}	0	—	—	—	—	—	—	—	—	—	—

Table 4: Comparison metrics obtained by the use of AI and MLR in the case of isolated drugs. The best model, according to the MAPE values, is highlighted in bold. The values were computed relative to the validation set.

Error	Model 1		Model 2		Model 3		Model 4		Model 5		Model 6	
	AI	MLR	AI	MLR	AI	MLR	AI	MLR	AI	MLR	AI	MLR
MSE ($kcal^2/mol^2$)	0.93	1.69	0.64	1.73	**0.30**	**1.02**	0.43	1.51	0.82	1.37	0.73	1.10
MAPE (%)	11.51	16.11	9.65	16.37	**6.17**	**11.98**	6.70	15.69	10.92	14.10	10.34	12.49
MAE (kcal/mol)	0.77	1.11	0.64	1.13	**0.46**	**0.82**	0.51	1.08	0.71	0.98	0.66	0.83
RMSE (kcal/mol)	0.97	1.30	0.80	1.32	**0.55**	**1.01**	0.66	1.23	0.91	1.17	0.85	1.05

case of Watson AI model 3. In contrast, the maximum error was obtained in MLR model 2. Thus, the variables denoted in this work can be used for other authors to propose novel chemotherapy drugs assuming CXCR7 as a target.

As mentioned above, the best model was AI model 3 with a MAPE of about 6.17%. Since the AI models are not exportable, our best model is represented by the following functional form: $AI3_{DRUG} = f$(WS, LogS, α, NOR, ω, E_{LUMO}, E_{HOMO}, PSA, pK_a, LogP). The model with the lowest MAPE among those obtained by MLR, computed as 11.98%, is model 3, represented as follows:

$$\begin{aligned} MLR3_{DRUG} = &-5.288 + 0.049 \times WS + 0.318 \times LogS \\ &+0.048 \times \alpha - 0.637 \times NOR + 0.009 \times \omega \\ &-0.054 \times E_{HOMO} + 0.113 \times E_{LUMO} \\ &-0.008 \times PSA - 0.234 \times LogP - 0.014 \times pK_a. \end{aligned} \quad (3)$$

Thus, the AI was useful in selecting the most relevant variables for the formulation of the linear, accurate, and exportable model. Thus, AI is a valuable guide to obtain mathematical models with other methodologies such as MLR. Another significant model is MLR model 6 with the second lowest MAPE of 12.49%. It is worth noting that the model is compact and includes the computed descriptors E_{HOMO} and ω, as well as experimentally determined ones.

$$\begin{aligned} MLR6_{DRUG} = &-4.2179 + 0.4131 \times LogS - 0.5274 \times NOR \\ &+0.2869 \times E_{HOMO} + 0.0009 \times MW \\ &+0.0088 \times \omega. \end{aligned} \quad (4)$$

Although the best AI model was model 3, model 4 is relevant as well. It has the following functional form: $AI4_{DRUG} = f$(LogS, MW, NOR, WS, ω, E_{LUMO}, E_{HOMO}, PSA, pK_a). For this model, the MAPE is about 6.70%. The variables used can be mostly evaluated by computational methods, except for pK_a and LogS.

Drugs modified with C_{60}

Since this study aims to elucidate the potential use of AI suites, such as Watson, to predict the docking score of pristine and modified chemotherapy drugs, the following paragraphs detail the extension of our datasets and models to drugs modified with potential nanocarriers. First, a dataset with 28 drugs, extracted from public datasets or modified from the data annotated in the previous case, was built with the corresponding quantitative descriptors to study complexes of the drugs with fullerene C_{60} or a simple C_{60}–COOH derivative [29]. The resultant dataset is shown in Supporting Information File 1, Table S3. Complexes of the drugs with C_{60} or its derivative with more than one hundred atoms were excluded to save computational resources. Because of that, some maximums and minimums were modified in the dataset. Also, quantities such as the molecular weight or number of rings were shifted to the correspondent values for the drug–fullerene complexes since these modifications are only additive constants. Molecules interacting with C_{60} were studied in this subsection and those modified with the fullerene derivative are the described in the subsequent subsection.

In case of the complexes with C_{60}, the molecular weight is obtained with values above 907.1639 g/mol. The above imposes some restrictions on the usage of fullerene derivatives as drug nanocarriers, since it is accepted that common pharmacological agents applied in topical therapies are under 500 Da [69]. For simplicity, WS, LogP, LogS, pK_a, and α values were taken from isolated drugs. In the case of Dn, Ac, RBC, and PSA, values of the isolated drugs were also used. This is because fullerene is not expected to modify these descriptors since its chemical constitution lacks polar groups or donor/acceptor atoms. The number of rings was only modified with the addition of the fullerene rings from 32 to 39.

As stated in the Methods section, HSAB descriptors were computed for the drug–C_{60} complexes in their ground states while drugs with C_{60} were structurally optimized at the DFTB3 level. Since introducing a species known to act as an electron acceptor, such as fullerene C_{60}, could modify the electron struc-

ture of the modified species [70,71], the energies of the frontier orbitals were recomputed for the modified drugs in their ground states. The energy of the HOMO varied between −3.458 and −5.718 eV. The energy of LUMO ranged from −3.179 to −5.388 eV. The electrophilicity, computed through Koopman's theorem, varied from −134.88 to 280.8 eV. Once the drugs with fullerene C_{60} were globally optimized, molecular docking was conducted with the CXCR7 protein to acquire the docking score, number of established hydrogen bonds, and protein residues interacting with the complex at a distance of 3 Å. The results obtained with Autodock Vina for the 24 complexes and the validation set are presented in Table 5.

The protein–ligand docking score between drug–C_{60} and CXCR7 varied from −13.6 to −9.2 kcal/mol. These values are consistently higher than those computed for the isolated drugs.

Table 5: Docking score, number of established H-bonds after docking, and protein–ligand interacting residues up to 3 Å distance obtained for the drugs modified with C_{60} fullerene. Drugs with the asterisk were used as an external validation set.

Ligands	Score (kcal/mol)	H-bonds	Interacting residues
doxorubicin	−9.2	2	Arg323, Ser316, Val313, Leu326, Phe330, Leu340, Leu343, Val64, Ile57, Ile60
epirubicin	−9.2	0	Arg323, Ser316, Leu326, Tyr322, Leu340, Leu343, Lys342, Val64, Pro312, Ala61, Ile60
lapatinib ditosylate	−9.4	0	Arg323, Ser316, Phe330, Leu326, Tyr322, Leu340, Lys342, Leu343, Val64, Ala61, Ile60
fulvestrant	−11.7	0	Tyr322, Pro312, Leu326, Ala61, Val64, Ile60, Leu340, Leu343, Lys342
dinaciclib	−10.2	1	Val313, Ile60, Ala61, Val64, Leu326, Leu340, Thr340
abemaciclib	−10	0	Arg323, Leu326, Ser316, Tyr322, Leu340, Leu343, Lys342, Val64, Ala61, Ile60
gemcitabine	−10.9	1	Val313, Ile57, Ala61, Ile60, Val64, Leu326, Leu340, Leu343, Phe330
voruciclib	−10.2	0	Val64, Ala61, Ile57, Ile60, Val313, Leu326, Leu340, Thr341, Leu343
fluorouracil	−11.6	0	Pro312, Tyr322, Leu326, Leu340, Leu343, Lys342, Ala61, Val64, Ile60
olaparib	−12.4	2	Val313, Ala61, Ile60, Ile57, Arg323, Leu326, Leu340, Lys342
ixabepilone	−11.7	2	Arg323, Ser316, Val313, Ala61, Val64, Ile60, Leu326, Leu340, Lys342, Leu343
alvocidib	−12.1	0	Val313, Ser316, Tyr322, Leu326, Leu340, Leu343, Lys342, Val64, Ala61, Ile60, Ile57
methotrexate	−9.7	2	Ser316, Pro312, Tyr322, Leu326, Val65, Ala61, Val64, Ile60, Phe330, Leu340, Leu343, Thr341, Lys342
ribociclib	−12.4	0	Ser198, Arg197, Cys196, Tyr195, Trp110, Asn108, Leu104, Lys40, Ser90, Phe94, Asn36, Asp30, Val28
exemestane	−13.6	0	Val313, Pro312, Ser316, Tyr322, Val65, Ala61, Ile57, Val64, Ile60, Leu326, Leu340, Leu343, Lys34
tamoxifen	−9.8	0	Ile66, Leu84, Ile70, Ile88, Leu91, Trp92
idarubicin	−10.1	1	Ser316, Tyr322, Leu326, Leu340, Leu343, Lys342, Ile57, Ile60, Ala61, Val64
palbociclib	−11.2	0	Val313, Ala61, Ile57, Ile60, Val64, Leu343, Leu326
toremifene	−9.9	0	Val313, Ile57, Ile60, Val64, Leu326, Ser350, Leu340, Leu343
roniciclib	−11	2	Met33, Pro35, Asn36, Asp30, Val28, Asn39, Pro38, Ile27, Leu43, Lys40, His107
capecitabine	−9.5	0	Ser316, Tyr322, Leu326, Ala61, Val64, Ile60, Ile57, Leu340, Leu343, Lys342
sulfanilamide	−10.6	1	Cys165, Arg162, Ile166, Leu84, Ile70, Trp92
zoledronic acid hydrate	−9.8	2	Val313, Ile60, Ala61, Ile57, Leu326, Leu340, Lys342, Thr341
pamidronic acid	−9.9	1	Val313, Ser316, Tyr322, Pro312, Leu326, Val64, Ala61, Ile60, Leu340, Lys34, Leu343
topotecan*	−10.1	0	Lys342, Leu343, Leu340, Phe330, Leu326, Ser316, Val313, Ala61, Ile57, Val64, Ile60
tucatinib*	−11	0	Lys342, Leu343, Leu340, Tyr322, Leu326, Val64, Ala61, Ile60, Ile67
pemetrexed*	−11.5	0	Lys342, Thr341, Leu343, Leu340, Phe330, TTyr322, Val64, Ser316, Ala61, Ile60
thiotepa*	−9.9	0	Lys342, Leu343, Leu340, Tyr322, Leu326, Ser316, Val313, Val64, Ile60

In this case, examestane had the highest docking score, whereas epirubicine had the lowest docking score. The number of hydrogen bonds was between 0 and 2. Considering the results of the interacting residues, two things can be highlighted. First, drugs modified with fullerene C_{60} bind outside the protein; second, these binding sites are similar for the analyzed compounds (Figure 3). For example, the serine residue labeled as Ser316 is shared by 14 drugs, indicating that their binding zone is close to each other. Figure 3 shows the binding site between the protein and gemcitabine and the interacting residues.

The predictive QSAR/QSPR models were obtained as in the previous section. Table 6 shows the used quantum descriptors and the importance that each one has in the mathematical models for the drug–C_{60} complexes. The docking score was the predicted variable in all cases. The models for C_{60} were taken directly from the models of the isolated drugs. For example, model 1 for drug–C_{60} complexes considered variables with importance greater than zero from model 1 in the case of isolated drugs. The previous procedure was performed for all models. The most critical variables for the six models were LogP, pK_a, and PSA. The least important variables in the six models were WS and Ac because they have less than 10% importance in the models.

To give a quantitative reference about the performance of the predictive models, Supporting Information File 1, Table S4, shows the scores obtained for the validation set using both methods, the Extra Tree algorithm of IBM Watson and multiple linear regression. With these values, it is possible to appreciate the difference between the docking score obtained by molecular docking and the predictive models for the drug–C_{60} complexes. Table 7 shows the values obtained for the different evaluation metrics for each predictive model. The MSE ranges from 0.44 to 12.77 kcal^2/mol^2, and the MAPE varies from 4.97 to 31.5%. The MAE ranged from 0.5 to 3.26 kcal/mol, whereas the RMSE varied from 0.66 to 3.57 kcal/mol. The minimum

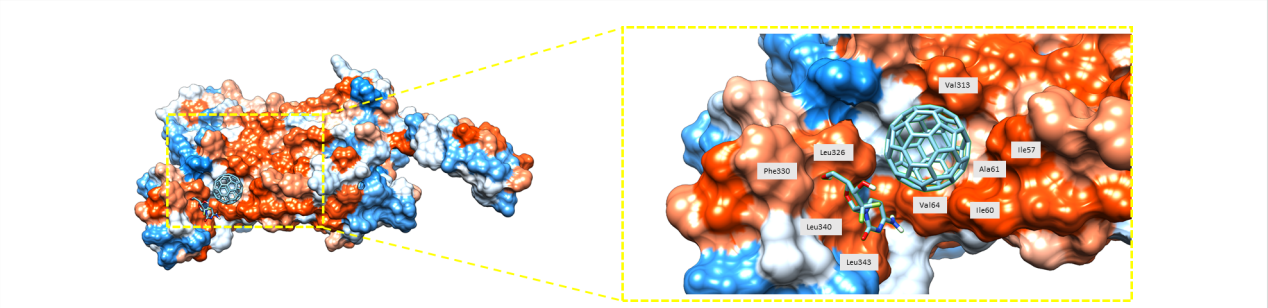

Figure 3: Binding site of gemcitabine–C_{60} and protein CXCR7. Blue color indicates the most hydrophilic sites and orange-red the most hydrophobic ones. Interacting residues are labeled as well.

Table 6: Input variables (IV) and output importance (OI) for six Extra Tree regressor models obtained from IBM Watson. Variables are annotated according to the notation introduced in Table 1. The best models, according to their MAPE values, are highlighted in bold.

Model 1		Model 2		Model 3		Model 4		Model 5		Model 6	
IV	OI (%)	IV	OI (%)	IV	OI (%)	IV	OI (%)	IV	OI (%)	IV	OI (%)
LogP	100	pK_a	100	pK_a	100	**pK_a**	**100**	LogP	100	**MW**	**100**
PSA	97	LogP	55	PSA	69	**PSA**	**66**	Dn	58	**E_{LUMO}**	**96**
RBC	24	PSA	49	LogP	56	**LogS**	**32**	α	18	**ω**	**71**
E_{HOMO}	23	E_{LUMO}	29	E_{LUMO}	24	**E_{LUMO}**	**25**	E_{LUMO}	10	**NOR**	**34**
Dn	17	Dn	20	WS	8	**NOR**	**20**	NOR	6	**LogS**	**0**
ω	11	LogS	7	E_{HOMO}	5	**WS**	**8**	LogS	1	—	—
α	8	E_{HOMO}	1	ω	3	**E_{HOMO}**	**3**	WS	0	—	—
MW	4	Ac	0	α	3	**ω**	**1**	—	—	—	—
LogS	3	RBC	0	LogS	0	**MW**	**0**	—	—	—	—
NOR	1	MW	0	NOR	0	—	—	—	—	—	—
WS	1	NOR	0	—	—	—	—	—	—	—	—
Ac	0	WS	0	—	—	—	—	—	—	—	—

Table 7: Metrics obtained by using IA and MLR for drug–C_{60} complexes. The best models, according to their MAPE values, are highlighted in bold. The values were computed relative to the validation set.

Error	Model 1		Model 2		Model 3		Model 4		Model 5		Model 6	
	AI	MLR	AI	MLR	AI	MLR	AI	MLR	AI	MLR	AI	MLR
MSE (kcal^2/mol^2)	1.62	12.77	3.9	0.86	3.61	3.75	2.38	**0.44**	1.96	2.22	**0.93**	1.77
MAPE (%)	10.99	31.5	18.62	7.58	17.3	17.36	12.96	**4.97**	12.6	12.8	**7.53**	11.94
MAE (kcal/mol)	1.17	3.26	1.97	0.77	1.8	1.8	1.38	**0.5**	1.36	1.34	**0.82**	1.24
RMSE (kcal/mol)	1.27	3.57	1.97	0.92	1.9	1.94	1.54	**0.66**	1.4	1.49	**0.96**	1.33

error for all four metrics was obtained in MLR model 4, while the maximum error was obtained in MLR model 1. Considering the MAPE, the best model, with a value of 4.97%, to predict the docking score is MLR model 4. The explicit form of this model is:

$$\begin{aligned}\mathrm{MLR4}_{\mathrm{DRUG+C60}} = &-10.253 + 0.179\times \mathrm{p}K_{\mathrm{a}} - 0.003\times \mathrm{PSA}\\ &+0.292\times \mathrm{LogS} + 0.719\times E_{\mathrm{LUMO}}\\ &-0.071\times \mathrm{NOR} - 0.057\times \mathrm{WS}\\ &-1.020\times E_{\mathrm{HOMO}} + 0.006\times \omega.\end{aligned} \quad (5)$$

This linear model exhibited a higher performance than the non-exportable approaches provided by the AI. However, one needs to remember that the variables included in model 4 were selected by the initial AI screening. Thus, the selection of variables using AI offers a significant improvement for modeling using other mathematical methods. In addition, all metrics obtained in the case of MLR model 4 are better than those calculated in the case of the best MLR model of the isolated drugs and are comparable to those of the best AI model. Another significant MLR model is the model 2 with a MAPE of 7.58% and the following linear function:

$$\begin{aligned}\mathrm{MLR2}_{\mathrm{DRUG+C60}} = &-12.884 + 0.141\times \mathrm{p}K_{\mathrm{a}} + 0.139\times \mathrm{LogP}\\ &-0.10\times \mathrm{PSA} + 0.649\times E_{\mathrm{LUMO}}\\ &-0.261\times \mathrm{Dn} + 0.268\times \mathrm{LogS}\\ &-0.828\times E_{\mathrm{HOMO}}.\end{aligned} \quad (6)$$

The best AI model is model 6 with a MAPE of about 7.53% and the functional form $\mathrm{AI6}_{\mathrm{DRUG+C60}} = E(\mathrm{MW}, E_{\mathrm{LUMO}}, \omega, \mathrm{NOR})$; all variables can be evaluated by theoretical approaches without the necessity of experimental results. The other significant model from AI, model 1, yielded a higher MAPE value of about 10.99%. In this case, the functional form is $\mathrm{AI1}_{\mathrm{DRUG+C60}} = E(\mathrm{LogP}, \mathrm{PSA}, \mathrm{RBC}, E_{\mathrm{HOMO}}, \mathrm{Dn}, \omega, \alpha, \mathrm{MW}, \mathrm{LogS}, \mathrm{NOR}, \mathrm{WS})$. Despite the large number of variables, including theoretical and experimental ones, the error is larger than those of the previously discussed models.

Drugs modified with C_{60}–COOH

To elucidate the effect of a fullerene derivative, the carboxyfullerene C_{60}–COOH was chosen. A dataset with 19 drugs for the predictive model and four drugs as the validation set was built. The resultant dataset is shown in Supporting Information File 1, Table S5. As in the previous systems, the dataset was reduced to systems with less than 100 atoms. Because of this, ranges of the descriptors and their contributions to the predictive models were modified in the dataset. The molecular weights were increased to values ranging from 915.8022 to 1292.425 g/mol. As in the previous case, WS, LogS, pK_{a}, and LogP are the same as those obtained for the isolated drugs. The hydrogen acceptor count varied between 3 and 13, whereas the hydrogen donor count varied from 1 to 7. Since the carboxylic group is polar, polar surface area values, ranging from 49.77 to 243.22 Å^2, were modified. Also, after the introduction of the polar group, the RBC varied from 1 to 10.

The fullerene derivative C_{60}–COOH was expected to modify the electronic structure of the composed systems. In consequence, the energy of the HOMO of the complexes was recomputed for the globally optimized systems at the DBTB3 level with solvation effects; the results ranged from −3.504 to −5.164 eV. Similarly, the energy of the LUMO varied from −3.48 to −4.437 eV. The electrophilicity computed by Koopman's theorem had variations between 21.675 and 508.086 eV. Molecular docking was performed with the CXCR7 protein to obtain the docking score, number of established hydrogen bonds, and protein residues interacting with the complex at a distance of 3 Å. The results obtained with Autodock Vina for the 19 complexes and the validation set are shown in Table 8.

The resultant docking score between drug–C_{60}–COOH and CXCR7 ranged from −11.7 to −8.8 kcal/mol. As in the previous case, the water-soluble fullerene increased the docking score compared with the isolated drugs (Table 2). Modified ixabepilone had the highest docking score, and the capecitabine had the lowest. The numbers of hydrogen bonds were obtained in a narrow range from 0 to 3.

Table 8: Docking score, number of H-bonds established after docking, and interacting residues of CXCR7 with drug–fullerene C_{60}–COOH complexes at 3 Å distance.

Ligand	Score (kcal/mol)	H-bonds	Interacting residues
dinaciclib	−9.7	0	Lys342, Leu340, Phe330, Leu343, Leu326, Tyr322, Val64, Ile60, Ala61
gemcitabine	−10.6	0	Phe294, Asn36, Asp30, Leu104, Arg197. Trp100, Tyr195, Ser190, Asn108, Lys40, Leu43
voruciclib	−10.3	0	Lys342, Leu343, Leu340, Val64, Leu326, Ser316, Val313, Ala61, Ile60, Ile57, Val56
fluorouracil	−11.4	1	Lys342, Leu343, Leu340, Thr341, Phe330, Leu326, Tyr322, Ser316, Val64, Ile60
olaparib	−11.6	0	Lys342, Leu343, Leu340, Phe330, Val64, Leu326, Tyr322, Arg323, Ser316, Ile60, Ala61, Val313
ixabepilone	−11.7	0	Ser190, Glu193, His107, Lys40, Arg197, Ile205, Pro38, Val28, Ile27
alvocidib	−10.9	1	Lys342, Leu343, Leu340, Val64, Leu326, Tyr322, Ala61, Ile60, Ile57
methotrexate	−10.9	2	Asn108, Lys40, Tyr195, Ser190, Arg197, Ser198, Tyr200, Leu43, Gln301, Tyr268, His298, Phe294, Asn39, Pro38, Asn36, Met37, His291, Asp30, Val28
ribociclib	−11.2	0	Leu104, Asn36, Phe294, Met33, Val32, Arg197, Ser190, Trp110, Tyr195, Asp30, Ile205, Lys206
exemestane	−11.6	1	Lys342, Leu343, Leu340, Leu326, Phe330, Ala61, Ile60, Ile57, Val313
tamoxifen	−9.1	0	Leu340, Leu326, Phe330, Ser316, Ile60, Val313, Ala61, Ile60, Ile57, Val56
idarubicin	−10.6	0	Leu343, Leu340, Lys342, Val64, Tyr322, Pro312, Ser316, Val313, Phe330, Ile60, Ile57
palbociclib	−11.4	0	Ile166, Arg162, Cys165, Cys81, Asn85, Ile88, Trp92, Ile70, Val66
toremifene	−9	0	Leu343, Lys342, Ser350, Leu340, Val64, Leu326, Ala61, Ser316, Ile60, Ile57
roniciclib	−9.2	0	Lys342, Leu343, Leu340, Leu326, Arg323, Val64, Ala61, Ile60, Ile57
capecitabine	−8.8	0	Thr341, Leu343, Leu340, Val64, Phe330, Leu326, Ala61, Ile60, Ile57, Val313
sulfanilamide	−10.7	1	Lys342, Leu343, Thr341, Leu340, Leu326, Tyr322, Ser316, Pro312, Val64, Ala61, Ile60
zoledronic acid hydrate	−10	0	Lys342, Leu343, Val64, Val65, Leu326, Tyr322, Ser316, Val313, Pro312, Ala61, Ile57
pamidronic acid	−10.6	3	Leu122, Ile126, Ile123, Trp169, Trp92, Ile166, Asn85, Cys165
topotecan*	−12.6	2	Thr341, Phe330, Leu340, Leu343, Leu326, Val64, Tyr322, Ser316, Val65, Pro312, Val313, Ala61, Ile60, Ile57
tucatinib*	−10.9	1	Leu343, Lys342, Leu340, Thr341, Val64, Tyr322, Leu326, Ser316, Val313, Ile60, Ala61, Val56, Ile57
pemetrexed*	−9.9	1	Ile166, Arg162, Trp92, Ile88, Leu84, Asn85, Thr75, Cys81
thiotepa*	−9.4	0	Lys342, Leu343, Leu340, Thr341, Val64, Leu326, Phe330, Ile60

Considering the residues shown in Table 8 for the drug–fullerene complex with the protein, there are three possible binding sites. The first one is located inside the protein, near the pocket determined for isolated drugs. This binding site is near phenylalanine Phe294 and arginine Arg197 (Figure 4a) as prominent residues. The second possible binding site is outside the protein, near where drug–C_{60} binds; common residues are serine Ser316 and valine Val313 (Figure 4b). The third binding site is also at the outside of the protein and characterized by isoleucine Ile166 and arginine Arg162 (Figure 4c).

Table 9 shows the quantitative descriptors used and the importance that each one has in the predictive models for drug–C_{60}–COOH. The docking score was the predicted variable in all the cases. In addition, the variables used to obtain the models in the case of drug–C_{60} were initially considered. The variables to model the interaction with C_{60}–COOH were taken directly from those of drug–C_{60}. For example, AI model 1 with C_{60}–COOH used the variables that had an importance greater than zero from AI model 1 of drug–C_{60}. The most important variables in the six models were LogP, RBC, and Dn. The least important variable in the six models was WS because had less than 10% importance in all models.

Supporting Information File 1, Table S6 shows the docking scores obtained for the validation set using both methods, that

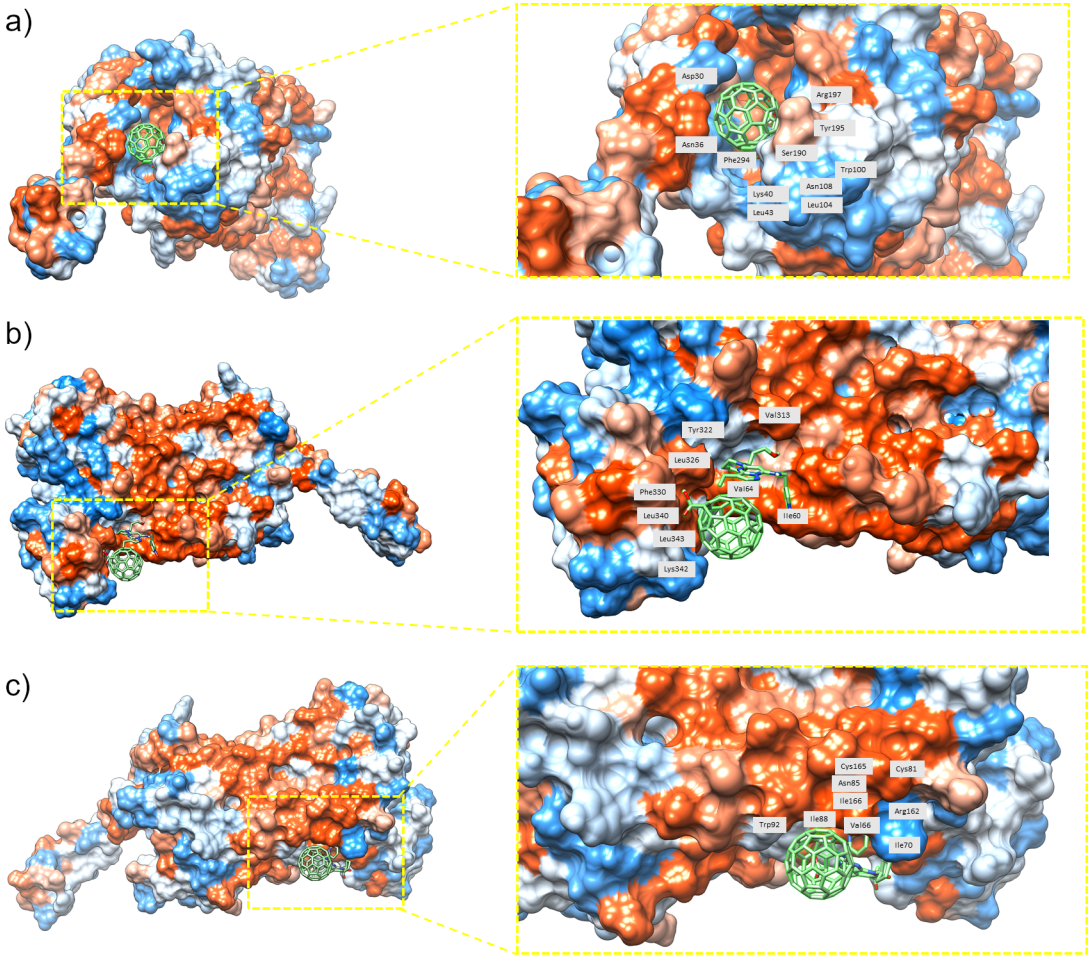

Figure 4: Binding sites for (a) gemcitabine, (b) dinaciclib, and (c) palbociclib with C_{60}–COOH and protein CXCR7. Blue color indicates the most hydrophilic sites and orange-red the most hydrophobic ones. Interacting residues are labeled as well.

Table 9: Input variables (IV) and output importance (OI) obtained for six Extra Tree regressor models obtained from IBM Watson. Variables are annotated according to the notation introduced in Table 1. The best models, according to their MAPE values, are highlighted in bold.

Model 1		Model 2		Model 3		Model 4		Model 5		Model 6	
IV	OI (%)	IV	OI (%)	IV	OI (%)	IV	OI (%)	IV	OI (%)	IV	OI (%)
RBC	**100**	pK_a	100	PSA	100	**Ω**	**100**	LogP	100	MW	100
LogP	**34**	LogP	96	LogP	77	**pK_a**	**93**	LogS	90	NOR	96
Dn	**20**	Dn	69	pK_a	72	**PSA**	**70**	α	83	E_{LUMO}	38
WS	**10**	LogS	64	A	42	**E_{LUMO}**	**31**	NOR	61	ω	0
LogS	**6**	E_{HOMO}	30	E_{HOMO}	32	**NOR**	**5**	Dn	52	—	—
NOR	**5**	PSA	12	E_{LUMO}	26	**E_{HOMO}**	**2**	E_{LUMO}	0	—	—
ω	**2**	E_{LUMO}	0	WS	3	**LogS**	**1**	—	—	—	—
MW	**1**	—	—	ω	0	**WS**	**0**	—	—	—	—
E_{HOMO}	**0**	—	—	—	—	—	—	—	—	—	—
PSA	**0**	—	—	—	—	—	—	—	—	—	—
α	**0**	—	—	—	—	—	—	—	—	—	—

is, the Extra Tree regressors implemented in IBM Watson and the MLR. With these values, it is possible to compare the difference in the docking score obtained by molecular docking and the prediction of the mathematical models for drug–C_{60}–COOH and the protein CXCR7. Table 10 shows the values obtained for the different types of errors in each of the models. The MSE ranged from 0.77 to 4.73 kcal^2/mol^2, whereas the MAPE varied from 6.70 to 16.22%. Also, the MAE was obtained ranging from 0.69 to 6.52 kcal/mol. Finally, the RMSE varied from 0.88 to 2.18 kcal/mol. Considering the MAPE, the best model, with a value of 6.7%, to predict the docking score is MLR model 1. Once again, the synergistic effect of using AI with a mathematical tool such as MLR is observed. The benefits are the predictive model's clarity, whereas AI was useful in determining the most important descriptors to be included in the QSAR/QSPR model. The explicit form of this model is:

$$\begin{aligned}\mathrm{MLR1}_{\mathrm{DRUG+C60\text{-}COOH}} = &-13.597 + 0.047\times \mathrm{p}K_a + 0.33\times \mathrm{LogP} \\ &+0.18\times \mathrm{Dn} + 0.284\times \mathrm{LogS} \\ &-0.696\times E_{\mathrm{HOMO}} - 0.007\times \mathrm{PSA}.\end{aligned} \quad (7)$$

The other significant model is MLR model 5 with a MAPE of 10.17%. In this model, experimental and theoretical descriptors were mixed. The following is the explicit form of MLR model 5:

$$\begin{aligned}\mathrm{MLR5}_{\mathrm{DRUG+C60\text{-}COOH}} = &\ 2.480 + 0.552\times \mathrm{LogP} \\ &+0.21\times \mathrm{LogS} + 0.002\times \alpha \\ &-0.402\times \mathrm{NOR} + 0.186\times \mathrm{Dn}.\end{aligned} \quad (8)$$

Considering the MAPE, the best AI model is model 4 with a value of 8.18% and the functional form $\mathrm{AI4}_{\mathrm{DRUG+C60\text{-}COOH}} = f$ (E_{HOMO}, ω, pK_a, PSA, E_{LUMO}, LogS, NOR). The other significant model obtained from AI is model 5, with a MAPE value of 8.69%; the functional form of this model is $\mathrm{AI5}_{\mathrm{DRUG+C60\text{-}COOH}} = f$ (LogP, α, LogS, NOR, Dn). Thus, although the Extra Trees algorithm was competitive in the case of drugs modified with a carboxyfullerene, this approach was surpassed by the MLR with the AI choosing the most important variables.

Doxorubicin and gemcitabine with a water-soluble fullerene

Finally, doxorubicin and gemcitabine were selected to compare the DFTB3 approach with the regular DFT method. In addition, their interactions with a water-soluble fullerene derivative were studied as well. Both anticancer agents are presented in Figure 5 interacting with a water-soluble fullerene [36,37]. Doxorubicin, an antibiotic that belongs to the family of tetracycline pharmaceutical agents, has gained popularity among chemotherapy agents and was recently modified with fullerene C_{60} [72-75]. Its anticarcinogenic activity comes from its ability to intercalate into DNA, inducing damage of the DNA strands and inhibiting its replication. Also, doxorubicin contributes to stopping the action of the enzyme topoisomerase II, leading to apoptosis of living tissues [71]; therefore, it is important to study its intrinsic chemical reactivity.

At the B3PW91/6-31G level of DFT, it is possible to appreciate that the periphery of the doxorubicin molecule is saturated by organic substituents. Its oxy, carbonyl, and carboxy terminal groups are active sites to interact with DNA or amino acids. The molecular orbital scheme of this molecule is shown in Supporting Information File 1, Figure S2, together with its molecular electrostatic potential (ESP). In the case of doxorubicin, from frontier molecular orbitals theory, HOMO and LUMO were found on the tetracycline moiety. However, the HOMO is confined to the quinoid ring, whereas the LUMO is completely delocalized (Supporting Information File 1, Figure S2). Oxygen atoms are the regions with the most negative ESP (red color in Supporting Information File 1, Figure S2). In contrast, a high electrostatic potential (blue color in Supporting Information File 1, Figure S2) is found on the lateral substituted cycle. Both central rings, the aromatic one and the quinoid one, are the main regions for the reactivity, including all the substituent oxygen atoms. The frontier molecular orbitals are similar, and it is ex-

Table 10: Metrics obtained by the use of AI and MLR in the case of drug–C_{60}–COOH. The best models, according to their MAPE values, are highlighted in bold. Values were computed relative to the validation set.

Error	Model 1		Model 2		Model 3		Model 4		Model 5		Model 6	
	AI	MLR	AI	MLR	AI	MLR	AI	MLR	AI	MLR	AI	MLR
MSE (kcal^2/mol^2)	0.97	**0.77**	1.67	1.77	1.80	4.73	**1.05**	1.53	1.41	2.08	1.46	1.80
MAPE (%)	8.75	**6.70**	10.51	12.03	10.71	16.22	**8.18**	10.26	8.69	10.17	10.86	11.39
MAE (kcal/mol)	0.93	**0.69**	1.13	1.29	1.17	6.52	**0.86**	1.10	0.93	0.99	1.16	1.18
RMSE (kcal/mol)	0.98	**0.88**	1.29	1.33	1.34	2.18	**1.02**	1.24	1.19	1.44	1.21	1.34

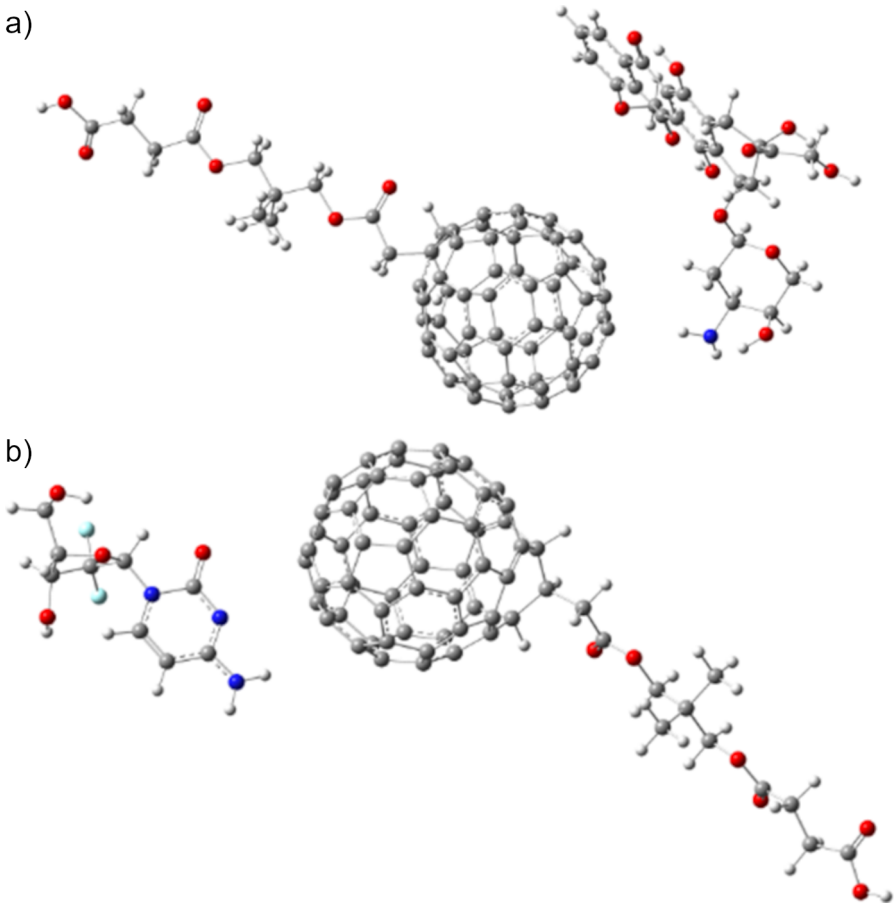

Figure 5: Ground state structures of (a) doxorubicin and (b) gemcitabine interacting with a water-soluble fullerene.

pected that electronic transit can occur in this region accepting and donating negative charges. The ESP map reinforces this suggestion showing negative density sites as well as a positive center, which can receive electrons. The energy of the HOMO was computed as −5.978 eV and that of the LUMO as −4.221 eV at the DFTB3 level. In comparison, the B3PW91 method yielded −6.116 and −3.242 eV, respectively. Thus, to consider the models obtained here, it is recommended to use DFTB3 to compute the electronic and energetic properties instead of DFT calculations.

Gemcitabine includes an active pyrimidinone fragment as a very reactive zone. The frontier molecular orbitals and the ESP map are shown Supporting Information File 1, Figure S2. Again, there is a strong polarization, which can induce a route for reaction. The ring nitrogen atom in alpha position concerning the carbonyl group is the more nucleophilic center, whereas there are two positive-density regions near the carbonyl group and in the C–C bond next to the amine-substituted carbon atom.

Both pharmaceutical agents are susceptible to interaction with fullerenes to form a force dispersion complex as it has been previously suggested. However, these complexes should be water-soluble to be delivered to their host. Considering all these factors, a water-soluble species was used to form such complexes, the structure of which [76] is shown in Figure 5. In both cases, a strong hydrogen bond is present; the distances are 1.97 Å for the doxorubicin complex and 2.25 Å for the gemcitabine complex. Furthermore, the energy of these interactions was calculated taking advantage of the Grimme module; they are 23.7 kcal/mol for doxorubicin and 18.9 kcal/mol for gemcitabine.

Conclusion

A QSAR/QSPR study of drugs commonly used for breast cancer chemotherapy modified with fullerene derivatives as drug nanocarriers was carried out. The CXCR7 protein was selected as a target for molecular docking calculations; the drugs were studied in the isolated form and modified with C_{60}

fullerene and with the water-soluble C_{60}–COOH fullerene derivative. An initial dataset was built by analyzing more than 30 drugs. The models to predict the docking score were obtained concerning Pearson's HSAB concept and common QSAR/QSPR descriptors. The energetic descriptors were computed quantum chemically by using density functional-based tight binding at the DFTB3 level. The highest docking score in the case of isolated drugs was −10.1 kcal/mol for olaparib. In contrast, in the case of the drugs modified with pristine C_{60} fullerene, it was −13.6 kcal/mol for exemestane. In the case of the drugs modified with the water-soluble fullerene derivative C_{60}–COOH, the maximum docking score was −11.7 kcal/mol for ixabepilone. Hence, the complexes are supposed to dock with stronger interactions with the CXCR7 protein than the isolated drugs. Also, characteristic binding sites were determined. The pocket of the isolated drugs was found within the protein, sharing residues including Trp100, Leu297, and Ser198. In the case of the drugs with fullerene C_{60}, the binding site was outside the protein with the complex pointing away from the pocket. The interacting residues included Arg323, Ser316, and Lys342. In the case of the drugs with C_{60}–COOH fullerene, there were three possible binding sites. The first two are the same as those in the previous cases The third binding site was found outside the protein, near the residues Ile166, Arg192, and Cys165. The docking score for the drug–fullerene complex is higher than that of the isolated drugs. QSAR/QSPR predictive models for the docking score were obtained from MLR and from IBM Watson artificial intelligence, yielding models with a MAPE of lower than 12% in all three cases. Although MLR exhibits the best evaluation metrics in the case of drug–C_{60} and drug–C_{60}–COOH complexes, an improvement is obtained based on the variables detected by the AI as the most important ones.

Supporting Information

Supporting Information File 1

Additional tables and figures.
[https://www.beilstein-journals.org/bjnano/content/supplementary/2190-4286-15-95-S1.pdf]

Acknowledgements

The authors thankfully acknowledge the computer resources, technical expertise, and support provided by Laboratorio de Supercómputo del Bajío, a member of the network of national laboratories. Also, the authors thank the Hasso Plattner Institute. Dedicated to the strongest and bravest woman ever, a survivor of breast cancer, my mom (A.M.).

Funding

A. Miralrio thanks the Challenge Based Research Funding program of Tecnológico de Monterrey.

Author Contributions

Jonathan-Siu-Loong Robles-Hernández: data curation; formal analysis; investigation; software; validation; visualization; writing – original draft. Dora Iliana Medina: formal analysis; funding acquisition; project administration; supervision; writing – review & editing. Katerin Aguirre-Hurtado: data curation; investigation; software; writing – original draft. Marlene Bosquez: data curation; formal analysis; investigation; software; writing – original draft. Roberto Salcedo: conceptualization; data curation; formal analysis; funding acquisition; investigation; methodology; project administration; supervision; writing – review & editing. Alan Miralrio: conceptualization; formal analysis; funding acquisition; investigation; methodology; project administration; resources; supervision; validation; writing – review & editing.

ORCID® iDs

Jonathan-Siu-Loong Robles-Hernández - https://orcid.org/0009-0004-8982-0650
Dora Iliana Medina - https://orcid.org/0000-0001-5325-0079
Katerin Aguirre-Hurtado - https://orcid.org/0009-0000-5084-8008
Marlene Bosquez - https://orcid.org/0009-0008-1268-1153
Roberto Salcedo - https://orcid.org/0000-0003-1909-7757
Alan Miralrio - https://orcid.org/0000-0002-7992-3718

Data Availability Statement

The data that supports the findings of this study is available from the corresponding author upon reasonable request.

References

1. Giaquinto, A. N.; Miller, K. D.; Tossas, K. Y.; Winn, R. A.; Jemal, A.; Siegel, R. L. *Ca-Cancer J. Clin.* **2022,** *72,* 202–229. doi:10.3322/caac.21718
2. Miller, K. D.; Ortiz, A. P.; Pinheiro, P. S.; Bandi, P.; Minihan, A.; Fuchs, H. E.; Martinez Tyson, D.; Tortolero-Luna, G.; Fedewa, S. A.; Jemal, A. M.; Siegel, R. L. *Ca-Cancer J. Clin.* **2021,** *71,* 466–487. doi:10.3322/caac.21695
3. Wendt, C.; Margolin, S. *Acta Oncol.* **2019,** *58,* 135–146. doi:10.1080/0284186x.2018.1529428
4. Faruk, T.; Islam, M. K.; Arefin, S.; Haq, M. Z. *Clin. Breast Cancer* **2015,** *15,* 313–324. doi:10.1016/j.clbc.2015.01.002
5. Giaquinto, A. N.; Sung, H.; Miller, K. D.; Kramer, J. L.; Newman, L. A.; Minihan, A.; Jemal, A.; Siegel, R. L. *Ca-Cancer J. Clin.* **2022,** *72,* 524–541. doi:10.3322/caac.21754
6. Siegel, R. L.; Miller, K. D.; Wagle, N. S.; Jemal, A. *Ca-Cancer J. Clin.* **2023,** *73,* 17–48. doi:10.3322/caac.21763
7. Sung, H.; Ferlay, J.; Siegel, R. L.; Laversanne, M.; Soerjomataram, I.; Jemal, A.; Bray, F. *Ca-Cancer J. Clin.* **2021,** *71,* 209–249. doi:10.3322/caac.21660

8. Arnold, M.; Morgan, E.; Rumgay, H.; Mafra, A.; Singh, D.; Laversanne, M.; Vignat, J.; Gralow, J. R.; Cardoso, F.; Siesling, S.; Soerjomataram, I. *Breast* **2022,** *66,* 15–23. doi:10.1016/j.breast.2022.08.010
9. Anderson, D. *Mutat. Res., Fundam. Mol. Mech. Mutagen.* **1995,** *329,* 37–47. doi:10.1016/0027-5107(95)00017-d
10. Hay, J.; Shahzeidi, S.; Laurent, G. *Arch. Toxicol.* **1991,** *65,* 81–94. doi:10.1007/bf02034932
11. Meyer, K. B.; Madias, N. E. *Miner Electrolyte Metab.* **1994,** *20,* 201–213.
12. Bentzen, S. M. *Nat. Rev. Cancer* **2006,** *6,* 702–713. doi:10.1038/nrc1950
13. Delanian, S.; Porcher, R.; Rudant, J.; Lefaix, J.-L. *J. Clin. Oncol.* **2005,** *23,* 8570–8579. doi:10.1200/jco.2005.02.4729
14. Dunnwald, L. K.; Rossing, M. A.; Li, C. I. *Breast Cancer Res.* **2007,** *9,* R6. doi:10.1186/bcr1639
15. Asif, H. M.; Sultana, S.; Ahmed, S.; Akhtar, N.; Tariq, M. *Asian Pac. J. Cancer Prev.* **2016,** *17,* 1609–1615. doi:10.7314/apjcp.2016.17.4.1609
16. Shi, Y.; Riese, D. J., II; Shen, J. *Front. Pharmacol.* **2020,** *11,* 574667. doi:10.3389/fphar.2020.574667
17. Sherif, M. F.; Ismail, I. M.; Ata, S. M. S. *Ann. Diagn. Pathol.* **2020,** *49,* 151621. doi:10.1016/j.anndiagpath.2020.151621
18. Xu, L.; Li, C.; Hua, F.; Liu, X. *Med. Oncol.* **2021,** *38,* 58. doi:10.1007/s12032-021-01481-2
19. Ding, C.; Li, Z. *Mater. Sci. Eng., C* **2017,** *76,* 1440–1453. doi:10.1016/j.msec.2017.03.130
20. Hossen, S.; Hossain, M. K.; Basher, M. K.; Mia, M. N. H.; Rahman, M. T.; Uddin, M. J. *J. Adv. Res.* **2019,** *15,* 1–18. doi:10.1016/j.jare.2018.06.005
21. Krätschmer, W.; Lamb, L. D.; Fostiropoulos, K.; Huffman, D. R. *Nature* **1990,** *347,* 354–358. doi:10.1038/347354a0
22. Krusic, P. J.; Wasserman, E.; Keizer, P. N.; Morton, J. R.; Preston, K. F. *Science* **1991,** *254,* 1183–1185. doi:10.1126/science.254.5035.1183
23. Markovic, Z.; Trajkovic, V. *Biomaterials* **2008,** *29,* 3561–3573. doi:10.1016/j.biomaterials.2008.05.005
24. Castro, E.; Garcia, A. H.; Zavala, G.; Echegoyen, L. *J. Mater. Chem. B* **2017,** *5,* 6523–6535. doi:10.1039/c7tb00855d
25. Lichota, A.; Krokosz, A. *Med. Pr.* **2016,** *67,* 817–831. doi:10.13075/mp.5893.00466
26. Krishna, V.; Singh, A.; Sharma, P.; Iwakuma, N.; Wang, Q.; Zhang, Q.; Knapik, J.; Jiang, H.; Grobmyer, S. R.; Koopman, B.; Moudgil, B. *Small* **2010,** *6,* 2236–2241. doi:10.1002/smll.201000847
27. Kumar, M.; Raza, K. *Pharm. Nanotechnol.* **2018,** 5. doi:10.2174/2211738505666170301142232
28. Panova, G. G.; Zhuravleva, A. S.; Khomyakov, Y. V.; Vertebnyi, V. E.; Ageev, S. V.; Petrov, A. V.; Podolsky, N. E.; Morozova, E. I.; Sharoyko, V. V.; Semenov, K. N. *J. Mol. Struct.* **2021,** *1235,* 130163. doi:10.1016/j.molstruc.2021.130163
29. Ye, S.; Zhou, T.; Cheng, K.; Chen, M.; Wang, Y.; Jiang, Y.; Yang, P. *Nanoscale Res. Lett.* **2015,** *10,* 246. doi:10.1186/s11671-015-0953-9
30. Danishuddin; Khan, A. U. *Drug Discovery Today* **2016,** *21,* 1291–1302. doi:10.1016/j.drudis.2016.06.013
31. Chen, X.; Li, H.; Tian, L.; Li, Q.; Luo, J.; Zhang, Y. *J. Comput. Biol.* **2020,** *27,* 1397–1406. doi:10.1089/cmb.2019.0323
32. Pearson, R. G. *J. Am. Chem. Soc.* **1963,** *85,* 3533–3539. doi:10.1021/ja00905a001
33. Chattaraj, P. K.; Giri, S. *Annu. Rep. Prog. Chem., Sect. C: Phys. Chem.* **2009,** *105,* 13. doi:10.1039/b802832j
34. Bağlayan, Ö.; Parlak, C.; Dikmen, G.; Alver, Ö. *Comput. Theor. Chem.* **2023,** *1221,* 114036. doi:10.1016/j.comptc.2023.114036
35. Parlak, C.; Alver, Ö. *J. Indian Chem. Soc.* **2022,** *99,* 100769. doi:10.1016/j.jics.2022.100769
36. Pérez-Manríquez, L.; Ramos, E.; Rangel, E.; Salcedo, R. *Mol. Simul.* **2013,** *39,* 612–620. doi:10.1080/08927022.2012.758845
37. Bosquez, M.; Fomina, L.; Salcedo, R. *Mol. Simul.* **2020,** *46,* 398–407. doi:10.1080/08927022.2020.1714042
38. Muratov, E. N.; Bajorath, J.; Sheridan, R. P.; Tetko, I. V.; Filimonov, D.; Poroikov, V.; Oprea, T. I.; Baskin, I. I.; Varnek, A.; Roitberg, A.; Isayev, O.; Curtalolo, S.; Fourches, D.; Cohen, Y.; Aspuru-Guzik, A.; Winkler, D. A.; Agrafiotis, D.; Cherkasov, A.; Tropsha, A. *Chem. Soc. Rev.* **2020,** *49,* 3525–3564. doi:10.1039/d0cs00098a
39. Selassie, C.; Verma, R. P. History of Quantitative Structure–Activity Relationships. In *Burger's Medicinal Chemistry and Drug Discovery;* Abraham, D. J., Ed.; Wiley, 2010; pp 1–96. doi:10.1002/0471266949.bmc001.pub2
40. Hourahine, B.; Aradi, B.; Blum, V.; Bonafé, F.; Buccheri, A.; Camacho, C.; Cevallos, C.; Deshaye, M. Y.; Dumitrică, T.; Dominguez, A.; Ehlert, S.; Elstner, M.; Van Der Heide, T.; Hermann, J.; Irle, S.; Kranz, J. J.; Köhler, C.; Kowalczyk, T.; Kubař, T.; Lee, I. S.; Lutsker, V.; Maurer, R. J.; Min, S. K.; Mitchell, I.; Negre, C.; Niehaus, T. A.; Niklasson, A. M. N.; Page, A. J.; Pecchia, A.; Penazzi, G.; Persson, M. P.; Řezáč, J.; Sánchez, C. G.; Sternberg, M.; Stöhr, M.; Stuckenberg, F.; Tkatchenko, A.; Yu, V. W.-z.; Frauenheim, T. *J. Chem. Phys.* **2020,** *152,* 124101. doi:10.1063/1.5143190
41. Gaus, M.; Goez, A.; Elstner, M. *J. Chem. Theory Comput.* **2013,** *9,* 338–354. doi:10.1021/ct300849w
42. Vainio, M. J.; Johnson, M. S. *J. Chem. Inf. Model.* **2007,** *47,* 2462–2474. doi:10.1021/ci6005646
43. Wang, C.; Chen, W.; Shen, J. *Front. Pharmacol.* **2018,** *9,* 10.3389/fphar.2018.00641. doi:10.3389/fphar.2018.00641
44. Yang, J.; Zhang, Y. *Nucleic Acids Res.* **2015,** *43,* W174–W181. doi:10.1093/nar/gkv342
45. Muthiah, I.; Rajendran, K.; Dhanaraj, P.; Vallinayagam, S. *J. Biomol. Struct. Dyn.* **2021,** *39,* 4807–4815. doi:10.1080/07391102.2020.1783365
46. Laskowski, R. A.; MacArthur, M. W.; Moss, D. S.; Thornton, J. M. *J. Appl. Crystallogr.* **1993,** *26,* 283–291. doi:10.1107/s0021889892009944
47. Eberhardt, J.; Santos-Martins, D.; Tillack, A. F.; Forli, S. *J. Chem. Inf. Model.* **2021,** *61,* 3891–3898. doi:10.1021/acs.jcim.1c00203
48. Ganapathiraju, M.; Balakrishnan, N.; Reddy, R.; Klein-Seetharaman, J. *BMC Bioinf.* **2008,** *9,* S4. doi:10.1186/1471-2105-9-s1-s4
49. Tusnády, G. E.; Simon, I. *Bioinformatics* **2001,** *17,* 849–850. doi:10.1093/bioinformatics/17.9.849
50. Chen, Y.; Elenee Argentinis, J.; Weber, G. *Clin. Ther.* **2016,** *38,* 688–701. doi:10.1016/j.clinthera.2015.12.001
51. Geurts, P.; Ernst, D.; Wehenkel, L. *Mach. Learn.* **2006,** *63,* 3–42. doi:10.1007/s10994-006-6226-1
52. Suzuki, J. *Statistical Learning with Math and Python: 100 Exercises for Building Logic;* Springer Singapore: Singapore, 2021. doi:10.1007/978-981-15-7877-9
53. Costa, A.; Nannicini, G. *Math. Program. Comput.* **2018,** *10,* 597–629. doi:10.1007/s12532-018-0144-7

54. Methods in molecular biology. In *Topics in Biostatistics;* Ambrosius, W. T., Ed.; Humana Press: Totowa, N.J., 2007. doi:10.1007/978-1-59745-530-5
55. Yang, L.; Sang, C.; Wang, Y.; Liu, W.; Hao, W.; Chang, J.; Li, J. *Chemosphere* **2021,** *285,* 131456. doi:10.1016/j.chemosphere.2021.131456
56. Keshavarz, M. H.; Shirazi, Z.; Kiani Sheikhabadi, P. *Process Saf. Environ. Prot.* **2021,** *150,* 137–147. doi:10.1016/j.psep.2021.04.011
57. Lomba, L.; Ribate, M. P.; Zuriaga, E.; García, C. B.; Giner, B. *Ecotoxicol. Environ. Saf.* **2019,** *172,* 232–239. doi:10.1016/j.ecoenv.2019.01.081
58. Sadeghi, F.; Afkhami, A.; Madrakian, T.; Ghavami, R. *J. Iran. Chem. Soc.* **2021,** *18,* 2785–2800. doi:10.1007/s13738-021-02233-9
59. Zuriaga, E.; Giner, B.; Valero, M. S.; Gómez, M.; García, C. B.; Lomba, L. *Chemosphere* **2019,** *227,* 480–488. doi:10.1016/j.chemosphere.2019.04.054
60. Fadilah, F.; Arsianti, A.; Yanuar, A.; Andrajati, R.; Indah Paramita, R.; Hernawati Purwaningsih, E. *Orient. J. Chem.* **2018,** *34,* 2656–2660. doi:10.13005/ojc/340558
61. El Rhabori, S.; El Aissouq, A.; Chtita, S.; Khalil, F. *J. Indian Chem. Soc.* **2022,** *99,* 100675. doi:10.1016/j.jics.2022.100675
62. Er-Rajy, M.; ElFadili, M.; Mrabti, N. N.; Zarougui, S.; Elhallaoui, M. *Chin. J. Anal. Chem.* **2022,** *50,* 100163. doi:10.1016/j.cjac.2022.100163
63. Silva, A. M.; Martins-Gomes, C.; Silva, T. L.; Coutinho, T. E.; Souto, E. B.; Andreani, T. *Toxics* **2022,** *10,* 378. doi:10.3390/toxics10070378
64. Hansch, C.; Steinmetz, W. E.; Leo, A. J.; Mekapati, S. B.; Kurup, A.; Hoekman, D. *J. Chem. Inf. Comput. Sci.* **2003,** *43,* 120–125. doi:10.1021/ci020378b
65. Sudhakaran, S.; Calvin, J.; Amy, G. L. *Chemosphere* **2012,** *87,* 144–150. doi:10.1016/j.chemosphere.2011.12.006
66. Ogunyemi, B. T.; Latona, D. F.; Adejoro, I. A. *Sci. Afr.* **2020,** *8,* e00336. doi:10.1016/j.sciaf.2020.e00336
67. Bodun, D. S.; Omoboyowa, D. A.; Omotuyi, O. I.; Olugbogi, E. A.; Balogun, T. A.; Ezeh, C. J.; Omirin, E. S. *Comput. Biol. Chem.* **2023,** *104,* 107865. doi:10.1016/j.compbiolchem.2023.107865
68. Trott, O.; Olson, A. J. *J. Comput. Chem.* **2010,** *31,* 455–461. doi:10.1002/jcc.21334
69. Bos, J. D.; Meinardi, M. M. H. M. *Exp. Dermatol.* **2000,** *9,* 165–169. doi:10.1034/j.1600-0625.2000.009003165.x
70. Haddon, R. C. *Philos. Trans. R. Soc., A* **1993,** *343,* 53–62. doi:10.1098/rsta.1993.0040
71. Sergio, M.; Behzadi, H.; Otto, A.; van der Spoel, D. *Environ. Chem. Lett.* **2013,** *11,* 105–118. doi:10.1007/s10311-012-0387-x
72. Panchuk, R. R.; Prylutska, S. V.; Chumak, V. V.; Skorokhyd, N. R.; Lehka, L. V.; Evstigneev, M. P.; Prylutskyy, Y. I.; Berger, W.; Heffeter, P.; Scharff, P.; Ritter, U.; Stoika, R. S. *J. Biomed. Nanotechnol.* **2015,** *11,* 1139–1152. doi:10.1166/jbn.2015.2058
73. Butowska, K.; Kozak, W.; Zdrowowicz, M.; Makurat, S.; Rychłowski, M.; Hać, A.; Herman-Antosiewicz, A.; Piosik, J.; Rak, J. *Struct. Chem.* **2019,** *30,* 2327–2338. doi:10.1007/s11224-019-01428-4
74. Grebinyk, A.; Prylutska, S.; Grebinyk, S.; Prylutskyy, Y.; Ritter, U.; Matyshevska, O.; Dandekar, T.; Frohme, M. *Nanoscale Res. Lett.* **2019,** *14,* 61. doi:10.1186/s11671-019-2894-1
75. Liu, J.-H.; Cao, L.; Luo, P. G.; Yang, S.-T.; Lu, F.; Wang, H.; Meziani, M. J.; Haque, S. A.; Liu, Y.; Lacher, S.; Sun, Y.-P. *ACS Appl. Mater. Interfaces* **2010,** *2,* 1384–1389. doi:10.1021/am100037y
76. Martín, N.; Altable, M.; Filippone, S.; Martín-Domenech, A. *Synlett* **2007,** 3077–3095. doi:10.1055/s-2007-990939

License and Terms

BEILSTEIN JOURNAL OF NANOTECHNOLOGY

Heterogeneous reactions in a HFCVD reactor: simulation using a 2D model

Xochitl Aleyda Morán Martínez*[1], José Alberto Luna López*[2], Zaira Jocelyn Hernández Simón[1], Gabriel Omar Mendoza Conde[1], José Álvaro David Hernández de Luz[2] and Godofredo García Salgado[2]

Full Research Paper

Open Access

Address:
[1]CONAHCYT-Posdoctorado-Centro de Investigaciones en Dispositivos Semiconductores (CIDS-ICUAP), Benemérita Universidad Autónoma de Puebla (BUAP). Col. San Manuel, Cd. Universitaria, Av. San Claudio y 14 sur, Edif. IC5 y IC6. Puebla, Pue., 72507 México and [2]Centro de Investigaciones en Dispositivos Semiconductores (CIDS-ICUAP), Benemérita Universidad Autónoma de Puebla (BUAP). Col. San Manuel, Cd. Universitaria, Av. San Claudio y 14 sur, Edif. IC5 y IC6. Puebla, Pue., 72507 México

Email:
Xochitl Aleyda Morán Martínez* - col538335@colaborador.buap.mx; José Alberto Luna López* - jose.luna@correo.buap.mx

* Corresponding author

Keywords:
2D model; chemical reactions; flow dynamics; HFCVD; hot filament chemical vapor deposition; SiO_x films

Beilstein J. Nanotechnol. **2024,** *15,* 1627–1638.
https://doi.org/10.3762/bjnano.15.128

Received: 08 August 2024
Accepted: 20 November 2024
Published: 17 December 2024

This article is part of the thematic issue "Symposium of Nanoscience and Nanomaterials 2024 (SNN 2024)".

Guest Editor: R. D. Cadena-Nava

Abstract

In this study, a simulation of the elementary chemical reactions during SiO_x film growth in a hot filament chemical vapor deposition (HFCVD) reactor was carried out using a 2D model. For the 2D simulation, the continuity, momentum, heat, and diffusion equations were solved numerically by the software COMSOL Multiphysics based on the finite element method. The model allowed for the simulation of the key parameters of the HFCVD reactor. Also, a thermochemical study of the heterogeneous reaction between the precursors quartz and hydrogen was carried out. The obtained equilibrium constants (K_{eq}) were related to the temperature profile in the deposition zone and used in the proposed simulation. The validation of the model was carried out by measuring the temperature experimentally, where the temperature range on the substrate is 450 to 500 °C for different deposition parameters. In the simulation, the laminar flow of species contributing to the film growth was confirmed, and the simulated concentration profiles of H° and SiO near the filaments and the sources were as expected. H° and SiO are essential species for the subsequent growth of the SiO_x films. These SiO_x films have interesting properties and embedded nanostructures, which make them excellent dielectric, optoelectronic, and electroacoustic materials for the fabrication of devices compatible with silicon-based technology.

Introduction

The growth of materials such as non-stoichiometric silicon oxide (SiO_x) is an important step in semiconductor devices development. Control of deposition parameters determines the success of the process and the properties of the films, with the most important parameters being substrate temperature, gas pressure, species concentration, and flow velocity [1]. The structural, optical, and electrical properties of the SiO_x, more generally known as silicon-rich oxide (SRO), films are determined by the ratio x = [O]/[Si], which is determined by controlling key parameters in the deposition process [2]. This ratio determines optical and electrical properties such as bandgap energy, absorption coefficient, photoluminescence, refractive index, and electrical conductivity [3]. SiO_x cannot only be obtained by different CVD techniques, but also by sputtering and ion implantation, among others [4,5]. The key parameters are particular for each of these techniques. Hot filament chemical vapor deposition (HFCVD) is an excellent alternative for obtaining SRO films. It is also very versatile and economical because the input gases and materials are accessible; also, it is scalable to larger areas [6].

The SiO_x films obtained by HFCVD possess excellent optical and electrical properties, which makes such films suitable for applications in the manufacture of metal–insulator–semiconductor and metal–insulator–metal devices exhibiting blue and white electroluminescence [7,8]. It was found that these films exhibit photoconductive and photoelectric effects suitable for electroluminescence and photovoltaics applications [9,10], as well as for other applications such as solar cells and anodes for Li batteries [11]. The basic steps of the general CVD process are classified and described in [12].

The optimization of this technique improves the properties of the films; however, the complexity of the CVD processes makes it difficult to understand clearly the different mechanisms involved in such optimization. Different tools such as ab initio density functional theory [13,14], kinetic Monte Carlo simulations [15,16], and reactive molecular dynamics simulations [17,18] have been used to understand the chemical reactions underlying the growth of the films [19].

Modeling the reaction mechanism in both two-dimensional (2D) and three-dimensional (3D) systems is a tool that allows us to understand the key steps regarding the reproducibility and uniformity of the films [19,20]. From a computational point of view, prior works focused on the growth mechanism of SiO_x in a plasma-enhanced chemical vapor deposition reactor in zero dimensions (0D); the model used was solved using CHEMKIN III and AURORA software. In the model, a set of reactions was established that approximately describe the mechanisms of the material growth, and the model results were compared with those obtained by experimental measurements [21]. Also, modeling of CVD microreactors at atmospheric pressure using tetraethyl orthosilicate as a source to obtain SiO_2 has been achieved through computational fluid dynamics (CFD) simulations [22]. The gas-phase and surface reactions were analyzed using direct Monte Carlo simulations of a hot wire chemical vapor deposition reactor for the growth of polycrystalline SiO_2 [23]. Most of these models describe CVD reactors at low pressure and low temperature, but there are not enough models regarding CVD systems at high temperature (>800 K) and high pressure (atmospheric pressure).

In this investigation, we focus on the simulation and analysis of key steps in a HFCVD deposition process to obtain SiO_x films by means of continuity, momentum, heat, and diffusion equations, which were solved numerically by the software COMSOL Multiphysics based on the finite element method; we also carry out a thermochemical analysis using FactSage. Some of the theoretical results are compared to experimental results. This work consists of five sections apart from this one. In Section “Experimental”, there is a complete description of the HFCVD reactor and the deposition parameters. Section “Theoretical and Numerical Simulations” explains the equations for the 0D and 2D models. Also, the hypothesis used to develop this study and the methodology for the use of COMSOL and FactSage are given. In section “Results and Discussion”, some theoretical results are compared with experimental ones. Further, the results obtained from the simulation are discussed regarding the profiles of temperature, gas velocity, and concentration of the species. Finally, the main conclusions of this research are expressed in section “Conclusion”.

The study focuses on the convective transfer of the reactive gases to the solid source and the surface diffusion to the substrate. The main objective is to optimize the process for an HFCVD reactor and, thus, improve the quality and reproducibility of the films.

Experimental

The analyzed HFCVD system is a vertical reactor that can be divided into three zones. The first zone is the gas inlet, the second one is the reaction zone, and the third one is the gas outlet. In the first zone, molecular hydrogen (H_2) gas is pumped in through a stainless steel piping system that reaches a diffuser inside the reaction chamber. The gas gets in contact with eleven tungsten filaments from incandescent lamps, which are activated by an externally applied voltage generating a current; these filaments have a temperature of approximately 2300 K. The second zone includes the region where the chemical reac-

tions takes place. Here, molecular hydrogen, exposed to the high temperature of the filaments, dissociates to form atomic hydrogen, which reacts with the eleven solid quartz sources. A cloud or plasma is formed and finally reaches the substrate for the formation of the thin films. Finally, zone three is the exit of the gases that were not deposited in the film. The entire process is carried out under atmospheric pressure. Table 1 summarizes the values of the parameters and dimensions complementary to the experimental conditions in the reactor for the deposition of SRO films previously described and depicted below in Figure 2 [24], as well as the corresponding boundary conditions.

Theoretical and Numerical Simulations

Hypothesis

Obtaining non-stoichiometric silicon oxide films in a HFCVD reactor is mainly based on two main heterogeneous reactions, which are the dissociation of atomic hydrogen and the reaction of atomic hydrogen with a solid source. The thermochemical study will allow us to obtain thermodynamic parameters of the heterogeneous reaction between H° in the gas phase and quartz to describe its behavior as a function of temperature at constant pressure. The thermodynamic data obtained and those taken from the bibliography will be used in the Arrhenius equation to calculate the thermodynamic and transport properties of the system in the gas phase in a dimensionless and temporal model. The thermodynamic and transport properties of the mixture will permit a study in the steady state considering the dimensions of the HFCVD reactor and the deposition parameters through numerically solving the equations of continuity, momentum, and heat transfer by the finite element method.

Mathematical method and equations

The complex growth of non-stoichiometric silicon oxide films in a HFCVD reactor involves different physics. For the description of the behavior of all systems, it is necessary to incorporate mathematical models that can explain the different phenomena involved. In this section, the mathematical models and the different pieces of software used in this study will be described. Figure 1 shows a flowchart that describes the modeling and simulation process. The different mathematical models used, and their mathematical equations will be described in detail in the following sections.

The well-mixed reactor equations (0D model)

The modeling of reactions is based on the mass action law given by Equation 1:

$$aA + bB + \cdots \underset{k_j^r}{\overset{k_j^f}{\rightleftharpoons}} xX + yY + \cdots, \tag{1}$$

where A, B,… are the reactants and X, Y,… are the products. a, b,… are the stoichiometric coefficients of the reactants, and x, y,… are the coefficients of the products. In the case of a set of reactions, the reaction rates r_j (mol·m^{-3}·s^{-1}) can be described by the law of mass action given by Equation 2:

$$r_j = k_j^f \prod_{i\in\text{react}} c_i^{-v_{ij}} - k_j^r \prod_{i\in\text{prod}} c_i^{v_{ij}}, \tag{2}$$

where k_j^f and k_j^r refer to the forward and reverse rate constants, respectively. The concentration of species i is indicated as c_i (mol·m^{-3}). The stoichiometric coefficients are expressed by v_{ij} and are negative for reactants and positive for products [25].

The dependence of concentration and temperature on reaction rates can be included using the Arrhenius expression (Equation 3):

$$k = AT^n e^{\left(-E_A/RT\right)}, \tag{3}$$

where A is the frequency factor, T (K) is the absolute temperature, n is the temperature exponent, E_A (J·mol^{-1}) is the activation energy, and R is the gas constant (8.314 J·mol^{-1}·K^{-1}).

Table 1: Elements, dimensions, and parameters of the deposition in the HFCVD reactor.

Parameters and dimensions of the HFCVD reactor		Deposition parameters and boundary conditions	
parameter	value	parameter	value
filament diameter	0.5 [mm]	temperature of the filament (no-slip wall)	2000 [°C]
filament length	10 [mm]	pressure (outlet)	1 [atm]
distance between filaments	3.8 [mm]	mass flow (inlet)	25, 50, and 100 [sccm]
deposition time	3 [min]	substrate temperature (no-slip wall)	26 [°C]
reactor volume	0.009 [m^3]	distance source–substrate (DSS)	3, 4, and 5 [mm]
surface area of the sources	2.19 × 10^{-5} [m^2]	distance filament–source	6 mm
		substrate diameter	50.8 mm

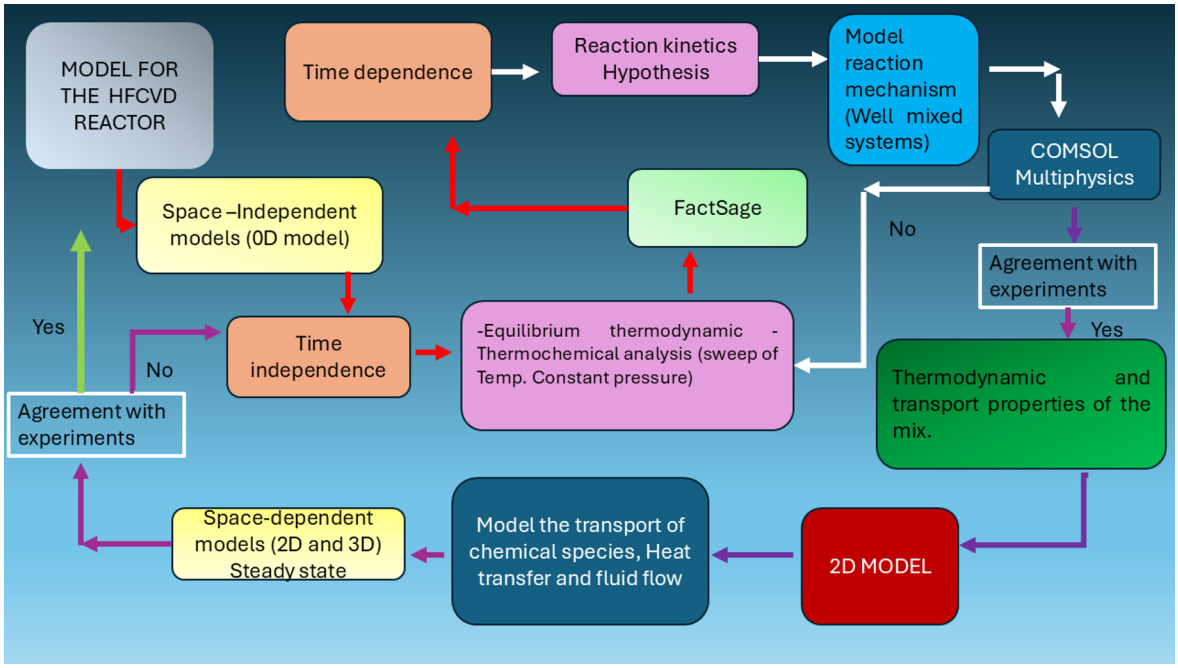

Figure 1: Flowchart of the modeling and simulation process and the use of different pieces of software.

For chemical reactions in equilibrium, the equilibrium constants are defined in terms of the equilibrium expression K_{eq} by Equation 4:

$$K_{eq} = \prod_i c_i^{\nu_i} = \frac{\prod_{i\in \text{prod}} c_i^{\nu_i}}{\prod_{i\in \text{react}} c_i^{-\nu_i}}. \quad (4)$$

The constants K_{eq} were calculated through data obtained below from Table 2 and using Equation 5:

$$\Delta G^\circ = -RT \ln K_{eq}, \quad (5)$$

where ΔG is the change in the Gibbs energy and R is the gas constant.

The equations in the spatial model

The used model assumes conservative species transport by diffusion and convection through a mass balance as described by Equation 6:

$$\nabla \cdot \mathbf{J}_i + \mathbf{u} \cdot \nabla c_i = R_i. \quad (6)$$

In this equation, $\mathbf{J}_i$ (mol·m^{-2}·s^{-1}) is the diffusive flow vector, R_i (mol·m^{-3}·s^{-1}) is a rate expression for the species, and $\mathbf{u}$ (m·s^{-1}) is the mass-averaged velocity vector. The suffix i denotes the species.

The laminar behavior of the gas-phase fluid is based on the Navier–Stokes equations; for an incompressible flow, ρ = constant. The continuity equation in the general form is expressed by Equation 7, the momentum equation in the general form is given by Equation 8, and the transfer of heat in fluids is described by Equation 9:

$$\nabla \cdot (\rho \mathbf{u}) = 0, \quad (7)$$

$$\rho(\mathbf{u} \cdot \nabla)\mathbf{u} = \nabla \cdot \left[-p\mathbf{I} + \mu\left(\nabla \mathbf{u} + (\nabla \mathbf{u})^T\right)\right] + \mathbf{F}, \quad (8)$$

$$\rho C_p (\mathbf{u} \cdot \nabla T) + \nabla \cdot (\mathbf{q} + \mathbf{q}_r) = -\frac{1}{\rho}\frac{\partial \rho}{\partial T} T(\mathbf{u} \cdot \nabla p) + \boldsymbol{\tau} : \nabla \mathbf{u} + Q, \quad (9)$$

$$\boldsymbol{\tau} : \nabla \mathbf{u} = \sum_i \sum_j \left[\frac{\boldsymbol{\tau}_{ij}}{2} + \frac{1}{3} \nabla \cdot \mathbf{u} \delta_{ij} \right]^2, \quad (10)$$

$$\boldsymbol{\tau}_{ij} = -\mu \left(\frac{\partial u_i}{\partial x_j} + \frac{\partial u_j}{\partial x_i} \right), \quad (11)$$

where $\mathbf{u}$ is the velocity vector (m·s^{-1}), ρ is the density (kg·m^{-3}), p is the pressure (Pa), $\mathbf{F}$ is the volume force vector (N·m^{-3}), C_p is the specific heat capacity at constant pressure (J·kg^{-1}·K^{-1}), T is the absolute temperature (K), $\mathbf{q}$ is the heat flux vector

($W{\cdot}m^{-2}$), $\mathbf{q}_r$ is the heat flux vector by radiation ($W{\cdot}m^{-2}$), $\mathbf{I}$ is the identity matrix (unitless), $(\nabla\mathbf{u})^T$ is the transposed velocity gradient tensor, $\boldsymbol{\tau}$ is the viscous stress tensor (Pa), μ is the dynamic viscosity (Pa·s), Q includes heat sources other than viscous dissipation ($W{\cdot}m^{-3}$), and δ_{ij} is the Kronecker delta symbol. All equations in this section were taken from [26], except Equation 5, which was taken from [27].

The modeling of chemical reactions

A prior thermodynamic equilibrium study of the heterogeneous reaction of SiO_2 (s) + H° (g) at 1 atm pressure in the temperature range from 100 to 2000 °C using FactSage software found that the gas species with higher concentrations were H°, SiO, OH, H_2O, and O_2; those with lower concentrations were SiH_4, SiH, Si, O, Si_2, and Si_3 [24]. This study was the basis for establishing the four main chemical reactions in zone 2 in the HFCVD reactor, which are listed below in Table 3. Here, an additional thermochemical study of the reaction SiO_2 (s) + H° (g) was developed to obtain the extensive properties of this reaction using FactSage in the temperature range from 500 to 1500 °C. Enthalpy (H), Gibbs energy (G), entropy (S), heat capacity (C_p), and Helmholtz energy (A) were obtained to calculate K_{eq} through Equation 5 [27]. The thermodynamic properties are listed in Table 2.

It should be noted that the surface film growth reactions are not considered in this study. The approximation of the thermodynamic properties of the superficial species is a study that we are still developing.

Numerical simulation

A 2D model of the HFCVD reactor was created using COMSOL Multiphysics 5.3 software [28]. Figure 2 shows the 2D geometry model with the three zones of the HFCVD reactor. For the numerical solution, the finite element method discretizes the domain into a mesh of smaller parts called elements. The computational time for the numerical solution is related to the mesh in the 2D model with longer computational time for a greater number of elements.

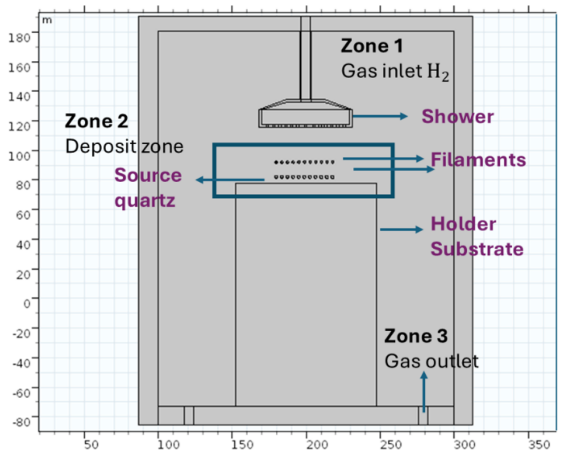

Figure 2: The HFCVD reactor zones and elements of the 2D model built in COMSOL Multiphysics 5.3.

Based on the thermodynamic equilibrium study, we propose four main reactions in zone 2, which are listed in Table 3. For the generation of atomic hydrogen, reactions 1 and 2 are considered, where M is a tertiary species or H_2. Atomic hydrogen diffuses and reacts superficially with the quartz sources; this corresponds to the process described by the heterogeneous reaction 3. Finally, reaction 4 is considered for the generation of OH, considering that the source of oxygen is the interaction of atomic H° with the sources. The Arrhenius parameters used are described in Table 3.

Initially, a well-mixed reactor approach will be used. This is a 0D model in which the reactor volume is assumed to be con-

Table 2: Thermodynamic properties for reaction 3 in Table 3.

Temperature T (°C)	Enthalpy H (J)	Gibbs energy G (J)	Entropy S (J/K)	Volume V (L)	Heat capacity C_p ($J{\cdot}K^{-1}$)	Helmholtz energy A (J)	Equilibrium constant K_{eq}
500	−677803.9	−774752.6	193.897	4.11×10^1	80.284	−778912.2	8.62784×10^{80}
600	−669523.0	−794911.9	208.981	4.93×10^1	85.279	−799902.9	1.59062×10^{69}
700	−660742.4	−816497.1	222.507	5.75×10^1	90.434	−822319.6	8.43911×10^{60}
800	−651404.4	−839377.8	234.967	6.57×10^1	96.539	−846031.8	6.37426×10^{54}
900	−645606.2	−863342.5	241.929	7.39×10^1	20.828	−870827.9	1.27612×10^{50}
1000	−643523.4	−887647.1	244.124	8.21×10^1	20.828	−895964.0	2.31640×10^{46}
1100	−641440.6	−912160.3	246.109	9.03×10^1	20.828	−921308.6	2.05986×10^{43}
1200	−639357.8	−936863.1	247.921	9.85×10^1	20.828	−946842.9	6.02018×10^{40}
1300	−637275.1	−961739.7	249.588	1.07×10^1	20.828	−972551.0	4.38780×10^{38}
1400	−635192.3	−986776.6	251.132	1.15×10^1	20.828	−998419.4	6.54940×10^{36}
1500	−633109.5	−1011962.0	252.569	1.2311×10^1	20.828	−1024436.7	1.73301×10^{35}

Table 3: Reactions for the 0D and 2D models.

Reaction	Frequency factor A	Temperature exponent n	Activation energy E_A	Ref.
1. $H + H + M = H_2 + M$	1.00×10^{18}	–1.00	0.0	[16]
2. $H + H + H_2 = H_2 + H_2$	9.2×10^{16}	–0.6	0.0	[16]
3. SiO_2 (s) + H° (g) = SiO + OH	4.0×10^{12}	0.0	5700	[17,18]
4. $H_2 + O_2 = OH + OH$	1.7×10^{13}	0	48100	[16]

stant and spatially uniform; the calculated concentrations of the species, and the temperature are instantaneous values within the reactor. The 0D model scales to a spatial 2D model. For the numerical solution, the following considerations are made: Molecular hydrogen behaves like an ideal gas in a two-dimensional model with position coordinates (x,y). The fluid is considered laminar and incompressible. The mathematical equations that describe the motion of gas are the conservation of mass (continuity equation), momentum (Navier–Stokes equations), and energy. The boundary conditions used in this model are listed in Table 1. Through the finite element method, all equations were solved via COMSOL Multiphysics. The Dirichlet boundary conditions were employed to solve this model numerically. The types of boundaries are listed in Table 1. For the boundary wall on the filaments, we use a constraints boundary condition; for the outlet, a pressure boundary condition was used. For the inlet, we use a mass flow boundary condition.

The simulations give us a broad overview on the probable reaction mechanisms during the deposition of thin films in the HFCVD reactor. This allows us to get an estimate of the types of species that will be deposited for the growth of thin films, which depend strongly on the parameters and precursors employed.

Results and Discussion

Experimental results

The SiO_x films obtained using the HFCVD reactor have already been characterized using different optical, electrical, and structural characterization techniques [29-31]. Also, the process of the growth of the films was optimized through a computational fluid analysis study, which made it possible to increase the deposition area, in addition to enhancing the optoelectronic properties of the films [24].

Theoretical results

The 2D model was numerically solved in the steady state with a computing time of 286 s. For the simulation, the 2D model was analyzed with a mesh of 45,769 elements. First, the distribution of temperature and velocity of the fluid and, second, the approx-

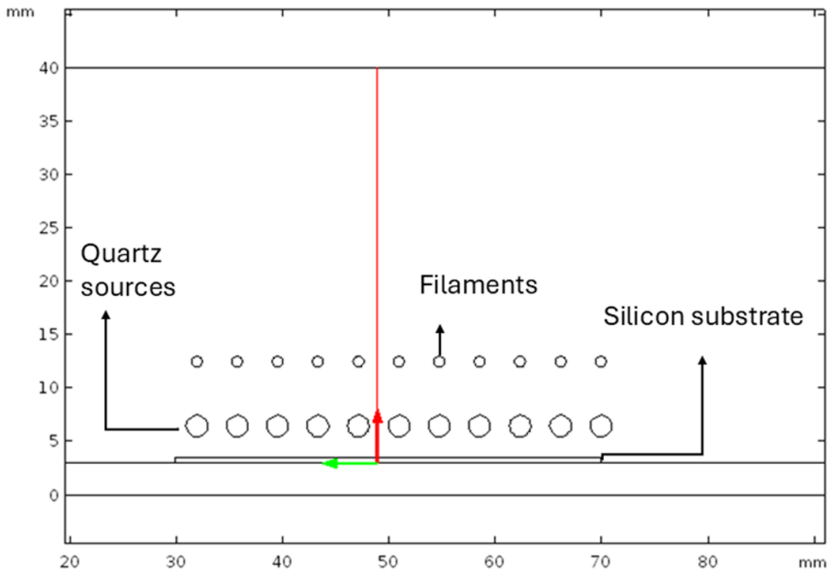

Figure 3: The red line along the y direction in the deposition area (zone 2) built in COSMOL Multiphysics.

imation of the concentration and distribution of the species are presented. All results reported in this research were obtained along a line on the *y* axis of the 2D model in zone 2. The line crosses all horizontal zones of the HFCVD reactor. Figure 3 shows the line in red. The data obtained on the mentioned line is presented and analyzed separately according to the main variables in the HFCVD system during deposition.

Temperature

The theoretical model was experimentally validated through temperature profiles for 20 and 30 sccm flows, which are shown in Figure 4a and Figure 4b, respectively [32]. The temperature measurements were made using a K-type thermocouple located on the surface of the deposition area. The deposition time for SiO_x was 3 min at a fixed position of the thermocouple on the substrate. Thereafter, the position of the sources was moved by 3, 4, and 5 mm. The experimental temperature measurements range from 450 to 550 °C after a deposition time of 3 min considering the mentioned DSSs.

The 2D temperature map of the HFCVD reactor is shown in Figure 5. The temperature map of deposition zone 2 is shown in Figure 6a. Figure 6b describes the temperature profile along the *y* coordinate from the substrate to the diffuser for the different DSSs in the steady state. The maximum temperature is near the filaments, and the minimum temperatures are found on substrate and diffuser. Heat transfer in the reactor is due to different mechanisms, such as radiation, conduction, convection, and diffusion. The theoretical and experimental temperature results were compared and analyzed near the position of the thermocouple, where the experimental temperature is only a function of the deposition time but not of the position. From the theoretical results, the temperature increases from 300 K at the substrate to 1000 K near the quartz sources, that is 3–5 mm away from the sources in the steady state.

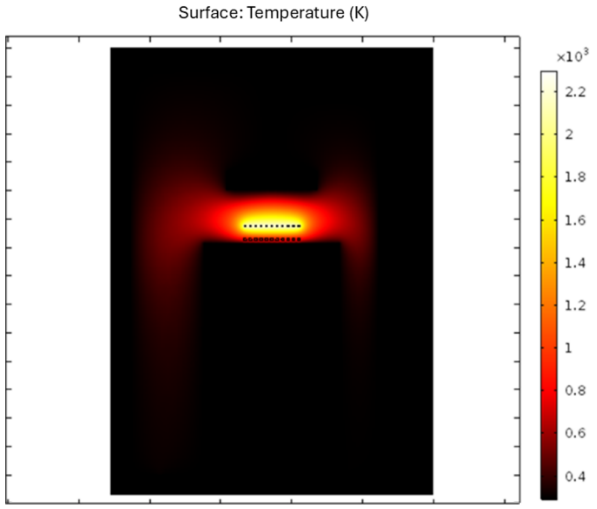

Figure 5: Temperature map of the HFCVD reactor.

The results obtained show us that the HFCVD is a high-temperature system regarding the filaments (2300 K), compared with other CVD reactors like low-pressure CVD (800 K). Hence, diffusion is expected to dominate the reactions for the formation of the precursor species. The growth of SiO_x films is controlled by nucleation effects. According to results for high temperatures over 700 K, the supersaturation is high and the nucleation is homogeneous in the process, leading to the precipitation of solid particles on the substrate and powder formation

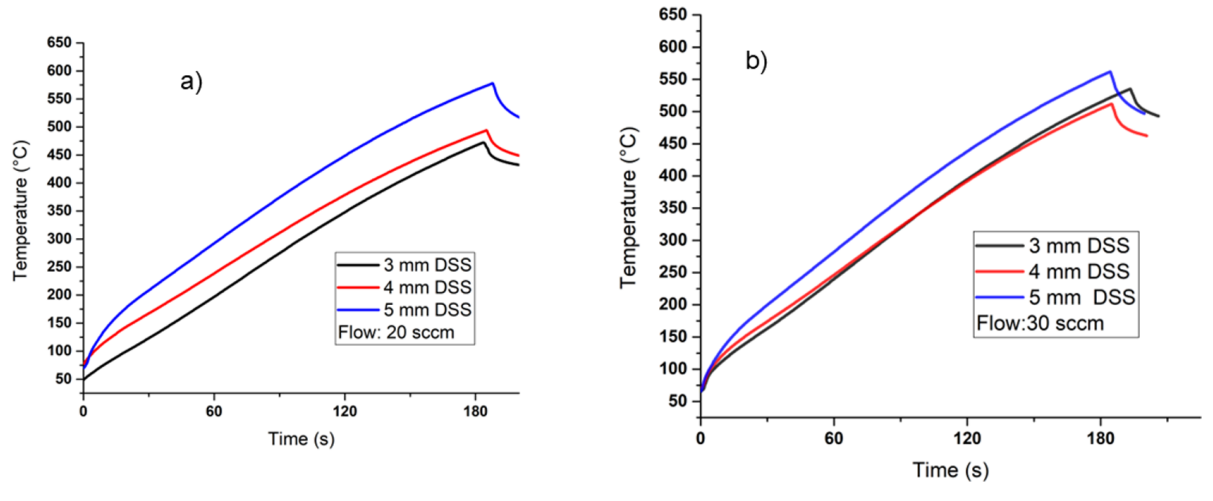

Figure 4: Experimental temperature measured by a thermocouple located on the deposition zone for (a) 20 sccm and (b) 30 sccm.

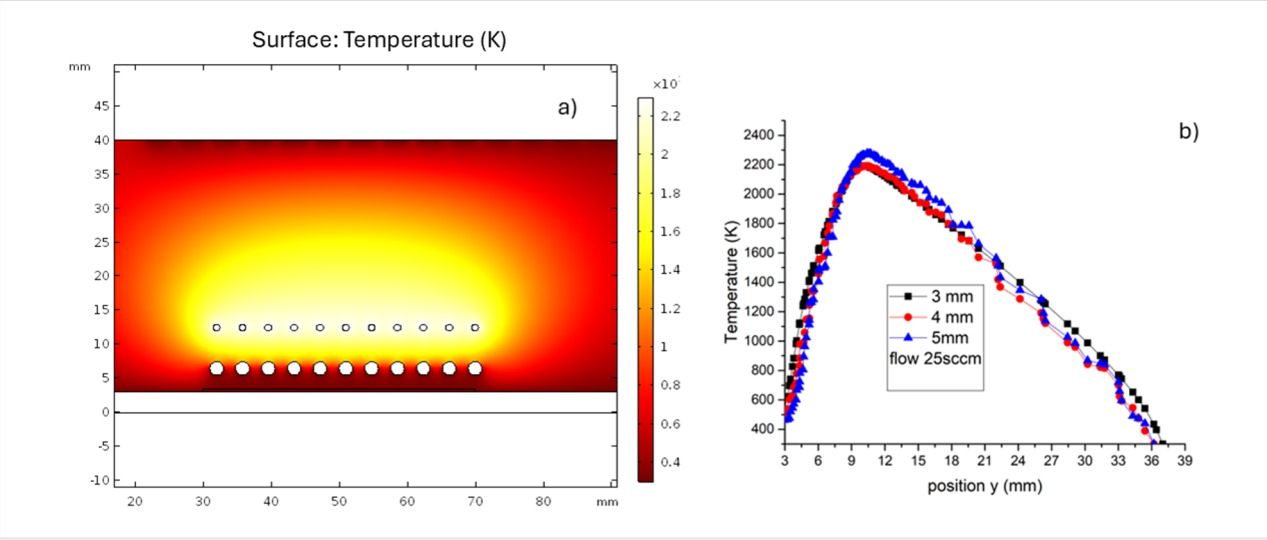

Figure 6: (a) Temperature map of the surroundings of the deposition zone. (b) Temperature profile along the *y* axis from the substrate to the diffuser for the different DSSs in the steady state.

[23]. SiO_x powders are obtained in the HFCVD reactor when the distance between the filaments and the source is less than 6 mm. According to what was discussed above, the distance decreases the temperature, increases the size of the clusters, and decreases the diffusion of the species, resulting in powder formation. Heterogeneous nucleation on the substrate promotes the growth of SiO_x films. The distance between the filaments and the substrate is greater than 9 mm; this reduces the temperature below 700 K according to experimental and theoretical results, promoting the growth of films. Temperature control in these systems can be modulated through the longitudinal distance between filaments, sources, and substrates. The transverse distance between sources and filaments also plays an important role in the deposition process; however, the proposed 2D model limits the study of this effect.

Velocity

Flow dynamics play a critical role when the deposition takes place at atmospheric pressure. Fluid velocity and distribution analysis were previously performed and analyzed by CFD using ANSYS Fluent [24], as depicted in Figure 7b. From this study, it was determined that it is necessary to make a change in the configuration of the reaction chamber outlets to homogenize the flow distribution and, thus, be able to optimize the deposition area to two inches. The previously reported ANSYS velocity profile is in very good agreement with that obtained in COMSOL, which is shown in Figure 7a. Both profiles in Figure 7 describe the laminar flow of the gas in zone 2 and the formation of a turbulent flow at the diffuser due to the interaction with the walls. In a study of the deposition of silicon dioxide using an atmospheric-pressure plasma-enhanced CVD

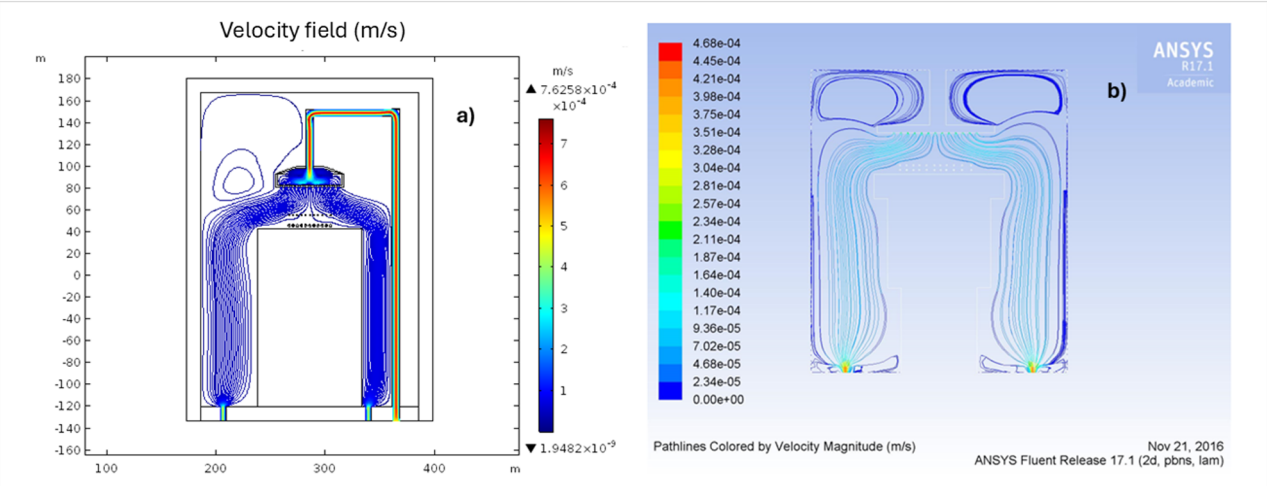

Figure 7: Velocity profile in the HFCVD reactor obtained with (a) COMSOL and (b) ANSYS.

reactor, the reactor performance was shown to be strongly affected by the flow dynamics [33,34].

Distribution and concentration of species

As previously mentioned, temperature and fluid dynamics play a very important role in the formation and diffusion of precursor species. The solution of the model allowed us to obtain preliminary results for the concentration of the species in the reactions proposed in Table 3. The concentration profiles for H°, SiO, O_2, and OH were analyzed at three different flow levels of 25, 50, and 100 sccm. The H° concentration map is shown in Figure 8a, and the concentration as a function of the *y* position is shown in Figure 8b. Figure 8b shows different concentration profiles for different H_2 fluxes. The profiles vary slightly, and the concentration increases with the flux of H_2. This effect was already studied experimentally, and the most significant results were the analysis of how the hydrogen flow influences the composition SiO_x films by X-ray photoelectron spectroscopy; as the hydrogen flow increases, the concentration of Si also increases in comparison with that of oxygen, modifying stoichiometry and bandgap [35]. The distribution of H° in zone 2 is a result of the temperature distribution. The concentration is greater near the filaments, decreasing with distance along the *y* axis away from the quartz sources, where the temperature varies in the range of 800–1200 K. When the distances from the filament to the source are greater, no film deposition occurs. This effect is mainly due to the recombination of H° to H_2 as the temperature decreases.

The formation of these gaseous species is an important step since they contain the radical species that give rise to the surface reactions for the growth of the films. In the reaction mechanisms reported for the growth of SiO_2 films, the role of intermediate •H and •OH and $•O_2$ radicals has been pointed out through in situ Fourier-transform infrared spectroscopy. These species react with silane-derived and surface hydroxy groups, which leads to deposition. They are also responsible for the incorporation of Si–OH bonds into the silicon oxide matrix. The •H and •OH species attack unsaturated surface species with dangling bonds. Oxidation of surface hydrogens is the predominant reaction for O to convert H to OH. Finally, •H and •OH radicals can attack saturated surface species, removing H to form H_2 and H_2O, respectively, in the gas phase [21,36]. The presence of dangling bonds in the SiO_x films was detected previously. In this study, SiO_x films with thermal treatment and without thermal treatment were analyzed, and a decrease in thickness, refractive index, and excess silicon was observed. This behavior was attributed to the structural rearrangement at the atomic level by the thermal treatment due to the desorption of hydrogen from dangling bonds. The films after thermal treatment exhibited greater photoluminescence compared to those that did not undergo thermal treatment [29].

The SiO species plays an important role in the proposed mechanism; the reaction of SiO with •OH and •H radicals leads to the formation of HSiO and silanes [15]. Silane and silanol species were also found in the equilibrium thermodynamic study; they can be the precursors of nanocrystalline silicon (nc-Si) in the SiO_x films [24]. The nc-Si obtained by this technique has been studied and characterized [35]. The calculated concentration of SiO and OH is shown in Figure 9a. These species exhibit a higher concentration in the region among the quartz sources and in the vicinity of the substrate. These concentrations are gener-

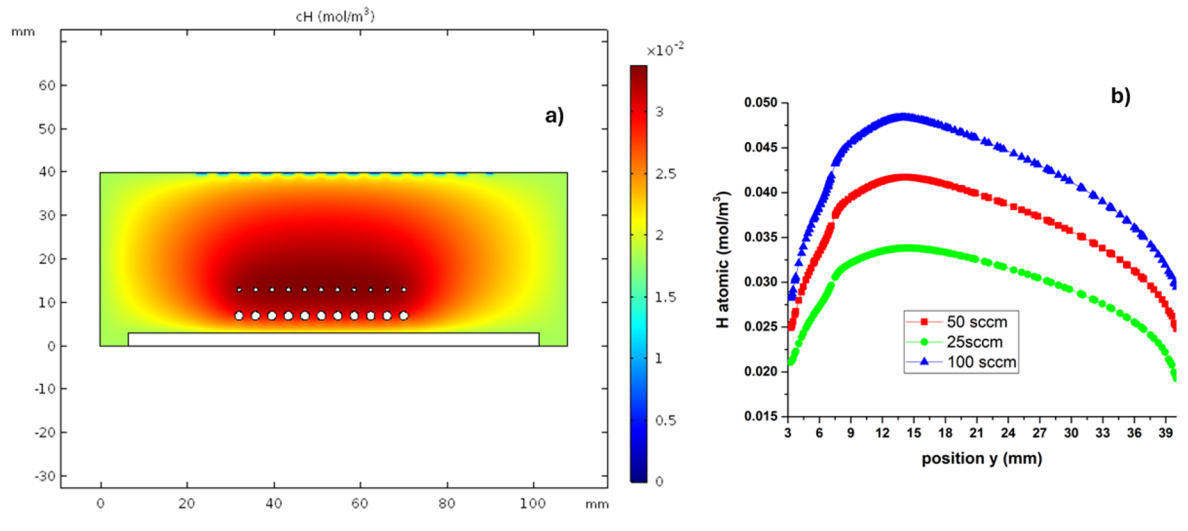

Figure 8: (a) Concentration map of atomic H in the deposition zone. (b) Concentration as a function of the position on the *y* axis.

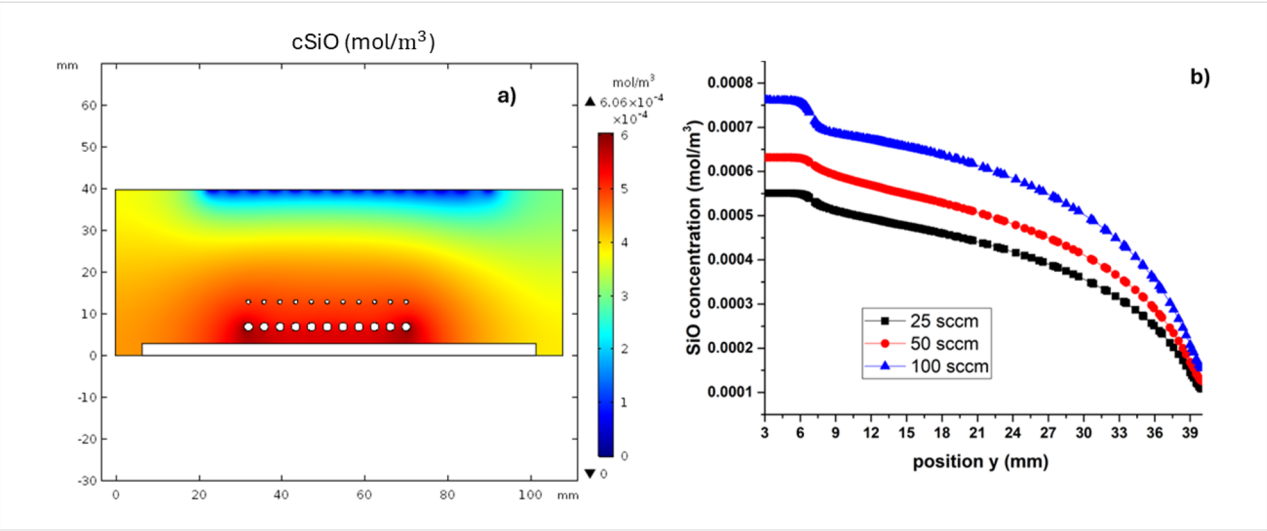

Figure 9: (a) Concentration map of SiO in the deposition zone. (b) SiO concentration vs *y* position.

ated in chemical equilibrium by reaction 3 in Table 3. Figure 9a shows the SiO concentration map, and Figure 9b shows the concentration as a function of the *y* position for different hydrogen fluxes.

The oxygen in the deposition process is only from the solid quartz sources. In our model, there is not an additional source for O_2. According to the proposed mechanism in reaction 4 in Table 3, the formed O_2 reacts with H_2 on the surface of the quartz sources to form OH. The O_2 content is lower than that of the other species because it reacts with H_2 and H°. Therefore, this species is predominantly found below the quartz sources. The O_2 concentration map is shown in Figure 10b. The concentration of O_2 above the sources is almost zero due to the reaction with atomic H leading to the formation of OH. Figure 10a shows the concentration of O_2 as a function of the position.

Conclusion

A model of the reaction mechanism of quartz sources with atomic hydrogen was established in thermodynamic equilibrium, and a thermochemical study of the heterogeneous chemical reaction was carried out using FactSage. We obtained the thermodynamic and transport properties to set up a 2D model. Through 2D simulation with COMSOL Multiphysics® software, it was possible to obtain the concentration profiles of the main species H°, O_2, OH, and SiO, which contribute to the growth of SRO films. In addition, the temperature and flow velocity profiles were obtained. Furthermore, it was possible to make a comparison between the theoretical results and those obtained from experiments. It was observed that the effect of the temperature on the distribution of the species is the most important. Regarding the temperature variation on the substrate, it was found that it is mainly caused by the increase in the dis-

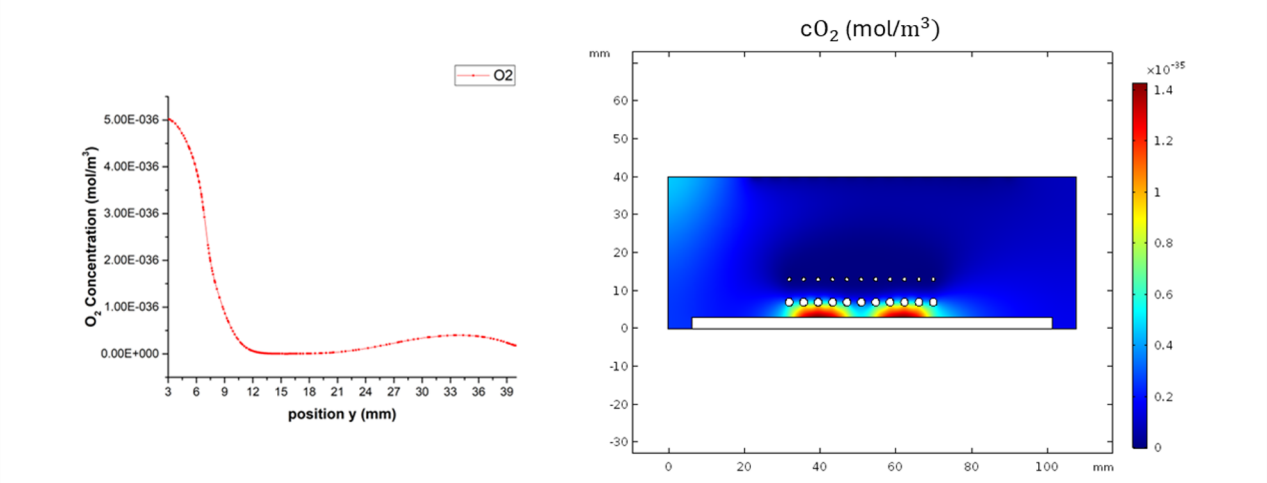

Figure 10: (a) Concentration of O_2 as a function of the *y* position. (b) O_2 concentration map in zone 2.

tance between sources and substrate. The temperature on the substrate is influenced by radiation, conduction, und convection mechanisms. The transport of species is due to the convection and diffusion effects.

Funding

This work has been partially supported by VIEP 00335-PV/2024 and CONAHCYT scholarship CVU:461337.

Acknowledgements

The authors thankfully acknowledge computer resources, technical advice, and support provided by Laboratorio Nacional de Supercómputo del sureste de México (LNS), member of the CONAHCYT National Laboratories Group, under project no. 202304068c. Also, we thank CIDS for the access to the laboratories.

ORCID® iDs

Xochitl Aleyda Morán Martínez - https://orcid.org/0009-0009-1883-0989
José Alberto Luna López - https://orcid.org/0000-0002-7647-3184
Zaira Jocelyn Hernández Simón - https://orcid.org/0000-0003-4185-4101
Gabriel Omar Mendoza Conde - https://orcid.org/0000-0001-5451-9770
José Álvaro David Hernández de Luz - https://orcid.org/0000-0002-7913-0240

Data Availability Statement

Data generated and analyzed during this study is available from the corresponding author upon reasonable request.

References

1. Wang, M.; Jia, L.; Xu, H.; Li, A.; Peng, Y.; Tang, Z. *Ceram. Int.* **2020,** *46,* 4843–4849. doi:10.1016/j.ceramint.2019.10.218
2. Iskhakzay, R. M. K.; Kruchinin, V. N.; Aliev, V. S.; Gritsenko, V. A.; Dementieva, E. V.; Zamoryanskaya, M. V. *Russ. Microelectron.* **2022,** *51,* 24–35. doi:10.1134/s1063739721060081
3. Simón, Z. J. H.; López, J. A. L.; de la Luz, Á. D. H.; Salgado, G. G.; Leyva, K. M.; López, J. C.; Conde, G. O. M.; Lara, A. B.; Hernández, H. P. M.; Hernández, E. G.; Méndez, J. F. *Surf. Interfaces* **2021,** *26,* 101411. doi:10.1016/j.surfin.2021.101411
4. Tong, L. Z. *J. Phys.: Conf. Ser.* **2014,** *518,* 012006. doi:10.1088/1742-6596/518/1/012006
5. Miyazaki, H.; Goto, T. *J. Non-Cryst. Solids* **2006,** *352,* 329–333. doi:10.1016/j.jnoncrysol.2005.12.008
6. Jansen, F.; Machonkin, M. A.; Kuhman, D. E. *J. Vac. Sci. Technol., A* **1990,** *8,* 3785–3790. doi:10.1116/1.576494
7. Martínez, H. P.; Luna, J. A.; Morales, R.; Casco, J. F.; Hernández, J. A. D.; Luna, A.; Hernández, Z. J.; Mendoza, G.; Monfil, K.; Ramírez, R.; Carrillo, J.; Flores, J. *Nanomaterials* **2021,** *11,* 943. doi:10.3390/nano11040943
8. Gao, W.; Li, T.-k.; Ono, Y.; Hsu, S.-T. *J. Rare Earths* **2006,** *24,* 673–678. doi:10.1016/s1002-0721(07)60007-6
9. Koryazhkina, M. N.; Filatov, D. O.; Tikhov, S. V.; Belov, A. I.; Serov, D. A.; Kryukov, R. N.; Zubkov, S. Y.; Vorontsov, V. A.; Pavlov, D. A.; Gryaznov, E. G.; Orlova, E. S.; Shchanikov, S. A.; Mikhaylov, A. N.; Kim, S. *Nanomaterials* **2023,** *13,* 2082. doi:10.3390/nano13142082
10. Jambois, O.; Garrido, B.; Pellegrino, P.; Carreras, J.; Pérez-Rodríguez, A.; Montserrat, J.; Bonafos, C.; BenAssayag, G.; Schamm, S. *Appl. Phys. Lett.* **2006,** *89,* 253124. doi:10.1063/1.2423244
11. Chen, T.; Wu, J.; Zhang, Q.; Su, X. *J. Power Sources* **2017,** *363,* 126–144. doi:10.1016/j.jpowsour.2017.07.073
12. Sabzi, M.; Mousavi Anijdan, S.; Shamsodin, M.; Farzam, M.; Hojjati-Najafabadi, A.; Feng, P.; Park, N.; Lee, U. *Coatings* **2023,** *13,* 188. doi:10.3390/coatings13010188
13. Hohenberg, P.; Kohn, W. *Phys. Rev.* **1964,** *136,* B864–B871. doi:10.1103/physrev.136.b864
14. Kohn, W.; Sham, L. J. *Phys. Rev.* **1965,** *140,* A1133–A1138. doi:10.1103/physrev.140.a1133
15. Gillespie, D. T. *J. Comput. Phys.* **1976,** *22,* 403–434. doi:10.1016/0021-9991(76)90041-3
16. Voter, A. F. Introduction to the Kinetic Monte Carlo Method. In *Radiation Effects in Solids;* Sickafus, K. E.; Kotomin, E. A.; Uberuaga, B. P., Eds.; NATO Science Series, Vol. 235; Springer Netherlands: Dordrecht, Netherlands, 2007; pp 1–23. doi:10.1007/978-1-4020-5295-8_1
17. van Duin, A. C. T.; Dasgupta, S.; Lorant, F.; Goddard, W. A. *J. Phys. Chem. A* **2001,** *105,* 9396–9409. doi:10.1021/jp004368u
18. Senftle, T. P.; Hong, S.; Islam, M. M.; Kylasa, S. B.; Zheng, Y.; Shin, Y. K.; Junkermeier, C.; Engel-Herbert, R.; Janik, M. J.; Aktulga, H. M.; Verstraelen, T.; Grama, A.; van Duin, A. C. T. *npj Comput. Mater.* **2016,** *2,* 15011. doi:10.1038/npjcompumats.2015.11
19. De Wilde, J.; Lorant, C.; Descamps, P. *J. Phys. D: Appl. Phys.* **2017,** *50,* 135202. doi:10.1088/1361-6463/aa5c1d
20. Wu, Y.; Zhang, H.; Yan, G.; Liu, L.; Cristea, D.; Wang, H.; Yang, Y.; Shen, J. *Mater. Res. Express* **2021,** *8,* 116403. doi:10.1088/2053-1591/ac3278
21. Riera, M.; Rodríguez, J. A.; Barreto, J.; Domínguez, C. *Thin Solid Films* **2007,** *515,* 3380–3386. doi:10.1016/j.tsf.2006.09.032
22. Konakov, S. A.; Krzhizhanovskaya, V. V. *J. Phys.: Conf. Ser.* **2015,** *574,* 012145. doi:10.1088/1742-6596/574/1/012145
23. Holt, J. K.; Swiatek, M.; Goodwin, D. G.; Muller, R. P.; Goddard, W. A., III; Atwater, H. A. *Thin Solid Films* **2001,** *395,* 29–35. doi:10.1016/s0040-6090(01)01202-0
24. Morán Martínez, X. A.; Luna-López, J. A.; Apreza Sies, A.; Hernández-de La Luz, Á. D.; Martinez Hernández, H. P. *Adv. Mater. Res.* **2021,** *1165,* 99–111. doi:10.4028/www.scientific.net/amr.1165.99
25. Zanoni, M. A. B.; Gardner, L.; Gnanapragasam, N.; Liang, Z. *Int. J. Hydrogen Energy* **2024,** *57,* 39–51. doi:10.1016/j.ijhydene.2023.12.192
26. COMSOL. Multiphysics 5.5 Reference Manual. https://doc.comsol.com/5.5/doc/com.comsol.help.comsol/COMSOL_ReferenceManual.pdf (accessed Nov 29, 2024).
27. Bale, C. W.; Bélisle, E.; Chartrand, P.; Decterov, S. A.; Eriksson, G.; Gheribi, A. E.; Hack, K.; Jung, I.-H.; Kang, Y.-B.; Melançon, J.; Pelton, A. D.; Petersen, S.; Robelin, C.; Sangster, J.; Spencer, P.; Van Ende, M.-A. *CALPHAD:Comput. Coupling Phase Diagrams Thermochem.* **2016,** *54,* 35–53. doi:10.1016/j.calphad.2016.05.002

28. *COMSOL Multiphysics®,* v.5.3; COMSOL AB: Stockholm, Sweden, https://www.comsol.com.
29. Mendoza Conde, G. O.; Luna López, J. A.; Hernández Simón, Z. J.; Hernández de la Luz, J. Á. D.; García Salgado, G.; Gastellou Hernández, E.; Martínez Hernández, H. P.; Flores Méndez, J. *Sensors* **2022,** *22,* 3904. doi:10.3390/s22103904
30. Martínez Hernández, H.; Luna López, J.; Hernández de la Luz, J.; Luna Flores, A.; Monfil Leyva, K.; García Salgado, G.; Carrillo López, J.; Ordoñez Flores, R.; Pérez García, S.; Hernández Simón, Z.; Mendoza Conde, G.; Ramírez Amador, R. *Crystals* **2020,** *10,* 127. doi:10.3390/cryst10020127
31. López, J. A. L.; Valerdi, D. E. V.; Salgado, G. G.; de la Luz, A. D. H.; Conde, G. M.; Simon, Z. H.; Gracia, F. J. F.; Sanchez, A. M.; Dominguez, M. A. *Procedia Eng.* **2016,** *168,* 1296–1299. doi:10.1016/j.proeng.2016.11.349
32. Tépox, N. C. Efectos Fotoconductivos de Heteroestructuras Con Oxidos Nanoestructurados. Ph.D. Thesis, Benemérita Universidad Autónoma de Puebla, México, 2021.
33. Descamps, P.; Asad, S. S.; Wilde, J. D. *J. Phys. D: Appl. Phys.* **2013,** *46,* 365201. doi:10.1088/0022-3727/46/36/365201
34. Meshkova, A. S.; Elam, F. M.; Starostin, S. A.; van de Sanden, M. C. M.; de Vries, H. W. *Surf. Coat. Technol.* **2018,** *339,* 20–26. doi:10.1016/j.surfcoat.2018.02.010
35. Luna López, J. A.; Vázquez Valerdi, D. E.; Benítez Lara, A.; García Salgado, G.; Hernández-de la Luz, A. D.; Morales Sánchez, A.; Flores Gracia, F. J.; Dominguez, M. A. *J. Electron. Mater.* **2017,** *46,* 2309–2322. doi:10.1007/s11664-016-5271-1
36. Meeks, E.; Larson, R. S.; Ho, P.; Apblett, C.; Han, S. M.; Edelberg, E.; Aydil, E. S. *J. Vac. Sci. Technol., A* **1998,** *16,* 544–563. doi:10.1116/1.581096

License and Terms

BEILSTEIN JOURNAL OF NANOTECHNOLOGY

TiO_2 immobilized on 2D mordenite: effect of hydrolysis conditions on structural, textural, and optical characteristics of the nanocomposites

Marina G. Shelyapina[*1], Rosario Isidro Yocupicio-Gaxiola[2], Gleb A. Valkovsky[1] and Vitalii Petranovskii[*3]

Full Research Paper

Open Access

Address:
[1]Department of Nuclear Physics Research Methods, Saint-Petersburg State University, 7/9 Universitetskaya nab., St. Petersburg 199034, Russia, [2]Tecnológico Nacional de México/Instituto Tecnológico Superior de Guasave, Carretera a La Brecha Sin Número, Ejido Burrioncito, Guasave 81149, Sin., Mexico and [3]Center for Nanoscience and Nanotechnology, National Autonomous University of Mexico (CNyN, UNAM), Ensenada, Baja California 22860, Mexico

Email:
Marina G. Shelyapina[*] - marina.shelyapina@spbu.ru;
Vitalii Petranovskii[*] - vitalii@ens.cnyn.unam.mx

* Corresponding author

Keywords:
2D zeolite; hierarchical porosity; mordenite; TEOT; TiO_2; titanium tetraethoxide

Beilstein J. Nanotechnol. **2025,** *16,* 128–140.
https://doi.org/10.3762/bjnano.16.12

Received: 10 June 2024
Accepted: 06 January 2025
Published: 10 February 2025

This article is part of the thematic issue "Symposium of Nanoscience and Nanomaterials 2024 (SNN 2024)".

Guest Editors: R. D. Cadena-Nava and U. Caudillo-Flores

Abstract

A series of novel TiO_2/2D mordenite nanocomposites were synthetized by the introduction of titanium tetraethoxide (TEOT) into the interlamellar space of 2D mordenite, its subsequent hydrolysis in water or a solution of 70% ethanol in water for 6, 12, and 24 h, and calcination. The resulting TiO_2/2D mordenite materials were studied by a set of complementary characterization techniques, including XRD, SEM-EDX, TGA, N_2 sorption, NMR, XPS and UV–vis spectrometry. It was observed that treatment in 70% ethanol solution preserves the ordered layered structure of 2D mordenite because TEOT hydrolysis is slowed down. This, in turn, leads to higher mesoporosity after calcination due to anatase nanoparticles of about 4 nm preventing the collapse of the interlamellar space. Immobilization of TiO_2 on the zeolite surface is evidenced by the formation of Si–O–Ti bonds. The bandgap width of the synthetized nanocomposites was found to be sensitive to the hydrolysis medium.

Introduction

Zeolites are important heterogeneous catalysts in various industrial processes. More and more functional materials based on zeolites are being searched for, including zeolites with hierarchical micro- and mesoporosity [1-6]. Zeolites with hierarchical porous structures can be synthesized using different strategies [4], for example, aggregation of nanocrystals, use of

templates, and creation of mesoporosity by forming pillars between 2D lamellae of zeolites separated by cetyltrimethylammonium bromide (CTAB) layers. The latter method involves the synthesis of layered 2D zeolites in the presence of CTAB and organic structure directing agents (OSDAs), followed by calcination to remove them from the resulting products [1].

The choice of the OSDA determines not only the interlamellar distance and, hence, the mesopore size, but also the aluminum distribution and acidic properties of the obtained material, which are key parameters for catalysts [5,7-10]. One widely used component for the synthesis of 2D zeolites is CTAB [5,9,11-13].

To prepare mesoporous materials from hybrid zeolite–CTAB aggregates, inorganic pillars are pre-formed in the CTAB layers, which will keep the zeolite lamellae from collapsing when burning the organic phase. The flexibility in the choice of material to form pillars creates a wide range of potential new materials for targeted applications. Typically, such pillars are amorphous SiO_2 nanoparticles formed during the hydrolysis of tetraethoxysilane (TEOS) introduced into liquid crystalline 2D CTAB layers that fill the interlamellar space between the 2D zeolite nanosheets. Tetraethoxytitanium (TEOT) is a homolog of TEOS, and its hydrolysis similarly leads to the formation of TiO_2.

TiO_2 is a well-known photocatalyst whose efficiency depends on a number of factors, including the crystalline phase, particle size, and degree of crystallinity. The most active phase of TiO_2 is considered to be anatase. Its nanoparticles usually show higher efficiency than the bulk phase, but the bandgap of anatase particles smaller than 10 nm is very sensitive to their size [14].

One of the disadvantages of such free photocatalyst nanoparticles is the limitation of mass transfer between solid and liquid phases. From this perspective, the problem of immobilization of TiO_2 nanoparticles is of great importance. Many materials are considered as a possible support for immobilization, including porous ceramics [15], glass [16,17], porous carbon materials [18,19], mesoporous silica [20-23], and zeolites [24-27]. Recent studies have confirmed that direct synthesis of TiO_2 in mesoporous silica or zeolites provides strong immobilization of TiO_2 nanoparticles through Ti–O–Si bonding [21-23].

Previously, we reported the results of the trial synthesis of a new TiO_2/2D mordenite nanocomposite [28]. The material was obtained from a composite consisting of lamellar mordenite separated by CTAB layers through the substitution of TEOS for TEOT and subsequent hydrolysis. As a result, the pillars separating the mordenite layers were not made of silica as in the routine synthesis method for the preparation of mesoporous materials, but of anatase nanoparticles of about 4 nm in size. It was found that the textural properties of the resulting materials are sensitive to the environment in which TEOT hydrolysis takes place.

Alkoxides are, generally, not stable in protic solvents such as water. However, because of this property they are widely used as starting products in a large number of reactions. The hydrolysis of various metal alkoxides by pure water, or its mixtures with primarily alcohols or other solvents, are the basis of the sol–gel method to obtain oxide materials. The tendency of metal alkoxides to this reaction can be considered as their most important chemical property. For various reasons, the sol–gel method is mainly associated with the hydrolysis of $Si(OR)_4$; this reagent is readily available, inexpensive, and its hydrolysis proceeds relatively smoothly, as discussed in numerous original papers and reviews [29]. However, the hydrolysis of $M(OR)_4$ (M = metal), unlike the hydrolysis of $Si(OR)_4$, is an extremely fast process. Thus, the basic concepts that were developed specifically for $Si(OR)_4$ cannot be applied to the hydrolysis of any arbitrary metal alkoxides. The higher coordination number of metals in their alcoholic and hydroxy derivatives compared to $Si(OR)_4$ leads to a high propensity for oligomerization and polymerization of metal alkoxides after the first stages of hydrolysis.

In the case of tetraethoxysilane, the overall reaction can be written as [29]:

$$\mathrm{Si(OEt)_4 + 2H_2O \Rightarrow SiO_2 + 4HOEt.} \quad (1)$$

The situation in the case of titanium alkoxides is more ambiguous. In a calorimetric hydrolysis study of $Ti(OR)_4$ at different concentrations, the values of reaction enthalpy of the first hydrolysis stage were measured for R = Et, iPr, and *n*-Bu [29]. It turned out that further hydrolysis proceeds much slower and with very little heat release (for R = Et its value is zero within the accuracy of the experiment).

$$\mathrm{Ti(OR)_4 + H_2O = Ti(OR)_2(OH) + ROH} \quad (2)$$

Therefore, this step is immediately followed by condensation:

$$n\mathrm{Ti(OR)_3(OH) \Rightarrow Ti}_n\mathrm{O}_x\mathrm{(OR)}_{4n-2x}. \quad (3)$$

The final composition of the hydrolysis products of alkoxides of titanium roughly corresponds to $TiO_{1.5}(OR)\cdot yROH$, where y = 0.15–1.00 depending on the nature of the alcohol. The residual carbon during thermal treatment in air is eliminated in the process of crystallization at 400–550 °C; thus, titanium dioxide nanoparticles are obtained [29].

In this study we investigate in detail the influence of the hydrolysis medium and the duration of the hydrolytic process on composition, local structure, morphology, texture, and optical properties of TiO_2/2D mordenite nanocomposites.

Results and Discussion

TiO_2/2D mordenite compounds were synthetized from the parent layered MOR-L by introduction of TEOT, its further hydrolysis, and calcination. Further details are given in the Experimental section. The calcined (C) samples are labeled as Ti-W*N*h-C and Ti-E*N*h-C with N = 6, 12, and 24 for materials hydrolyzed in water (W) and 70% ethanol solution (E) for 6, 12, and 24 h, respectively. The non-calcined samples are designated as Ti-W*N*h and Ti-E*N*h.

XRD, ^{27}Al NMR, and SEM-EDX studies

Figure 1a and Figure 1b show small-angle and full X-ray diffraction (XRD) patterns, respectively, for the samples containing hydrolyzed forms of Ti after hydrolysis of TEOT. The full XRD patterns of the hydrolyzed samples after calcination are shown in Figure 1c. For comparison, the corresponding patterns for the parent compound MOR-L are also given.

As it was shown in our previous study [5], the as-synthetized lamellar MOR-L exhibits peaks characteristic of a 3D mordenite structure and small-angle peaks at 2θ = 2.7° and 5.5°, which correspond to the (001) and (002) peaks of the ordered layered structure with an interplanar distance of 3.2 nm. According to Figure 1b, the introduction of TEOT and its further hydrolysis do not significantly perturb the mordenite peaks. But the small-angle reflection peaks corresponding to the lamellar structure disappear (Figure 1a); traces of a blurred peak are observed only for the sample with minimal hydrolysis time in 70% ethanol solution. An obvious reason for the loss of lamellar structure is the rate of hydrolysis, which is much higher for TEOT than for TEOS [5]. The rapid and apparently uneven growth of oligomers in different regions of the interlamellar layers leads to a disruption of the long-range order of the lamellae.

In addition, the full XRD patterns evidence the formation of an amorphous phase, presumably nanosized TiO_2 (Figure 1b). Zang et al. [30] showed that the XRD pattern of nanometer-sized amorphous TiO_2 consists of broad humps at 2θ values of 35°, 53°, and 75°. In the TiO_2/2D mordenite composites studied in our work, the first hump is masked by the main zeolite peaks, but the remaining two are identical to the ones reported in [30]. Amorphous TiO_2 particles exhibiting such an XRD pattern can be described as small strained anatase-like crystalline cores with strongly distorted shells. These amorphous nanoparticles are responsible for the formation of single-phase nanocrystalline anatase upon heating [30]. This is exactly what we observe.

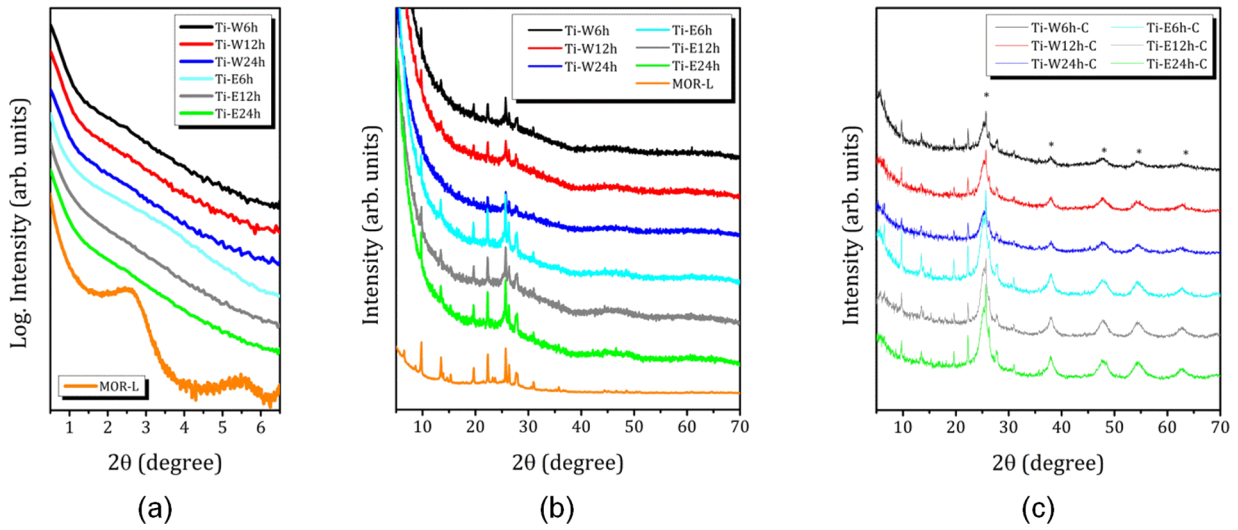

Figure 1: (a) Small-angle powder patterns for the parent compound MOR-L and the samples after TEOT hydrolysis. (b, c) Full XRD powder patterns for the Ti-loaded samples after (b) TEOT hydrolysis and (c) subsequent calcination. Asterisks indicate the anatase structure formed after calcination.

Figure 1c shows that, after calcination, additional large peaks appear in all samples, which can be attributed to anatase TiO_2 nanoparticles. The average size of the TiO_2 nanoparticles, as determined from single diffraction peaks of experimental patterns using the Scherrer formula, is about 4.0 nm for the composites prepared by hydrolysis in water, and slightly larger, about 4.3 nm, after hydrolysis in 70% ethanol solution (Table 1).

In addition, it should be noted that calcination, independent of the medium of TEOT hydrolysis, leads to the complete disappearance of the long-range ordering of the zeolite lamellae (no peak at $2\theta < 5°$; the SAXS patterns are not shown here). This is an important difference between TEOS and TEOT, studied in our previous work [5], for which even after hydrolysis for 12 h in water the long-range order of the lamellae was preserved.

The results of the elemental analysis using energy dispersive X-ray (EDX) and X-ray photoelectron spectroscopy (XPS) of the parent lamellar sample and TiO_2-loaded samples are summarized in Table 1. Upon formation of TiO_2 nanoparticles, a partial dealumination of mordenite occurs. However, the Al distribution over the sample depth is not homogenous. XPS shows that Al is accumulated on the sample surface. The hydrolysis medium does not significantly affect the total Si/Al ratio, but hydrolysis reactions longer than 6 h result in a higher aluminum concentration on the surface. It should be also noted that all TiO_2-loaded samples are characterized by low sodium content. We remind the readers that Na^+ is a charge compensating cation; for an ideal sodium zeolite, Na/Al = 1. The parent MOR-L compound even exhibits a small excess of positive charge (Na/Al > 1) that is balanced by Br^- anions [5]. In the process of post-hydrolysis calcination, the removal of CTAB results in the creation of protonated centers, and the role of compensating cations is eventually passed to protons.

According to the elemental analysis data (Table 1), the TiO_2 loading exceeds 50 wt % in all studied composites. Comparing the data of methods with different measuring depths (i.e., EDX and XPS), we can conclude that Ti is more or less uniformly distributed over the depth in the presented samples. This allows us to state that TiO_2 nanoparticles not only accumulate on the sample surface but are also present in the interlamellar space, which correlates with the nitrogen adsorption data reported next. For both hydrolysis media, the maximum TiO_2 content is reached after 12 h of treatment. For Ti-E24h-C, the lower TiO_2 content compared to TI-E12h-C can be attributed to the formation of 3D mordenite fibers, clearly visible in the SEM images (see below in Figure 3).

From the comparison of the surface (XPS) and volume (EDX) content of TiO_2, we can not only deduce a fairly uniform distribution of titania over the volume, but also a somewhat higher volume content for samples obtained by hydrolysis in water. This suggests that the formation of anatase particles occurs both on the surface and in the entire accessible mesoporous volume, creating titania pillars for the mesoporous system.

Figure 2 shows the ^{27}Al magic angle spinning nuclear magnetic resonance (MAS NMR) spectra of the parent compound MOR-L and the TiO_2-loaded samples. They confirm the regularity of the zeolite frameworks of the as-prepared samples. The

Table 1: Average TiO_2 particle size ⟨*d*⟩ and elemental composition, determined by EDX and XPS, of the as-synthetized and Ti-loaded samples, and their TiO_2 content.

Sample	Method	Si/Al	Na/Al	Ti/Al	TiO_2 (wt %)	⟨*d*⟩ (nm) XRD	Ref.
MOR-L	EDX	8.4 ± 0.3	1.14 ± 0.03	—	—	—	[5]
Ti-W6h-C	EDX	10.2 ± 0.4	0.5 ± 0.1	16 ± 1	63 ± 1	4.0 ± 0.1	[28]
	XPS	6.2 ± 0.1	ND[a]	7.6 ± 0.3	52 ± 1		
Ti-W12h-C	EDX	10.2 ± 0.1	0.2 ± 0.1	29 ± 1	73 ± 1	4.1 ± 0.1	this paper
	XPS	4.6 ± 0.1	ND[a]	6.8 ± 0.3	60 ± 1		
Ti-W24h-C	EDX	10.9 ± 0.2	0.4 ± 0.1	30 ± 1	72 ± 1	3.9 ± 0.1	this paper
	XPS	4.8 ± 0.1	ND[a]	8.2 ± 0.3	63 ± 1		
Ti-E6h-C	EDX	9.3 ± 0.6	0.3 ± 0.2	15 ± 2	61 ± 2	4.2 ± 0.1	[28]
	XPS	6.9 ± 0.1	ND[a]	7.0 ± 0.3	51 ± 1		
Ti-E12h-C	EDX	10.6 ± 0.2	0.3 ± 0.1	20 ± 1	66 ± 1	4.3 ± 0.1	this paper
	XPS	4.2 ± 0.1	ND[a]	10.5 ± 0.3	70 ± 1		
Ti-E24h-C	EDX	10.5 ± 0.2	0.4 ± 0.1	10 ± 1	50 ± 1	4.4 ± 0.1	this paper
	XPS	5.3 ± 0.1	ND[a]	6.3 ± 0.3	55 ± 1		

[a]The Na 1s peak overlaps with the Ti LMM Auger peak, which impedes correct evaluation of the Na content.

spectrum consists of only one line at 54 ppm, which corresponds to aluminum in regular tetrahedral sites of the zeolite framework. As it was reported earlier for 2D mordenite pillared by amorphous SiO_2, obtained by hydrolysis of TEOT in water, the removal of CTAB leads to a partial removal of Al from the zeolite frameworks [5]. The same is observed for the TiO_2-loaded samples. An additional line at about 0 ppm corresponds to extra-framework six-coordinated Al species [31-34], and the relative content of this extra-framework Al does not depend much on duration or medium of hydrolysis (about 20% for all samples except Ti-E6h-C, for which it is 15%) and is mainly determined by the mutual arrangement of the CTA^+ cations and Al in the zeolite lamellae in the parent MOR-L compound. The CTA^+ cations are localized near $[AlO_4]^-$ tetrahedra; the removal of organics upon calcination results in a partial collapse of the local zeolite structure.

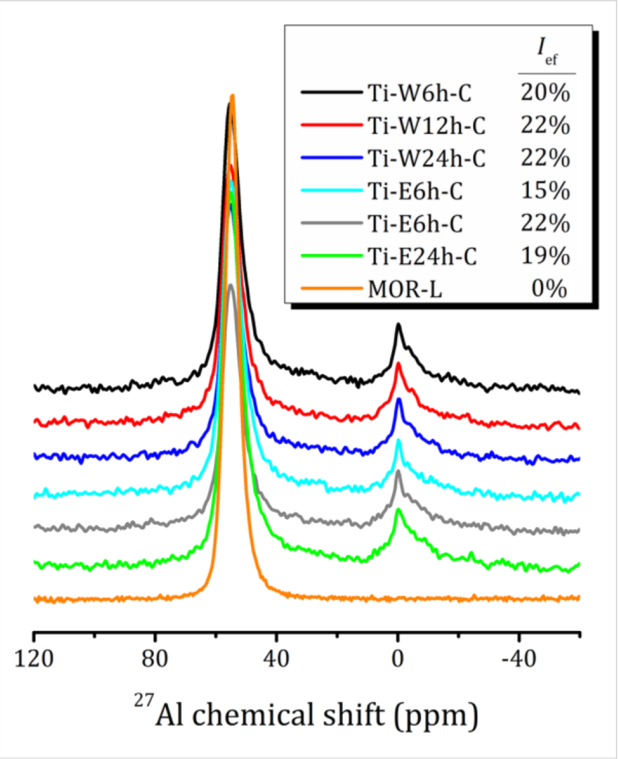

Figure 2: ^{27}Al MAS NMR spectra of the studied samples. The relative integral intensity of the line at 0 ppm corresponding to extra-framework Al species I_{ef} is shown in the legend.

Figure 3 shows images of all studied composites. The scanning electron microscopy (SEM) image of the initial lamellar mordenite sample MOR-L is also shown for comparison. As can be seen, MOR-L exhibits elongated plates up to 1 μm long and 0.1 μm wide, combined into stacks. After introduction of TEOT followed by hydrolysis and calcination, all composites have a similar morphology. Thin plates of about 0.5 μm in size covered with nanoparticles of about 10 nm in size. The samples obtained by hydrolysis in 70% ethanol solution exhibit a more foam-like shape. Moreover, hydrolysis in 70% ethanol solution for 24 h results in the formation of thin single-crystalline fibers of mordenite.

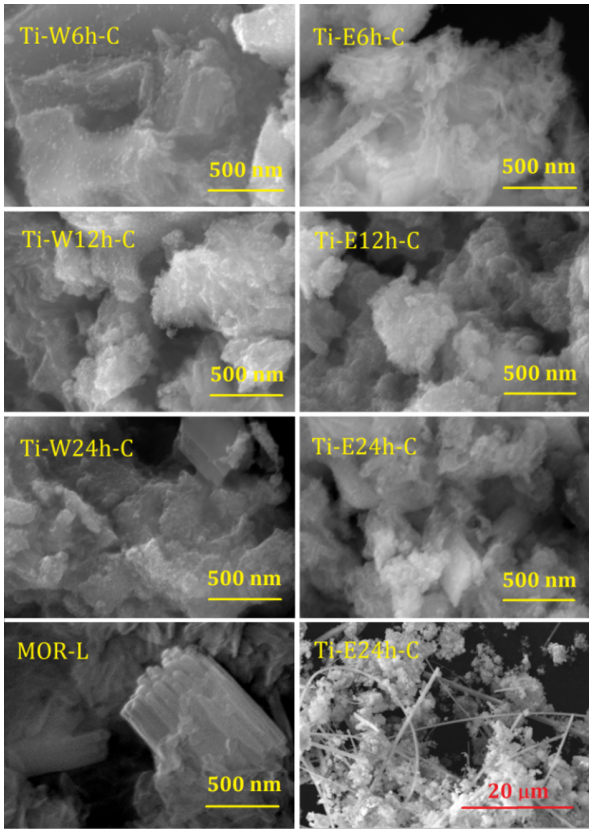

Figure 3: SEM images of the parent lamellar mordenite MOR-L (bottom left) and TiO_2-loaded samples. The bottom-right image shows the formation of mordenite crystals in the Ti-E24h-C sample.

Al 2p, Ti 2p, and O 1s XPS studies

The XPS spectra of Al 2p, Ti 2p, and O 1s for the composites are shown in Figure 4. Figure 4a and Figure 4c also show the Al 2p and O 1s spectra of the starting MOR-L compound. No perturbation is observed in the Si 2p region. The only peak at 104.0 eV, corresponding to Si 2p in MOR-L, is slightly shifted towards a lower binding energy (103.3 eV) for all Ti-loaded samples.

The Al 2p XPS spectra of the Ti-loaded composites show differences compared to the initial MOR-L compound (peak at 75.5 eV). The peak is shifted towards lower binding energies (74.6–74.8 eV), and a shoulder appears at 77.5–76.9 and 76.8–76.4 eV for Ti-W*N*h-C and Ti-E*N*h-C, respectively. An exemplary decomposition of the Al 2p XPS spectrum for Ti-W24h-C is shown in the inset of Figure 4a. For the Ti-W*N*h-C series, the position of the additional peak strongly

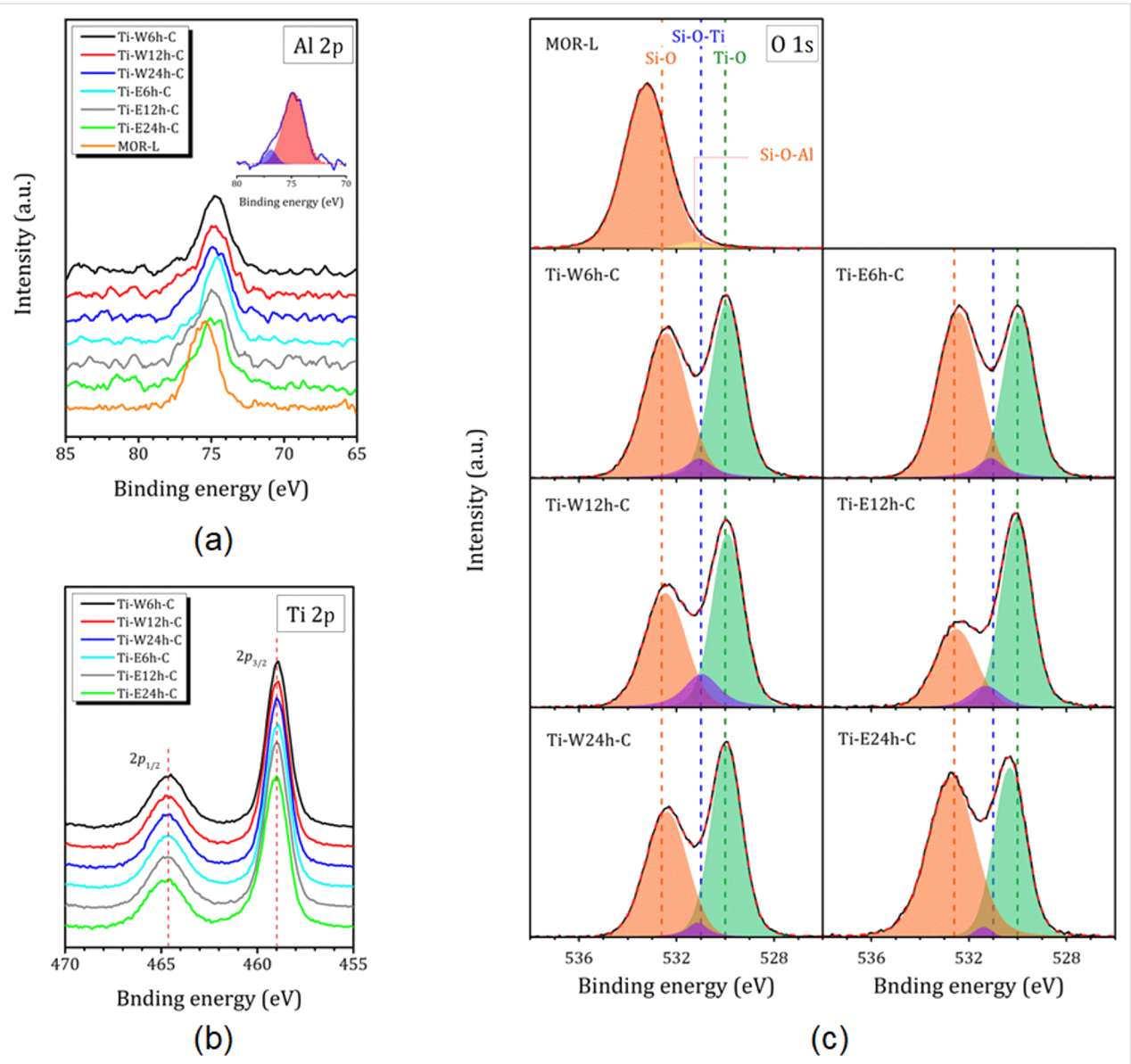

Figure 4: (a) Al 2p, (b) Ti 2p, and (c) decomposed O 1s XPS spectra of the Ti-loaded samples. The Al 2p and O 1s XPS spectra of the MOR-L compound are given for comparison. The inset in (a) shows the decomposition of the Al 2p spectrum for Ti-W24h-C.

depends on the duration of hydrolysis (shift towards lower binding energy with increasing hydrolysis time), whereas the duration of hydrolysis in 70% ethanol solution has no significant effect on the position of the additional peak, but only on its intensity. This peak can be associated with extra-framework Al species, which according to ^{27}Al NMR amount to a total of about 20% (Figure 2). For Ti-E24h-C, a low intensity peak appears at 72.7 eV. This peak can be related to framework Al in the 3D mordenite fibers, which are clearly seen in the SEM image (Figure 3). It should be noted that very often in zeolites the peak at 74.5–74.8 eV is attributed to the presence of Al_2O_3 [35,36]; however, as it will be shown further, this contradicts to the ^{27}Al NMR spectra.

The Ti 2p XPS spectra of the Ti-W*N*h-C and Ti-E*N*h-C samples show peaks corresponding to Ti $2p_{1/2}$ (464.6 eV) and Ti $2p_{3/2}$ (459.0 eV) transitions, indicating that Ti is in the Ti(IV) state [37] (Figure 3b). To identify the interactions between TiO_2 nanoparticles and zeolite layers in the composites, O 1s XPS spectra were analyzed (Figure 4c). The starting compound MOR-L shows a characteristic peak of Si–O bonds (533.2 eV) with a small shoulder at 531.3 eV, which can be attributed to Si–O–Al. The introduction of TiO_2 shifts the Si–O peak down to 532.4–532.6 eV, and a characteristic peak of Ti–O bonds at 529.9 eV appears (for samples hydrolyzed in 70% ethanol solution for 24 h, it is shifted towards 530.3 eV). The signals from Al–O and Al–OH, expected at 532 and

533 eV, respectively, are evidently masked by a broad signal from the Si–O bonds. The O 1s spectra also reveal the emergence of a new O state at about 530.9–531.2 eV, which can be assigned to the formation of Si–O–Ti bonds [27]. A decrease of the Si–O–Ti signal with the hydrolysis duration suggests that the shortest hydrolysis time provides the most efficient immobilization of TiO_2 nanoparticles on zeolites sheets. However, this conclusion is difficult to confirm quantitatively as Si–O–Al bonds also may provide a contribution to this line.

Nitrogen sorption and thermogravimetric studies

Figure 5a,b shows the N_2 adsorption/desorption isotherms of the studied nanocomposites. They demonstrate features charac-

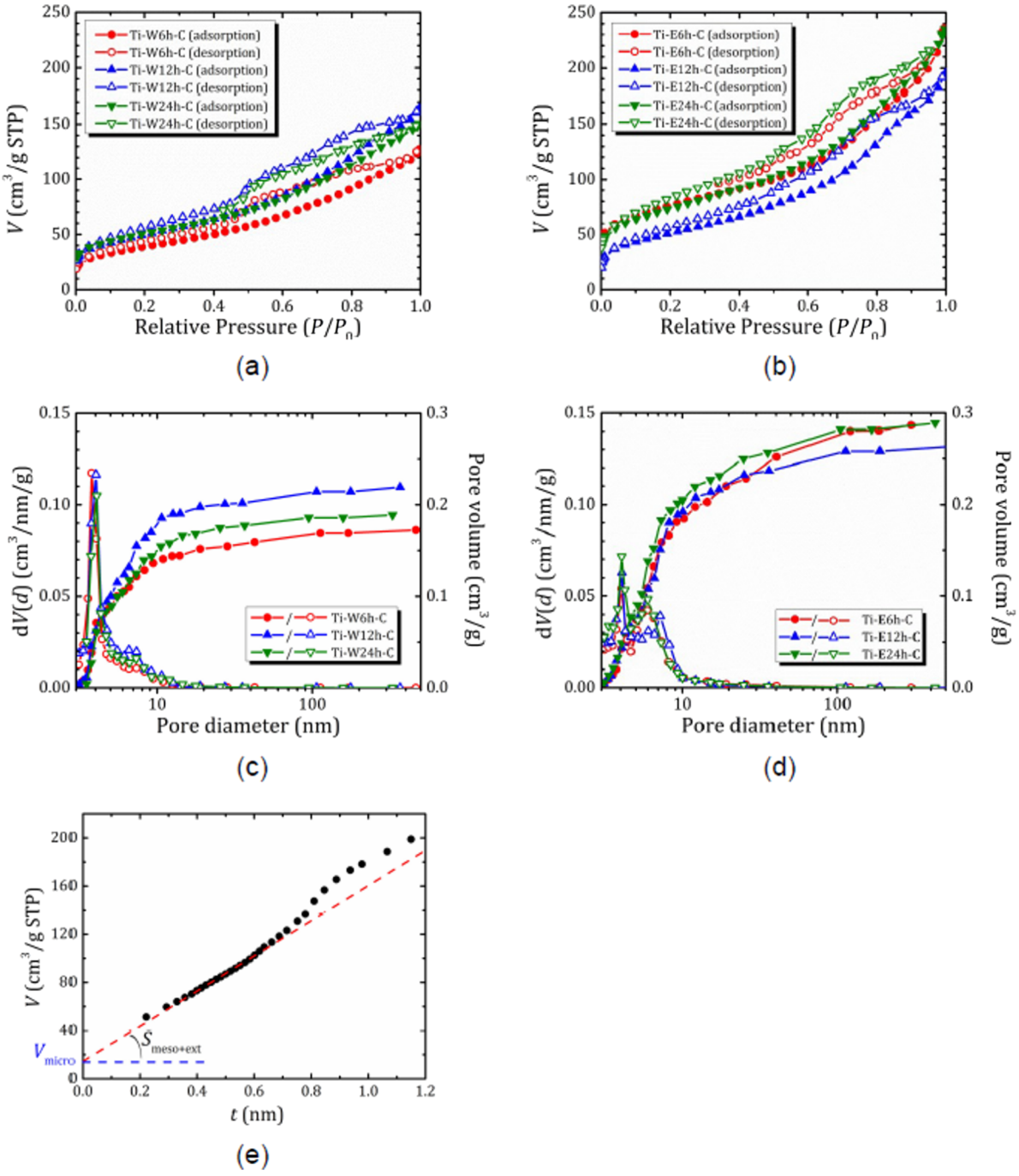

Figure 5: (a, b) Nitrogen adsorption isotherms at 77 K, (c, d) pore size distribution and pore volume in calcined nanocomposites Ti-W*N*h-C (a, c) and Ti-E*N*h-C (b, d); (e) *t*-plot for Ti-E6h-C with a linear fit in the *t* range from 0.33 to 0.6 nm.

teristic of hierarchical porous structures possessing both micro- and mesoporosity. At low pressure, there is a sharp gas absorption (isotherm I or II according to IUPAC classification); at increasing pressure, the absorption continues and is accompanied by a hysteresis loop (isotherm IV according to IUPAC classification). For the series of Ti-W*N*h-C samples hydrolyzed in pure water, the inflection point on the desorption curves appears around $P/P_0 = 0.5$, and it is followed by a broad hysteresis loop. The shape of this loop mainly corresponds to bottle-shaped pores (type H2, more precisely H2b, which corresponds to a pore blocking effect but without percolation, which may also indicate a narrow size distribution of pore cavities), with some presence of slit-shaped pores (type H3). Hydrolysis in 70% ethanol solution (i.e., Ti-E*N*h-C series) results in a wider distribution of mesopores by size. Volume V_{BJH} and diameter D_{BJH} of the mesopores determined from the desorption branch of the hysteresis loops are given in Table 2. The surface area S_{BET} of the samples were calculated using adsorption data in the range of relative pressures of 0.07–0.22. In addition, to estimate micropore surface area and volume, we applied the *t*-plot method, which plots the adsorbed volume as a function of the effective thickness (*t*) of the adsorbed layer. For a correct transformation of relative pressure (P/P_0) to *t,* we used the formulas proposed in [38,39] for hierarchical microporous/mesoporous zeolites. In this method, a linear fit at low thickness of adsorbate film (low relative pressure) provides the micropore volume V_{micro} (the intercept) and the mesopore plus external surface area $S_{meso+ext}$ (the slope). Then the micropore surface area can be roughly estimated as follows [38]: $S_{micro} = S_{BET} - S_{meso+ext}$. An example of *t*-plot analysis is shown in Figure 5e. The pore volumes and surface areas evaluated from *t*-plot are also listed in Table 2.

According to the *t*-plot analysis, the contribution of micropores to the total pore volume does not exceed 10% and is even lower for the sample hydrolyzed in water. As can be seen from Figure 5c, hydrolysis in water leads to the formation of mesopores of about 3.8 nm in size with a mesopore volume of 0.17 cm^3/g. Increasing the hydrolysis time up to 12 h results in a slight increase of mesopore size and volume (both evaluated from BJH and *t*-plot methods) that correlates with a more developed surface area. However, prolongation of hydrolysis time does not affect the textural properties of the resulting composites. With an increase hydrolysis duration in the presence of ethanol, first, there is a sharp decrease in porosity. Then, there is an increase to almost the same value as it was after the minimum processing time, which may be due to the formation of microporous zeolite. The decrease in specific surface area for Ti-E12h-C compared to Ti-E6h-C is most likely due to the formation of larger mesopores, which are not observed in Ti-E6h-C and T-E24h-C.

It is interesting to note that the surface area of the studied composites obtained by pillaring of lamellar mordenite with anatase nanoparticles formed in the interlamellar space via hydrolysis is very close to the one reported for TiO_2/ZSM-5 composites obtained by a related method (by adding the presynthesized zeolite in the synthesis medium of TiO_2 and, vice versa, by adding presynthesized TiO_2 in the synthesis medium of zeolite [27]), lower than in a mechanical mixture of TiO_2 with microporous zeolite, but higher than for composites obtained by a liquid impregnation method [40].

Thermogravimetric (TG) profiles of the studied samples together with the derivative thermogravimetric (DTG) curves are shown in Figure 6. As can be seen, mass loss occurred in two main steps, namely, the rapid desorption of surface water or weakly bound water molecules in the temperature range of 40–100 °C and further mass loss in the temperature range of 100–300 °C, attributed to desorption of the remaining water enclosed in voids and channels [41,42]. However, even at temperatures above 300 °C, all samples exhibit a small peak in the DTG curves at about 400 °C, which can be attributed either to water molecules trapped in hardly accessible voids or, more probably, to a removal of specific hydroxy groups [34]. Moreover, all samples except Ti-W4h-C show a linear mass loss

Table 2: Textural properties of the Ti-loaded samples from N_2 adsorption isotherms.

Sample	S_{BET} (m^2/g)	$S_{meso+ext}$ (m^2/g)	S_{micro} (m^2/g)	V_{BJH} (cm^3/g)	V_{micro} (cm^3/g)	D_{BJH} (nm)
Ti-W6h-C	134	131	3	0.17	0.004	3.8
Ti-W12h-C	178	178	0	0.22	0.005	4.0
Ti-W24h-C	178	170	8	0.19	0.007	4.1
Ti-E6h-C	268	226	42	0.29	0.022	4.1/6.0[a]
Ti-E12h-C	183	179	4	0.26	0.005	4.1/7.2[a]
Ti-E24h-C	259	241	18	0.29	0.015	4.1/6.0[a]

[a]For the Ti-E*N*h-C series two pore diameter values correspond to two maxima in the pore size distribution curves.

starting from 300 °C that is not reflected by DTG and can be attributed to progressive dehydroxylation (for hydroxy groups with a significant inhomogeneity) [41]. For the sample Ti-W12h-C, this effect is most pronounced and corresponds to about 7.6% of the total mass loss. The total mass loss Δw as well as the mass loss below and above 300 °C (Δw_1 and Δw_2, respectively) are listed in Table 3. It should be noted that the samples contain different amounts of TiO_2 (Table 1). Water is mainly located in zeolite voids. Hence, for a more appropriate determination of the amount of water by mass loss, we need to take it into account. The mass losses below and above 300 °C, recalculated assuming that they are due to the zeolite phase alone, $\Delta w_1'$ and $\Delta w_2'$, respectively are also listed in Table 3.

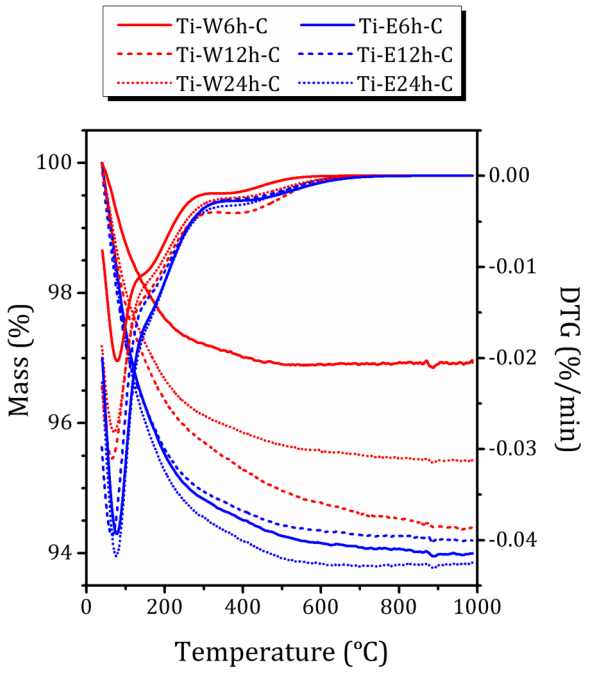

Figure 6: TG and DTG profiles for the studied nanocomposites.

As one can see, there is now obvious correlation between water content determined from $\Delta w_1'$ and the mesopore volume V_{BJH} estimated from nitrogen adsorption. Despite the larger pore volume and surface area, there is about the same amount of water in the samples obtained by hydrolysis in 70% ethanol solution and in pure water. Nevertheless, there is a strong correlation between the water content $\Delta w_1'$ and the amount of hydroxy groups, $\Delta w_2'$. This points out to a strong interaction of nanoconfined water with hydroxy groups on the inner surface of mesopores, a part of which formed upon calcination [6]. Moreover, the samples obtained in 70% ethanol solution may exhibit different hydrophilic/hydrophobic properties than the samples hydrolyzed in pure water. It is known that the hydrophilicity of TiO_2 depends on the crystalline phase and surface composition, but not on the size [43]. Moreover, it was found that introduction of TiO_2 into an amorphous siliceous matrix increases the hydrophilicity of the material. However, as it was shown in [44], the formation of a dense anatase phase has a strong influence on both the value of water adsorption energy and the distribution of water adsorption centers.

UV–vis spectrometry

To determine the bandgap energy E_g, the Tauc method was applied to the diffuse reflectance spectra. In this method, it is assumed that the energy-dependent absorption coefficient α can be written as

$$(\alpha \cdot h\nu)^{1/n} = B\left(h\nu - E_g\right), \tag{4}$$

where h is the Planck constant, $h\nu$ is the photon energy, and B is a constant. The factor n depends on the nature of the electron transition, that is, n = 1/2 for direct and n = 2 for indirect transition bandgaps. The Kubelka–Munk method allows one to transform the reflectance spectra into the corresponding adsorption spectra using the function

Table 3: Mass loss below (Δw_1, $\Delta w_1'$) and above (Δw_2, $\Delta w_2'$) 300 °C as directly determined from TG curves (Δw_1, Δw_2) and recalculated accounting for TiO_2 content ($\Delta w_1'$, $\Delta w_2'$). The total mass losses Δw and $\Delta w'$ are also provided.

Sample	40 °C < T < 300 °C		300 °C < T < 1000 °C		300 °C < T < 1000 °C	
	Δw_1 (%)	$\Delta w_1'$ (%)	Δw_2 (%)	—	Δw_1 (%)	$\Delta w_1'$ (%)
Ti-W6h-C	2.8 ± 0.1	7.6 ± 0.3	0.3 ± 0.1	Ti-W6h-C	2.8 ± 0.1	7.6 ± 0.3
Ti-W12h-C	3.9 ± 0.1	14.4 ± 0.3	0.7 ± 0.1	Ti-W12h-C	3.9 ± 0.1	14.4 ± 0.3
Ti-W24h-C	4.3 ± 0.1	15.3 ± 0.3	1.3 ± 0.1	Ti-W24h-C	4.3 ± 0.1	15.3 ± 0.3
Ti-E6h-C	5.2 ± 0.1	13.3 ± 0.5	0.9 ± 0.1	Ti-E6h-C	5.2 ± 0.1	13.3 ± 0.5
Ti-E12h-C	5.0 ± 0.1	14.8 ± 0.3	0.8 ± 0.1	Ti-E12h-C	5.0 ± 0.1	14.8 ± 0.3
Ti-E24h-C	5.5 ± 0.1	10.9 ± 0.3	0.7 ± 0.1	Ti-E24h-C	5.5 ± 0.1	10.9 ± 0.3

$$F(R)=\frac{K}{S}=\frac{(1-R)^2}{2R}, \quad (5)$$

where R is the reflectance of a thick uniform sample, and K and S are the adsorption and scattering coefficients, respectively. When $F(R_\infty) \sim \alpha$, by combing Equation 4 and Equation 5, one obtains

$$\left(F(R)\cdot h\nu\right)^{1/n}=B\left(h\nu-E_g\right). \quad (6)$$

Figure 7a shows the diffuse reflectance spectra of the prepared TiO_2/2D mordenite nanocomposite. All samples exhibit absorption edges near 400 nm due to the anatase TiO_2 bandgap absorption. Figure 7b shows the reflectance spectra of the studied nanocomposites transformed using Equation 6 with $n = 2$ (since TiO_2 is an indirect bandgap semiconductor). Semiconductor materials are characterized by a steep linear increase in light absorption with increasing energy. The bandgap energy can be estimated from the point of intersection of the x-axis of the linear fit of the Tauc plot.

As one can see from Figure 7b, the E_g values for the studied TiO_2/2D mordenite nanocomposites are sensitive to the hydrolysis medium. The samples obtained by hydrolysis in water exhibit E_g values of about 3.22 eV, which is close to the value of bulk anatase [45,46]. Hydrolysis in 70% ethanol solution results in higher E_g values, about 3.27 eV, which are typical for anatase nanoparticles [45].

It should be noticed that according to a number of studies, the bandgap width in TiO_2/zeolite composites depends both on the topology of the zeolite framework [47] and on the ratio between TiO_2 and zeolite [47,48]. Alvarez et al. [47] reported that for TiO_2 deposited on mordenite during the TiO_2 sol–gel synthesis in a ratio of 75:25, which is close to that in our work (i.e., between 50:50 and 70:30), leads to a noticeable increase in the bandgap (3.47 eV) [47]. It should also be noted that TiO_2/zeolite composites that were obtained by either incorporating the presynthesized zeolite in the synthesis medium of TiO_2 or incorporating presynthesized TiO_2 in the synthesis medium of ZSM-5 [27] exhibit optical properties very similar to those found in our work.

Conclusion

A series of pillared TiO_2/2D mordenite nanocomposites were successfully synthetized from the initial lamellar CTAB/2D mordenite by introducing TEOT, hydrolyzing the resulting composite in either water or 70% ethanol solution with hydrolysis reaction times of 6, 12, and 24 h, and subsequent calcination. The main results of the comprehensive study of the obtained composites can be summarized as follows. (1) A study of the TEOT hydrolysis process was carried out, and it was found that the properties of the samples depend significantly on the hydrolysis medium and the duration of the process. The hydrolysis of TEOT in the interlamellar CTAB layers in all cases disrupts the long-range ordering of zeolite lamellae. Ethanol allows one to attenuate and slow down this process compared to pure water. In samples prepared in 70% ethanol solution, the residual ordering of the lamellar structure at the first stage of the process is preserved to some extent, and the textural characteristics are better compared to samples prepared in pure water. Further calcination, regardless of the medium in which TEOT hydrolysis occurred, leads to the final disappearance of the long-range ordering of zeolite lamellas. (2) According to XRD data, ana-

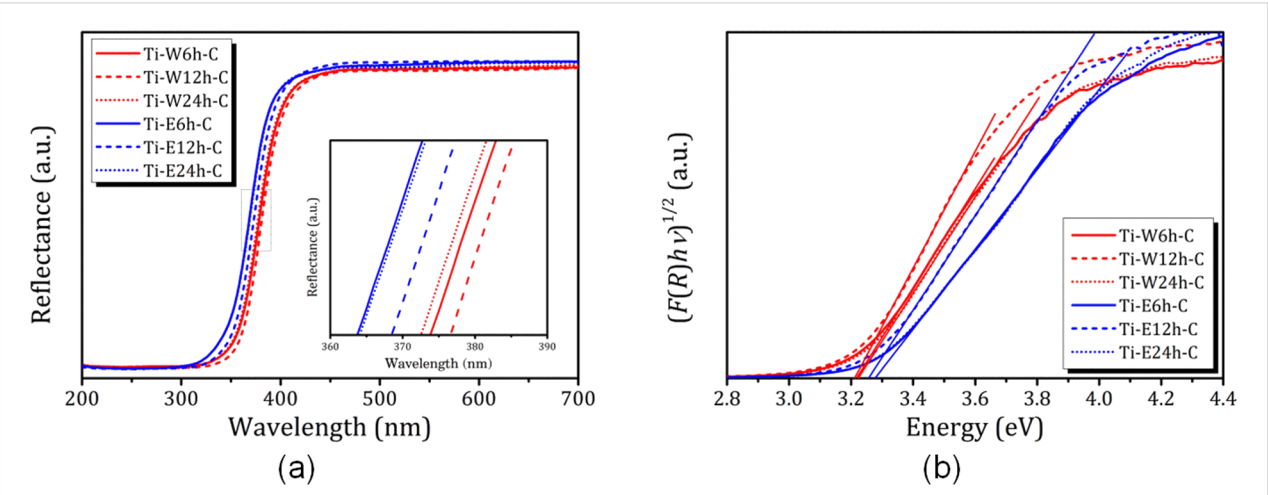

Figure 7: (a) UV–vis diffuse reflectance spectra and (b) plots of $(F(R)h\nu)^{1/2}$ versus photon energy for calculation of bandgap energies of TiO_2-loaded mordenite.

tase nanoparticles of about 4 nm in size form pillars separating the mordenite layers, creating the mesoporosity observed in the experiment. The textural properties of the samples strongly depend on the hydrolysis medium. Hydrolysis in 70% ethanol solution leads to a bimodal distribution of pore sizes, with peaks at 4 and 6 nm, as well as to an increase in the volume of mesopores. (3) Hydrolysis in 70% ethanol solution for 24 h leads to recrystallization of 2D mordenite and to the formation of thin single-crystalline fibers of 3D mordenite. (4) Immobilization of TiO_2 nanoparticles on the zeolite support was confirmed by XPS. (5) Samples obtained by hydrolysis in water exhibit a bandgap of 3.22 eV, which is close to that of bulk anatase. Hydrolysis in 70% ethanol solution results to higher bandgap values, around 3.27 eV, which are characteristic of anatase nanoparticles.

Despite the still large bandgap, the immobilization of TiO_2 on the zeolite matrix, combined with the mesopore structure important for high mass transfer properties, suggests that these materials may be promising catalysts under flow conditions. However, it is necessary to further search for parameters to regulate the growth of nanoparticles in the interlayer space (e.g., the temperature of hydrolysis) and their morphology, as well as to investigate the influence of synthesis conditions on the target properties. Nevertheless, the successful application of zeolite pillaring using an oxide material other than SiO_2 opens up a wide range of opportunities for the development of new materials for specific applications.

Experimental

The synthesis of nanocomposites was carried out similarly to the method first proposed in [49] and used previously in [5,50] for the insertion of SiO_2 nanopillars. The latter includes the following steps: (1) synthesis of layered zeolite by self-assembly using CTAB as an organic structural guiding agent that creates regular mesopores, (2) introduction of TEOS molecules into the interlayer space, (3) hydrolysis and formation of pillars of amorphous SiO_2 separating the layers of two-dimensional zeolite, and (4) calcination for the removal of organic molecules. In this work, to obtain TiO_2/2D mordenite composites (layers of two-dimensional mordenite separated by TiO_2 pillars), the synthesis method was slightly adjusted and TEOS was replaced by TEOT. This substitution, taking into account the differences in the properties of these compounds, required changes in both the reagents for hydrolysis (processes in pure water and in 70% ethanol solution were compared) and in the choice of process time intervals.

In the synthesis of TiO_2/2D mordenite compounds, the layered MOR-L sample obtained in step (1), was stirred in TEOT at a mass ratio of 1:5 for 6 h at 25 °C. The sample was filtered off and then dried at 35 °C for 12 h. To hydrolyze TEOT that had diffused into the CTAB layers and to obtain TiO_2 nanoparticles in the interlamellar space, 1.0 g of TEOT-impregnated MOR-L sample was stirred in either 10.0 g of distilled water or a 70% ethanol-in-water solution, at 90 °C, for 6, 12, and 24 h. After completion of the hydrolysis, the samples were filtered, washed with distilled water, dried at 120 °C, and finally calcined at 550 °C for 4 h in air. The calcined (C) samples are labeled as Ti-W*N*h-C and Ti-E*N*h-C with N = 6, 12, and 24 for materials hydrolyzed in water (W) and 70% ethanol solution (E) for 6, 12, or 24 h, respectively. The non-calcined samples are labeled as Ti-W*N*h and Ti-E*N*h.

Powder XRD analysis was carried out on a Bruker D8 DISCOVER diffractometer with monochromatic Cu Kα radiation. XRD patterns of the studied compounds were recorded in the 2θ range of 5–70° with a step width of 0.0302°. SAXS patterns were recorded over a 2θ scanning range of 0.2–7.0° with a step width of 0.01°.

Elemental analysis and morphology of synthetized TiO_2/2D mordenite nanocomposites were probed by SEM-EDX using a Zeiss Merlin microscope equipped with an Oxford Instruments INCAx-act EDX console.

N_2 sorption isotherms were recorded at 77 K using a Quadra-Sorb SI instrument. Before analysis, samples were outgassed under vacuum for 6 h at 300 °C. The surface areas were estimated within the mBET method. Thermal gravimetric analysis (TGA) was carried out using a Netzsch STA 449 F1 Jupiter instrument in the temperature range of 40–990 °C at a heating rate of 10 °C/min in an Ar flow of 90 mL/min.

^{27}Al MAS NMR spectra were recorded using a Bruker Avance IIIWB 400 MHz solid-state NMR spectrometer (operating with Topspin version 3.2) using a double-resonance 4 mm MAS probe with a rotor speed of 12.5 kHz.

XPS spectra of the samples were taken using a Thermo Fisher Scientific Escalab 250Xi spectrometer with non-monochromatic Al Kα radiation (photon energy 1486.6 eV). Bandgaps energies were determined by diffuse reflectance spectroscopy using a Lambda 1050 spectrophotometer (Perkin Elmer) equipped with an integrating sphere in the spectral range of 200–700 nm. Barium sulfate ($BaSO_4$) was used as a reference.

Acknowledgements

The materials were synthetized at the Center for Nanoscience and Nanotechnology, National Autonomous University of Mexico and characterized at the Research Park of Saint Petersburg State University (Centre for X-ray Diffraction Studies;

Interdisciplinary Resource Centre for Nanotechnology; Centre for Physical Methods of Surface Investigation; Centre for Diagnostics of Functional Materials for Medicine, Pharmacology and Nanoelectronics; Thermogravimetric and Calorimetric Research Centre; Centre for Optical and Laser Materials Research). The authors thank the Department of Zeolite Research of the Institute of Science of the BUAP (ICUAP), and its staff, for fruitful discussions of the results obtained.

Funding

This research was supported by DGAPA-PAPIIT grant IG101623.

Author Contributions

Marina G. Shelyapina: funding acquisition; project administration; supervision; visualization; writing – original draft; writing – review & editing. Rosario Isidro Yocupicio-Gaxiola: conceptualization; investigation; resources. Gleb A. Valkovsky: data curation; formal analysis; funding acquisition; investigation. Vitalii Petranovskii: conceptualization; methodology; supervision; writing – original draft; writing – review & editing.

ORCID® iDs

Marina G. Shelyapina - https://orcid.org/0000-0003-3769-941X
Gleb A. Valkovsky - https://orcid.org/0000-0002-5651-8234
Vitalii Petranovskii - https://orcid.org/0000-0002-8794-0593

Data Availability Statement

The data that supports the findings of this study is available from the corresponding author upon reasonable request.

References

1. Roth, W. J.; Nachtigall, P.; Morris, R. E.; Čejka, J. *Chem. Rev.* **2014,** *114,* 4807–4837. doi:10.1021/cr400600f
2. Zhang, K.; Ostraat, M. L. *Catal. Today* **2016,** *264,* 3–15. doi:10.1016/j.cattod.2015.08.012
3. Ge, T.; Hua, Z.; He, X.; Zhu, Y.; Ren, W.; Chen, L.; Zhang, L.; Chen, H.; Lin, C.; Yao, H.; Shi, J. *Chin. J. Catal.* **2015,** *36,* 866–873. doi:10.1016/s1872-2067(14)60263-1
4. Jia, X.; Khan, W.; Wu, Z.; Choi, J.; Yip, A. C. K. *Adv. Powder Technol.* **2019,** *30,* 467–484. doi:10.1016/j.apt.2018.12.014
5. Shelyapina, M. G.; Yocupicio-Gaxiola, R. I.; Zhelezniak, I. V.; Chislov, M. V.; Antúnez-García, J.; Murrieta-Rico, F. N.; Galván, D. H.; Petranovskii, V.; Fuentes-Moyado, S. *Molecules* **2020,** *25,* 4678. doi:10.3390/molecules25204678
6. Shelyapina, M. G.; Nefedov, D. Y.; Antonenko, A. O.; Hmok, H.; Egorov, A. V.; Egorova, M. I.; Ievlev, A. V.; Yocupicio-Gaxiola, R.; Petranovskii, V.; Antúnez-García, J.; Fuentes, S. *Appl. Magn. Reson.* **2023,** *54,* 915–928. doi:10.1007/s00723-023-01589-w
7. Guo, G.-q.; Sun, Y.-j.; Long, Y.-c. *Chem. Commun.* **2000,** 1893–1894. doi:10.1039/b005453o
8. Migliori, M.; Aloise, A.; Giordano, G. *Catal. Today* **2014,** *227,* 138–143. doi:10.1016/j.cattod.2013.09.033
9. Li, H.-J.; Zhou, X.-D.; Di, Y.-H.; Zhang, J.-M.; Zhang, Y. *Microporous Mesoporous Mater.* **2018,** *271,* 146–155. doi:10.1016/j.micromeso.2018.05.039
10. Catizzone, E.; Migliori, M.; Mineva, T.; van Daele, S.; Valtchev, V.; Giordano, G. *Microporous Mesoporous Mater.* **2020,** *296,* 109988. doi:10.1016/j.micromeso.2019.109988
11. Xu, D.; Feng, J.; Che, S. *Dalton Trans.* **2014,** *43,* 3612–3617. doi:10.1039/c3dt53308e
12. Wang, X.; Chen, H.; Meng, F.; Gao, F.; Sun, C.; Sun, L.; Wang, S.; Wang, L.; Wang, Y. *Microporous Mesoporous Mater.* **2017,** *243,* 271–280. doi:10.1016/j.micromeso.2017.02.054
13. Xu, L.; Ji, X.; Li, S.; Zhou, Z.; Du, X.; Sun, J.; Deng, F.; Che, S.; Wu, P. *Chem. Mater.* **2016,** *28,* 4512–4521. doi:10.1021/acs.chemmater.6b02155
14. Brus, L. E. *J. Chem. Phys.* **1984,** *80,* 4403–4409. doi:10.1063/1.447218
15. de Araujo Scharnberg, A. R.; de Loreto, A. C.; Wermuth, T. B.; Alves, A. K.; Arcaro, S.; dos Santos, P. A. M.; de Assis Lawisch Rodriguez, A. *Bol. Soc. Esp. Ceram. Vidrio* **2020,** *59,* 230–238. doi:10.1016/j.bsecv.2019.12.001
16. Cunha, D. L.; Kuznetsov, A.; Achete, C. A.; da Hora Machado, A. E.; Marques, M. *PeerJ* **2018,** *6,* e4464. doi:10.7717/peerj.4464
17. Zvereva, I. A.; Kalinkina, L. M.; Rodionov, I. A.; Sankovich, A. M.; Kolesnik, I. V.; Gudilin, E. A. *Glass Phys. Chem.* **2012,** *38,* 504–510. doi:10.1134/s1087659612060065
18. Zou, X.-X.; Li, G.-D.; Zhao, J.; Su, J.; Wei, X.; Wang, K.-X.; Wang, Y.-N.; Chen, J.-S. *Int. J. Photoenergy* **2012,** *2012,* 720183. doi:10.1155/2012/720183
19. Scaria, J.; Karim, A. V.; Divyapriya, G.; Nidheesh, P. V.; Suresh Kumar, M. *Carbon-supported semiconductor nanoparticles as effective photocatalysts for water and wastewater treatment;* Nano-Materials as Photocatalysts for Degradation of Environmental Pollutants; Elsevier: Amsterdam, Netherlands, 2020; pp 245–278. doi:10.1016/b978-0-12-818598-8.00013-4
20. Vanichvattanadecha, C.; Jaroenworaluck, A.; Henpraserttae, P.; Wimuktiwan, P.; Manpetch, P.; Singhapong, W. *J. Porous Mater.* **2021,** *28,* 1137–1153. doi:10.1007/s10934-021-01065-5
21. Degirmenci, V.; Erdem, Ö. F.; Ergun, O.; Yilmaz, A.; Michel, D.; Uner, D. *Top. Catal.* **2008,** *49,* 204–208. doi:10.1007/s11244-008-9078-z
22. Zaccariello, G.; Moretti, E.; Storaro, L.; Riello, P.; Canton, P.; Gombac, V.; Montini, T.; Rodríguez-Castellón, E.; Benedetti, A. *RSC Adv.* **2014,** *4,* 37826–37837. doi:10.1039/c4ra06767c
23. Zhu, L.; Nguyen, D. C. T.; Woo, J.-H.; Zhang, Q.; Cho, K. Y.; Oh, W.-C. *Sci. Rep.* **2018,** *8,* 12759. doi:10.1038/s41598-018-31188-w
24. Fukahori, S.; Ichiura, H.; Kitaoka, T.; Tanaka, H. *Appl. Catal., B* **2003,** *46,* 453–462. doi:10.1016/s0926-3373(03)00270-4
25. Diban, N.; Pacuła, A.; Kumakiri, I.; Barquín, C.; Rivero, M. J.; Urtiaga, A.; Ortiz, I. *Catalysts* **2021,** *11,* 1367. doi:10.3390/catal11111367
26. Znad, H.; Abbas, K.; Hena, S.; Awual, M. R. *J. Environ. Chem. Eng.* **2018,** *6,* 218–227. doi:10.1016/j.jece.2017.11.077
27. Fernández-Catalá, J.; Sánchez-Rubio, M.; Navlani-García, M.; Berenguer-Murcia, Á.; Cazorla-Amorós, D. *ACS Omega* **2020,** *5,* 31323–31331. doi:10.1021/acsomega.0c04793
28. Shelyapina, M. G.; Mazur, A.; Yocupicio-Gaxiola, R. I.; Caudillo-Flores, U.; Urtaza, A.; Rodionov, I. A.; Zvereva, I. A.; Petranovskii, V. *Appl. Magn. Reson.* **2022,** *53,* 1609–1620. doi:10.1007/s00723-022-01498-4

29. Turova, N. Ya.; Turevskaya, E. P.; Kessler, V. G.; Yanovskaya, M. I. *The Chemistry of Metal Alkoxides;* Kluwer Academic Publishers: Boston, 2002. doi:10.1007/b113856
30. Zhang, H.; Chen, B.; Banfield, J. F.; Waychunas, G. A. *Phys. Rev. B: Condens. Matter Mater. Phys.* **2008,** *78,* 214106. doi:10.1103/physrevb.78.214106
31. Deng, F.; Yue, Y.; Ye, C. *J. Phys. Chem. B* **1998,** *102,* 5252–5256. doi:10.1021/jp9801929
32. Li, S.; Zheng, A.; Su, Y.; Fang, H.; Shen, W.; Yu, Z.; Chen, L.; Deng, F. *Phys. Chem. Chem. Phys.* **2010,** *12,* 3895–3903. doi:10.1039/b915401a
33. Zhukov, Y. M.; Efimov, A. Yu.; Shelyapina, M. G.; Petranovskii, V.; Zhizhin, E. V.; Burovikhina, A.; Zvereva, I. A. *Microporous Mesoporous Mater.* **2016,** *224,* 415–419. doi:10.1016/j.micromeso.2015.12.058
34. Shelyapina, M. G.; Krylova, E. A.; Zhukov, Y. M.; Zvereva, I. A.; Rodriguez-Iznaga, I.; Petranovskii, V.; Fuentes-Moyado, S. *Molecules* **2019,** *24,* 4216. doi:10.3390/molecules24234216
35. Singh, B. K.; Kim, Y.; Kwon, S.; Na, K. *Catalysts* **2019,** *9,* 885. doi:10.3390/catal9110885
36. Lee, J. S.; Kim, H. S.; Park, N.-K.; Lee, T. J.; Kang, M. *Chem. Eng. J.* **2013,** *230,* 351–360. doi:10.1016/j.cej.2013.06.099
37. Domoroshchina, E. N.; Chernyshev, V. V.; Kuz'micheva, G. M.; Dorokhov, A. V.; Pirutko, L. V.; Kravchenko, G. V.; Chumakov, R. B. *Appl. Nanosci.* **2018,** *8,* 19–31. doi:10.1007/s13204-018-0648-5
38. Galarneau, A.; Mehlhorn, D.; Guenneau, F.; Coasne, B.; Villemot, F.; Minoux, D.; Aquino, C.; Dath, J.-P. *Langmuir* **2018,** *34,* 14134–14142. doi:10.1021/acs.langmuir.8b02144
39. Desmurs, L.; Galarneau, A.; Cammarano, C.; Hulea, V.; Vaulot, C.; Nouali, H.; Lebeau, B.; Daou, T. J.; Vieira Soares, C.; Maurin, G.; Haranczyk, M.; Batonneau-Gener, I.; Sachse, A. *ChemNanoMat* **2022,** *8,* e202200051. doi:10.1002/cnma.202200051
40. Mergenbayeva, S.; Abitayev, Z.; Batyrbayeva, M.; Vakros, J.; Mantzavinos, D.; Atabaev, T. S.; Poulopoulos, S. G. *Catalysts* **2024,** *14,* 147. doi:10.3390/catal14020147
41. Shelyapina, M. G.; Nefedov, D. Y.; Antonenko, A. O.; Valkovskiy, G. A.; Yocupicio-Gaxiola, R. I.; Petranovskii, V. *Int. J. Mol. Sci.* **2023,** *24,* 15898. doi:10.3390/ijms242115898
42. Krylova, E. A.; Shelyapina, M. G.; Nowak, P.; Harańczyk, H.; Chislov, M.; Zvereva, I. A.; Privalov, A. F.; Becher, M.; Vogel, M.; Petranovskii, V. *Microporous Mesoporous Mater.* **2018,** *265,* 132–142. doi:10.1016/j.micromeso.2018.02.010
43. Bolis, V.; Busco, C.; Ciarletta, M.; Distasi, C.; Erriquez, J.; Fenoglio, I.; Livraghi, S.; Morel, S. *J. Colloid Interface Sci.* **2012,** *369,* 28–39. doi:10.1016/j.jcis.2011.11.058
44. Boffa, V.; Parmeggiani, L.; Nielsen, A. H.; Magnacca, G. *Microporous Mesoporous Mater.* **2016,** *221,* 81–90. doi:10.1016/j.micromeso.2015.09.017
45. López, R.; Gómez, R. *J. Sol-Gel Sci. Technol.* **2012,** *61,* 1–7. doi:10.1007/s10971-011-2582-9
46. Makuła, P.; Pacia, M.; Macyk, W. *J. Phys. Chem. Lett.* **2018,** *9,* 6814–6817. doi:10.1021/acs.jpclett.8b02892
47. Alvarez, K. M.; Alvarado, J.; Soto, B. S.; Hernandez, M. A. *Optik (Munich, Ger.)* **2018,** *169,* 137–146. doi:10.1016/j.ijleo.2018.05.028
48. Munguti, L. K.; Dejene, F. B.; Muthee, D. K. *Mater. Sci. Eng., B* **2023,** *289,* 116281. doi:10.1016/j.mseb.2023.116281
49. Na, K.; Choi, M.; Park, W.; Sakamoto, Y.; Terasaki, O.; Ryoo, R. *J. Am. Chem. Soc.* **2010,** *132,* 4169–4177. doi:10.1021/ja908382n
50. Yocupicio-Gaxiola, R. I.; Petranovskii, V.; Antúnez-García, J.; Fuentes Moyado, S. *Appl. Nanosci.* **2019,** *9,* 557–565. doi:10.1007/s13204-018-0935-1

License and Terms

BEILSTEIN JOURNAL OF NANOTECHNOLOGY

Zeolite materials with Ni and Co: synthesis and catalytic potential in the selective hydrogenation of citral

Inocente Rodríguez-Iznaga[*1], Yailen Costa Marrero[2], Tania Farias Piñeira[1], Céline Fontaine[3], Lexane Paget[3], Beatriz Concepción Rosabal[1], Arbelio Penton Madrigal[4], Vitalii Petranovskii[5] and Gwendoline Lafaye[3]

Full Research Paper

Open Access

Address:
[1]Instituto de Ciencia y Tecnología de Materiales (IMRE), Universidad de La Habana, Zapata y G, 10400, La Habana, Cuba, [2]Universidad de las Ciencias Informáticas, Carretera a San Antonio km 21/2, 19370, La Habana, Cuba, [3]Université de Poitiers, CNRS, Institut de Chimie des Milieux et Matériaux de Poitiers (IC2MP), 4 rue Michel Brunet, Poitiers, France, [4]Facultad de Física, Universidad de La Habana, San Lázaro y L, 10400, La Habana, Cuba and [5]Centro de Nanociencia y Nanotecnología (CNyN), Universidad Nacional Autónoma de México (UNAM), 22860, Ensenada, B.C., México

Email:
Inocente Rodríguez-Iznaga* - inocente@imre.uh.cu

* Corresponding author

Keywords:
citral hydrogenation; cobalt–nickel mixture; impregnation; ion exchange; natural zeolite

Beilstein J. Nanotechnol. **2025,** *16,* 520–529.
https://doi.org/10.3762/bjnano.16.40

Received: 24 December 2024
Accepted: 01 April 2025
Published: 14 April 2025

This article is part of the thematic issue "Symposium of Nanoscience and Nanomaterials 2024 (SNN 2024)".

Guest Editor: R. D. Cadena-Nava

Abstract

Zeolitic materials incorporating mono- and bimetallic systems of nickel and cobalt were obtained from natural zeolite modified with Ni^{2+} and Co^{2+} chloride solutions through traditional ion exchange (IE) and impregnation (Imp) processes. Special attention was given to analyzing the cationic and anionic composition of the resulting materials. The catalytic potential was evaluated in the selective hydrogenation of citral, focused on the formation of unsaturated alcohols. The IE process replaced mainly Ca^{2+} and Na^{+} with Ni^{2+} and Co^{2+} cations in the zeolite phases (clinoptilolite and mordenite mix), while Imp resulted in higher metal content (2.0–2.7%) but retained significant amounts of chloride (1.9–3.8%), as confirmed by XRD and temperature-programmed reduction. The materials prepared by IE had negligible chloride content (0.02–0.07%), and their specific surface areas (138–146 m^2/g) were greater than those of the materials obtained by Imp (54–67 m^2/g). The bimetallic systems exhibited enhanced reducibility of the Co^{2+} and Ni^{2+} isolated cations, attributed to synergistic interactions that weakened the cation–framework binding. Catalytic activity tests showed that nickel species were primarily responsible for citronellal formation. Among all materials, the bimetallic $CoNi_{IE}$ catalyst, prepared by IE, was the only one to produce unsaturated alcohols, suggesting that synergistic Ni–Co interactions played a role in their formation.

Introduction

Numerous publications in the literature highlight zeolites modified with metallic species for various applications, leading to the invention of new functional materials for sustainable development, such as catalysts [1-3]. Among the various methods used to modify zeolites, ion exchange is the most widely employed. Different ion exchange methods are known, such as ion exchange in conventional solutions, in the solid phase with molten salts, and with gaseous phases. Depending on the chosen modification method, particularities regarding the elemental composition and application of the resulting materials occur [4-6]. Cu–Y zeolites were obtained by contacting Na–Y zeolite and Cu(II) nitrate solution, using two different methods, namely, conventional solution ion exchange and incipient wetness impregnation, followed by calcinations at 600 °C in air [5]. The authors reported that, among both zeolites, the Cu–Y material obtained by impregnation followed by calcination exhibited a higher surface area and pore volume, which can positively influence its potential application as a material to reduce greenhouse gas emissions.

While most studies focus on monocationic exchange, multicationic exchange has raised significant interest. The synergy of properties in multicationic systems enables the creation of materials with enhanced properties compared to monocationic zeolites, which is crucial for the development of advanced catalysts and other materials [7-10]. Natural zeolites attract significant attention because of their abundance, low cost, non-toxic nature, and other valuable physical and chemical properties.

Modifying these materials with inexpensive metals leads to low-cost catalysts for various different processes. The selective hydrogenation of α,β-unsaturated aldehydes, such as citral, to unsaturated alcohols is a crucial reaction for producing fine chemicals, fragrances, and other high-value products [11]. The catalysts preferred for this reaction are currently based on noble metals because of their excellent performance [12,13]. However, their high cost and scarcity requires strategies to reduce their use or replace them with non-noble alternatives offering comparable catalytic properties.

Despite extensive research on zeolite-supported transition metal catalysts, their application to citral hydrogenation remains very little explored [11]. Most recent studies focus on the selective hydrogenation of related biomass-derived compounds, such as furfural and cinnamaldehyde [3,14,15]. Zeolites modified with nickel and cobalt have shown promising results in selective hydrogenation reactions, owing to their high dispersion of active sites and tunable acidity. For instance, a zeolite-supported Ni catalyst has demonstrated selectivity in furfural hydrogenation by leveraging controlled acidity to prevent over-hydrogenation and optimize product yields [15]. Similarly, Co-modified zeolites have been effectively used in cinnamaldehyde hydrogenation, where the balance between acidity and metal dispersion facilitates the selective reduction of the carbonyl group while preserving other reactive sites [3].

Building on these insights, this work presents research on the selective hydrogenation of citral using both monometallic and bimetallic nickel and cobalt catalysts supported on natural zeolite, which was modified with Ni^{2+} and Co^{2+} chloride solutions through traditional ion exchange (IE) and impregnation (Imp) processes. Emphasis is put on analyzing the cationic and anionic composition of the materials resulting from both methods and the catalytic performance in citral hydrogenation with a focus on enhancing the formation of unsaturated alcohols.

Results and Discussion

Composition and characterization of the materials

XRD patterns and a SEM micrograph of the starting zeolite mineral (ZSA) are shown in Figure 1 and Figure 2, respectively. The diffraction patterns are normalized and evidence the presence of mordenite and clinoptilolite–heulandite-type zeolites through their main diffraction peaks indicated on the ZSA graph. Other minor phases such as quartz are also present.

The SEM image shows a variety of crisscross crystals, which have the morphology expected for the zeolite types evidenced by XRD [16,17]. Very elongated crystals with acicular to fibrous characteristics, associated with mordenite, can be observed. Additionally, clinoptilolite–heulandite crystals with slats and tabular morphology are present. The amounts of clinoptilolite–heulandite and mordenite crystals displayed in the SEM image correspond to the intensity order of these zeolites shown in the XRD pattern (Figure 1). This indicates that zeolitic mineral from the San Andrés deposit is mainly composed of a mordenite and clinoptilolite–heulandite mixture. Furthermore, the SEM micrographs reveal free spaces between crystallites, contributing to the material's porosity and mesoporosity.

The XRD patterns of the materials obtained using both Imp and IE showed that the framework of both zeolites remains largely unchanged after the applied treatments. However, the materials obtained by Imp exhibit new peaks, such as those observed at 16.1° and 39.3° in CoZ_{Imp}, at 29.5° in NiZ_{Imp}, and at 28.5° in $CoNiZ_{Imp}$. These peaks are attributed to impurities, such as mixed metal chloride salts, deposited on the zeolite surface.

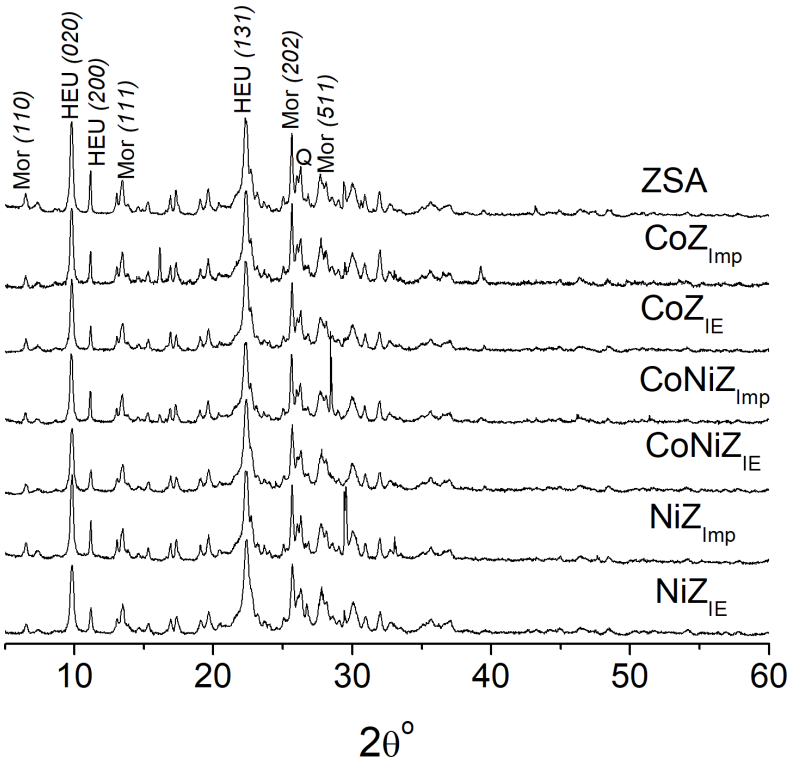

Figure 1: XRD pattern of the starting zeolite mineral (ZSA) and the materials obtained through traditional ion exchange (IE) and impregnation (Imp) methods. The Miller indexes (*hkl*) corresponding to the zeolite phases are shown in the pattern of the ZSA. Mor, HEU, and Q are associated to the phases of mordenite, clinoptilolite–heulandite, and quartz, respectively.

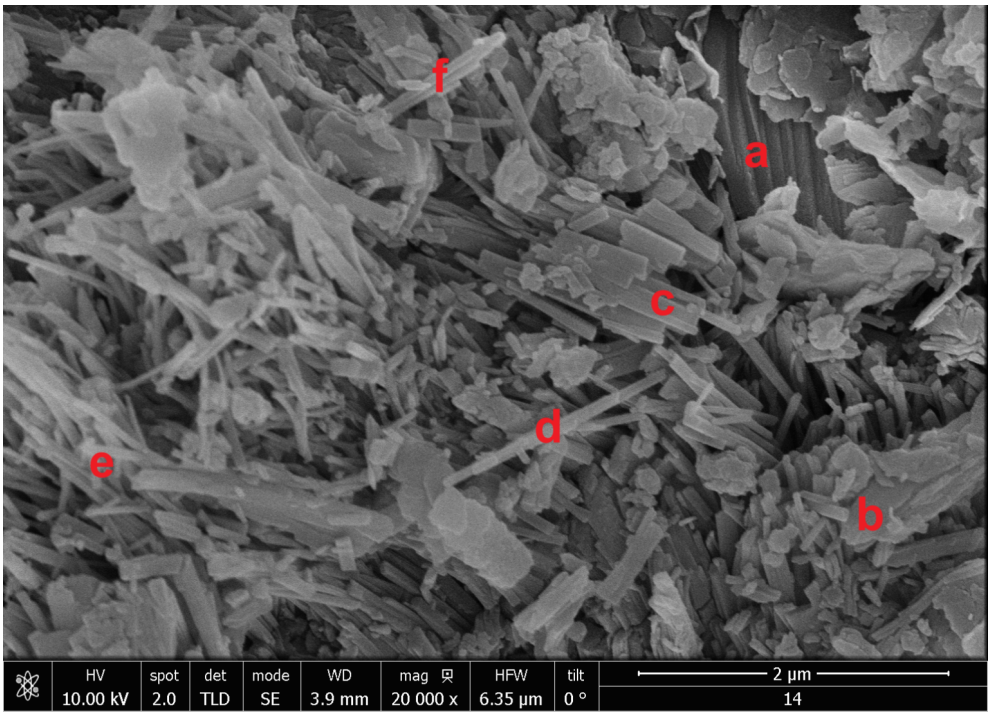

Figure 2: SEM micrograph of ZSA from the San Andrés deposit. Some HEU crystals are indicated by a, b, and c, where a and b exhibit tabular characteristics while c has slat morphology. Mordenite crystals, marked by d, e, and f, show acicular to fibrous shapes.

Specifically, the peaks at 16.1° and 39.3° correspond to both cobalt(II) chloride ($CoCl_2{\cdot}2H_2O$, card 96-900-9874) and cobalt(II) hydroxychloride ($Co_2Cl(OH)_3$, card 96-231-0849). The diffraction peak at 29.5° is associated with $NiCl_2$ (card 96-900-9133), but it could also be assigned to $FeCl_2$ (lawrencite, card 96-901-9129) or $CaCl_2{\cdot}2H_2O$ (sinjarite, card 96-100-1836). The peak at 28.5° can be related to $FeCl_2{\cdot}2H_2O$ (card 96-231-0808), NaCl (halite, card 96-900-0630), or $CaCl_2O_4$ (calcium hypochlorite, card 96-220-7380). The low nickel and cobalt contents in the $CoNiZ_{Imp}$ material (Table 1) may limit the detectability of diffraction peaks associated to cobalt and nickel chloride salts on the zeolite support.

Table 1: Cobalt and nickel contents and Si/Al ratio values for the materials obtained through IE and Imp.

Sample	Co, wt %	Ni, wt %	Si/Al
CoZ_{IE}	1.54 ± 0.08	—	5.47
NiZ_{IE}	—	1.29 ± 0.1	5.20
$CoNiZ_{IE}$	0.97 ± 0.07	1.00 ± 0.08	5.47
CoZ_{Imp}	2.56 ± 0.20	—	5.35
NiZ_{Imp}	—	2.71 ± 0.21	5.22
$CoNiZ_{Imp}$	1.16 ± 0.08	0.87 ± 0.06	5.17
ZSA	—	—	5.20

The contents of cobalt and nickel and other elements, as well as the Si/Al ratios for the obtained materials are shown in Table 1 and/or Figure 3. The Si/Al ratio shows no significant change (Table 1), indicating a high degree of stability for the clinoptilolite–heulandite and mordenite phases after the applied hydrothermal treatments. Additionally, it can be observed that the Ni and Co concentrations are generally higher in materials obtained through Imp compared to those produced via IE. However, it is important to note that materials obtained by Imp tend to have high chloride contents, whereas those produced by IE exhibit negligible chloride levels (Figure 3). The chloride originates from the $NiCl_2$ and $CoCl_2$ solutions used in the treatments, which remain as residues on the materials. The residual solution may be retained through surface adsorption within the porosity and mesoporosity formed between the zeolite crystallites, as shown in the SEM image (Figure 2). To remove excess solution, water washes are typically applied. The materials obtained via IE underwent extensive washing with distilled water, while those obtained via Imp were only lightly washed, leading to the observed differences in chloride content. According to this, there are color differences between the obtained materials and the starting zeolitic mineral (see Figure S1 of Supporting Information File 1), which are stronger in the materials obtained by Imp due to their higher content of residual salts.

Figure 3 also presents the Na, K, Ca, and Mg contents for the monometallic materials obtained from both treatments. Despite the previously mentioned observations, both types of materials (from IE and Imp) exhibit a reduction in Na, K, Ca, and Mg levels compared to ZSA, with this decrease being more pronounced in the materials obtained via IE. This suggests that in both treatments an ion exchange process occurred between the Ni^{2+} and Co^{2+} cations from solutions and the Ca^{2+}, Na^{+}, K^{+}, and Mg^{2+} cations from the zeolite phases (mordenite and clinoptilolite-heulandite) contented within ZSA, as represented by Equation 1:

$$A_2^{n+} - Z_{(s)} + nM_{(aq)}^{2+} = M_n^{2+} - Z_{(s)} + 2A_{(aq)}^{n+}, \qquad (1)$$

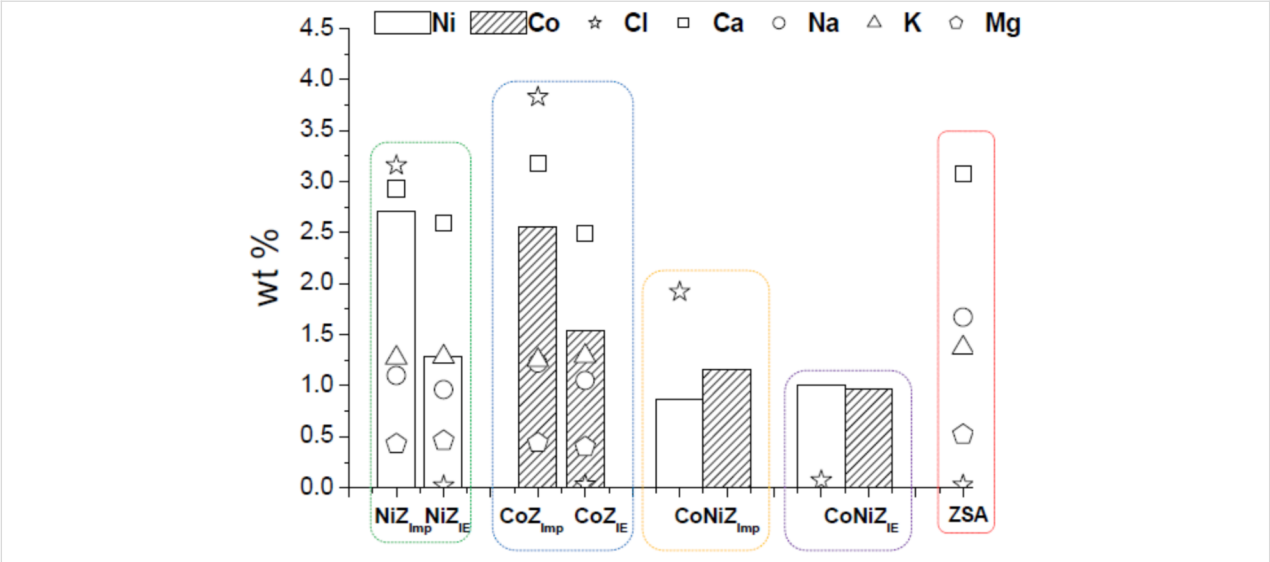

Figure 3: Elemental composition determined by X-ray fluorescence of the materials obtained by IE and Imp.

where $Z_{(s)}$ is the solid zeolite phase, and A^{n+} denotes the Ca^{2+}, Na^{+}, K^{+}, and Mg^{2+} cations within the zeolite. $M^{2+}{}_{(aq)}$ represents the Ni^{2+} and Co^{2+} cations from the solution.

Table 2 presents the quantities of Co^{2+}, Ni^{2+}, and Cl^{-} in equivalent moles per 100 g of each material, as well as the equivalent mole ratio of Cl^{-} anions relative to Co^{2+}, Ni^{2+}, and the Co^{2+}–Ni^{2+} mixture. These values were determined from the elemental contents reported in Table 1 and Figure 3. It is evident that the equivalent mole ratios are different from unity, which suggests that these ions are not totally neutralizing their charges (i.e., 2 equivalents of Cl^{-} per 1 equivalent of metal cation (see M^{2+} in Equation 1)). Moreover, in most cases they are less than unity, which indicates that a portion of the Co^{2+} and Ni^{2+} cations have not neutralized their positive charges with Cl^{-} anions. Instead, these cations likely neutralize their charge with negative charges from the zeolite framework, suggesting they occupy extra-framework cationic positions as compensation cations. This observation aligns with the earlier discussion that an ion exchange process occurred between these metal cations and the cations from the zeolite phases (as represented in Equation 1). For samples obtained by impregnation, the equivalent mole ratios are much higher mainly because of the large amount of chloride remaining on the surface. However, this does not mean that there are no Ni^{2+} and Co^{2+} cations occupying exchange positions. Note that chloride can also form salts with iron, sodium, and calcium cations leaving the zeolite, as proven by XRD.

In line with expectations for a natural zeolite, the studied materials exhibited hybrid type-I/IV adsorption isotherms (see Figure S2 in Supporting Information File 1), indicating the presence of both microporous and mesoporous structures. The isotherms showed a hysteresis loop, which is associated with capillary condensation within the materials' pores and is expected to be more pronounced in HEU than in Mor. This can be attributed to the smaller channel diameter of HEU (maximum opening of 0.31×0.75 nm^2) compared to Mor (maximum opening of 0.70×0.65 nm^2). Additionally, the kinetic diameter of a nitrogen molecule (0.36 nm) is closer to the HEU channel diameter, further influencing the observed behavior.

Table 3 displays the specific surface area (SSA) and microporous volume (V_{micro}) values determined for the obtained materials. It is evident that all materials acquired through Imp have lower SSA and V_{micro} values compared to those obtained via IE. This reduction is attributed to the presence of more adsorbed salts (chlorides) on the materials' surface, which is in agreement with the XRD results.

Conversely, the SSA and V_{micro} values for materials obtained by IE are higher than those of ZSA. This increase is consistent with expectations [17,18], as the ion exchange and water washing treatments effectively clean the materials' surface, thereby enhancing the available surface area and porosity (microporosity) for adsorption.

The temperature-programmed reduction (TPR) profiles of the materials obtained by both methods are shown in Figure 4. These profiles vary significantly depending on the used modification method. It has been reported that the cations supported on zeolites can be thermally reduced by hydrogen, which is

Table 2: Equivalent mole values of Co^{2+}, Ni^{2+}, and Cl^{-} per 100 g of material (equiv/100 g) and the equivalent mole ratio (Cl^{-}/M^{2+}) of Cl^{-} anions relative to metal cations (Co^{2+}, Ni^{2+}, and Co^{2+}–Ni^{2+} mixture) of materials obtained by IE and Imp.

Sample	Co^{2+}, equiv/100 g	Ni^{2+}, equiv/100 g	Cl^{-}, equiv/100 g	Cl^{-}/M^{2+}
CoZ_{IE}	0.052 ± 0.003	—	$8.60 \pm 0.47 \times 10^{-4}$	0.0165
NiZ_{IE}	—	0.0438 ± 0.0033	$5.69 \pm 0.34 \times 10^{-4}$	0.0130
$CoNiZ_{IE}$	0.032 ± 0.0023	0.034 ± 0.0027	$1.90 \pm 0.13 \times 10^{-4}$	0.0287
CoZ_{Imp}	0.086 ± 0.0067	—	0.1080 ± 0.0097	1.2558
NiZ_{Imp}	—	0.092 ± 0.0071	0.0891 ± 0.0071	0.9684
$CoNiZ_{Imp}$	0.039 ± 0.0026	0.029 ± 0.002	0.0541 ± 0.0037	0.7955

Table 3: Specific surface area (SSA) and microporous volume (V_{micro}) of the ZSA and the materials obtained using IE and Imp.

Sample	ZSA	CoZ_{IE}	CoZ_{Imp}	NiZ_{IE}	NiZ_{Imp}	$CoNiZ_{IE}$	$CoNiZ_{Imp}$
SSA (m^2/g)	134	138	67	146	54	142	64
V_{micro} (cm^3/g)	0.0316	0.0326	0.0015	0.0385	0.0067	0.0439	0.0139

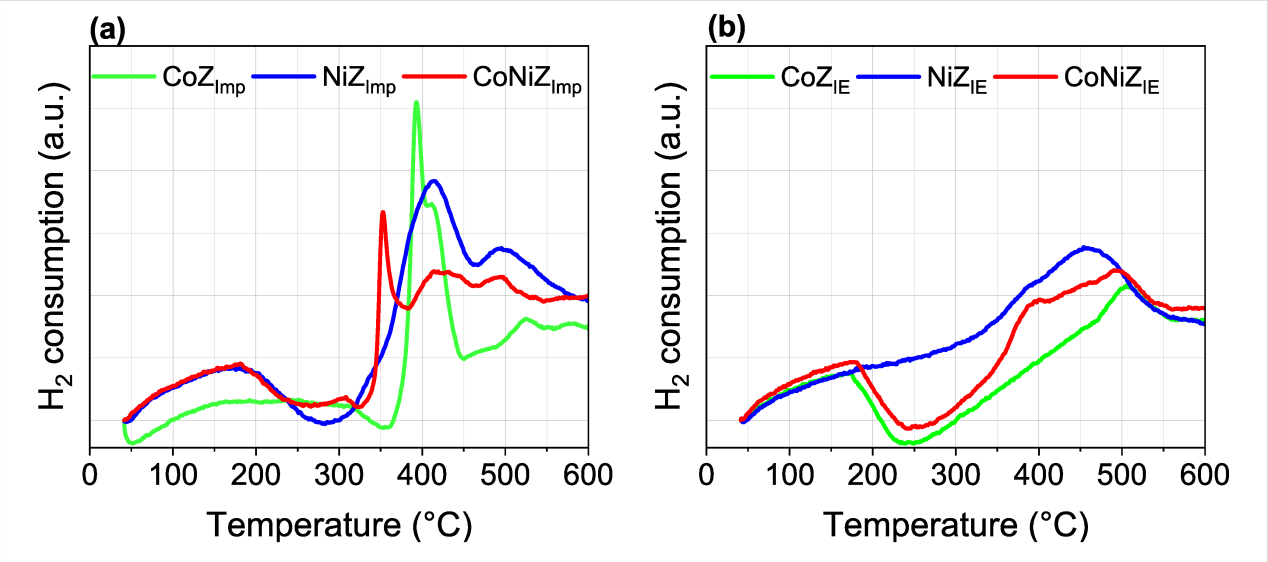

Figure 4: TPR profiles for the mono- and bimetallic materials obtained by (a) Imp and (b) IE.

influenced by the nature of co-cations present [19-22]. The TPR profiles display hydrogen consumption peaks at different temperatures, corresponding to the reduction of the nickel and cobalt cations arranged on the zeolite support. The TPR profiles of materials prepared via Imp show a greater number of hydrogen consumption peaks compared to those obtained by IE. Two peaks appeared centered at 170 °C and 500 °C for CoZ_{IE}, while CoZ_{Imp} exhibits hydrogen consumption in the 150–350 °C range and three additional peaks centered at 390 (intense), 410, and 515 °C. Similarly, NiZ_{IE} exhibits two peaks at 380 (low) and 450 °C, whereas NiZ_{Imp} displays three peaks at 150, 410, and 500 °C. Regarding the bimetallic systems, $CoNiZ_{IE}$ shows three peaks at 170, 380, and 500 °C, while $CoNiZ_{Imp}$ shows five peaks at 170, 310, 350 (intense), 420, and 500 °C. In line with the elemental composition (Figure 3, Table 1 and Table 2), the textural parameters (Table 2) and previous discussions, hydrogen consumptions peaks can be attributed to the reduction of cobalt and nickel cations present as both isolated cations (compensation cations in extra-framework ionic positions) and chloride salts adsorbed on the zeolitic support. This distinction explains the differences between the TPR profiles. Thus, materials obtained by IE exhibit peaks associated only with isolated cations, while materials obtained by Imp show peaks linked to both isolated cations and chlorides.

Careful analysis of the profiles suggests that isolated Co^{2+} cations in extra-framework ionic positions undergo two hydrogen consumption events for their complete reduction, that is, one at 170 °C and another one in the 500–515 °C region. Similarly, isolated Ni^{2+} cations in these positions experience two reduction events, namely, one at 380 °C and another one in the 450–500 °C region. This behavior is consistent across both modification methods and is observed in both monometallic and bimetallic systems. Beside this, the reduction of isolated cations is thermally favored in the bimetallic systems. Note that the intensity of the 380 °C peak, associated with isolated Ni^{2+} cation reduction, increases in bimetallic $CoNiZ_{IE}$ compared to monometallic NiZ_{IE}. Furthermore, the reduction of isolated Co^{2+} cations that takes place at 510 °C in the monometallic CoZ_{IE} is shifted to a lower temperature (500 °C) in the bimetallic $CoNiZ_{IE}$. This suggests a mutual synergistic influence between Ni^{2+} and Co^{2+} cations with each facilitating the reduction of the other, likely due to a weakening of the interaction between isolated cations and the zeolite framework.

In bimetallic systems, Ni^{2+} and Co^{2+} cations compete for extra-framework cationic positions in the zeolite phases. As a result, these cations occupy positions where their interaction with the zeolite framework is diminished compared to monometallic system, facilitating their reduction at lower temperature.

Catalytic test in citral hydrogenation

The main pathway of citral hydrogenation is illustrated in Figure 5, and the corresponding results are presented in Figure 6. Catalysts were tested as obtained, that is, without prior thermal activation. Although the conversion of citral after 3 h of reaction is relatively low for all catalysts, it indicates that the active sites are accessible to citral molecules. Overall, citral hydrogenation and the formation of citronellal are higher for catalysts containing nickel compared to those containing cobalt (Figure 6). This suggests that the most active catalytic sites for the conversion of citral to citronellal are associated with nickel species. Notably, the bimetallic $CoNiZ_{IE}$ catalyst is the only one to show activity for the hydrogenation of citral to the unsatu-

rated alcohols geraniol and nerol (Figure 5), albeit in small quantities. In contrast, the bimetallic $CoNiZ_{Imp}$ shows lower citral conversion, with no formation of unsaturated alcohols detected. This discrepancy between the bimetallic catalysts may be attributed to differences in ionic species, as well as variation in specific surface area (Table 3) and nickel content (Table 1 and Figure 3). The $CoNiZ_{IE}$ catalyst has higher values for both parameters compared to $CoNiZ_{Imp}$. Additional factors contributing to these differences will be discussed later.

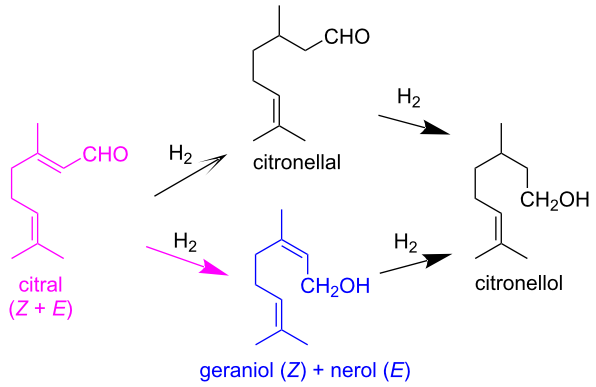

Figure 5: Main pathways of citral hydrogenation.

The catalytic activity of the $CoNiZ_{IE}$ catalyst in the selective hydrogenation of citral to unsaturated alcohols (geraniol and nerol) can be attributed to a synergistic interaction between cobalt and nickel species. These active species are likely associated with isolated cations or those formed during the hydrogenation process. For this reaction to proceed effectively, citral and hydrogen must interact directly with the active catalytic centers, such as isolated Ni^{2+} cations located in extra-framework cationic positions in the zeolite channels. Given that citral has a molecular diameter of around 0.3 nm, it can enter the channels of clinoptilolite (maximum opening of 0.31 × 0.75 nm) and mordenite (maximum opening of 0.70 × 0.65 nm), particularly the latter because of the larger channel diameter. The diffusion of reactants (citral and hydrogen) through the zeolite channels is expected to be favored by a higher specific surface area and unobstructed channel entrances. This is consistent with the superior surface area of $CoNiZ_{IE}$ and the presence of impurities of mixed metal chloride salts on the surface of $CoNiZ_{Imp}$, as evidenced by elemental analysis, XRD, and TPR profiles.

In order to improve these results, the $CoNiZ_{IE}$ catalyst was subjected to in situ reduction at 500 °C for 2 h under H_2 flow prior to the catalytic test. However, this high reduction temperature resulted to be deleterious to the catalytic performance. While the catalytic performance of $CoNiZ_{IE}$ in the selective hydrogenation of citral to unsaturated alcohols remains low, the ability of this material to produce such alcohols indicates its potential. Future work will focus on optimizing the reduction temperature as lower reduction temperatures are expected to enhance performance. These findings will be addressed in subsequent studies.

Conclusion

A detailed investigation was conducted on zeolitic materials featuring mono- and bimetallic systems of nickel and cobalt, derived from natural zeolite rich in clinoptilolite and mordenite. These materials were prepared using Ni^{2+} and Co^{2+} chloride solutions through traditional ion exchange (IE) and impregna-

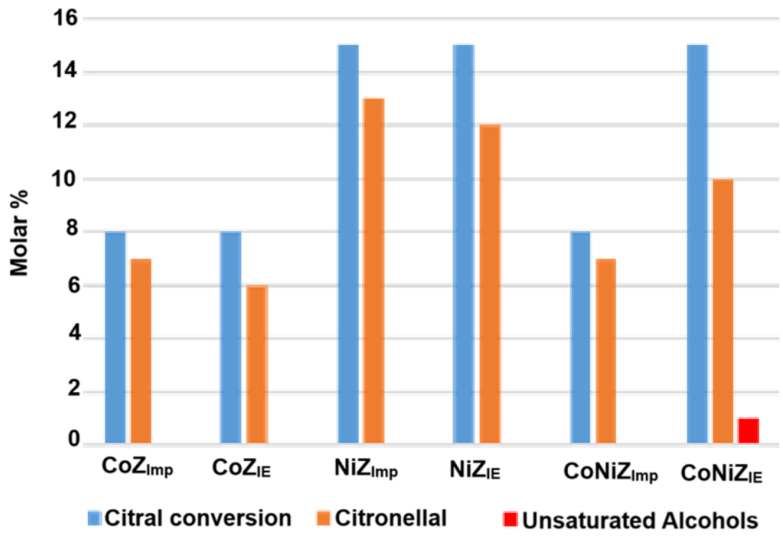

Figure 6: Citral hydrogenation results on the mono- and bimetallic catalyst materials obtained by IE and Imp.

tion (Imp) methods. The Imp-prepared materials exhibited higher nickel and cobalt contents but also contained significant amounts of chlorides. Conversely, the IE-prepared materials showed negligible chloride content and larger specific surface areas. These differences were attributed to the substantial presence of chloride salts adsorbed on the surface of the Imp-prepared materials, as evidenced by XRD analysis. This also impacted the TPR profiles, with the Imp-prepared materials displaying hydrogen consumption patterns different from those of the IE-prepared materials. The TPR profiles further revealed that the thermal reduction of isolated Co^{2+} and Ni^{2+} ions (compensation cations in extra-framework ionic positions) was facilitated in the bimetallic systems, likely because of the synergetic interaction of multiple species and a reduced interaction between the cations and the zeolite framework. In line with these findings, the catalytic performance of the materials in the selective hydrogenation of citral showed marked differences. The most active catalytic sites for converting citral to citronellal were associated with nickel species. Among the catalysts, the bimetallic $CoNi_{IE}$ material, prepared by IE, emerged as the most promising. It was the only catalyst to exhibit activity for the hydrogenation of citral to form unsaturated alcohols, suggesting a synergistic interaction between cobalt and nickel species. The active species are likely associated with isolated cations or those formed during the hydrogenation process.

This work highlights the potential of bimetallic $CoNiZ_{IE}$ materials as efficient catalysts for selective hydrogenation reactions, paving the way for further optimization and exploration of similar catalytic systems.

Experimental

Material and methods

Natural zeolite from the San Andrés deposit in Cuba, with a particle size range of 40–160 μm, was used. This zeolitic material consists primarily of mordenite and clinoptilolite-type zeolites (around 80%), along with minor accompanying phases (quartz, montmorillonite, feldspar) [23]. It underwent a purification process following a method similar to one described previously [18]. Its elemental chemical composition in oxide form is 65.7% SiO_2, 11.4% Al_2O_3, 3.4% CaO, 2.4% Na_2O, 1.3% K_2O, 1.1% MgO, and 2.6% Fe_2O_3. For simplicity, this purified zeolite is referred to as ZSA.

Monometallic (CoZ and NiZ) and bimetallic (CoNiZ) systems of nickel and cobalt were prepared from ZSA with $NiCl_2$, $CoCl_2$, and mixed $NiCl_2/CoCl_2$ solutions through both IE and Imp. The mixed $NiCl_2/CoCl_2$ solution was prepared by combining equal volumes of $NiCl_2$ and $CoCl_2$ solutions. The $NiCl_2$ and $CoCl_2$ used were reagent-grade, supplied by Sigma-Aldrich, St. Louis, MO, USA.

The IE processes were performed at 80 °C with reflux for 24 h, using a total of 2 milliequivalents of the corresponding cations (Ni^{2+}, Co^{2+}, and Ni^{2+}/Co^{2+}) in solution per gram of ZSA and 1 g/10 mL solid/solution ratio. The solid phases were washed with distilled water to remove chloride ions and oven-dried at 110 °C.

The Imp processes were conducted using a total of 6% of corresponding metals (Ni, Co, and Ni/Co) per gram of ZSA and solutions with total metal contents of 0.2 mol/L. Both the ZSA and the solutions were heated to 80 °C before being mixed. After 24 h, the solid phases were separated, lightly washed with distilled water, and oven-dried at 110 °C.

Characterization

The elemental composition of ZSA and the modified materials from both treatments was determined using X-ray fluorescence analysis, performed with a ZETIUM PANalytical system. To characterize the specific surface area and pore structure of the materials, they were analyzed using Micro-Active software for TriStar II Plus instruments. Approximately 200 mg of each sample was degassed at 30 °C for 30 min and then at 250 °C for 4 h before surface area measurements via nitrogen adsorption at 77 K. The initial natural zeolite samples were also examined via powder X-ray diffraction (XRD) and scanning electron microscopy (SEM).

XRD patterns were recorded using a PW 1218 diffractometer (Philips, Almelo, Netherlands) equipped with a curved graphite monochromator and Cu Kα radiation (λ = 1.5406 Å). Data were collected at a scan speed of 2°/min with a step size of 0.05°. SEM images were acquired using a FEI Nova NanoSEM 450 electron microscope. For this purpose, samples were mounted on holders and coated with a thin layer of gold prior to observation.

Temperature-programmed reduction (TPR) analyses were performed on an AutoChem 2910 instrument (Micromeritics, USA) equipped with a thermal conductivity detector (TCD). The procedure for TPR involved heating the sample in a 1.0 vol % H_2/Ar gas mixture at a flow rate of 30 mL/min, from room temperature to 600 °C, at a ramp rate of 5 °C/min. Hydrogen uptake was monitored using the TCD.

Catalytic test in citral hydrogenation

In a manner analogous to [24], the hydrogenation of citral was conducted in a 250 mL autoclave equipped with a magnetic stirrer and a temperature control unit. The catalysts (400 mg) were immersed in 90 mL of isopropanol and transferred into the autoclave. The reactor was first purged with nitrogen and then with hydrogen before raising the temperature to 130 °C. A mix-

ture of 3 mL citral and 10 mL isopropanol was then introduced into the reactor via a cylinder under 75 bar of hydrogen pressure. Time zero was considered at this point. During the catalytic test, the reaction was carried out under constant pressure using a pressure control system. After various reaction times, liquid samples were manually collected and analyzed by gas chromatography to determine conversion and selectivity values.

It is opportune to outline that preliminary experiments [25] conducted under various stirring conditions, catalyst loadings, and grain sizes confirmed the absence of both external and internal diffusion limitations.

Supporting Information

Supporting Information File 1

Additional figures.
[https://www.beilstein-journals.org/bjnano/content/supplementary/2190-4286-16-40-S1.pdf]

Acknowledgements

This work pertains to the French government program "Investissements d'Avenir" (EUR INTREE, reference ANR-18-EURE-0010). I. Rodríguez-Iznaga acknowledges support from Programa de Estancias de Investigación (PREI)-2023 de la DGAPA, UNAM, México. The zeolite structure images in the Graphical Abstract were adapted from https://europe.iza-structure.org/IZA-SC/framework_main_image.php?ID=101 (© 2017 Structure Commission of the International Zeolite Association), with permission from Ch. Baerlocher, Darren Brouwer, Bernd Marler and L.B. McCusker, Database of Zeolite Structures http://www.iza-structure.org/databases/. This content is not subject to CC BY 4.0.

Funding

This work was partially supported by the "PHC CARLOS FINLAY" programme (project no. 49743VE), funded by the French Ministry for Europe and Foreign Affairs (MEAE), the French Ministry for Higher Education and Research (MESR), and the Cuban Ministry of Foreign Trade and Foreign Investment (MINCEX).

ORCID® iDs

Inocente Rodríguez-Iznaga - https://orcid.org/0000-0002-0729-1096
Tania Farias Piñeira - https://orcid.org/0000-0002-0171-1790
Lexane Paget - https://orcid.org/0009-0009-8380-8980
Beatriz Concepción Rosabal - https://orcid.org/0000-0003-1418-2186
Arbelio Penton Madrigal - https://orcid.org/0000-0001-7943-4909
Vitalii Petranovskii - https://orcid.org/0000-0002-8794-0593

Data Availability Statement

Data generated and analyzed during this study is available from the corresponding author upon reasonable request.

References

1. Roth, W. J.; Opanasenko, M.; Mazur, M.; Gil, B.; Čejka, J.; Sasaki, T. *Adv. Mater. (Weinheim, Ger.)* **2024,** *36,* 2307341. doi:10.1002/adma.202307341
2. Liu, M.; Miao, C.; Wu, Z. *Ind. Chem. Mater.* **2024,** *2,* 57–84. doi:10.1039/d3im00074e
3. Sánchez-López, P.; Kotolevich, Y.; Yocupicio-Gaxiola, R. I.; Antúnez-García, J.; Chowdari, R. K.; Petranovskii, V.; Fuentes-Moyado, S. *Front. Chem. (Lausanne, Switz.)* **2021,** *9,* 716745. doi:10.3389/fchem.2021.716745
4. Rodríguez-Iznaga, I.; Shelyapina, M. G.; Petranovskii, V. *Minerals (Basel, Switz.)* **2022,** *12,* 1628. doi:10.3390/min12121628
5. Worathanakul, P.; Rakpasert, N. *Int. J. Environ. Sci. Dev.* **2016,** *7,* 885–888. doi:10.18178/ijesd.2016.7.12.899
6. Zamaro, J. M.; Miró, E. E.; Boix, A. V.; Martínez-Hernández, A.; Fuentes, G. A. *Microporous Mesoporous Mater.* **2010,** *129,* 74–81. doi:10.1016/j.micromeso.2009.08.035
7. Ramírez-Garza, R. E.; Rodríguez-Iznaga, I.; Simakov, A.; Farías, M. H.; Castillón-Barraza, F. F. *Mater. Res. Bull.* **2018,** *97,* 369–378. doi:10.1016/j.materresbull.2017.09.001
8. Jiang, B.; Zhao, S.; Wang, Y.; Wenren, Y.; Zhu, Z.; Harding, J.; Zhang, X.; Tu, X.; Zhang, X. *Appl. Catal., B* **2021,** *286,* 119886. doi:10.1016/j.apcatb.2021.119886
9. Rodríguez-Iznaga, I.; Petranovskii, V.; Chávez-Rivas, F.; Shelyapina, M. G. *Inorganics* **2022,** *10,* 34. doi:10.3390/inorganics10030034
10. Rodríguez-Iznaga, I.; Petranovskii, V.; Castillón-Barraza, F. F.; Fuentes-Moyado, S.; Chávez-Rivas, F.; Pestryakov, A. *Materials* **2023,** *16,* 221. doi:10.3390/ma16010221
11. Stolle, A.; Gallert, T.; Schmöger, C.; Ondruschka, B. *RSC Adv.* **2013,** *3,* 2112–2153. doi:10.1039/c2ra21498a
12. Chung, S.-H.; Park, Y.-M.; Kim, M.-S.; Lee, K.-Y. *Catal. Today* **2012,** *185,* 205–210. doi:10.1016/j.cattod.2011.08.011
13. Hong, U. G.; Kim, J. K.; Lee, J.; Lee, J. K.; Song, J. H.; Yi, J.; Song, I. K. *Appl. Catal., A* **2014,** *469,* 466–471. doi:10.1016/j.apcata.2013.10.029
14. Popova, M.; Dimitrov, M.; Boycheva, S.; Dimitrov, I.; Ublekov, F.; Koseva, N.; Atanasova, G.; Karashanova, D.; Szegedi, Á. *Molecules* **2024,** *29,* 99. doi:10.3390/molecules29010099
15. Taghavi, S.; Mäki-Arvela, P.; Vajglová, Z.; Peurla, M.; Angervo, I.; Eränen, K.; Ghedini, E.; Menegazzo, F.; Zendehdel, M.; Signoretto, M.; Murzin, D. Y. *Catal. Lett.* **2023,** *153,* 2674–2692. doi:10.1007/s10562-022-04178-x
16. Giordani, M.; Ballirano, P.; Pacella, A.; Meli, M. A.; Roselli, C.; Di Lorenzo, F.; Fagiolino, I.; Mattioli, M. *Minerals (Basel, Switz.)* **2022,** *12,* 627. doi:10.3390/min12050627
17. de la Nuez Pantoja, E. Y.; Rodríguez Iznaga, I.; Rodríguez Fuentes, G.; Petranovskii, V.; Martínez García, A.; Calvino Gámez, J. J.; Goma Jiménez, D.; Cauqui, M. Á.; Rivero González, L. A.; Collazo García, O. *J. Inorg. Organomet. Polym. Mater.* **2024,** *34,* 2522–2542. doi:10.1007/s10904-023-02991-4
18. Chávez Rivas, F.; Rodríguez-Iznaga, I.; Berlier, G.; Tito Ferro, D.; Concepción-Rosabal, B.; Petranovskii, V. *Catalysts* **2019,** *9,* 866. doi:10.3390/catal9100866

19. Herd, A. C.; Pope, C. G. *J. Chem. Soc., Faraday Trans. 1* **1973,** *69,* 833–838. doi:10.1039/f19736900833
20. Suzuki, M.; Tsutsumi, K.; Takahashi, H.; Saito, Y. *Zeolites* **1989,** *9,* 98–103. doi:10.1016/0144-2449(89)90056-0
21. Suzuki, M.; Tsutsumi, K.; Takahashi, H.; Saito, Y. *Zeolites* **1988,** *8,* 381–386. doi:10.1016/s0144-2449(88)80175-1
22. Peron, D. V.; Zholobenko, V. L.; Rodrigues de la Rocha, M.; Oberson de Souza, M.; Feris, L. A.; Marcilio, N. R.; Ordomsky, V. V.; Khodakov, A. Y. *J. Mater. Sci.* **2019,** *54,* 5399–5411. doi:10.1007/s10853-018-03250-5
23. Selvam, T.; Schwieger, W.; Dathe, W. *Clay Miner.* **2014,** *49,* 501–512. doi:10.1180/claymin.2014.049.4.01
24. Di, X.; Lafaye, G.; Especel, C.; Epron, F.; Qi, J.; Li, C.; Liang, C. *ChemSusChem* **2019,** *12,* 807–823. doi:10.1002/cssc.201802744
25. Lafaye, G.; Micheaud-Especel, C.; Montassier, C.; Marecot, P. *Appl. Catal., A* **2002,** *230,* 19–30. doi:10.1016/s0926-860x(01)00980-2

License and Terms

BEILSTEIN JOURNAL OF NANOTECHNOLOGY

Mechanical stability of individual bacterial cells under different osmotic pressure conditions: a nanoindentation study of *Pseudomonas aeruginosa*

Lizeth García-Torres[1], Idania De Alba Montero[2], Eleazar Samuel Kolosovas-Machuca[1,2], Facundo Ruiz[2], Sumati Bhatia[3], Jose Luis Cuellar Camacho[*4,5] and Jaime Ruiz-García[6]

Full Research Paper

Open Access

Address:
[1]Coordinación para la Innovación y Aplicación de la Ciencia y la Tecnología, Universidad Autónoma de San Luis Potosí, 550 Sierra Leona Ave., 78210 San Luis potosí, SLP, México, [2]Facultad de Ciencias, Universidad Autónoma de San Luis Potosí, Parque Chapultepec 1570, Privadas del Pedregal 78295, San Luis Potosí, S.L.P. México, [3]Department of Chemistry, Faculty of Science and Engineering, Swansea University, Singleton Campus, Swansea SA2 8PP, United Kingdom, [4]Secretaría de Ciencia, Humanidades, Tecnología e Innovación, México, [5]Master program in Sciences and Material Engineering (MCIM-UAZ), Autonomous University of Zacatecas, 801 López Velarde St, 9800 Zacatecas, Mexico and [6]Instituto de Física, Parque Chapultepec 1570, Privadas del Pedregal 78295, San Luis Potosí, S.L.P. México

Email:
Jose Luis Cuellar Camacho[*] - jose.cuellar@uaslp.mx

* Corresponding author

Keywords:
AFM; force spectroscopy; membrane rigidity; nanomechanical mapping; osmotic shock

Beilstein J. Nanotechnol. **2025,** *16,* 1171–1183.
https://doi.org/10.3762/bjnano.16.86

Received: 03 March 2025
Accepted: 30 June 2025
Published: 21 July 2025

This article is part of the thematic issue "Symposium of Nanoscience and Nanomaterials 2024 (SNN 2024)".

Guest Editor: R. D. Cadena-Nava

Abstract

Nanomechanical maps to test the mechanical response of the outer envelope of *Pseudomonas aeruginosa* were obtained utilizing atomic force microscopy in force–volume mode in the low range of loading forces when exposed to hypotonic (Milli-Q water), isotonic (PBS), and hypertonic (0.5 M NaCl) solutions. Imaging and mechanical testing showed that bacteria are highly resilient to deformation and can withstand repetitive indentations in the range of 500 pN. Analysis of force spectra revealed that although there are differences in the mechanical response within the first stages of nanoindentation, similar values in the slopes of the curves reflected a stable stiffness of about k_B = 20 mN/m and turgor pressures of P_t = 12.1 kPa. Interestingly, a change in the nonlinear regime of the force curves and a gradual increase in maximal deformation by the AFM tip from hypotonic to hypertonic solutions suggest a softening of the outer envelope, which we associate with intense dehydration and membrane separation between inner and outer envelopes. Application of a contact mechanics model to account for the minute differences in mechanical behavior upon deformation provided Young's moduli in the range of 0.7–1.1 kPa. Implications of the presented results with previously reported data in the literature are discussed.

Introduction

Pseudomonas aeruginosa (PA) is a Gram-negative bacterium belonging to the *Pseudomonas* genus. It is well known for its versatility and adaptability in various environments, as it can be found in multiple habitats, including soil, water, plants, and animals. It can also prosper in artificial environments such as metal or plastic pipes and medical devices [1-5]. Although PA is part of the normal microbiota of the skin and mucous membranes of many healthy individuals, it can cause serious opportunistic infections in the respiratory and urinary tracts and during wound healing in people with weakened immune systems or in hospitalized patients [6-8]. As a Gram-negative bacterium, PA is characterized by a distinctive cell wall structure constituted by a thin peptidoglycan layer enclosed by an outer membrane which contains lipopolysaccharides (LPS) [9-11]. The outer membrane also contains numerous proteins, lipoproteins, and channels contributing to its selective permeability [12,13]. Also integrated into the outer membrane, specific tension-activated channel proteins are responsible for the osmoregulation of the membrane envelope and its protection from threatening conditions such as severe osmotic downshocks, which can lead to an excessive increase in the membrane tension resulting in rupture [14,15]. The mechanosensitive (MS) family of channel proteins have been identified as the main efflux pumps required by PA to regulate the exit of osmolytes and reduce the membrane tension to acceptable life-compatible values. Therefore, the type and density of these MS channels triggered at different threshold values of membrane tension determine the survival capacity of the bacteria under drastic changes in osmotic pressure [16-20]. PA is also known to use other channel proteins to overcome the attack by antibiotics via rapid extrusion of the uptaken drugs, which confers remarkable resistance to this pathogen [21-34]. To hinder this difficulty, natural and synthetic molecular inhibitors with high binding affinity towards these channel proteins have been proposed [25-32]. Likewise, the application of silver and copper nanoparticles to block these molecular pores has been reported for PA and other bacteria as well [33-37]. In the latter cases, a direct consequence of this highly controlled membrane permeability is that membrane tension and rigidity are two intertwined physical parameters with a dynamic behavior dictated by the internal turgor pressure of the bacteria during swelling or plasmolysis. Therefore, understanding the dynamics of their mechanical response due to changes in external conditions or exposure to specific molecular agents is critical in generating strategies to control their undesired propagation.

Atomic force microscopy (AFM) is a powerful, sensitive technique that scans the surface topography of a sample with an ultra-sharp tip while monitoring the interaction forces between this tip and the sample at the nanoscale. The force applied by the AFM tip on the sample is controlled by monitoring the deflection of an extremity of a micrometer mechanical lever onto which the tip is attached. In the study of pathogens, AFM excels in providing high-resolution topographic images while measurements are performed in solution in a fluid chamber under controlled environmental conditions. Thus, critical structural changes on the lifestyle of the pathogen can be investigated [38-42]. Beyond imaging, AFM force spectroscopy capabilities are essential to extract material properties of the investigated sample [11,43,44]. The force–volume (FV) mode allows for mapping surface physical parameters of the analyzed sample via controlled nanoindentations on a pre-programmed grid on the sample surface [44-47]. In conventional scanning modes (e.g., contact and tapping) the changes in displacement by the piezoelectric element are gathered in order to maintain a constant cantilever deflection or amplitude while a surface is scanned line by line Conversely, in FV quantitative information is extracted after analysis of a force–separation curve obtained from a performed nanoindentation. Therefore, the preprogramed grid in FV defines the amount of information (number of nanoindentations per scanned line) taken from the sample surface and also its resolution. Typical parameters obtained using the FV mode are the height, stiffness, adhesion, elasticity modulus, and dissipation of the sample. The mentioned parameters derived from force–separation curves are analyzed and mapped in real time as shown below in Figure 1. In the present study, we investigated the mechanical response of the outer membrane of PA at the single bacterium level in FV mode when exposed to relevant osmolarity conditions. Of particular interest was the extraction and comparison of nanomechanical maps obtained in the low range of loading forces to quantify its morphology, membrane stiffness, Young's modulus of elasticity and adhesion when PA was tested in hypotonic (Milli-Q water), isotonic (0.1 M phosphate buffered solution), and hypertonic (0.5 M NaCl) solutions.

Materials and Methods

Bacterial culture

The strain of *Pseudomonas aeruginosa* (ATCC® 27853™) was reactivated by transferring it to Mueller–Hinton broth and incubating it for 24 h at a temperature of 37 °C. Subsequently, it was cultured on Mueller–Hinton agar and again incubated for 24 h under the same conditions. Isolated colonies of PA were collected using a calibrated loop and suspended in 5 mL of phosphate buffer supplemented with 50 µL of Mueller–Hinton broth. The suspension was vortexed for 10 s before its preparation for AFM analysis.

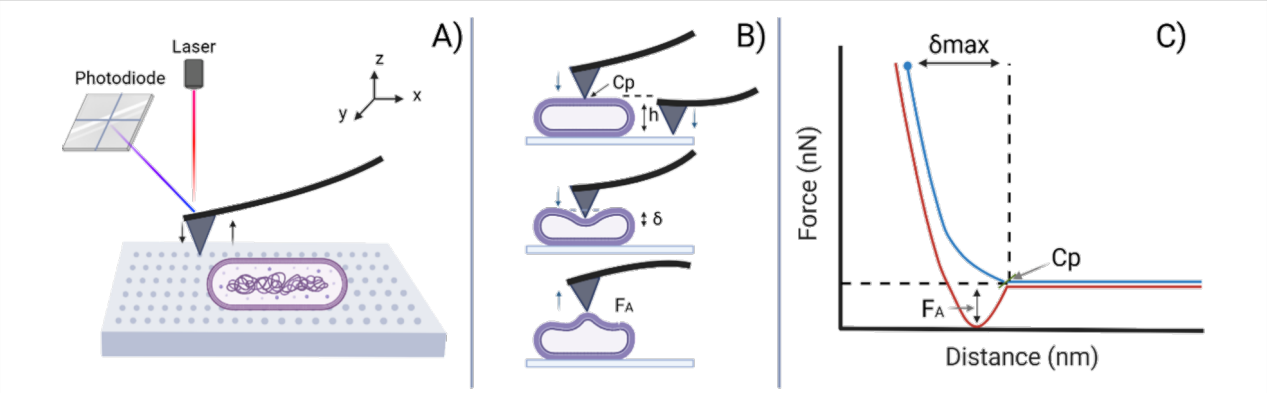

Figure 1: Schematic representation of the force–volume approach to quantify nanomechanical interactions with the atomic force microscope. A) A pre-selected grid that indicates the multiple specific points the AFM tip follows to perform individual indentations with a predefined maximal loading force. B) Drawing that shows how the tip indents on the sample surface in approach/retraction cycles, from which quantitative information such as height, stiffness, Young's modulus, and adhesion are extracted. In C), a schematic illustration of a representative force–separation curve taken on a deformable sample shows the profile of the interaction of the AFM tip with the sample surface and its contact point, maximal deformation, and adhesion force. Created in BioRender. García-torres, L. (2025) https://BioRender.com/zpchrmj. This content is not subject to CC BY 4.0.

Sample preparation for atomic force microscopy

For AFM, the sample was initially firmly adhered to a substrate for subsequent scanning, with the tip first used to identify the objects of study on the surface. In this case, PA in suspension was adhered to a solid mica substrate, previously cleaved with regular adhesive tape, and coated with 5 µL of the cationic polymer poly-L-lysine (PLL, MW 40 kDa, Sigma-Aldrich). The drop of PLL was not allowed to dry but incubated for 10 min, and then the surfaces were repeatedly rinsed with Milli-Q water to allow the formation of a thin film. This coating promotes bacterial adhesion through short-range electrostatic and hydrophobic interactions. Before deposition on the PLL-coated substrate, the bacterial suspension was centrifuged at 2500 rpm for 3 min, and the resulting supernatant was removed. The bacteria were then resuspended in 150 µL of PBS to increase their concentration and before the previous deposition of 5 µL on the PLL-coated substrate. A liquid cell was assembled to measure changes in bacterial membrane rigidity response when transitioning between different solutions. Once inside the fluid cell chamber, bacteria were imaged and tested in PBS solution and then exposed to the desired osmolarity conditions for investigation. The applied solutions were ultrapure water (Milli-Q), phosphate-buffered saline solution (PBS), and 0.5 M sodium chloride. Bacteria were first analyzed in tapping mode to determine their location and observe their morphology. Following this, the FV mode was used to create maps, and indentations at higher force loads were also performed using the point-and-shoot tool.

Atomic force microscopy measurements

The surface analysis and mechanical characterization of living bacteria was performed with an AFM Multimode 8 from Bruker with a NanoScope V controller operated in fluid conditions throughout all experiments, using a pre-assembled fluid chamber with the appropriate solutions within a sealed O-ring. The instrument was operated in contact mode using MLCT probes from Bruker, cantilever D with a nominal spring constant of 0.03 N/m, and tip radius of 20–60 nm as provided by the manufacturer (Bruker), to study the morphological features of bacteria under different tested conditions. The deflection set point was adjusted during the measurement to optimize imaging conditions. Nanoindentations were performed using a maximum loading force of 500 pN for each nanoindentation applied in a pre-programmed grid of 48 points per line to quantify surface interactions and the mechanical response of bacteria. This allowed us to simultaneously acquire maps with enough resolution on the sample surface to identify individual bacteria and obtain the mechanical response from the membrane rigidity within a reversible regime. The advantage of mapping bacteria at low loading forces is that surface interactions between the tip and cell membrane can be analyzed, and information related to its adhesion or surface charge could be revealed with minimum damage to the mechanical integrity of the cell membrane. Before each experiment in FV mode, the cantilever was calibrated using the thermal-noise method which is integrated in the multimode AFM software and is briefly described next. First, the optical-lever sensitivity (OLS) of the cantilever was extracted. A force–distance curve was taken on a clean (previously cleaved) mica surface and a linear fit to the approach trace within the region following contact was performed to obtain the OLS from its slope. Afterwards, the cantilever was withdrawn above the surface and a thermal tune was performed to obtain the spectrum of the cantilever. A Lorentzian fit was then performed to the obtained peak and finally the cantilever constant was calculated.

To take into account any potential change in the dimensions of PA at different osmolarities, the cross section tool from the NanoScope software was used to measure the long (length) and short (width) axes of the bacteria after being tested in FV mode. At least 20 bacteria were measured for each investigated condition. In AFM, the half-width distance is usually reported to take into account the influence of the AFM tip due its curvature close to the apex. A single measurement was taken along the length of each bacteria, while three measurements were performed and averaged to take its width. This is presented below in Figure 2A and Figure 2B.

All obtained images, FV maps, and force–distance curves were analyzed with the NanoScope analysis software 1.7 from Bruker. Once data for nanomechanical mapping at low loading forces was extracted, it was also attempted to produce maps at high loading forces of about 3 nN, as described below in the results section.

Results

Before any nanoindentation measurements were performed, bacteria were first localized on the surface of poly-L-lysine-coated mica. Supporting Information File 1, Figure S1 shows some 3D images of PA taken in contact mode when in PBS. Bacteria and the substrate can be observed. For a straightforward interpretation using quantitative nanomechanics in FV mode, the object to be mechanically tested must be clearly distinguished from a rigid substrate used as background. In this case, the thin layer of PLL (1–2 nm) on mica is expected to provide such background. Regions especially crowded with bacteria were intentionally avoided when applying FV. The capacity of AFM as a quantitative analysis tool when operated in FV mode is illustrated in Figure 1. Once a region has been selected with conventional AFM imaging, a grid is defined with a special resolution of points per line and tip velocity upon approach/retraction (see Figure 1A). Each approach/retraction cycle to a maximum load generates a force–separation curve analyzed in real time by the software. A color-coded map is obtained according to the physical parameters extracted from the curve, as shown in Figure 1B,C.

Figure 2 shows an FV image of the topography or height channel for several individual PA bacteria on the substrate. An estimation of the size of PA by AFM was made using the cross-

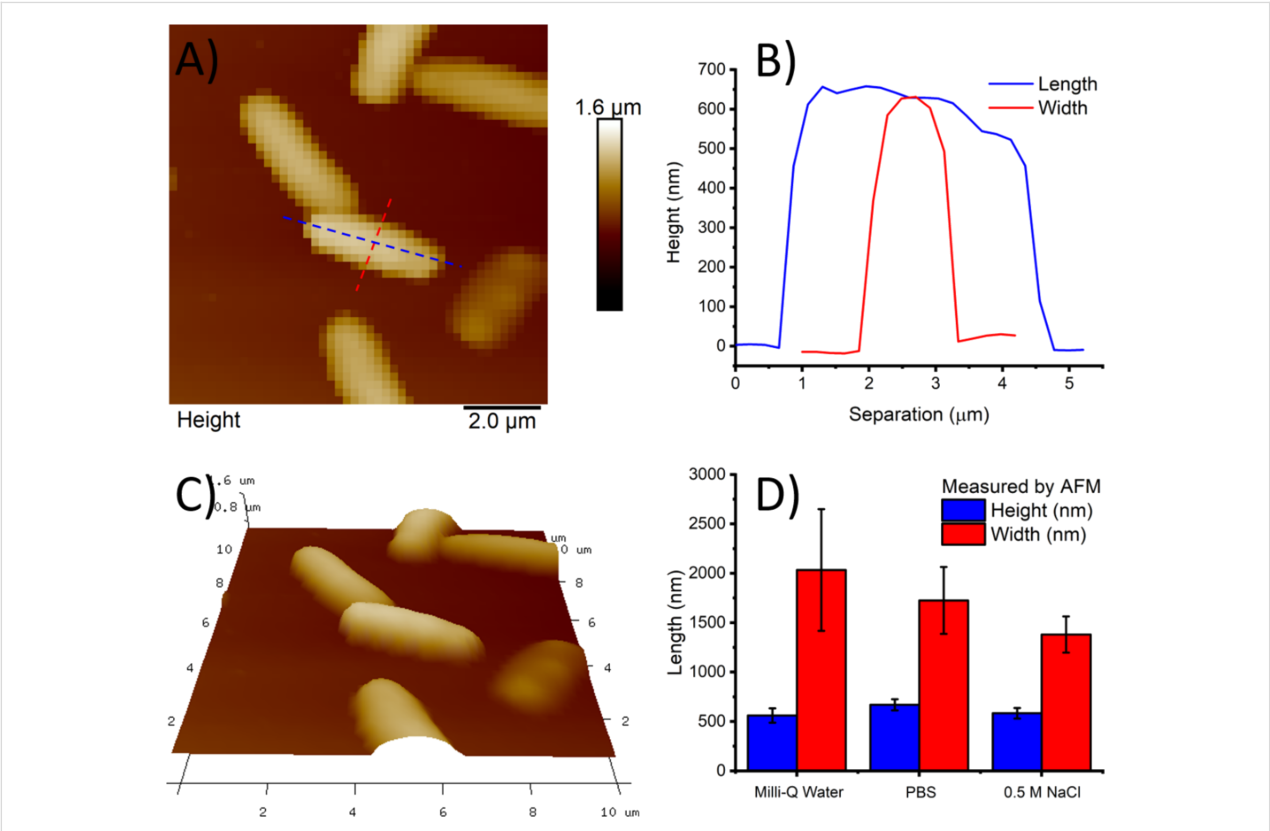

Figure 2: Mapping living bacteria with force–volume AFM. A) 2D height image of *Pseudomonas aeruginosa* obtained in FV mode where pixels indicating the location of single nanoindentations can be easily discerned. B) Cross-section profiles taken from both main axes of the bacteria shown in A) with dashed lines for length (blue) and width (red). C) 3D reconstruction of the image shown in A) shows how FV can also accurately represent the topography of the sample. D) Dimensions of PA obtained from AFM in different measured osmolarity conditions.

section tool along both axes to obtain its length, width, and height, as shown in Figure 2A and 2B. With a resolution of 48 points or pixels per line, FV can also provide accurate morphological measurements for bacteria, as shown in the 3D reconstruction in Figure 2C (see also Supporting Information File 1, Figure S2). These measurements were taken for bacteria in the three investigated conditions (i.e., Milli-Q water, PBS, and 0.5 M NaCl) and the results are shown in Figure 2D. Larger values for the length and width of the bacteria are expected in AFM measurements when compared to other experimental techniques such as optical microscopy or electron microscopy. This is due to the fact that the finite size of the tip apex introduces an overestimation in the lateral dimensions of the imaged object but not of its height, where AFM excels in accuracy. From the plot in Figure 2D, we can observe that while its height remains around the same value of 500–700 nm, the change of its width shows a slight trend towards shrinkage of PA from hypotonic to hypertonic conditions. This might be a consequence or a first sign of readjustment of the cell volume when the adhered bacteria are abruptly exposed to different osmotic pressures.

In Figure 3, maps for three of the main physical parameters, height (h), stiffness (k), and Young's modulus (Y) obtained in

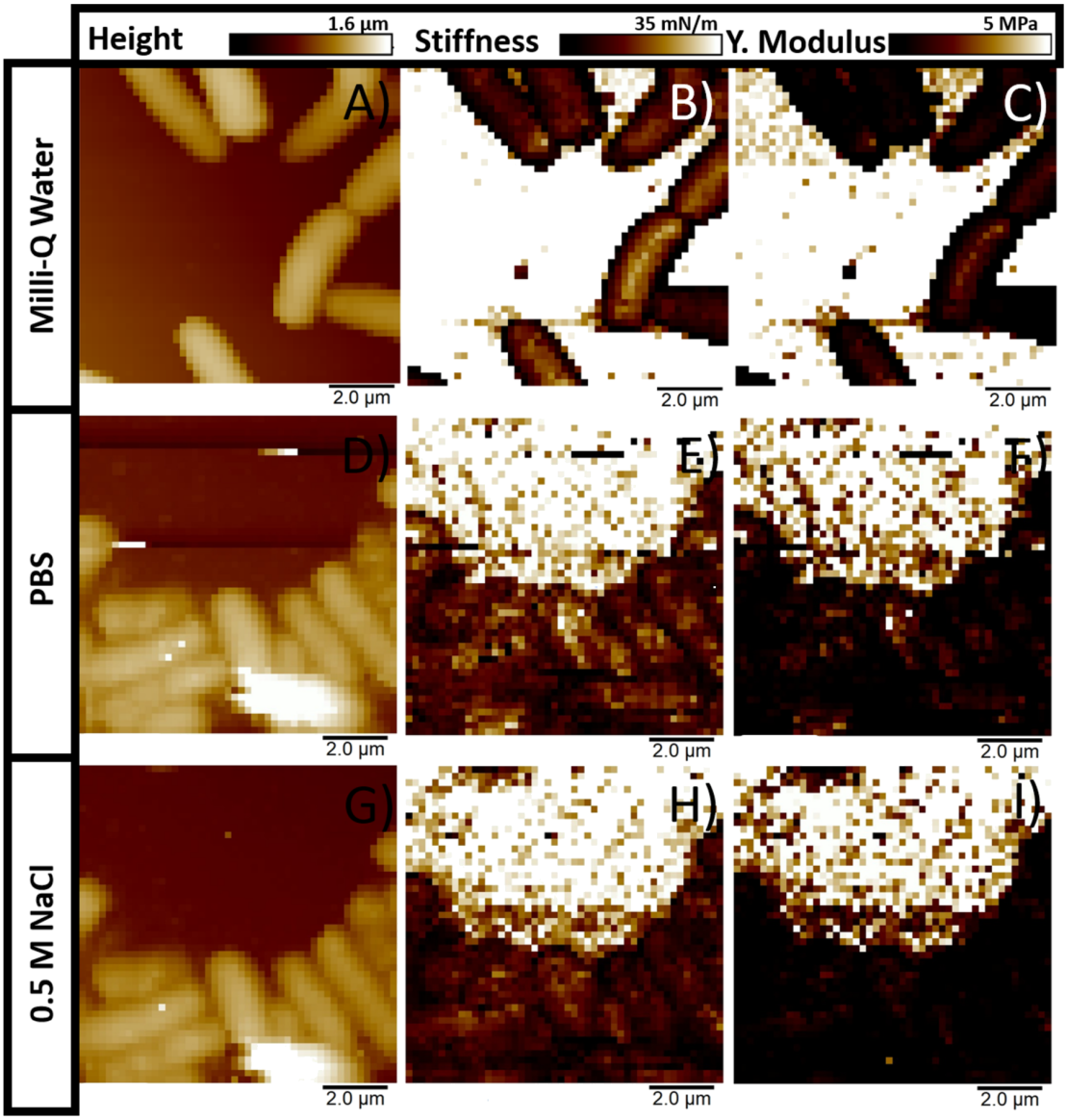

Figure 3: Nanomechanical maps of PA were obtained in FV mode for the three investigated conditions with a maximal loading force of 500 pN. The physical parameters shown are height (A, D, G), stiffness (B, E, H), and Young's modulus (C, F, I). As observed, PA is identified on the surface in contrast with the background due to its different interaction with the AFM tip under the same loading force. Measuring conditions are given as rows, while colored scales for each extracted parameter are shown as columns.

FV, are shown as columns, while the measuring conditions are given as rows. For the height channel in the first column, the identification of individual bacterium is possible even when they are aggregated. As expected, PA appears brighter than the substrate plane since the offset of the color-coded scale has been set for the best contrast and clarity for both. Bacteria appear dark to a brighter background for stiffness and Young's modulus. In these cases, the offset in the color-coded scales has been set to 0–35 mN/m and 0–5 MPa, respectively, for an easier and more direct interpretation of the obtained values. The stiffness is obtained from the slope of the curve during compression by the AFM tip from the point of contact (C_p) until it reaches its maximum predefined loading force. For this reason, the rigidity of the underlying substrate can be assumed to behave as an impenetrable substrate for the range of the applied loads. In the present case, the rigidity of muscovite mica represents a good approximation for the last assumption. However, the thin polymer layer of PLL applied to enhance the adhesion of PA is expected to introduce a certain but rather small degree of mechanical resistance. Visually, from the maps in the column for stiffness, it is difficult to discern a difference in the brightness on the surface of PA from the hypotonic (Milli-Q water) to isotonic (PBS) and finally to the hypertonic solution (0.5 M NaCl). Nonetheless, in the case of Young's modulus, bacteria in the maps seem to become slightly darker with the increase in ionic strength.

Contrary to stiffness, the map for Young's modulus is extracted after a mechanics model has been chosen in the analysis software and the appropriate parameters between the AFM tip and sample have been given. Although the apex of the tip used in this case is not a perfect cone, and the radius of the tip is about 10% of that of PA, analysis of the force response obtained in the force curves suggests that the Sneddon model provides a better description for the induced deformation than that of the Hertz model for the case when a spherical tip indents on an elastic planar half-space. Under the frame of the Sneddon model, a rigid conical indenter pushes a planar elastic semi-space characterized by a particular elastic modulus Y. The Sneddon model then provides a relation between the applied force load (F), the induced deformation (δ), and the modulus of elasticity (Y) of the tested material in the following way:

$$F(\delta) = \frac{2Y \tan(\alpha)\delta^2}{\pi\left(1-\upsilon^2\right)},$$

with α as the half angle distended by the apex of the AFM tip, and υ is a unitless factor known as the Poisson ratio, which takes values between 0 and 0.5. In the present study, we use $\upsilon = 0.49$, as usually reported for biological samples [48,49].

Figure 4A shows the approach component of representative force–separation curves obtained on PLL and PA for each investigated condition for a maximal loading force of 500 pN. These curves show the mechanical response from the polymer layer on the mica surface and the outer membrane of PA. From the black line, it is easy to observe how the tip, upon contact, almost immediately attains full compression on the PLL layer, and no further deformation can be observed as the slope of the curve almost reaches verticality. The necessary deformation depth required to fully compress the PLL layer was 1–3 nm. An obvious difference in the force response is obtained on PA (blue, red, and green lines). For these low regimes of loading forces, it can be observed that the force response is nonlinear within the first 70 pN for Milli-Q water and about 100 pN for PBS. For 0.5 M NaCl, the curve remains nonlinear up to about 250 pN. For the maximal applied loading force of 500 pN, a maximal attained membrane deformation δ_{max} occurred at 55, 80, and 145 nm for Milli-Q water, PBS, and 0.5 M NaCl, respectively. Consequently, we observed a clear increase in the maximal induced deformation with an increase in the osmolarity. For this extent of induced deformation, the outer envelope of PA showed a reversible behavior in the mechanical response. Figure 4B shows a schematic representation of the AFM tip indenting on the outer membrane of PA and its maximum deformation δ_{max}. A fit to the obtained force response using the Sneddon model in the NanoScope software for the curves shown in A) is given in Supporting Information File 1, Figure S3. These representative force curves have been selected from nanoindentations captured along the middle region of the longer axis of the bacteria in FV maps. This is of central importance since it was observed that the force response drastically changes according to the direction of the scanning in relation to the orientation of the bacteria. Especially at the edges, the influence of the finite 3D size and angle of the AFM tip became evident because indentation can take place perpendicularly, along the longer axis of PA, or in an intermediate diagonal direction of the bacterial body, which ultimately significantly alters the profile of the obtained force response. In Figure 4C,D, histograms from FV maps for the obtained values for k and Y are given for the case of Milli-Q water. The rest of the data is given in Supporting Information File 1, Figure S4. Although expected, a main feature in the obtained histograms for k and Y for all measured samples was the presence of bimodal distributions, which reflects the mechanical response from a homogeneous substrate coated at some percentage with bacteria. Therefore, one distribution corresponded to the mechanical response from the PLL-coated mica, while the other to PA. In the case of stiffness, both distributions appear Gaussian, with the substrate stiffness (k_s) at higher values than that for the bacteria (k). Nevertheless, for Young's modulus, only the distribution arising from the substrate (Y_s) is Gaussian, while the one

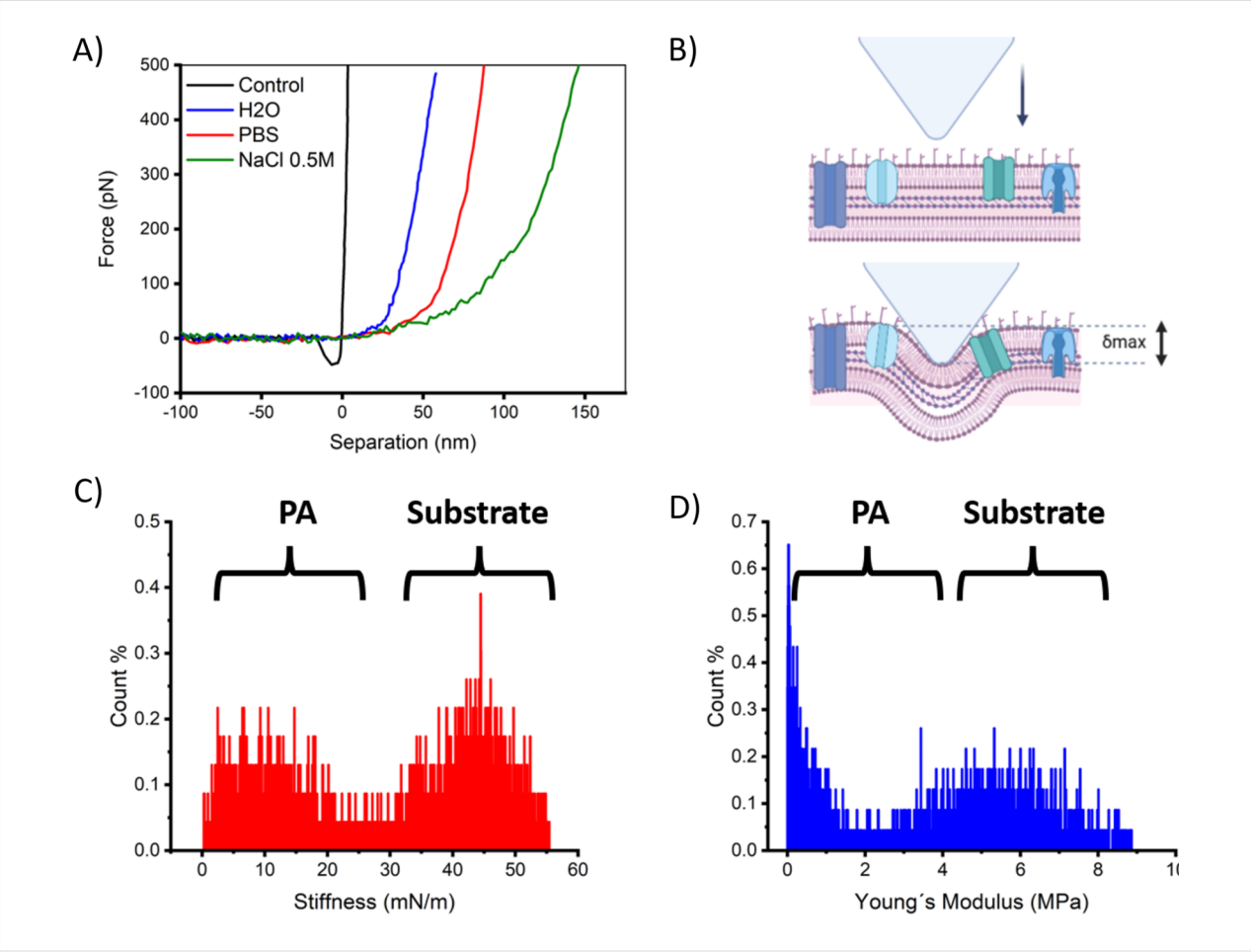

Figure 4: Degree of compression by nanoindentations in FV mode at low loading forces of 500 pN. In A) representative force–separation curves were obtained from the force response of PA indented under different tested conditions. Force curves were taken from the middle region of the bacteria to minimize variations arising from the finite size of the AFM tip interacting at the edges of the bacterial body. A control curve next to the bacteria is also shown as a reference for deformation (black line). In B), a drawing illustrates the outer membrane compression by the AFM tip (Created in BioRender. García-torres, L. (2025) https://BioRender.com/qynn0nv. This content is not subject to CC BY 4.0.). In C) and D), histograms for the stiffness and Young's modulus values obtained from a map taken in FV mode in Milli-Q are shown, respectively.

for the bacteria (Y) at lower values resembles a lognormal distribution. Supporting Information File 1, Figure S4 fits the obtained experimental data with Gaussian and lognormal distributions to obtain mean values. The obtained δ_{max} shows that in this low range of loading forces, the membrane rigidity is tested beyond the thickness of the bacterial outer cell wall, which, according to cryo-electron tomography, is about 25–30 nm [50]. In Table 1, the mean value obtained for the stiffness and Young's modulus from the distributions are given and compared with mean values of k_{PA} and Y_{PA} intentionally selected from the middle regions of PA. The corresponding mean values for the maximum deformation or penetration δ_{max}, attained by the AFM tip during compression on the central region of the bacteria, are also given. Table 1 shows that the mechanical resistance to deformation reflected in the stiffness remained almost unchanged when the mean values obtained from distributions for the different measuring conditions were compared. However, they differ from the mean values obtained from the middle region of bacteria. This accounts for the mechanical stability of the outer membrane of PA once a certain osmotic pressure is set. We can observe that mean values for k and Y obtained from the distributions were smaller than those obtained from the middle region of PA. This comparison also indicates how, in a nanoindentation map, the distribution overshadows the mean value taken where the geometrical conditions are usually preferred during mechanical testing since their number is just a small fraction of the entire set of indentations performed along a map. For mean values obtained along the central region of the bacteria, the stiffness also remained relatively unchanged for the different tested conditions. Still, we see a slight trend towards lower values from hypotonic to hypertonic solutions for the Young's modulus. This observation will be discussed below in the discussion section regarding the application of the mechanics model. Opposite to the Young's modulus,

Table 1: Mean values for stiffness and Young´s modulus obtained from distributions in FV maps and from the central region of PA.

Solutions	k (mN/m) from distributions	Y (MPa) from distributions	k_{PA} (mN/m) from the middle region of PA	Y_{PA} (MPa) from the middle region of PA	δ_{max} (nm) from the middle region of PA
Milli-Q	8.83 ± 0.46	0.51 ± 0.07	21.3 ± 4.9	1.13 ± 0.38	51.74 ± 10.94
PBS	9.32 ± 3.69	0.5 ± 0.08	17.6 ± 5.28	0.93 ± 0.39	88.5 ± 17.47
0.5 M NaCl	7.4 ± 0.17	0.14 ± 0.01	23.2 ± 5.36	0.69 ± 0.44	92.15 ± 27.85

the mean maximal induced deformation upon compression δ_{max} increases in the presence of a higher salt concentration.

Supporting Information File 1, Figures S5 and S6 show maps for the adhesion force between the AFM tip interacting with the substrate and bacteria. In Supporting Information File 1, Figure S5A–F a clear contrast in the adhesion force between the bacteria and the substrate can be observed for the case of Milli-Q water, where it was possible to quantify the adhesion force to the AFM tip as shown in the cross-sections in C) and F). When salt is introduced into the system, the contrast in the map is almost entirely lost, strongly suggesting that the electrostatic surface forces have been screened by the presence of ions, as shown in Figure S6 of Supporting Information File 1.

Finally, in Figure 5A and 5B, it was demonstrated how applying repetitive compressions via nanoindentations at high loading forces in hypertonic solution led to the destruction of previously imaged bacteria. In Figure 5A, a region heavily coated with PA was mapped in 0.5 M NaCl with FV with 500 pN as the maximum loading force, and in Figure 5B, the same region was imaged under the same conditions but with a maximal loading force of 3000 pN. A complete loss of identifiable bacterial structures is obtained. These results demonstrate the incapacity of PA to maintain the structural integrity of the outer membrane when exposed to larger loads within the time scale of the present experiment, as shown in the force curve in Figure 5C. The maximal force that the membrane could withstand before rupture was 2.1 ± 0.5 nN.

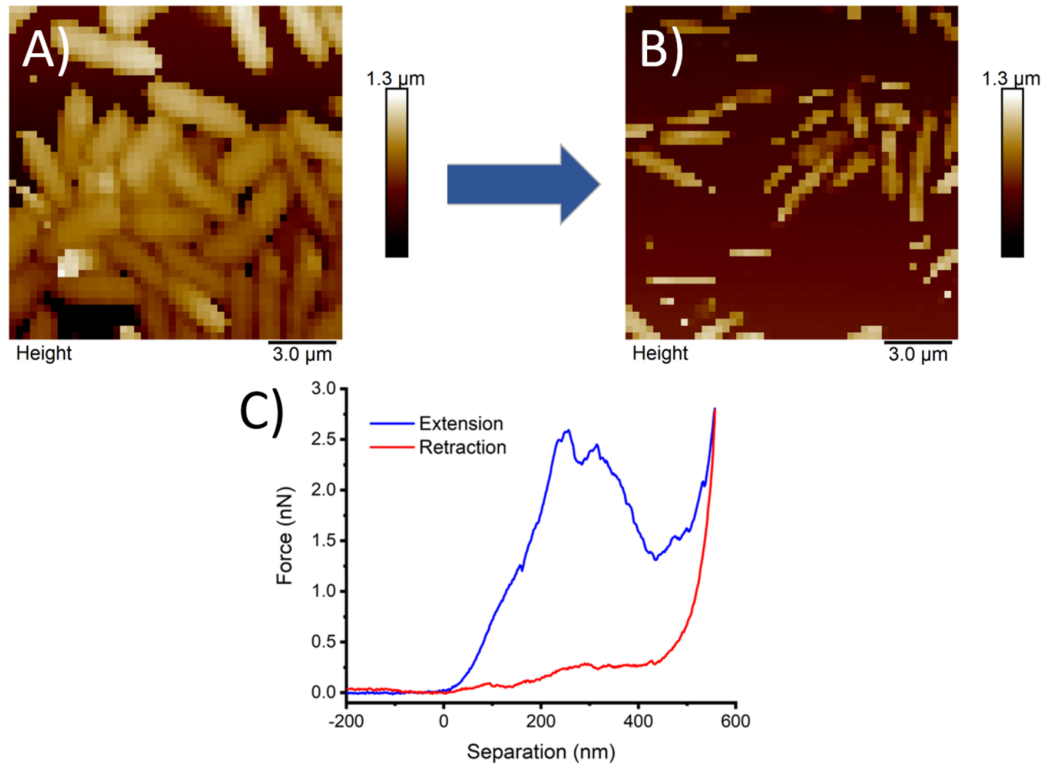

Figure 5: Force–volume maps were obtained at low A) and high B) loading forces in the same scanned region. The image clearly shows the entire destruction of previously mapped bacteria. C) A representative force–separation curve on PA where a drastic drop in the force is detected at about 2.5 nN.

Discussion

Based on the FV mode of AFM, the results presented here test the mechanical resilience of bacteria as a whole under different conditions of external osmotic pressure with repetitive nanoindentations. It was observed that histograms for the obtained physical parameters from nanoindentation maps provide a full picture of the landscape being imaged. However, they can obscure relevant mean values when there is a geometry-dependent interaction between the AFM tip and the sample. From the many individual nanoindentations across the bacteria surfaces along each scanned line, only a few test the central region of interest, where mechanics models can better estimate the rigidity or elastic modulus. The different orientations of the rod-shaped morphology of PA on the substrate while being scanned by the quasi-conical AFM tip with a particular apex half-angle provide a broader spectrum of values on the nanoindentation map. Consequently, meaningful data is present but hidden within the statistical set. For this reason, mean values extracted from histograms were compared with data taken by point nanoindentations from the central region of the long axes of bacteria. Further analysis of these force curves is the focus of the following discussion. Upon compression by the AFM tip, PA showed two main regimes directly after contact. A first nonlinear regime following the contact point is commonly associated with the elastic response of the outer envelope. At the same time, for deeper deformations, a linear behavior in the force curve reflects the magnitude of internal turgor pressure P_t [51]. It is worth mentioning that for our case, only a handful of force curves, particularly in Milli-Q, presented a long tail upon approach, which frequently makes it difficult to identify the position of the contact point. This has been previously reported in other nanoindentation studies on bacteria, and its origin has been related to the action of repulsive electrostatic forces with long Debye screening lengths [44,52]. Our results obtained for the changes in the mechanical response of PA in the low deformation range under different external osmotic pressures are summarized in the parameters of stiffness (k), Young's modulus (Y), and maximal induced deformation (δ_{max}) (see Table 1). These results suggest that the mean values for stiffness remain almost unchanged for the tested conditions. However, mean values obtained for Young's modulus show a shallow trend to decrease with higher osmolarities, particularly when point nanoindentations were used. On the other hand, a clear increase in the penetration depth δ_{max} is observed for higher osmolarities. This behavior of k and Y can be understood, considering the observed change in curvature in the force curves at the beginning of the indentation process and before the curve approaches linearity. The Sneddon model used here to extract the elasticity modulus is sensitive to these changes in curvature even when the slope within the linear regime at the final stage of the trace remains almost unchanged. The increase in δ_{max} (Figure 4a) from 55 to 145 nm accounts not only for this susceptibility of the outer envelope to deform at high osmolarities but also shows how the slope barely changes before it reaches the force threshold of 500 pN. These results are interpreted as follows. For the three investigated osmolarity levels, bacteria do not seem to be disrupted or damaged, at least from a morphological point of view when imaged in the low regime of loading forces or from its mechanical response to external deformation as given in the force curves. Consequently, these results suggest that in each tested solution, the tension exhibited by the outer envelope reflects the differences in the internal osmotic pressure built within the bacterial cell wall once the corresponding protein channels mitigate any threatening conditions to the integrity of the membrane (e.g., exceeding internal pressures due to drastic osmotic downshocks or shriveling caused by sudden shrinkage of the membrane in hypertonic solution). During exposure to a hypotonic solution, membrane lysis by osmotic shock is prevented by the rapid reaction of the MS channels, which act as safety valves which open as soon as the internal P_t causes an increase in the tension of the envelope above a specific threshold value. Then, it rapidly releases contained osmolytes to deflate the internal pressure and avoid membrane rupture. Using forward light scattering experiments, Çetiner et al. reported that the time required for PA to reach an equilibrium state after osmolyte release when exposed to drastic osmotic downshocks was about 150 ms [14]. In our experiments, PA was tested in different conditions after the solution was exchanged in situ in the liquid chamber of the AFM and allowed to settle. This time was about 5 min; therefore, is quite above the reaction time of PA to complete the osmolyte release. In our study, measurements were performed once these tension-triggered channels had already dissipated the exceeding internal pressure and reduced membrane tension below the activation threshold. On the other hand, a pronounced efflux of water leaves the bacterial body in hypertonic solutions. It drastically reduces the internal P_t, resulting in severe dehydration of macromolecules inside the bacteria and the inner membrane envelopes. Lewenza et al. reported the treatment of PA with high salt concentrations and showed that PA develops plasmolysis bays due to shriveling in hypertonic solutions [53]. These bays are generated by a separation between the inner and outer membrane envelopes due to water depletion. As a protective countermeasure of PA against osmotic upshock to avoid collapse by shrinkage, it is known that cationic ions such as K^+ are imported by special protein transporters and accumulated by bacteria to maintain homeostasis against hazardous external concentrations of sodium ions [54]. Also, other accumulated or internally synthesized osmoprotectants such as *N*-acetylglutaminylglutamine (NAGGN) and glutamate contribute to its survival under critical hypertonic solutions, while hydrophilins are also believed to confer protection [55]. Analysis of our force

curves with maximal loading forces of 500 pN in hypotonic and hypertonic solutions yielded mean values for the maximum penetration depths (δ_{max}) of about 52 and 92 nm, respectively. In contrast, for PBS, an intermediate value was obtained. Considering the above information regarding the states of swelling or plasmolysis, our results for the stiffening and softening of the outer envelope can be explained in terms of the internal pressure P_t. Although membrane rigidity is an intrinsic property of the two-dimensional material, membrane tension is not. Instead, membrane tension depends on the forces acting on the membrane, which is directly influenced by the internal turgor pressure [56]. As depicted in the force curves for the case of hypotonic solution, the combination of a high curvature with shorter δ_{max} strongly indicates a higher membrane tension as a result of osmolyte release in the final equilibrium phase by the MS channels, which is consistent with values similar or slightly above to those obtained in PBS. Meanwhile, in the hypertonic solution, the curvature at the beginning of the curve is lower, and further deformation is required to attain the linear behavior. Based on our force spectroscopy results and reported fluorescence microscopy images showing plasmolysis bays in PA under hypertonic conditions, we speculate that this mechanical response is explained by the detachment between the outer and inner bacterial envelope caused by dehydration [53]. A loose outer envelope that has lost its tight connection with the inner envelope due to severe water depletion could provide a consistent explanation for the lower mechanical resistance or softening observed during the first steps of deformation. Consequently, additional deformation would be necessary before reaching the mechanical resistance transmitted from the inner envelope.

As stated above, the contribution to the steepness in the linear regime in the force curves reflects the P_t. In our study, PA seems to keep its mechanical response within the same values in hypotonic and hypertonic solutions, which shows its mechanical fitness after the equilibration process to some extent. The elastic deformation of PA in the frame of AFM nanoindentation can be modeled as the simultaneous compression of two spring elements in series with different stiffness, where the system cantilever+tip with stiffness k_{cant} compresses PA with stiffness k_{PA}. Thus, in a force curve, the slope in the linear region represents the effective action of both springs acting together, which can be expressed as k_{eff}. Applying Hooke's law for a system of two springs being compressed in series and solving for k_{PA}, we obtain $k_{PA} = (K_{cant} \cdot K_{eff}) \cdot (k_{cant} - k_{eff})^{-1}$ [57]. Table 1 shows the mean values obtained from this calculation once the effective stiffness values were extracted from the force curves. Measurements and a detailed analysis of membrane deformation by AFM nanoindentations on the Gram-negative bacterium *Magnetospirillum gryphiswaldense* were first published by Arnoldi and Boulbitch [51,58]. Their study revealed a stiffness value for the membrane in the 0.04–0.07 N/m range. Their theoretical analysis allowed them to use this value to estimate turgor pressures within the 85–150 kPa range. To avoid the complex mathematical analysis of that first study on membrane elasticity, Yao and coworkers presented a tension-dominated model to derive the internal turgor pressure [52] of the Gram-positive and negative bacterium from the linear region of the slope obtained from force curves during deformation. For Gram-negative bacteria, they found that P_t increases an order of magnitude when bacteria are tested in distilled water ($\approx 1.9 \times 10^5$ Pa) compared with growth medium ($0.1–0.12 \times 10^5$ Pa). Under the framework of the tension-dominated model developed by Yao and coworkers for rod-shaped bacteria such as PA, we can estimate P_t in our present study. Considering a mean height for PA of about 600 nm, an inner radius of 250 nm, which considers the presence of the double membrane in Gram-negative bacteria, and a mean stiffness of k_B = 20 mN/m, we obtained a turgor pressure of P_t = 12.1 kPa. This obtained value for P_t is in the same order as that reported by Yao for the growth medium. The higher value they reported for the stiffness in distilled water directly impacted the estimation of P_t, as all other parameters were practically unchanged. We do not observe this substantial difference in stiffness between PBS and Milli-Q water in our measurements. Aware that both studies were performed with a similar experimental setup using a fluid chamber in the AFM, we can argue that time scales between measurements and between solutions were similar. We cannot explain the steeper slope reported in distilled water in that study. Furthermore, according to Çetiner et al., a rapid osmolyte release takes place within the first 150 ms following dilution, which should not only decelerate swelling but also return membrane tension below a threshold value during cell equilibration [14]. On the other hand, our reported values for Young's modulus seem to capture the combined features in the force curve, meaning the curved region and the linear response. Altogether, our study suggests that the induced nanoindentations reflect different states of tension of the outer envelope at shallow deformations for the different tested solutions. Still, a similar stiffness arising from the remaining contents dominates for larger deformations. We associate this membrane tension and mechanical response with the equilibration time of the bacteria once MS channels have dissipated the osmotic gradient.

Care must be taken when quantifying the strength of adhesion forces via repetitive nanoindentations with the AFM because the risk of tip contamination is always present, and also because the sensitive nature of the intermolecular forces during the measuring conditions (pH, ionic strength, temperature, etc.) can easily affect their magnitude. This was reflected in the obtained

adhesion maps (see Figures S5 and S6 of Supporting Information File 1). In Milli-Q water, it is well known that a silicon nitride AFM tip is negatively charged. Consequently, upon close contact, a negatively charged AFM tip will experience on one side an attractive force towards a positively charged surface given by the cationic PLL and on the other side a repulsive force arising from the negatively charged bacterial membrane. In Milli-Q water, electrostatic double-layer forces strongly enhance the magnitude of adhesion forces at close range. This effect can be observed in the force curve shown as the control in Figure 4A taken in Milli-Q water on the substrate coated with PLL. The black line shows the presence of a jump-in, indicating the existence of a pulling force ≈15–20 nm before contact. The obvious contrast in the map of the adhesion channels together with the cross-sections shown in Supporting Information File 1, Figure S5 indicate the magnitude of F_A. On PA, a negative F_A or repulsion of about 25 pN was obtained, while a positive adhesion F_A of about 50 pN on the PLL coat was measured. These results are consistent with the information gained by ξ-potential measurements of PA when measured in Milli-Q water, where a negative surface charge for PA of about −25 mV was obtained (data not shown). Introducing salts into the solution resulted in the electrostatic screening of the double-layer forces, which resulted in the cancelation of long-range forces upon approach. The implication of this is shown in the adhesion maps of Supporting Information File 1, Figure S6, where a loss in the strength of adhesion forces started to occur in PBS while in 0.5 M NaCl it was even more pronounced.

Conclusion

We performed shallow (500 pN) nanoindentations to quantify the changes in rigidity of the outer cell wall of *Pseudomonas aeruginosa* in hypotonic, isotonic, and hypertonic conditions. Force–volume AFM demonstrated its capacity for testing the mechanical properties of multiple bacteria at once. This mechanical nanoscale mapping allowed us to successfully discriminate the minute variations in the surface topography of bacteria (h), their mechanical resistance to external deformation (k), an estimation of their elasticity modulus (Y), and their adhesive behavior towards the AFM tip to the substrate (F_A). Generated maps from nanoindentations indicated that PA tolerates drastic changes in osmotic pressure from isotonic (0.35 Osm) to hypotonic (<0.05 Osm) or hypertonic (1 Osm) solutions without showing serious structural or morphological damage of the bacterial bodies. Deformation of PA by a pseudo-conical tip resulted in force curves with two main features, mainly a first nonlinear region we associated with the magnitude of membrane tension followed by a linear region related to the internal turgor pressure. Our results showed that for the time scale of our experiments, the stiffness given by the linear regime of the curves did not significantly change the range of tested osmolarities. Application of previously developed models for AFM nanoindentation that relate the stiffness of a rod-shaped bacteria under deformation to its internal turgor pressure was used. The obtained values were consistent with those reported for Gram-negative bacteria in growth medium but inconsistent with those reported in hypotonic solutions. We argue that osmotic shock and potential cell lysis are prevented by the rapid reaction of MS channels to low osmolarities, which also decreases membrane tension. Decompression of exceeding internal pressures within PA is then reduced, and obtained values for k_{PA} and P_t represent the equilibration phase of PA which counteracts exceeding swelling. This demonstrates the remarkable dynamic capacity of the MS channels to rapidly mitigate hazardous internal pressures in highly diluted solutions. Therefore, we expect high membrane tension values to occur but in a very narrow period (within ≈100 ms after exposure), making it challenging to monitor AFM experiments. However, it was observed that the nonlinear region was affected by changes in osmolarity, providing a soft mechanical response for hypertonic solutions. We conclude that this initial weak mechanical response to deformation originates from a loose outer membrane due to dehydration, known as plasmolysis bays. Despite this, PA still provided a considerable mechanical response consistent with an internal turgor pressure for larger deformations. These investigations using nanomechanical mapping with FV AFM unravel fine mechanical parameters of very resilient bacteria with high adaptability to diverse environments. They also highlight the potential of the experimental approach to study the activity of rationally designed molecular channel inhibitors that can specifically bind channel proteins.

Supporting Information

Supporting Information File 1

Additional figures.
[https://www.beilstein-journals.org/bjnano/content/supplementary/2190-4286-16-86-S1.pdf]

Acknowledgements

The graphical abstract was created in BioRender. García-Torres, L. (2025) https://BioRender.com/ide97j2. This content is not subject to CC BY 4.0.

Funding

SB acknowledges the funding from the Deutsche Forschungsgemeinschaft (DFG) – Project ID: 458564133, and the Royal Society of Chemistry (RSC) RG\R1\241050. The corresponding author would like to thank the National postdoctoral

Fellowship program SECIHTI (CONACYT) Mexico, for the financial support.

ORCID® iDs

Lizeth García-Torres - https://orcid.org/0000-0003-4833-1266
Idania De Alba Montero - https://orcid.org/0000-0002-4309-2350
Eleazar Samuel Kolosovas-Machuca - https://orcid.org/0000-0002-7583-8655
Facundo Ruiz - https://orcid.org/0000-0001-6589-5958
Sumati Bhatia - https://orcid.org/0000-0002-5123-4937
Jaime Ruiz-García - https://orcid.org/0000-0003-3730-3825

Data Availability Statement

Data generated and analyzed during this study is available from the corresponding author upon reasonable request.

References

1. Hall-Stoodley, L.; Costerton, J. W.; Stoodley, P. *Nat. Rev. Microbiol.* **2004,** *2,* 95–108. doi:10.1038/nrmicro821
2. Wiehlmann, L.; Wagner, G.; Cramer, N.; Siebert, B.; Gudowius, P.; Morales, G.; Köhler, T.; van Delden, C.; Weinel, C.; Slickers, P.; Tümmler, B. *Proc. Natl. Acad. Sci. U. S. A.* **2007,** *104,* 8101–8106. doi:10.1073/pnas.0609213104
3. Mena, K. D.; Gerba, C. P. Risk Assessment of Pseudomonas aeruginosa in Water. *Reviews of Environmental Contamination and Toxicology;* Springer: New York, NY, USA, 2009; Vol. 201, pp 71–115. doi:10.1007/978-1-4419-0032-6_3
4. Diggle, S. P.; Whiteley, M. *Microbiology (London, U. K.)* **2020,** *166,* 30–33. doi:10.1099/mic.0.000860
5. Tuon, F. F.; Dantas, L. R.; Suss, P. H.; Tasca Ribeiro, V. S. *Pathogens* **2022,** *11,* 300. doi:10.3390/pathogens11030300
6. Reynolds, D.; Kollef, M. *Drugs* **2021,** *81,* 2117–2131. doi:10.1007/s40265-021-01635-6
7. Restrepo, M. I.; Babu, B. L.; Reyes, L. F.; Chalmers, J. D.; Soni, N. J.; Sibila, O.; Faverio, P.; Cilloniz, C.; Rodriguez-Cintron, W.; Aliberti, S. *Eur. Respir. J.* **2018,** *52,* 1701190. doi:10.1183/13993003.01190-2017
8. Wood, S. J.; Kuzel, T. M.; Shafikhani, S. H. *Cells* **2023,** *12,* 199. doi:10.3390/cells12010199
9. López, C. A.; Zgurskaya, H.; Gnanakaran, S. *Biochim. Biophys. Acta, Biomembr.* **2020,** *1862,* 183151. doi:10.1016/j.bbamem.2019.183151
10. Matias, V. R. F.; Al-Amoudi, A.; Dubochet, J.; Beveridge, T. J. *J. Bacteriol.* **2003,** *185,* 6112–6118. doi:10.1128/jb.185.20.6112-6118.2003
11. Sun, J.; Rutherford, S. T.; Silhavy, T. J.; Huang, K. C. *Nat. Rev. Microbiol.* **2022,** *20,* 236–248. doi:10.1038/s41579-021-00638-0
12. Chevalier, S.; Bouffartigues, E.; Bodilis, J.; Maillot, O.; Lesouhaitier, O.; Feuilloley, M. G. J.; Orange, N.; Dufour, A.; Cornelis, P. *FEMS Microbiol. Rev.* **2017,** *41,* 698–722. doi:10.1093/femsre/fux020
13. Ude, J.; Tripathi, V.; Buyck, J. M.; Söderholm, S.; Cunrath, O.; Fanous, J.; Claudi, B.; Egli, A.; Schleberger, C.; Hiller, S.; Bumann, D. *Proc. Natl. Acad. Sci. U. S. A.* **2021,** *118,* e2107644118. doi:10.1073/pnas.2107644118
14. Çetiner, U.; Rowe, I.; Schams, A.; Mayhew, C.; Rubin, D.; Anishkin, A.; Sukharev, S. *J. Gen. Physiol.* **2017,** *149,* 595–609. doi:10.1085/jgp.201611699
15. Zhang, Y.; Daday, C.; Gu, R.-X.; Cox, C. D.; Martinac, B.; de Groot, B. L.; Walz, T. *Nature* **2021,** *590,* 509–514. doi:10.1038/s41586-021-03196-w
16. Blount, P.; Iscla, I. *Microbiol. Mol. Biol. Rev.* **2020,** *84,* e00055-19. doi:10.1128/mmbr.00055-19
17. Poolman, B.; Spitzer, J. J.; Wood, J. M. *Biochim. Biophys. Acta, Biomembr.* **2004,** *1666,* 88–104. doi:10.1016/j.bbamem.2004.06.013
18. Haswell, E. S.; Phillips, R.; Rees, D. C. *Structure* **2011,** *19,* 1356–1369. doi:10.1016/j.str.2011.09.005
19. Levina, N. *EMBO J.* **1999,** *18,* 1730–1737. doi:10.1093/emboj/18.7.1730
20. Reuter, M.; Hayward, N. J.; Black, S. S.; Miller, S.; Dryden, D. T. F.; Booth, I. R. *J. R. Soc., Interface* **2014,** *11,* 20130850. doi:10.1098/rsif.2013.0850
21. Lorusso, A. B.; Carrara, J. A.; Barroso, C. D. N.; Tuon, F. F.; Faoro, H. *Int. J. Mol. Sci.* **2022,** *23,* 15779. doi:10.3390/ijms232415779
22. Compagne, N.; Vieira Da Cruz, A.; Müller, R. T.; Hartkoorn, R. C.; Flipo, M.; Pos, K. M. *Antibiotics (Basel, Switz.)* **2023,** *12,* 180. doi:10.3390/antibiotics12010180
23. Amaral, L.; Martins, A.; Spengler, G.; Molnar, J. *Front. Pharmacol.* **2014,** *4,* 168. doi:10.3389/fphar.2013.00168
24. Li, X.-Z.; Plésiat, P. Antimicrobial Drug Efflux Pumps in Pseudomonas Aeruginosa. *Efflux-Mediated Antimicrobial Resistance in Bacteria;* Springer International Publishing: Cham, Switzerland, 2016; pp 359–400. doi:10.1007/978-3-319-39658-3_14
25. Tambat, R.; Mahey, N.; Chandal, N.; Verma, D. K.; Jangra, M.; Thakur, K. G.; Nandanwar, H. *ACS Infect. Dis.* **2022,** *8,* 255–270. doi:10.1021/acsinfecdis.1c00281
26. Ferrer-Espada, R.; Shahrour, H.; Pitts, B.; Stewart, P. S.; Sánchez-Gómez, S.; Martínez-de-Tejada, G. *Sci. Rep.* **2019,** *9,* 3452. doi:10.1038/s41598-019-39659-4
27. Laborda, P.; Alcalde-Rico, M.; Chini, A.; Martínez, J. L.; Hernando-Amado, S. *Environ. Microbiol.* **2021,** *23,* 7396–7411. doi:10.1111/1462-2920.15511
28. Alenazy, R. *Biology (Basel, Switz.)* **2022,** *11,* 1328. doi:10.3390/biology11091328
29. Rampioni, G.; Pillai, C. R.; Longo, F.; Bondì, R.; Baldelli, V.; Messina, M.; Imperi, F.; Visca, P.; Leoni, L. *Sci. Rep.* **2017,** *7,* 11392. doi:10.1038/s41598-017-11892-9
30. Sharma, A.; Gupta, V. K.; Pathania, R. *Indian J. Med. Res.* **2019,** *149,* 129–145. doi:10.4103/ijmr.ijmr_2079_17
31. Fujiwara, M.; Yamasaki, S.; Morita, Y.; Nishino, K. *J. Infect. Chemother.* **2022,** *28,* 595–601. doi:10.1016/j.jiac.2022.01.003
32. Shriram, V.; Khare, T.; Bhagwat, R.; Shukla, R.; Kumar, V. *Front. Microbiol.* **2018,** *9,* 2990. doi:10.3389/fmicb.2018.02990
33. Dey, N.; Kamatchi, C.; Vickram, A. S.; Anbarasu, K.; Thanigaivel, S.; Palanivelu, J.; Pugazhendhi, A.; Ponnusamy, V. K. *Environ. Res.* **2022,** *204,* 111968. doi:10.1016/j.envres.2021.111968
34. Madhi, M.; Hasani, A.; Mojarrad, J. S.; Rezaee, M. A.; Zarrini, G.; Davaran, S. *Gene Rep.* **2020,** *21,* 100915. doi:10.1016/j.genrep.2020.100915
35. Musiol, R. *Expert Opin. Ther. Targets* **2023,** *27,* 953–963. doi:10.1080/14728222.2023.2263910
36. Christena, L. R.; Mangalagowri, V.; Pradheeba, P.; Ahmed, K. B. A.; Shalini, B. I. S.; Vidyalakshmi, M.; Anbazhagan, V.; Sai subramanian, N. *RSC Adv.* **2015,** *5,* 12899–12909. doi:10.1039/c4ra15382k

37. Nefedova, E.; Shkil, N.; Luna Vazquez-Gomez, R.; Garibo, D.; Pestryakov, A.; Bogdanchikova, N. *Pharmaceutics* **2022,** *14,* 763. doi:10.3390/pharmaceutics14040763
38. Dufrêne, Y. F. *mBio* **2014,** *5,* e01363-14. doi:10.1128/mbio.01363-14
39. Dufrêne, Y. F. *Nat. Rev. Microbiol.* **2008,** *6,* 674–680. doi:10.1038/nrmicro1948
40. Benn, G.; Pyne, A. L. B.; Ryadnov, M. G.; Hoogenboom, B. W. *Analyst* **2019,** *144,* 6944–6952. doi:10.1039/c9an01185d
41. Jarosławski, S.; Duquesne, K.; Sturgis, J. N.; Scheuring, S. *Mol. Microbiol.* **2009,** *74,* 1211–1222. doi:10.1111/j.1365-2958.2009.06926.x
42. Dorobantu, L. S.; Gray, M. R. *Scanning* **2010,** *32,* 74–96. doi:10.1002/sca.20177
43. Olubowale, O. H.; Biswas, S.; Azom, G.; Prather, B. L.; Owoso, S. D.; Rinee, K. C.; Marroquin, K.; Gates, K. A.; Chambers, M. B.; Xu, A.; Garno, J. C. *ACS Omega* **2021,** *6,* 25860–25875. doi:10.1021/acsomega.1c03829
44. Longo, G.; Rio, L. M.; Roduit, C.; Trampuz, A.; Bizzini, A.; Dietler, G.; Kasas, S. *J. Mol. Recognit.* **2012,** *25,* 278–284. doi:10.1002/jmr.2171
45. Polyakov, P.; Soussen, C.; Duan, J.; Duval, J. F. L.; Brie, D.; Francius, G. *PLoS One* **2011,** *6,* e18887. doi:10.1371/journal.pone.0018887
46. Xu, X.; Feng, H.; Zhao, Y.; Shi, Y.; Feng, W.; Loh, X. J.; Vancso, G. J.; Guo, S. *Cell Rep. Phys. Sci.* **2024,** *5,* 101902. doi:10.1016/j.xcrp.2024.101902
47. Offroy, M.; Razafitianamaharavo, A.; Beaussart, A.; Pagnout, C.; Duval, J. F. L. *RSC Adv.* **2020,** *10,* 19258–19275. doi:10.1039/d0ra00669f
48. Han, R.; Vollmer, W.; Perry, J. D.; Stoodley, P.; Chen, J. *Nanoscale* **2022,** *14,* 12060–12068. doi:10.1039/d2nr02577a
49. Zhang, H.; Wang, H.; Wilksch, J. J.; Strugnell, R. A.; Gee, M. L.; Feng, X.-Q. *Soft Matter* **2021,** *17,* 2042–2049. doi:10.1039/d0sm02075c
50. Valentová, L.; Füzik, T.; Nováček, J.; Hlavenková, Z.; Pospíšil, J.; Plevka, P. *EMBO J.* **2024,** *43,* 4384–4405. doi:10.1038/s44318-024-00195-1
51. Arnoldi, M.; Fritz, M.; Bäuerlein, E.; Radmacher, M.; Sackmann, E.; Boulbitch, A. *Phys. Rev. E* **2000,** *62,* 1034–1044. doi:10.1103/physreve.62.1034
52. Yao, X.; Walter, J.; Burke, S.; Stewart, S.; Jericho, M. H.; Pink, D.; Hunter, R.; Beveridge, T. J. *Colloids Surf., B* **2002,** *23,* 213–230. doi:10.1016/s0927-7765(01)00249-1
53. Lewenza, S.; Mhlanga, M. M.; Pugsley, A. P. *J. Bacteriol.* **2008,** *190,* 6119–6125. doi:10.1128/jb.00603-08
54. Elabed, H.; González-Tortuero, E.; Ibacache-Quiroga, C.; Bakhrouf, A.; Johnston, P.; Gaddour, K.; Blázquez, J.; Rodríguez-Rojas, A. *BMC Microbiol.* **2019,** *19,* 142. doi:10.1186/s12866-019-1499-2
55. Aspedon, A.; Palmer, K.; Whiteley, M. *J. Bacteriol.* **2006,** *188,* 2721–2725. doi:10.1128/jb.188.7.2721-2725.2006
56. Steinkühler, J.; Sezgin, E.; Urbančič, I.; Eggeling, C.; Dimova, R. *Commun. Biol.* **2019,** *2,* 337. doi:10.1038/s42003-019-0583-3
57. Michel, J. P.; Ivanovska, I. L.; Gibbons, M. M.; Klug, W. S.; Knobler, C. M.; Wuite, G. J. L.; Schmidt, C. F. *Proc. Natl. Acad. Sci. U. S. A.* **2006,** *103,* 6184–6189. doi:10.1073/pnas.0601744103
58. Boulbitch, A. *J. Electron Microsc.* **2000,** *49,* 459–462. doi:10.1093/oxfordjournals.jmicro.a023829

License and Terms

BEILSTEIN JOURNAL OF NANOTECHNOLOGY

Internal 3D temperature mapping in biological systems using ratiometric light-sheet imaging and lipid-coated upconversion nanothermometers

Dannareli Barron-Ortiz[1], Enric Pérez-Parets[2], Rubén D. Cadena-Nava[3], Emilio J. Gualda[2,4], Jacob Licea-Rodríguez[5], Juan Hernández-Cordero[6], Pablo Loza-Álvarez[2] and Israel Rocha-Mendoza[*1]

Full Research Paper

Open Access

Address:
[1]Centro de Investigación Científica y de Educación Superior de Ensenada (CICESE), Carretera Ensenada-Tijuana, No. 3918, Zona Playitas, Ensenada 22860, México, [2]ICFO-Institut de Ciencies Fotoniques, The Barcelona Institute of Science and Technology, Av. Carl Friedrich Gauss, 3, 08860 Castelldefels, Spain, [3]Centro de Nanociencias y Nanotecnología (CNyN), Universidad Nacional Autónoma de México (UNAM), Km 107 Carretera Tijuana-Ensenada, Pedregal Playitas, Ensenada 22860, México, [4]Department of Agri-Food Engineering and Biotechnology (DEAB), Universitat Politècnica de Catalunya, Esteve Terradas 8, 08860 Castelldefels, Spain, [5]Centro de Investigación en Ingeniería y Ciencias Aplicadas (CIICAp), Universidad Autónoma del Estado de Morelos, Cuernavaca 62209, México and [6]Instituto de Investigaciones en Materiales, Universidad Nacional Autónoma de México, A.P. 70-360, México City 04510, México

Email:
Israel Rocha-Mendoza[*] - irocha@cicese.mx

* Corresponding author

Keywords:
C. elegans; 3D imaging; fluorescent intensity ratio; light-sheet microscopy; temperature mapping; upconversion fluorescent nanoparticles

Beilstein J. Nanotechnol. **2025,** *16,* 2306–2316.
https://doi.org/10.3762/bjnano.16.159

Received: 18 August 2025
Accepted: 02 December 2025
Published: 22 December 2025

This article is part of the thematic issue "Symposium of Nanoscience and Nanomaterials 2024 (SNN 2024)".

Associate Editor: L. Fu

Abstract

Upconversion nanoparticles (UCNPs) are well-known for their high efficiency, photostability, near-infrared excitation, and ability to estimate temperature through ratiometric imaging of two thermally coupled fluorescence bands. This work demonstrates the feasibility of volumetric temperature mapping in internal biological systems using light-sheet fluorescence microscopy and lipid-coated UCNPs as nanothermometry markers. This approach enables real-time thermal mapping with both high spatial and temporal resolution at the cellular and subcellular levels. To validate the method, we performed 3D temperature imaging on fixed *Caenorhabditis elegans* (*C. elegans*) after UCNP ingestion. The proposed technique represents a cutting-edge method for accurate 3D analysis of temperature-driven biological processes. It holds significant potential for applications in living organisms, offering a non-invasive tool to monitor intracellular and organ-specific temperature dynamics.

Introduction

Biological processes involving energy exchange often manifest as temperature fluctuations. Materials sought to measure such changes should exhibit high sensitivity, accuracy, high spatiotemporal resolution, good biocompatibility, low cytotoxicity, and stable optical and chemical properties. Additionally, given the conditions commonly presented in biological samples, these materials should also remain unaffected by changes in pH, concentration, ionic strength, and viscosity [1]. Traditional thermometers are macroscopic devices with several disadvantages, including limited sensitivity and low accuracy, and are generally restricted to contact surface measurements [2]. Beyond fundamental processes, temperature also serves as a key biomarker for pathological conditions such as cancer. Localized hyperthermia often arises from dysregulated metabolism (i.e., the Warburg effect) [3,4] and chaotic vasculature that impairs heat dissipation [5,6]. These factors can create thermal gradients of 0.5–2.0 °C between tumors and healthy tissue, with even greater differences at the subcellular level [7-9]. Consequently, the ability to map temperature with high spatial resolution is a critical tool for probing disease mechanisms, potentially aiding in diagnostics and therapeutic evaluation. To address these limitations, luminescent nanomaterial-based thermometers (LNTs) have emerged as promising alternatives for biological and non-biological applications. LNTs rely on the emission properties of a fluorophore and its thermal dependence to measure temperature changes, which can be measured as variations in the emission intensity [10-13] and lifetime [8,14-16], spectral shift [17], as well as intensity ratios [18-29] and polarization anisotropy [30,31].

In biological applications involving fluorescent nanothermometry, light–tissue interactions must be carefully considered for an accurate temperature measurement. To address this, a wide range of luminescent materials have been developed, including nanodiamonds [32], quantum dots [17,28], nanodots [11,13,33], fluorescent-based molecular systems [1,8,34], and lanthanide (Ln^{3+})-doped materials [10,35-37]. Among all these alternatives, lanthanide-doped materials offer a distinct advantage: upconversion (UC) fluorescence, enabling the conversion of low-energy excitation (longer wavelengths) into high-energy emission (shorter wavelengths). This is particularly advantageous for biomedical applications, as it eliminates the need for ultraviolet or visible excitation, which can cause photobleaching and phototoxicity [38]. The ladder-like energy level structure of Ln^{3+} ions enable efficient photon UC of near-infrared (NIR) light, even with moderate excitation intensities ($1–10^3$ W·cm^{-2}) attainable with gas-based lamps or continuous wave lasers [39].

Temperature measurements using Ln^{3+}-doped nanomaterials have mainly focused on using UC nanoparticles (UCNPs), which are inorganic crystalline structures, typically composed of sodium yttrium fluoride ($NaYF_4$) co-doped with rare-earth (RE) ions like ytterbium (Yb^{3+}), erbium (Er^{3+}), and gadolinium (Gd^{3+}). These RE ions act as sensitizers and emitters, allowing for photonic UC of multiple NIR photons into visible luminescence [38]. As an example, in the $NaYF_4$:Er^{3+}/Yb^{3+} composite (such as that used in this work), the $NaYF_4$ crystal matrix is co-doped with Yb^{3+} acting as the sensitizer to enhance the NIR absorption cross section, whereas the Er^{3+} ion acts as the emitter, as depicted in Figure 1.

When UCNPs of this composite are irradiated with 980 nm NIR light, they emit two thermally coupled green fluorescence bands

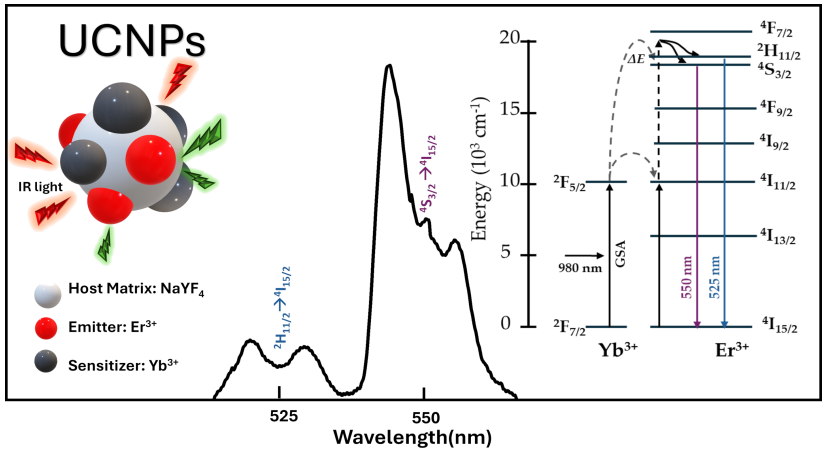

Figure 1: Characteristic UC fluorescent emission spectra of $NaYF_4$:Er^{3+}/Yb^{3+} in the green region when irradiated with 980 nm laser light. Insets: UC process scheme (right). Schematic representation of the energy transfer between Yb^{3+} and Er^{3+} ions and the UC emission in an upconversion nanoparticle UCNP (left).

at 525 and 550 nm. These bands arise from the $^2H_{11/2} \rightarrow {}^4I_{15/2}$ (blue) and $^4S_{3/2} \rightarrow {}^4I_{15/2}$ (purple) transitions of Er^{3+} ions, respectively [39-41]. Thermally coupled bands, defined as bands separated by less than 2000 cm^{-1} (<0.248 eV), favor a higher-level population with an increase in thermal energy, thereby enabling temperature-sensitive fluorescence emission [42]. For the $NaYF_4:Er^{3+}/Yb^{3+}$ composite, the energy bands ($^2H_{11/2}$ and $^4S_{3/2}$) are separated by approximately 866 cm^{-1}; they are thus thermally coupled, and the ratio of their intensities provides a reliable means for temperature monitoring. This approach is known as the fluorescence intensity ratio (FIR), described mathematically as:

$$\mathrm{FIR} = \frac{I_{525}}{I_{550}} = C \exp\left(\frac{-\Delta E}{kT}\right), \quad (1)$$

where I_{525} and I_{550} are the integrated intensities of the two fluorescence bands centered at 525 and 550 nm, respectively; ΔE is the energy difference between the $^2H_{11/2}$ and $^4S_{4/2}$ levels, k is Boltzmann's constant (0.695 $cm^{-1} \cdot K^{-1}$), T is the absolute temperature in Kelvin (K), and C is a constant associated with the host material and determined by the degeneracy of the coupled energy levels, emission frequencies, and spontaneous radiation transition rates [43].

The FIR-based technique has been widely used for optical thermometry given its inherent advantages, including noise cancellation capabilities, real-time temperature sensing, and high sensitivity [44]. These features make FIR-based thermometry appealing for remote optical measurements in biological applications. Indeed, upon imaging the thermally coupled fluorescent bands emitted by UCNPs with microscopy techniques, precise temperature measurements within biological systems can be readily obtained. For instance, Vetrone et al. [36] used UCNP@PEI as nanothermometers for two-dimensional (2D) temperature mapping inside Hella cells. Similarly, Piñol and co-workers [20] used the FIR of Ln^{3+} (Sm, Eu)-bearing polymeric micelles to achieve real-time 2D temperature maps of breast metastatic adenocarcinoma cells. Di et al. [45] used functionalized UCNPs to monitor mitochondrial thermal dynamics in HeLa cells, and Wang et al. [37] used core–shell UCNPs to monitor temperature and imaging inside and outside onion cells simultaneously. These studies underscore the versatility and potential of UCNP-based thermometry for non-invasive, precise temperature measurements and cell imaging.

Despite these advancements, most approaches rely on 2D imaging or point-scanning spectroscopic methods to generate temperature maps, which are limited in axial resolution and acquisition speed when applied to thick or heterogeneous biological samples. Earlier studies using luminescent nanothermometers have demonstrated spatially resolved, yet essentially planar, temperature mapping in transparent or thin systems [24,25]. More recently, efforts in luminescence-based 3D thermometry at the cellular scale [46,47] have explored volumetric temperature sensing through fluorescence-lifetime or UC nanothermometry. However, these approaches remain limited by point-by-point scanning, shallow penetration depth, and narrow fields of view (typically below 100 µm), restricting their applicability to intact organisms. Beyond these demonstrations, recent reviews [48,49] emphasize that achieving true 3D luminescence thermometry remains a major challenge as most implementations rely on complex instrumentation and confined imaging volumes. Therefore, extending nanothermometry toward fast, high-resolution volumetric mapping represents an essential step for advancing non-invasive thermal imaging in living biological systems.

We recently demonstrated the feasibility of combining light-sheet fluorescence microscopy (LSFM) with UC micro- and nanocomposites for volumetric temperature mapping across scales ranging from tens of micrometers to millimeters [40]. LSFM decouples excitation and detection, illuminating only the focal plane and thereby minimizing photobleaching and photothermal effects while enabling rapid volumetric acquisition. The present work aims to extend this technique to larger biological specimens, specifically *C. elegans*, an optically transparent model organism ideally suited for LSFM due to its simple "tube-within-a-tube" anatomy and clearly defined internal organs. When the nematode is fed with lipid-coated UCNPs, the nanoparticles localize within its digestive tract, acting as thermosensitive markers and enabling voxel-resolved, real-time 3D thermal mapping with exceptional spatial and temporal resolution [45,50,51], revealing internal temperature gradients inaccessible with 2D imaging. The results reported herein highlight the potential of LSFM and FIR-based thermometry as a non-invasive method for precise temperature mapping in living organisms.

Materials and Methods

Lipid-wrapped UCNPs

Due to their highly hydrophobic nature, commercial $NaYF_4:Yb^{3+}/Er^{3+}$ UCNPs (Sigma-Aldrich, No. 900556 1 ML) were coated with lipids to enhance their water dispersibility. This lipid coating (UCNPs@lipids) was applied using a modified thin-film hydration method based on Rojas-Gutierrez's procedure [52]. Based on the size distribution and concentration of the nanoparticles (10 $mg \cdot mL^{-1}$), a lipid layer was formed with DOPS, cholesterol, and DMPC at a molar ratio of 64:29:7. The three lipids were dispersed in chloroform and mixed with 100 µL of UCNPs in a round-bottomed flask. The resulting

mixture was then evaporated under a constant flow of N_2 gas while stirring in a circular motion for 30 min. After solvent evaporation, 2 mL of Milli-Q water were added to the flask for rehydration overnight at 4 °C. The resulting water-dispersible UCNPs@lipids solution had a UCNP concentration of 1 mg·mL^{-1} and was stored at room temperature for subsequent use and characterization. Evidence of obtaining such a water-dispersible solution was previously reported in [40]. Figure 2 compares the as-purchased nanoparticles dispersed in toluene with the lipid-functionalized UCNPs (inset), revealing a size distribution of approximately 15–20 nm. Because the lipid shell is an ultrathin organic layer (2–3 nm) with low electron contrast, no distinct morphological differences are expected between coated and uncoated nanoparticles in TEM images; however, the success of the coating is confirmed by the stable dispersion of UCNPs in water, which prevents aggregation.

C. elegans culture and maintenance

The nematodes used in our experiments, N2 wild-type *C. elegans,* were cultivated on nematode growth medium (NGM) plates previously seeded with *E. coli* OP50. Nematode transfer was performed every two days, moving a chunk of agar from a three-to-five-day-old plate to a new NGM plate seeded with *E. coli*. The nematodes were cultivated at room temperature (≈23 °C).

C. elegans feeding with UCNPs

To feed the nematodes with UCNPs, ten to twelve nematodes, each approximately 1 mm in length, were selected and individually transferred from a three-day-old cultivation plate to a fresh small NGM plate (35 mm in diameter) that was not seeded with *E. coli* OP50. The nematodes transfer was gently conducted using a stereomicroscope (ZEISS, Stemi 2000) equipped with a transmitted light source and thin tweezers. After the transfer, 50 µL of the UCNPs@lipids solution was carefully dropped onto the plate and spread to cover most of the plate. Before imaging, the nematodes were left in contact with the UCNPs@lipids solutions for approximately 17 h.

Samples used for temperature mapping

Two types of samples were prepared in our experiments, one for FIR-temperature calibration and the other for internal temperature mapping in nematodes. The first sample, S1, was an agarose phantom with lipid-coated UCNPs, as reported in [40]. It consisted of a mixture of 250 µL of UCNPs@lipids solution and 250 µL of 2% low-melting agarose gel. A few microliters

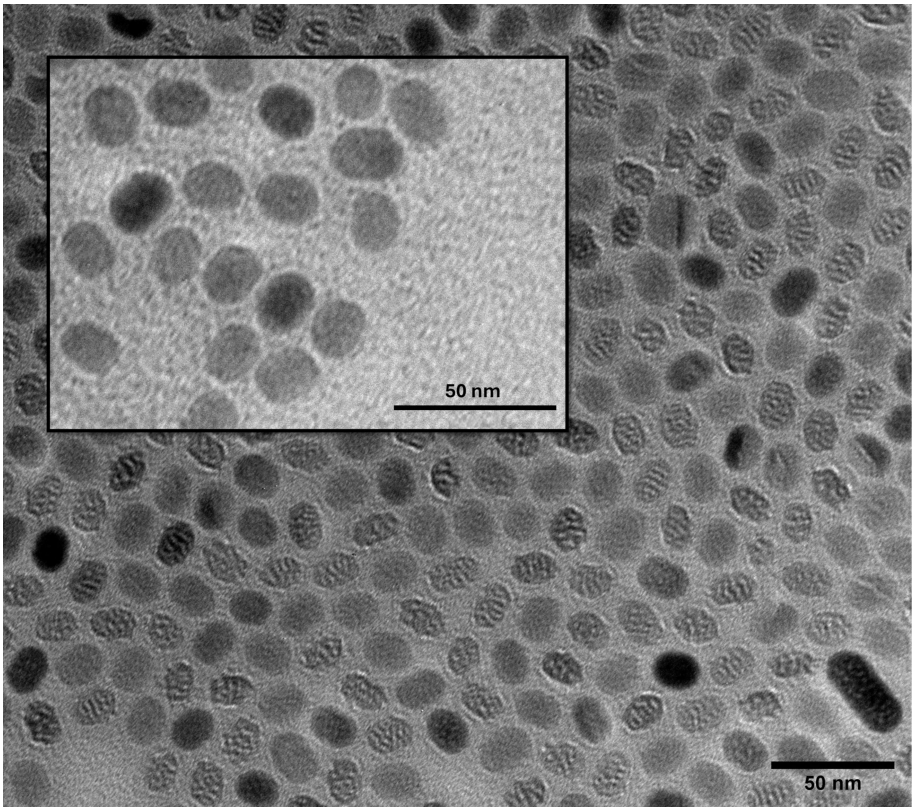

Figure 2: TEM micrograph of as-bought UCNPs dispersed in toluene. Inset: functionalized UCNPs@lipids dispersed in Milli-Q water. Scale bar: 50 nm.

of the liquid mixture were drawn into a fluorinated ethylene propylene (FEP) tube and solidified 30 min before imaging. The second sample, S2, consisted of a single UC-fed *C. elegans* immersed in agarose mixed with UCNPs@lipids. After feeding with UCNPs@lipids, live nematodes were placed into a drop of 2% low-melting agarose gel containing UCNPs@lipids and then fixed with 4% paraformaldehyde (PFA). The nematodes were oriented with their mouth and tail positioned at the ends of the FEP tube and left to solidify for 30 min before imaging. The FEP tubes were inserted into a capillary tube for structural support to mount the samples. Using a metal plunger, the samples were drawn into the exposed end of the FEP tube, as illustrated in Figure 3.

Light sheet microscopy

The LSFM setup is described in [40]. Here, the NIR excitation at 980 nm was provided by a fiber Bragg grating-stabilized laser (JDSU, 2900 Series), with collimated light focused onto the back focal plane of a 4×/0.13 NA excitation objective (Nikon, PlanFluor) using a 250 mm cylindrical lens (Thorlabs, LJ1267RM-A). The excitation objective generated the light sheet in the sample's *xy*-plane, with a capillary glass mounted on an *xyz*-motorized stage (Thorlabs, 3-axis NanoMax) for depth imaging. Images were captured using a CMOS camera (Hamamatsu, ORCA-Flash4.0) with a 10×/0.3 NA water immersion objective (Nikon, PlanFluor) and tube lens, achieving a 1.3 × 1.3 mm^2 FOV and ≈1.3 µm axial resolution. Two interferometric filters (Thorlabs, MF510-40, and MF559-34) isolated the 525 and 550 nm UC fluorescence bands, while a bandpass filter (Thorlabs, FESH-0650) blocked the excitation light.

To heat the immersed sample, a custom-made immersion chamber was used to house the capillary tube. The chamber featured a temperature-controlled water recirculation system consisting of a peristaltic pump (KF Technology, NE-9000), a solution heater (Warner Instruments, Hamden), and a temperature controller (Warner Instruments, TC-324C). This setup enabled precise control from 25 to 50 °C with ±0.2 °C accuracy.

Results and Discussion

Three-dimensional calibration curves

To accurately quantify temperature variations, a precise calibration curve must be established. Two UCNPs@lipids samples (S1) were prepared for FIR calibration, with concentrations of 0.5 and 2.5 $mg{\cdot}mL^{-1}$. Figure 4a presents the three-dimensional reconstruction of the UC fluorescence signal at 550 nm for the higher concentration (2.5 $mg{\cdot}mL^{-1}$) sample. The image reveals the characteristic aggregation of lipid-coated UCNPs, forming macroliposomes of approximately 30 µm diameter within the agarose gel. A corresponding volumetric image was also acquired at the 525 nm band (not shown) to compute the FIR. Pairs of these images were taken at different temperatures to establish the temperature-dependent FIR calibration. For each sample, approximately 25 macroliposomes were analyzed.

Although the FIR response follows a Boltzmann-type exponential temperature dependence (see Equation 1), our previous

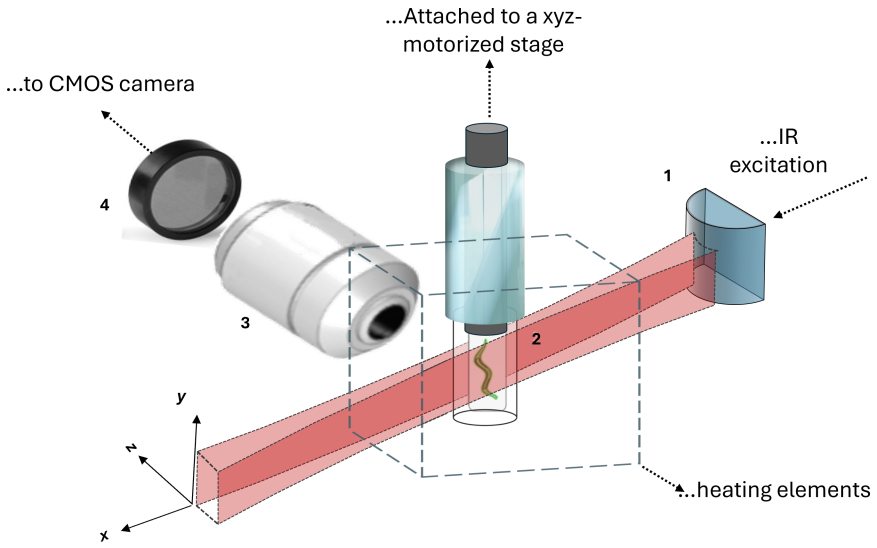

Figure 3: General scheme of the sample mounting holder used for temperature mapping in the light sheet microscopy system. The numbers in the figure stand for cylindrical optics (1), sample (2), collection objective (3), and optical filter set (4). Figure 3 was adapted from [40] (© 2023 D. Barron-Ortiz et al., published by MDPI, distributed under the terms of the Creative Commons Attribution 4.0 International License, https://creativecommons.org/licenses/by/4.0).

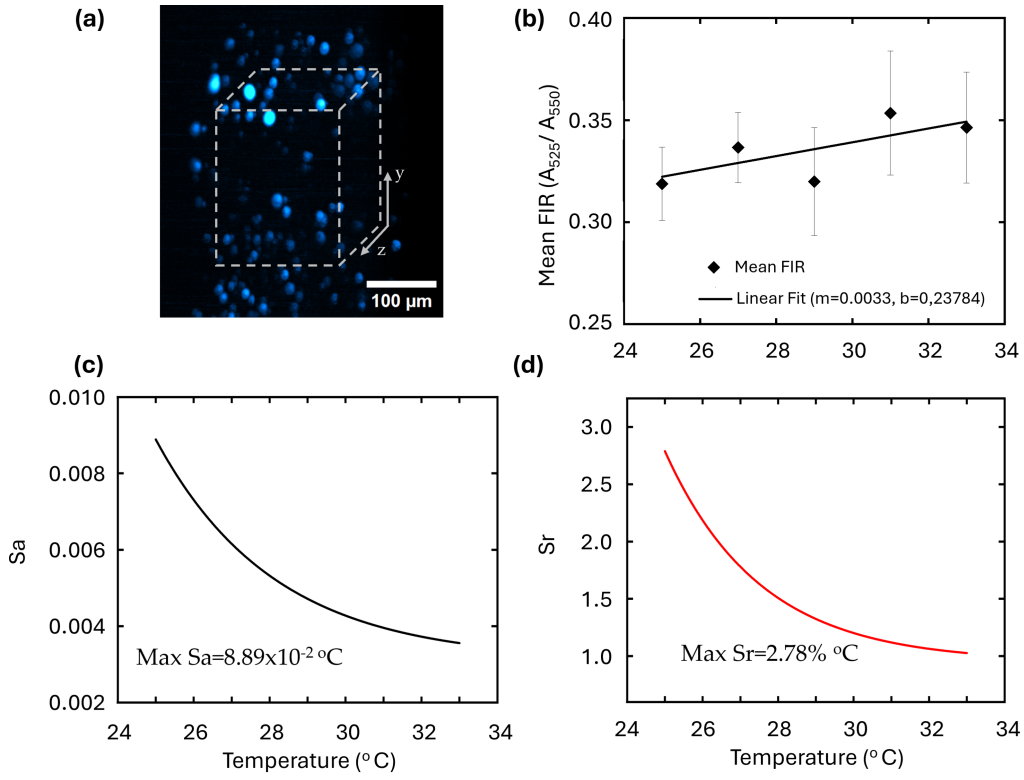

Figure 4: (a) Fluorescence intensity of UCNPs@lipids at 25 °C. (b) 3D temperature dependence from 25 to 33 °C. The black rhombs represent the mean values for S_1, S_2, and the combined selected nanoparticles. The solid line shows the linear fit of the calibration curve, obtained from the mean values of both UCNPs@lipids concentrations. (c) Absolute sensitivity (S_a). (d) Relative sensitivity (S_r). (a, b) where measured from 25 to 33 °C.

work demonstrated that within the 25–50 °C interval in $NaYF_4$:Yb^{3+}/Er^{3+}systems, the FIR behavior of lipid-coated UCNPs can be well approximated by a linear dependence with a slope of $m \approx 0.003$ °C^{-1} [40]. This finding is consistent with earlier experimental results showing a linear response up to 100 °C [44], confirming the robustness of this relationship across a broad thermal range. In the present study, the calibration was restricted to 25–33 °C to match the physiological temperature range of *C. elegans* and to evaluate the method's sensitivity in detecting subtle temperature variations relevant to biological processes.

The resulting temperature-dependent FIR response is illustrated in Figure 4b, covering the 25–33 °C range, with measurements taken at 2 °C intervals. This temperature range was chosen because (i) it remains below the high-stress temperature threshold of *C. elegans* (>35 °C) [53] and (ii) it falls within the linear, high-sensitivity region of the $NaYF_4$:Yb/Er nanoparticle thermometric response (20–100 °C) [44]. The black diamonds denote the combined mean values of both concentrations. A linear fit of the calibration curve (solid black line) was obtained for both UCNPs@lipids concentrations. The results closely align with Barron-Ortiz et al.'s previously reported calibration curve [40], showing a slope of $m = 0.33$ °C^{-1}.

The resolution performance of the optical thermometer is assessed through its absolute (S_a) and relative (S_r) thermal sensitivities [35,54]. These are defined as:

$$S_a = \left|\frac{\partial \mathrm{FIR}}{\partial T}\right|, \tag{2}$$

$$S_r = \frac{S_a}{\mathrm{FIR}} \times 100\%. \tag{3}$$

The absolute sensitivity (S_a) quantifies the FIR response to a 1 °C temperature change, and the relative sensitivity (S_r) describes the FIR rate of change as a percentage of its value. Notice that the complex nature of the dynamic UC process, particularly at higher temperatures, can influence the temperature-sensing properties of UCNPs [37,42]. However, even within the physiological temperature range (30–50 °C), other UC processes such as thermal quenching, shifts in the Boltzmann dis-

tribution, and cross-relaxation, can also affect temperature sensing [37,54]. These effects may introduce variations in the FIR calibration, requiring careful evaluation for accurate thermometry [35,55]. This concern is particularly relevant in Er^{3+}-based FIR thermometry as its sensitivity strongly depends on the energy gap between thermally coupled levels [42]. In our results, these effects are minimized, as the FIR calibration exhibits a consistent and linear temperature dependence over the 25–33 °C range, with no significant deviations from the expected response. This suggests that our UCNP system provides reliable temperature measurements, effectively mitigating potential distortions from UC artifacts. To demonstrate this, we calculated the thermal sensitivities S_a and S_r using Equation 2 and 3, based on the calibration obtained from the curve of Figure 4b. The calculated sensitivities are included in Figure 4c,d, showing that over the 25 to 33 °C temperature range, the absolute sensitivity S_a varied between 3.35×10^{-3} and 8.89×10^{-3} $°C^{-1}$ (Figure 4c), while the relative sensitivity S_r ranged from 1.0 to 2.78%·$°C^{-1}$ (Figure 4d). The largest values, $S_a = 8.89 \times 10^{-3}$ $°C^{-1}$ and $S_r = 2.78\%·°C^{-1}$, were observed at 25 °C, with a decreasing trend as the temperature increased. It is important to note that the relative sensitivity remained above the 0.5%·C^{-1} threshold, a benchmark for high-performance nanothermometry applications [55]. This confirms previous studies showing that the temperature-dependent electronic $4S_{3/2} \rightarrow 2H_{11/2}$ transitions in Er^{3+} provide optimal sensitivity within the 30–50 °C range, making them highly suitable for biological applications [42].

C. elegans internal temperature measurement

After evaluating the 3D temperature sensing capability of UCNPs@lipids, we applied this technique to measure the internal temperature within fixed *C. elegans* nematodes. The worms were fed with the UCNPs@lipids solution at a 1 mg·mL^{-1} concentration, consistent with imaging and toxicity studies [56].

Figure 5 illustrates the workflow for obtaining temperature maps. The process begins with identifying the nematode through its autofluorescence under 488 nm light-sheet excitation, highlighting key anatomical structures such as the pharynx and intestinal tract (Figure 5a). A *z*-stack is then acquired in steps of 2 µm to cover the whole volume of the nematode. Once the nematode is located, it is irradiated with a 980 nm NIR light sheet, and two emission filters (Thorlabs, MF510-40, and MF559-34) are used sequentially to collect the UC fluorescence bands centered at 525 and 550 nm. Figure 5b and Figure 5c show, respectively, the *z*-projections of the average fluorescence intensities for these bands. The FIR is then calcu-

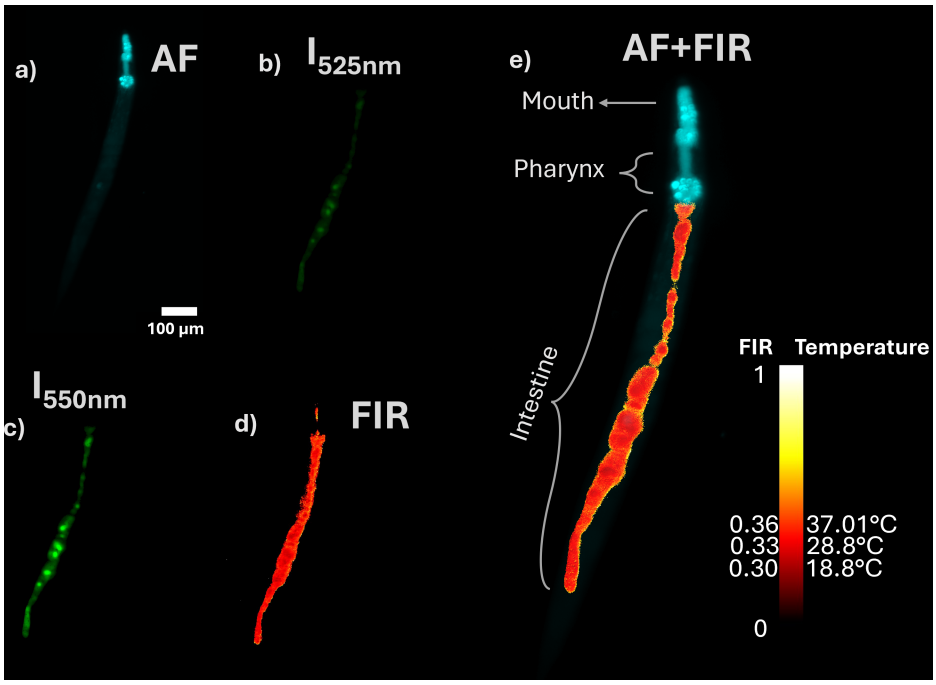

Figure 5: Temperature map inside of *C. elegans*. (a) Shows the autofluorescence in cyan, (b, c) Upconversion fluorescence images of the 525 and 550 nm emission bands at 25 °C. (d) FIR map. (e) The temperature map of *C. elegans* shows the FIR as a red-hot map and autofluorescence in cyan. The temperature signals are primarily localized within the intestinal lumen. Scale line: 100 µm. Temperature scale bar: to the left, FIR from 0 to 1, to the right, temperature, as a reference, 0.333 corresponds at approximately 28.8 °C.

lated plane-by plane, and the corresponding temperature map is generated using the calibration curve of Figure 4b. Figure 5e presents the *z*-axis projection of the FIR as a red-hot temperature map overlaid with the nematode's autofluorescence (cyan), which delineates its morphology across the entire volume. The *C. elegans* intestine is a simple, tubular organ composed of 20 epithelial cells arranged into nine rings (int1–int9), spanning approximately 80% of the worm's body length.

The lumen, located centrally within these rings, is lined with microvilli that facilitate nutrient uptake and particle retention [57]. Figure 5b–d shows the fluorescence emission throughout the intestinal structure post-ingestion, indicating UCNP accumulation within the lumen. This localization is strongly influenced by surface chemistry. The anionic character of our DOPS-rich lipid coating likely leads to electrostatic repulsion with the negatively charged glycocalyx of the intestinal cell membranes, thereby hindering endocytosis [58]. This contrasts with cationic coatings like polyethyleneimine (PEI), which promote endocytosis and lead to UCNP internalization into intestinal cells [59]. This observation is consistent with Chen et al. [50], who reported internalization of PEI-capped UCNPs into both the gut cavity and intestinal cells. They attributed UCNP uptake within the gut cavity to the favorable nanoparticle dispersibility and cellular internalization to endocytosis, facilitated by electrostatic interactions between the cationic PEI coating and negatively charged cell surfaces. The positive charge of PEI can be enhanced at lower pH levels, such as those found in parts of the *C. elegans* digestive tract [60], potentially promoting further endocytosis. In contrast, the UCNPs@lipids nanoparticles are negatively charged (due to abundant DOPS) and were observed in the intestine but not clearly within the intestinal cells. This suggests that endocytosis of these nanoparticles is sensitive to the specific capping ligand. Consequently, we attribute the recorded temperature distributions mainly to the luminal environment rather than intracellular regions, indicating that surface chemistry governs not only nanoparticle uptake but also the spatial interpretation of the thermal maps. This distinction is crucial, as it means our thermal maps report on the temperature within the digestive tract lumen, which may be influenced by ingested material and microbial activity, rather than the metabolic heat production of the intestinal cells themselves. To probe intracellular temperatures, a surface coating engineered for active cellular uptake would be required.

Conclusion

We successfully demonstrated volumetric temperature measurements in *C. elegans* by combining LSFM with lipid-coated $NaYF_4$:Yb^{3+}/Er^{3+} upconversion nanoparticles. The lipid coating strategy proved crucial, enhancing biocompatibility and colloidal stability while enabling precise localization of the thermal probes within the nematode's digestive tract. Our calibration achieved excellent thermal sensitivity (up to 8.9×10^{-3} °C^{-1} absolute and 2.8%·°C^{-1} relative), well above the benchmark for high-performance nanothermometry.

While our experiments focused on fixed biological specimens, the 980 nm wavelength excitation and millisecond-scale slice acquisition inherent to LSFM make real-time thermometry in living organisms entirely feasible. This capability would enable monitoring metabolic or stress-induced temperature fluctuations at the single-organ level and evaluating thermal side effects of optogenetic, photothermal, or pharmacological treatments. Although our experiments used fixed *C. elegans*, the present study was conceived as a proof of concept to demonstrate the feasibility of volumetric FIR thermometry in biological systems using LSFM. In this context, PFA fixation is applied externally and primarily affects the nematode's outer tissues. Aldehyde fixatives act at the organism's surface without significantly altering the internal optical environment where the UC nanoparticles are located. Because upconversion luminescence arises from lanthanide ions shielded within the nanoparticle matrix, its emission is largely insensitive to minor dielectric or chemical variations in the surrounding medium [61]. Therefore, the overall influence of fixation on the recorded fluorescence and thermal response is negligible [62].

Extending this method to live imaging presents additional challenges related to the simultaneous acquisition of the thermally coupled emission bands. Sequential filter exchange limits the frame rate when using a single detector, whereas dual-camera configurations require precise spatial registration to avoid pixel mismatches and artifacts in the FIR calculation. To mitigate these limitations, we are currently developing an alternative approach based on color CMOS detection, which retrieves the spectral intensity from a single RGB image and eliminates the need for mechanical filter switching. This strategy, though beyond the scope of the present work, is expected to enable true real-time 3D nanothermometry in vivo. Future work will also focus on engineering UCNP coatings for specific subcellular targeting to further expand the biological applicability of this technique.

The readily transferable nature of both the lipid-coating approach and the optical setup establishes a practical foundation for extending this technique to other small model organisms, organoids, or individual mammalian cells. In summary, LSFM-enabled upconversion nanothermometry emerges as a powerful, non-invasive platform for probing spatiotemporal temperature dynamics across diverse biomedical applications, from cellular metabolism to organ-specific stress responses.

Funding

This research was partially funded by CONAHCYT (Mexico) through APY CIENCIAFROTN-2 (grant no. 317184) and FORDECyT-PRONACES (Grant No. 246648). This work received funding from LASERLAB-EUROPE (the European Union's Horizon 2020 research and innovation program under grant agreement no. 871124) and was partially funded by CEX2019-000910-S. This project was partially funded by UNAM DGAPA PAPIIT-IT101822.

Conflict of Interest

The authors declare no conflicts of interest.

Author Contributions

Dannareli Barron-Ortiz: conceptualization; data curation; formal analysis; investigation; methodology; software; validation; visualization; writing – original draft; writing – review & editing. Enric Pérez-Parets: investigation. Rubén D. Cadena-Nava: conceptualization; funding acquisition; methodology; resources; supervision; writing – review & editing. Emilio J. Gualda: methodology; software. Jacob Licea-Rodríguez: investigation; writing – review & editing. Juan Hernández-Cordero: funding acquisition; methodology; resources; writing – review & editing. Pablo Loza-Álvarez: funding acquisition; methodology; project administration; resources; writing – review & editing. Israel Rocha-Mendoza: conceptualization; data curation; formal analysis; funding acquisition; investigation; methodology; project administration; resources; software; supervision; validation; visualization; writing – original draft; writing – review & editing.

ORCID® iDs

Dannareli Barron-Ortiz - https://orcid.org/0009-0007-1711-4732
Enric Pérez-Parets - https://orcid.org/0000-0002-6384-2593
Rubén D. Cadena-Nava - https://orcid.org/0000-0001-8428-6701
Emilio J. Gualda - https://orcid.org/0000-0001-5948-5493
Jacob Licea-Rodríguez - https://orcid.org/0000-0001-8500-3929
Juan Hernández-Cordero - https://orcid.org/0000-0003-3459-2158
Pablo Loza-Álvarez - https://orcid.org/0000-0002-3129-1213
Israel Rocha-Mendoza - https://orcid.org/0000-0002-2693-6304

Data Availability Statement

Data generated and analyzed during this study is available from the corresponding author upon reasonable request.

References

1. Blasi, D.; Gonzalez-Pato, N.; Rodriguez Rodriguez, X.; Diez-Zabala, I.; Srinivasan, S. Y.; Camarero, N.; Esquivias, O.; Roldán, M.; Guasch, J.; Laromaine, A.; Gorostiza, P.; Veciana, J.; Ratera, I. *Small* **2023,** *19,* 2207806. doi:10.1002/smll.202207806
2. Quintanilla, M.; Henriksen-Lacey, M.; Renero-Lecuna, C.; Liz-Marzán, L. M. *Chem. Soc. Rev.* **2022,** *51,* 4223–4242. doi:10.1039/d2cs00069e
3. Warburg, O.; Wind, F.; Negelein, E. *J. Gen. Physiol.* **1927,** *8,* 519–530. doi:10.1085/jgp.8.6.519
4. Vaupel, P.; Kallinowski, F.; Okunieff, P. *Cancer Res.* **1989,** *49,* 6449–6465.
5. Verduzco-Mendoza, A.; Olmos-Hernández, A.; Bueno-Nava, A.; Villanueva-García, D.; Domínguez-Oliva, A.; Avila-Luna, A.; Mora-Medina, P.; Gálvez-Rosas, A.; Hernández-Ávalos, I.; Casas-Alvarado, A.; Garnica, M. A.; Mota-Rojas, D. *Front. Vet. Sci.* **2025,** *12,* 1544112. doi:10.3389/fvets.2025.1544112
6. Knapp, J. P.; Kakish, J. E.; Bridle, B. W.; Speicher, D. J. *Biomedicines* **2022,** *10,* 2024. doi:10.3390/biomedicines10082024
7. Kucsko, G.; Maurer, P. C.; Yao, N. Y.; Kubo, M.; Noh, H. J.; Lo, P. K.; Park, H.; Lukin, M. D. *Nature* **2013,** *500,* 54–58. doi:10.1038/nature12373
8. Okabe, K.; Inada, N.; Gota, C.; Harada, Y.; Funatsu, T.; Uchiyama, S. *Nat. Commun.* **2012,** *3,* 705. doi:10.1038/ncomms1714
9. Lu, F.; Wang, X.; Ge, Y.; Sun, X.; Zhao, T.; Lu, X.; Fan, Q. *Ceram. Int.* **2024,** *50,* 25060–25067. doi:10.1016/j.ceramint.2024.04.233
10. Ye, Z.; Harrington, B.; Pickel, A. D. *Sci. Adv.* **2024,** *10,* eado6268. doi:10.1126/sciadv.ado6268
11. del Rosal, B.; Ruiz, D.; Chaves-Coira, I.; Juárez, B. H.; Monge, L.; Hong, G.; Fernández, N.; Jaque, D. *Adv. Funct. Mater.* **2018,** *28,* 1806088. doi:10.1002/adfm.201806088
12. González-Martínez, F.; González-Cortez, O.; Pimentel-Domínguez, R.; Hernández-Cordero, J.; Aguilar, G. *Opt. Mater. Express* **2018,** *8,* 3072–3081. doi:10.1364/ome.8.003072
13. Shen, Y.; Lifante, J.; Fernández, N.; Jaque, D.; Ximendes, E. *ACS Nano* **2020,** *14,* 4122–4133. doi:10.1021/acsnano.9b08824
14. Shen, Y.; Lifante, J.; Zabala-Gutierrez, I.; de la Fuente-Fernández, M.; Granado, M.; Fernández, N.; Rubio-Retama, J.; Jaque, D.; Marin, R.; Ximendes, E.; Benayas, A. *Adv. Mater. (Weinheim, Ger.)* **2022,** *34,* 2107764. doi:10.1002/adma.202107764
15. Chihara, T.; Umezawa, M.; Miyata, K.; Sekiyama, S.; Hosokawa, N.; Okubo, K.; Kamimura, M.; Soga, K. *Sci. Rep.* **2019,** *9,* 12806. doi:10.1038/s41598-019-49291-x
16. Sekulić, M.; Ristić, Z.; Milićević, B.; Antić, Ž.; Đorđević, V.; Dramićanin, M. D. *Opt. Commun.* **2019,** *452,* 342–346. doi:10.1016/j.optcom.2019.07.056
17. Yang, J.; Li, B. Q.; Li, R.; Mei, X. *Nanoscale* **2019,** *11,* 2249–2263. doi:10.1039/c8nr09096c
18. Suta, M.; Antić, Ž.; Đorđević, V.; Kuzman, S.; Dramićanin, M. D.; Meijerink, A. *Nanomaterials* **2020,** *10,* 543. doi:10.3390/nano10030543
19. Salerno, E. V.; Zeler, J.; Eliseeva, S. V.; Hernández-Rodríguez, M. A.; Carneiro Neto, A. N.; Petoud, S.; Pecoraro, V. L.; Carlos, L. D. *Chem. – Eur. J.* **2020,** *26,* 13792–13796. doi:10.1002/chem.202003239
20. Piñol, R.; Zeler, J.; Brites, C. D. S.; Gu, Y.; Téllez, P.; Carneiro Neto, A. N.; da Silva, T. E.; Moreno-Loshuertos, R.; Fernandez-Silva, P.; Gallego, A. I.; Martinez-Lostao, L.; Martínez, A.; Carlos, L. D.; Millán, A. *Nano Lett.* **2020,** *20,* 6466–6472. doi:10.1021/acs.nanolett.0c02163
21. Kaczmarek, A. M.; Suta, M.; Rijckaert, H.; Abalymov, A.; Van Driessche, I.; Skirtach, A. G.; Meijerink, A.; Van Der Voort, P. *Adv. Funct. Mater.* **2020,** *30,* 2003101. doi:10.1002/adfm.202003101
22. Ćirić, A.; Aleksić, J.; Barudžija, T.; Antić, Ž.; Đorđević, V.; Medić, M.; Periša, J.; Zeković, I.; Mitrić, M.; Dramićanin, M. D. *Nanomaterials* **2020,** *10,* 627. doi:10.3390/nano10040627

23. Bastos, A. R. N.; Brites, C. D. S.; Rojas-Gutierrez, P. A.; DeWolf, C.; Ferreira, R. A. S.; Capobianco, J. A.; Carlos, L. D. *Adv. Funct. Mater.* **2019,** *29,* 1905474. doi:10.1002/adfm.201905474
24. van Swieten, T. P.; van Omme, T.; van den Heuvel, D. J.; Vonk, S. J. W.; Spruit, R. G.; Meirer, F.; Garza, H. H. P.; Weckhuysen, B. M.; Meijerink, A.; Rabouw, F. T.; Geitenbeek, R. G. *ACS Appl. Nano Mater.* **2021,** *4,* 4208–4215. doi:10.1021/acsanm.1c00657
25. Sedmak, I.; Podlipec, R.; Urbančič, I.; Štrancar, J.; Mortier, M.; Golobič, I. *Sensors* **2022,** *22,* 1970. doi:10.3390/s22051970
26. Dong, B.; Cao, B.; He, Y.; Liu, Z.; Li, Z.; Feng, Z. *Adv. Mater. (Weinheim, Ger.)* **2012,** *24,* 1987–1993. doi:10.1002/adma.201200431
27. Carrasco, E.; del Rosal, B.; Sanz-Rodríguez, F.; de la Fuente, Á. J.; Gonzalez, P. H.; Rocha, U.; Kumar, K. U.; Jacinto, C.; Solé, J. G.; Jaque, D. *Adv. Funct. Mater.* **2015,** *25,* 615–626. doi:10.1002/adfm.201403653
28. Tanimoto, R.; Hiraiwa, T.; Nakai, Y.; Shindo, Y.; Oka, K.; Hiroi, N.; Funahashi, A. *Sci. Rep.* **2016,** *6,* 22071. doi:10.1038/srep22071
29. Geitenbeek, R. G.; Prins, P. T.; Albrecht, W.; van Blaaderen, A.; Weckhuysen, B. M.; Meijerink, A. *J. Phys. Chem. C* **2017,** *121,* 3503–3510. doi:10.1021/acs.jpcc.6b10279
30. Baffou, G.; Kreuzer, M. P.; Kulzer, F.; Quidant, R. *Opt. Express* **2009,** *17,* 3291–3298. doi:10.1364/oe.17.003291
31. Badon, A.; Marceau, J.-B.; Allard, C.; Fossard, F.; Loiseau, A.; Cognet, L.; Flahaut, E.; Recher, G.; Izard, N.; Martel, R.; Gaufrès, E. *Mater. Horiz.* **2023,** *10,* 983–992. doi:10.1039/d2mh01239a
32. Fujiwara, M.; Sun, S.; Dohms, A.; Nishimura, Y.; Suto, K.; Takezawa, Y.; Oshimi, K.; Zhao, L.; Sadzak, N.; Umehara, Y.; Teki, Y.; Komatsu, N.; Benson, O.; Shikano, Y.; Kage-Nakadai, E. *Sci. Adv.* **2020,** *6,* eaba9636. doi:10.1126/sciadv.aba9636
33. Mateos, S.; Lifante, J.; Li, C.; Ximendes, E. C.; Muñoz-Ortiz, T.; Yao, J.; de la Fuente-Fernández, M.; García Villalón, Á. L.; Granado, M.; Zabala Gutierrez, I.; Rubio-Retama, J.; Jaque, D.; Ortgies, D. H.; Fernández, N. *Small* **2020,** *16,* 1907171. doi:10.1002/smll.201907171
34. Inada, N.; Fukuda, N.; Hayashi, T.; Uchiyama, S. *Nat. Protoc.* **2019,** *14,* 1293–1321. doi:10.1038/s41596-019-0145-7
35. Suresh, K.; Monisha, K.; Bankapur, A.; Rao, S. K.; Mutalik, S.; George, S. D. *Anal. Chim. Acta* **2023,** *1273,* 341530. doi:10.1016/j.aca.2023.341530
36. Vetrone, F.; Naccache, R.; Zamarrón, A.; Juarranz de la Fuente, A.; Sanz-Rodríguez, F.; Martinez Maestro, L.; Martín Rodriguez, E.; Jaque, D.; García Solé, J.; Capobianco, J. A. *ACS Nano* **2010,** *4,* 3254–3258. doi:10.1021/nn100244a
37. Wang, P.; Cheng, S.; Xu, Y.; Nie, G.; Zhan, S.; Liu, Y. *Mater. Res. Bull.* **2023,** *162,* 112190. doi:10.1016/j.materresbull.2023.112190
38. Mackenzie, L. E.; Goode, J. A.; Vakurov, A.; Nampi, P. P.; Saha, S.; Jose, G.; Millner, P. A. *Sci. Rep.* **2018,** *8,* 1106. doi:10.1038/s41598-018-19415-w
39. Wang, F.; Liu, X. *J. Am. Chem. Soc.* **2008,** *130,* 5642–5643. doi:10.1021/ja800868a
40. Barron-Ortiz, D.; Cadena-Nava, R. D.; Pérez-Parets, E.; Licea-Rodriguez, J.; Gualda, E. J.; Hernandez-Cordero, J.; Loza-Alvarez, P.; Rocha-Mendoza, I. *Micromachines* **2023,** *14,* 2097. doi:10.3390/mi14112097
41. Wu, K.; Cui, J.; Kong, X.; Wang, Y. *J. Appl. Phys.* **2011,** *110,* 053510. doi:10.1063/1.3631822
42. Ćirić, A.; Gavrilović, T.; Dramićanin, M. D. *Crystals* **2021,** *11,* 189. doi:10.3390/cryst11020189
43. Cui, Y.; Meng, Q.; Lü, S.; Sun, W. *ChemistrySelect* **2019,** *4,* 4316–4323. doi:10.1002/slct.201900719
44. Sánchez-Escobar, S.; Hernández-Cordero, J. *Opt. Lett.* **2019,** *44,* 1194–1197. doi:10.1364/ol.44.001194
45. Di, X.; Wang, D.; Zhou, J.; Zhang, L.; Stenzel, M. H.; Su, Q. P.; Jin, D. *Nano Lett.* **2021,** *21,* 1651–1658. doi:10.1021/acs.nanolett.0c04281
46. Liu, M.; Sun, Y.; Teh, D. B. L.; Zhang, Y.; Cao, D.; Mei, Q. *Interdiscip. Med.* **2024,** *2,* e20230059. doi:10.1002/inmd.20230059
47. Ming, L.; Romelli, A.; Lifante, J.; Canton, P.; Lifante-Pedrola, G.; Jaque, D.; Ximendes, E.; Marin, R. *Nat. Commun.* **2025,** *16,* 6429. doi:10.1038/s41467-025-59681-7
48. Đačanin Far, L.; Dramićanin, M. *Nanomaterials* **2023,** *13,* 2904. doi:10.3390/nano13212904
49. Chen, R.; Shi, B.; Song, K.; LOK, M. M.-Z. G. C.; Jiang, M.; An, S.; Tao, P.; Fu, B.; Song, C.; Wang, J.; Deng, T.; Shang, W. *Adv. Mater. (Weinheim, Ger.)* **2025,** *37,* e15604. doi:10.1002/adma.202415604
50. Chen, J.; Guo, C.; Wang, M.; Huang, L.; Wang, L.; Mi, C.; Li, J.; Fang, X.; Mao, C.; Xu, S. *J. Mater. Chem.* **2011,** *21,* 2632–2638. doi:10.1039/c0jm02854a
51. Lim, S. F.; Riehn, R.; Ryu, W. S.; Khanarian, N.; Tung, C.-k.; Tank, D.; Austin, R. H. *Nano Lett.* **2006,** *6,* 169–174. doi:10.1021/nl0519175
52. Rojas-Gutierrez, P. A.; DeWolf, C.; Capobianco, J. A. *Part. Part. Syst. Charact.* **2016,** *33,* 865–870. doi:10.1002/ppsc.201600218
53. Link, C. D.; Cypser, J. R.; Johnson, C. J.; Johnson, T. E. *Cell Stress Chaperones* **1999,** *4,* 235–242.
54. Ezerskyte, E.; Morkvenas, A.; Venius, J.; Sakirzanovas, S.; Karabanovas, V.; Katelnikovas, A.; Klimkevicius, V. *ACS Appl. Nano Mater.* **2024,** *7,* 6185–6195. doi:10.1021/acsanm.3c06111
55. Brites, C. D. S.; Lima, P. P.; Silva, N. J. O.; Millán, A.; Amaral, V. S.; Palacio, F.; Carlos, L. D. *Nanoscale* **2012,** *4,* 4799–4829. doi:10.1039/c2nr30663h
56. Gonzalez-Moragas, L.; Roig, A.; Laromaine, A. *Adv. Colloid Interface Sci.* **2015,** *219,* 10–26. doi:10.1016/j.cis.2015.02.001
57. Dimov, I.; Maduro, M. F. *Cell Tissue Res.* **2019,** *377,* 383–396. doi:10.1007/s00441-019-03036-4
58. Imbert, P. R. C.; Saric, A.; Pedram, K.; Bertozzi, C. R.; Grinstein, S.; Freeman, S. A. *Curr. Biol.* **2021,** *31,* 77–89.e5. doi:10.1016/j.cub.2020.09.082
59. Casper, J.; Schenk, S. H.; Parhizkar, E.; Detampel, P.; Dehshahri, A.; Huwyler, J. *J. Controlled Release* **2023,** *362,* 667–691. doi:10.1016/j.jconrel.2023.09.001
60. Lay, A.; Sheppard, O. H.; Siefe, C.; McLellan, C. A.; Mehlenbacher, R. D.; Fischer, S.; Goodman, M. B.; Dionne, J. A. *ACS Cent. Sci.* **2019,** *5,* 1211–1222. doi:10.1021/acscentsci.9b00300
61. D'Este, E.; Lukinavičius, G.; Lincoln, R.; Opazo, F.; Fornasiero, E. F. *Trends Cell Biol.* **2024,** *34,* 671–684. doi:10.1016/j.tcb.2023.12.001
62. Ichikawa, T.; Wang, D.; Miyazawa, K.; Miyata, K.; Oshima, M.; Fukuma, T. *Commun. Biol.* **2022,** *5,* 487. doi:10.1038/s42003-022-03437-2

BEILSTEIN JOURNAL OF NANOTECHNOLOGY

Multilayered hyperbolic Au/TiO_2 nanostructures for enhancing the nonlinear response around the epsilon-near-zero point

Fernando Arturo Araiza-Sixtos[1], Mauricio Gomez-Robles[2,3], Rafael Salas-Montiel[2,3] and Raúl Rangel-Rojo[*1]

Full Research Paper

Open Access

Address:
[1]Department of Optics, Applied Physics Division, Centro de Investigación Científica y de Educación Superior de Ensenada, B.C., México, [2]Laboratoire Lumière, nanomatériaux, nanotechnologies - L2n CNRS UMR 7076, Université de Technologie de Troyes, 10004 Troyes, France and [3]EUT+ Institute of Nanomaterials and Nanotechnologies-EUTINN, European University of Technology, European Union

Email:
Raúl Rangel-Rojo[*] - rrangel@cicese.mx

* Corresponding author

Keywords:
epsilon-near-zero (ENZ); hyperbolic metamaterials; nonlinear optics (NLO)

Beilstein J. Nanotechnol. **2026,** *17,* 251–261.
https://doi.org/10.3762/bjnano.17.17

Received: 27 October 2025
Accepted: 22 January 2026
Published: 05 February 2026

This article is part of the thematic issue "Symposium of Nanoscience and Nanomaterials 2024 (SNN 2024)".

Associate Editor: A. J. Meixner

Abstract

In this work, we present the design, fabrication, and study of the optical properties of multilayered metal–dielectric Au/TiO_2 structures. The samples were fabricated using Joule effect evaporation for gold and electron beam evaporation for titanium dioxide. Their structure was designed to have an epsilon-near-zero (ENZ) point at different wavelengths around 800 nm, in order to study their nonlinear response as a function of the resonance conditions around the ENZ point. The characterization of the linear properties of the samples was done using spectrophotometry and spectral ellipsometry. We studied the nonlinear response with the z-scan technique at different incident irradiances using a Ti:sapphire femtosecond laser, enabling us to characterize both the refractive and absorptive contributions to the nonlinear response. Due to the high pulse repetition rate inherent to Ti:sapphire systems and the presence of linear absorption in the samples, cumulative pulse-to-pulse thermal effects may be present. A modified version of the z-scan technique that allowed us to separate the electronic from the thermal contribution was used. A clear enhancement of the nonlinear response was observed for the sample with an ENZ point around the laser wavelength 800 nm with a nonlinear refractive index of $n_2 = 0.103 \pm 0.006$ cm^2·GW^{-1}, a value that is comparable to other ENZ materials in literature.

Introduction

In recent years, the invention of new techniques to fabricate nanostructured materials led to the creation of metamaterials. These new materials combine known materials in arrays whose geometries are easy to manipulate in order to have properties that are different from those of the constituting materials. The principal characteristic of metamaterials is that the internal

structures of the constituents are much smaller than the wavelength of light. As a consequence, light does not differentiate between the constituting materials and only "sees" them as a single material. To study the interaction of light with these metamaterials, we use the effective media approximation to calculate the optical properties of these materials. These properties are completely different than those of the constituting materials and are not simply an average of them [1].

A type of metamaterials that we are particularly interested in are hyperbolic metamaterials (HMMs), whose dispersion relation generates an hyperboloid in the k-space. There are some readily available materials in nature that present hyperbolic dispersion, such as bismuth and 2D graphene sheets [2], indium tin oxide (ITO) [3], and aluminum-doped zinc oxide (AZO) [4]. HMMs are highly anisotropic and exhibit some interesting properties, including strong enhancement of spontaneous emission, negative refractive index, and near-zero permittivity. The main benefit of HMMs is that, with the correct manipulation of the design, we are able to choose the wavelength in which we would like these phenomena to appear. Hyperbolic dispersion can be achieved by combining a dielectric, which has a permittivity that is always positive, and a metal, which has a negative real part of the permittivity below the plasma frequency. The properties of the new material depend on the constituting materials and the geometry of the design.

The property of this type of materials we are interested in for this work is that, with the right manipulation of the geometry, we are able to make the electric permittivity near zero ("epsilon near zero", ENZ). The ENZ point causes light to travel through the medium with constant phase, it enhances the electric field, and it enhances the nonlinear response by combining coherently the response generated at different planes within the medium without the need of phase matching [5]. Ideally, we would like these materials not to have linear absorption, which prevents the full exploitation of these properties. The presence of linear absorption means that $\Im\{\varepsilon\} \neq 0$, which precludes the magnitude of the permittivity to become completely zero, hence the term "epsilon near zero". Also, we are able to make $\Re\{\varepsilon\}$ arbitrarily close to zero; as a consequence, we have a refractive index n_0 that is near zero. This near-zero refractive index allows us to enhance the nonlinear refractive index because $n_2 \propto 1/{n_0}^2$.

Various structures exhibiting hyperbolic dispersion have been fabricated and analyzed. The first experimental realization of a layered hyperbolic material took the form of a hyperlens [6]. In 2012, a significant advancement was made by Subramania et al., who fabricated layered Ag/TiO_2 and determined via spectroscopy that its ENZ point laid within the visible spectrum [7]. Since then, a wide array of layered metal–dielectric configurations have been demonstrated, including silver-based combinations such as Ag/SiO_2 [1], Ag/Al_2O_3 [6], Ag/LiF [8], Ag/TiO_2 [9], Ag/Ge [10], Ag/MgF_2 [11], and Ag/Ti_3O_5 [12]. Gold-based systems have also been prominent, such as Au/Al_2O_3 [13-15], Au/SiO_2 [16], Au/TiO_2 [17], and optical filters based on Au/TiO_2 multilayers [18]. Beyond classic metal–dielectric structures, research has explored ZnO/Al:ZnO [19] and doped semiconductors [20]. Work has also expanded into complex geometries, such as hybrid metal–dielectric layered pyramids [10], AZO nanotrenches for molecular absorption sensing [4], and the first nanowire array exhibiting hyperbolic properties with negative refraction at 780 nm [21].

Previously, our group has studied the nonlinear response of a Ru/TiO_2 multilayered structure as reported in [22]. This sample was designed to have an ENZ point at 800 nm and was fabricated using atomic layer deposition. During the linear characterization of the optical properties, spectral ellipsometry showed that the ENZ point actually was not at 800 nm, but rather at 600 nm. We tried to find the reason of this shift with our available resources. Transmission electron microscopy showed that there was no significant change in the geometry, which could have resulted in the ENZ shift. We could not study the composition of the structure so we could only assume that, during the fabrication process, the deposited Ru was oxidized, and the permittivity of the material substantially changed. We studied the nonlinear response of the structure using a tunable femtosecond source and found that, even with the shift in the ENZ point seen with ellipsometry, there was a clear enhancement at 800 nm. Unfortunately, due to time constraints, we could not study the nonlinear response at higher wavelengths; thus, we could not corroborate if this was a local maximum or a value found in the tail of the local maximum at a higher wavelength.

Considering our previous findings, in this work, we decided to change the fabrication methods and the metal used to avoid possible contamination due to oxidation. We chose to use gold instead of ruthenium because it is easier to deposit and has the correct permittivity to create a HMM. Gold also has a low oxidation rate, allowing us to avoid any changes in permittivity due to oxidation during the fabrication process. We kept using titanium dioxide because, during the simulation stage, we found that its permittivity allowed us to keep the overall sample thickness low. Also, during the fabrication process, we found that we could avoid problems like lack of adherence between the layers. We also decided that, instead of relying on a tunable femtosecond source, we would manipulate the material geometry to design different samples with an ENZ point at different wavelength values around 800 nm, that is, we will tune the material to the laser wavelength rather than the other way around.

We make a characterization of the linear optical properties of the samples and present a study of the nonlinear optical properties. For the linear characterization of the samples, we study the absorption using spectrophotometry and the complex effective permittivity using spectroscopic ellipsometry. Using a Ti:sapphire femtosecond pulsed laser, we study the third-order nonlinear response of the samples employing the z-scan technique [23].

Even though the use of femtosecond pulses allows us to avoid any thermal load to the sample due to absorption, the high repetition rate intrinsic to the Ti:sapphire oscillators leads to the possible accumulation of pulse-to-pulse thermal load. This thermal effect needs to be quantified. In order to do so, we modified the z-scan technique, adding a variable frequency chopper to limit the number of pulses incident on the sample without modifying the incident peak irradiance. The thermal load to the sample is reduced with the increase of the chopper's frequency while the electronic contribution to the third order nonlinear response is still excited. In this way, we can resolve the electronic and thermal contributions to the response as explained in [24]. We present results that enabled us to determine the thermal nonlinear response due to intrapulse heating.

Design and Fabrication of Nanostructured Metal–Dielectric HMM

For a multilayer system with layer widths of 10–100 nm, we can employ the effective medium approximation (EMA) to calculate the properties of the whole system. It is important to note that the layers must follow a metal–dielectric repetition sequence. For a metal and a dielectric with permittivities ε_m and ε_d, respectively, it is possible to obtain a relation for the principal components $\varepsilon_{\perp}^{\text{eff}}$ and $\varepsilon_{\parallel}^{\text{eff}}$ of the composite, which are given by [25]:

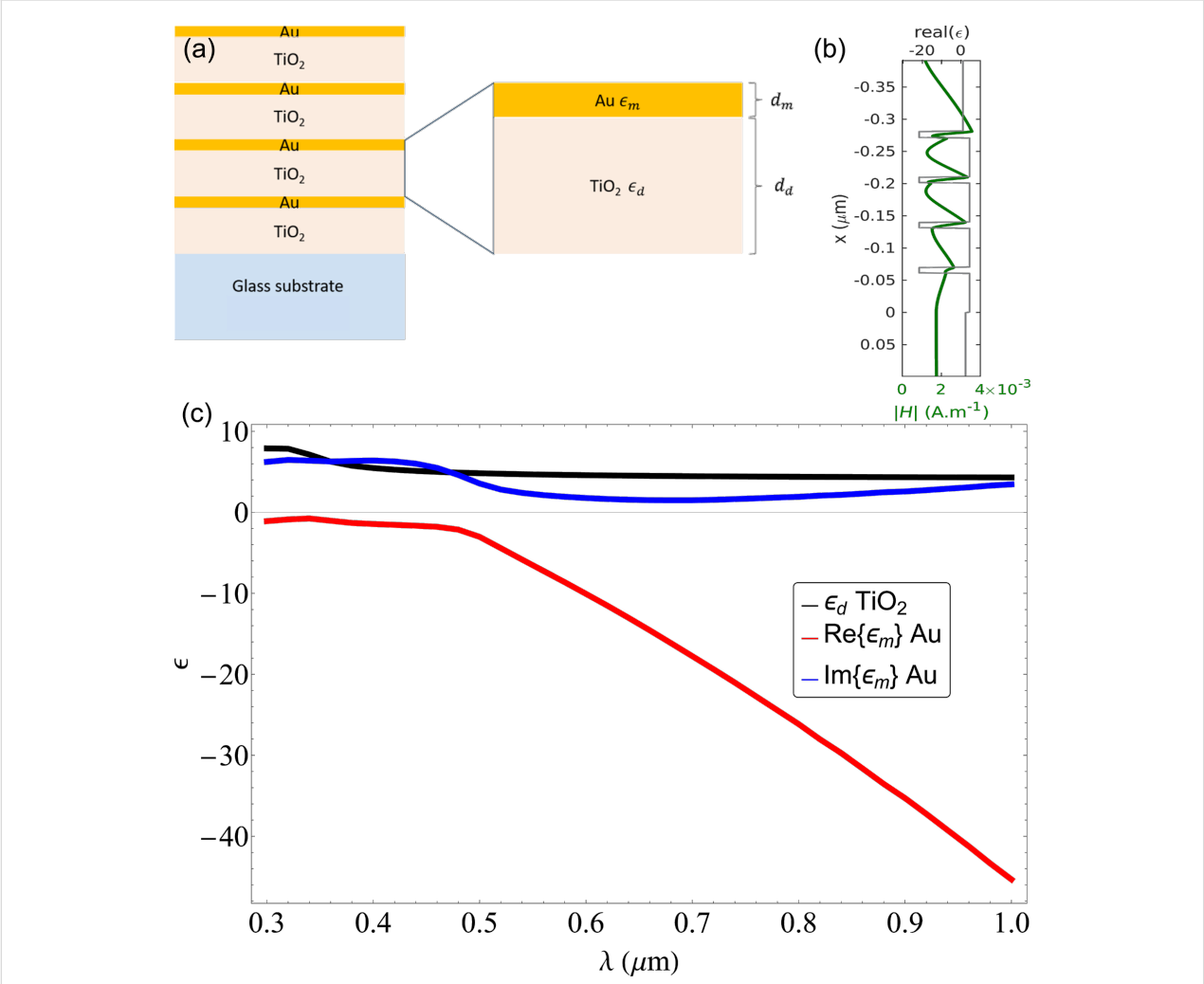

Figure 1: (a) Bilayer structure design. The metal and dielectric layers are characterized, respectively, by their permittivity ε_m and ε_d and their widths d_m and d_d. (b) Spatial distribution of the electric field inside the multilayer. (c) Permittivity of gold and titanium dioxide reported in literature [26,27].

$$\varepsilon_{\parallel}^{\text{eff}} = \frac{d_{\text{m}}\varepsilon_{m} + d_{\text{d}}\varepsilon_{\text{d}}}{d_{\text{m}} + d_{\text{d}}} \quad \text{and} \quad \frac{1}{\varepsilon_{\perp}^{\text{eff}}} = \frac{d_{\text{m}} / \varepsilon_{\text{m}} + d_{\text{d}} / \varepsilon_{\text{d}}}{d_{\text{m}} + d_{\text{d}}}, \quad (1)$$

where d_{m} and d_{d} are the widths of the metallic and dielectric layers, respectively, as seen in Figure 1a.

The z-scan technique employed to study the nonlinear properties of the samples involves normal incident light, where the only relevant component is $\varepsilon_{\parallel}^{\text{eff}}$; hence, we only calculate this component. We wish to produce samples with four metal–dielectric periods that have different ENZ wavelength values (λ = 740, 760, 780, 800, 820, 840, and 860 nm) to test the effect of the resonance conditions with the laser wavelength on the nonlinear effects. We also produced a set of single layers to study the properties of the constituting materials being deposited.

In order to calculate the point for which $\varepsilon_{\parallel}^{\text{eff}} = 0$, we use the permittivities of gold ε_{m} and titanium dioxide ε_{d} from [26,27], shown in Figure 1c. This leaves the layer thicknesses d_{m} and d_{d} as the only parameters to design the structures. In order to minimize losses due to absorption, we chose a fixed width as small as possible of the metallic layer d_{m}; then, we solve for $\varepsilon_{\parallel}^{\text{eff}} = 0$ to obtain the width of the dielectric layer d_{d}, which will give the ENZ at the desired wavelength. It has been found that layers of gold with a thickness below 10 nm would lead to an inhomogeneous layer with separated gold "islands" throughout the surface rather than a continuous layer [28]. Because of this, we chose to use a gold layer thickness of 10 nm, the limit to have uniform layers found in literature. We choose four metal–dielectric periods to also reduce absorption due to the gold and because it has been shown that using more than five periods produces no appreciable improvement in the nonlinear optical response [29].

In Table 1, we can see the thickness for the dielectric layers needed to yield an ENZ point at the desired wavelengths, calculated solving for $\varepsilon_{\parallel}^{\text{eff}} = 0$. We then simulate the permittivity of the stack as a whole. In Figure 2a, we present the real part of the perpendicular component of the effective permittivity; we can see the shift in the ENZ point for every multilayer due to the varying thickness of the dielectric layer. In Figure 2b, we present the imaginary part of the perpendicular component and see that $\Im\{\varepsilon\}$, which is related to absorption, has a small value around 800 nm; hence, we can expect to have minimum losses in the designed materials.

Table 1: Thicknesses of metallic and dielectric layers and their correspondent ENZ wavelengths.

Sample	Nominal			Experimental		
	λ_{ENZ} (nm)	d_{m} (nm)	d_{d} (nm)	λ_{ENZ} (nm)	d_{m} (nm)	d_{d} (nm)
ML740	740	10	48	730	13	52
ML760	760	10	52	789	11	57
ML780	780	10	56	780	12	58
ML800	800	10	60	803	12	62
ML820	820	10	64	842	12	69
ML840	840	10	68	862	11	69
ML860	860	10	72	892	11	77

Methods

The third-order nonlinear optical properties of the material were explored first using the z-scan technique [23] with femtosecond pulses at 800 nm from a Ti:sapphire oscillator. The laser em-

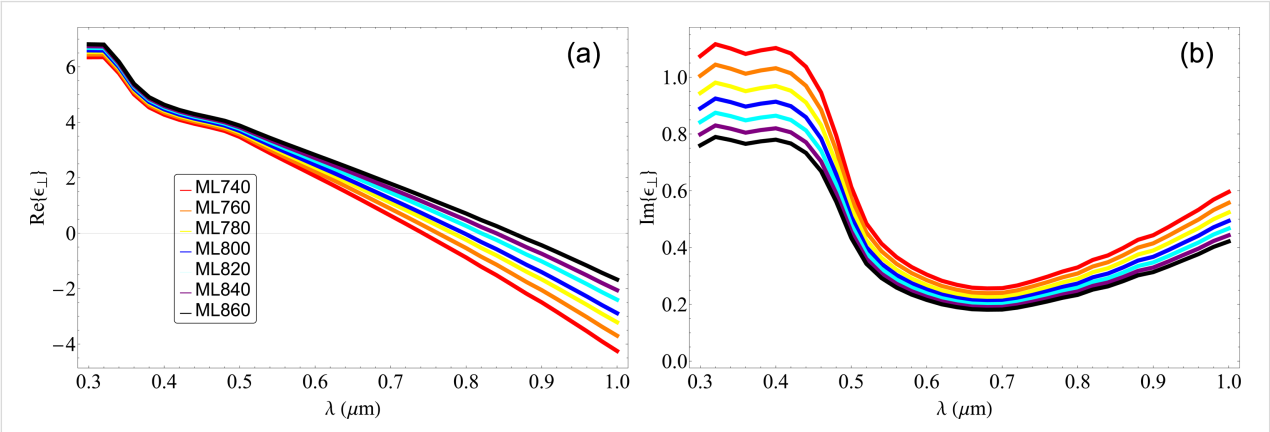

Figure 2: (a) Simulated real part of the perpendicular component of the permittivity of the Au/TiO_2 multilayered material having a fixed width of the metallic layer d_{m} = 10 nm with varying thickness of the dielectric layer. (b) Simulated imaginary part of the perpendicular component of the permittivity of the Au/TiO_2 multilayered material.

ployed in our studies is a Coherent Mira-900 mode-locked Ti:sapphire oscillator, which produces 100 fs pulses with a 76 MHz repetition rate. It has a spectral width of $\Delta\lambda$ = 10 nm centered around 800 nm with very little to no tuning capability. For the z-scan technique, a 200 mm focal length lens was used to focus the beam on the sample. The waist of the beam at the focal plane was ω_0 = 28 μm. Using an aperture before the detector, we are able to study both the nonlinear absorption when the aperture is fully open (open aperture, OA), and the nonlinear refraction when the aperture is partially open (closed aperture, CA).

To study the possible thermal contribution to the nonlinear response due to pulse-to-pulse temperature accumulation, we used a modified version of the z-scan technique, previously reported in [30]. This modification consists in the addition of a chopper with a duty cycle of 1:8, which will limit the incident pulses to the sample as a function of its frequency. The addition of this chopper will allow us to reduce the thermal load to the sample due to intrapulse heating whilst keeping the peak irradiance constant to still be able to excite the electronic contribution of the nonlinear response. In this way, the thermal effect will change with the chopper frequency, while the electronic contribution, function only of the input irradiance, will remain constant.

We fabricated the ENZ materials at the nano'mat platform, University of Technology at Troyes, France. Using a Plassys MEB400 evaporator, we deposited TiO_2 and Au layers on glass substrates without breaking vacuum. TiO_2 layers were evaporated via electron beam and Au layers via Joule effect deposition, both at a deposition rate of 0.15 nm·s^{-1} and a base pressure of 2 μTorr. The target thickness for Au was 10 nm, while that of TiO_2 was varied from 44 to 72 nm to achieve ENZ properties at or around the working wavelength of 800 nm. Every structure consisted of four metal–dielectric periods, leaving us with a total of eight layers.

We verified the total thickness of the multilayer stack using a Bruker Dektak XT profilometer. We used a Hach DR6000 UV–vis spectrophotometer to measure the linear absorption of each sample over the range from 300 to 1000 nm. Optical constants of Au and TiO_2 layers were measured via variable-angle spectroscopic ellipsometry (J.A. Woollam M-2000) over a wavelength range from 350 to 1650 nm and over an angular range from 45° to 70° in 5° steps. Even though we studied the effective permittivity in a wider range, we are only interested in the visible region because it is the region in which we are able to study the nonlinear response. Data analysis and multilayer modeling were performed using CompleteEASE software by J.A. Woollam. The optical constants were fitted using a B-splines layer with a Au thin film with KK oscillator as a starting material for Au, and with TiO_2 with Cody–Lorentz oscillators as starting material for TiO_2.

Scanning electron microscopy (Hitachi SU8030) was used to obtain the cross-sectional image (below in Figure 4a), with the sample oriented to expose the ENZ material edge to the electron beam.

Results and Discussion

Linear characterization

The linear absorption of the sample was studied using spectrophotometry to measure the transmittance of our samples (Figure 3a). We see that the structures have an absorption edge present in the UV region, which probably has a strong contribution from the glass substrate, then a dip in the visible region, and finally an increase towards the IR region. We can observe a relatively high absorbance around 800 nm with transmittances down to 40%, which could lead to losses and undesired thermal effects.

The complex permittivity of single layers of the constituting materials was studied by variable angular spectroscopic ellipsometry. Figure 3c shows the measured permittivity of the titanium dioxide compared to the values from literature. We observe that the values are very similar, indicating that the deposited film is almost the same as the one used for the initial simulations. Figure 3d shows the measured permittivity of the thin gold layer compared to the values of $\Re\{\varepsilon\}$ and $\Im\{\varepsilon\}$ from literature; they are very similar, indicating that the gold layers have a good morphology with no voids. Also using ellipsometry, we were able to measure the thicknesses of the deposited layers. In Table 1, we can see that we have widths for every stack that are different from the ones proposed for the simulated ENZ points. This change in thickness was also seen in scanning electron microscopy (SEM). In Figure 4a we present a SEM image of the ML800 structure; we see that the layers deposited have different thicknesses throughout the structure. Adding the change in permittivity of the deposited gold and titanium dioxide layers, together with the changes layer thickness, we repeated the simulations to see where the ENZ points will be.

With the measured permittivities and layer thicknesses, we simulated the transmittance of the multilayer structures using EMUstack. Figure 3b shows a comparison of the measured spectrum with the simulated spectrum for the samples ML740 (purple), ML800 (cyan), and ML860 (orange). We observe a good agreement with the experimental data with some differences in the positions and values of the different maxima ob-

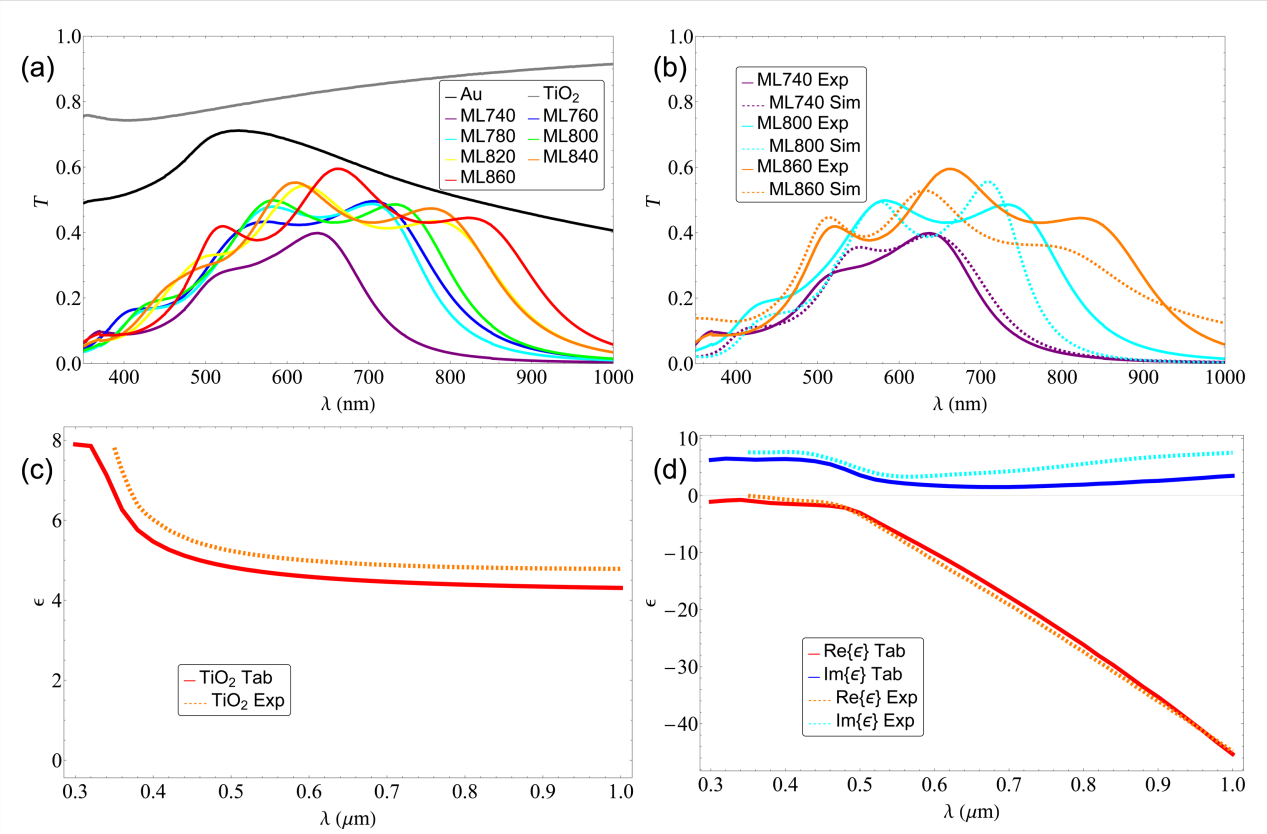

Figure 3: (a) Transmittance of the stacks with fixed gold layer d_m = 10 nm measured using spectrophotometry. We can observe a relatively high absorbance around 800 nm with transmittances down to 40%. (b) Comparison of the measured spectrum against the simulated spectrum for the samples ML740 (purple), ML800 (cyan), and ML860 (orange). (c) Permittivity of a single d_d = 60 nm titanium dioxide layer measured using spectral ellipsometry compared to the one reported in literature. We observe that the resulting permittivity is almost similar to the one used for the simulations. (d) Permittivity of a single d_m = 10 nm gold layer measured using spectral ellipsometry compared to the one reported in literature. We observe that the resulting permittivity is almost similar to the one used for the simulations.

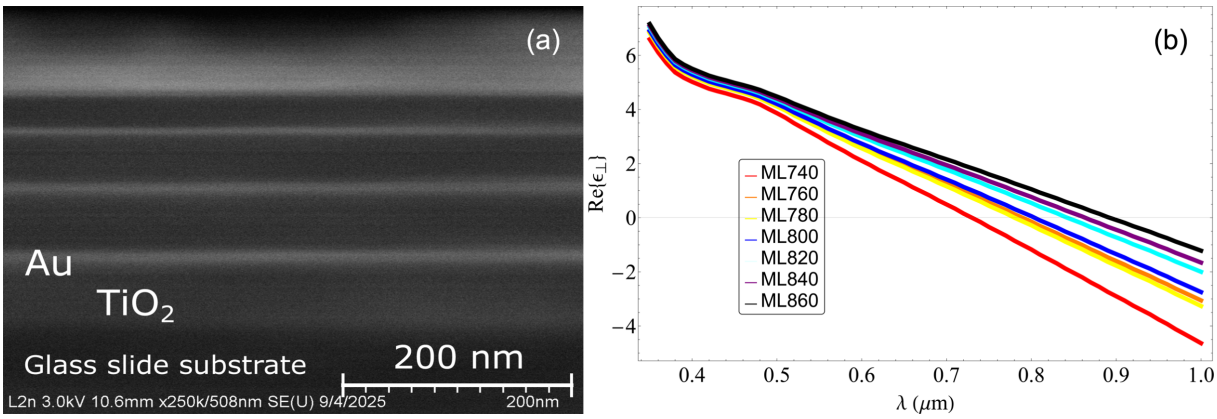

Figure 4: (a) Scanning electron microscopy image of the ML800 structure. We see that the deposited layers have different thicknesses throughout the structure, resulting in a shift in the ENZ points. (b) Calculated permittivity using the results from the ellipsometry. We observe that, although the ENZ points shifted, they still remain near the region of 800 nm.

served. This similitude tells us that no contamination occurred during the deposition process and that the deposited materials have almost identical properties.

Also, with the measured thicknesses and permittivities of the deposited layers, we repeated the simulations in order to check if the ENZ points remain the same. In Figure 4b, we present the

new simulated permittivities, and in Table 1, we can observe that the ENZ wavelengths have changed for every stack. Although the ENZ points have shifted slightly, they still remain near the region of 800 nm. Hence, we expect to be able to study the enhancement of the nonlinear response as a function of the ENZ position.

Nonlinear optical studies

We started studying the nonlinear response using the z-scan technique at different input peak irradiances, namely, 0.54, 0.60, 0.68, 0.82, 0.96, and 1.09 GW·cm^{-2}. We studied the nonlinear response as a function of the input peak irradiance in order to reduce the error in the determination of the nonlinear parameters when only using a single measurement.

We performed the z-scan for the single layers of the constituting materials. For both gold and titanium dioxide, we could not see a signal. This could mean that our system lacks the power output to excite the nonlinear response or that, even at our highest irradiance, the response was below the signal-to-noise ratio. Considering that, for 800 nm, our system has a minimum resolution of 2%, we can calculate an upper limit for the nonlinear refractive index that corresponds to a peak-to-valley transmittance difference of 0.02 ($\Delta T_{P-V} = 0.02$) giving us $n_2^{Au} \leq 0.024$ cm^2·GW^{-1} for gold and $n_2^{TiO_2} \leq 4.4 \times 10^{-6}$ cm^2·GW^{-1} for titanium dioxide.

First, we performed the OA z-scan measurements. Figure 5a shows the results obtained for three different input irradiances in the multilayer stack with an ENZ point at 800 nm. Usually, we should observe a signal that grows for high I at $z = 0$ in the case of saturable absorption or that diminishes in the case of induced absorption. What we observe in Figure 5a is a combination of two processes, namely, induced and saturable absorp-

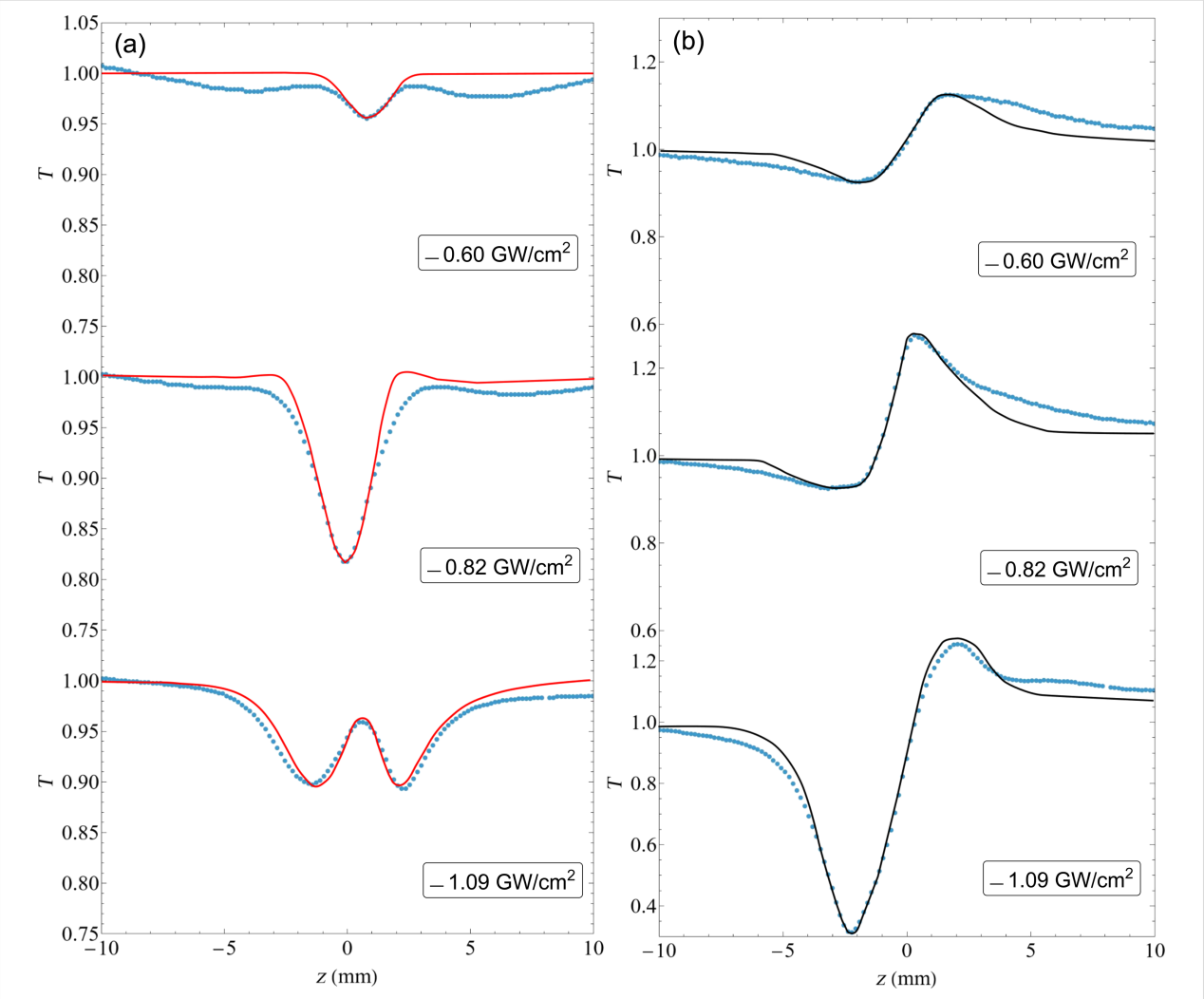

Figure 5: (a) OA z-scan results. The solid line is the fit using the method presented in [31]; we successfully emulated the signal with two effects of different sign. (b) For the CA z-scan results, we could produce a fit that is very similar to the experimental data.

tion, which change their relative contributions for the different input irradiances. Then we performed the CA z-scan. The results are presented in Figure 5b and show the presence of a positive n_2, that is, a prefocal minimum followed by a postfocal maximum, albeit somehow deformed. This deformation is due to the complicated nonlinear absorption observed in the OA z-scan.

In order to model the response, we used the approach found in [31], where the CA z-scan trace shows effects of both nonlinear absorption and refraction:

$$T = 1 + \frac{(1-S)^{\mu}\sin(\xi)}{S\left(1+z^2\right)}\Delta\Phi_0 - \frac{1-(1-S)^{\mu}\cos(\xi)}{S\left(1+z^2\right)}\Delta\Psi_0, \quad (2)$$

$$\mu = \frac{2\left(z^2+3\right)}{z^2+9}, \quad (3)$$

$$\xi = \frac{-4z\ln(1-S)}{z^2+9}, \quad (4)$$

$$\Delta\Phi_0 = \frac{2\pi}{\lambda} n_2 I_0 L_e, \quad (5)$$

$$\Delta\Psi_0 = \frac{\beta I_0 L_e}{2\sqrt{2}}, \quad (6)$$

where S is the aperture transmittance, I_0 is the peak irradiance, and $L_e = (1-e^{-\alpha_0 L})/\alpha_0$ is the effective length. Setting S = 1, we are left with $\Delta\Psi_0$, which is related only to nonlinear absorption effects, and we can then model the fit for the OA z-scan results. For the CA z-scan, we set S = 0.5 (from experiment), and we only need to find the value for $\Delta\Phi_0$ to fit the experimental data using the $\Delta\Psi_0$ values from the previous OA z-scan fits.

It can be noted that Equation 6 describes a single nonlinear absorption effect. However, since we observed the combination of two effects of opposite sign, we must modify β to describe both effects. Substituting

$$\beta(I) = \beta_{TPA}(I) + \beta_{SA}(I) = \frac{\beta_+}{1+\frac{I}{I_S^+}} + \frac{\beta_-}{1+\frac{I}{I_S^-}} \quad (7)$$

in Equation 6, we are now able to model the effect of both nonlinear absorption effects.

Then, for each different sample, we must find a set of constants β_+, β_-, I_S^+, and I_S^- that can be used to fit every z-scan data set obtained at different I_0 values. Figure 5 shows the fits made to the previous data set using Equation 2, showing good agreement with the experimental data. For the CA z-scan, we used the nonlinear absorption fit parameters from the OA z-scan data. We then fit $\Delta\Phi_0$ to model the CA z-scan; the results are shown in Figure 5, and the corresponding n_2 parameters are given in Table 2.

We see that the n_2 determined for the sample with the ENZ point at 800 nm is larger than all the others, by up to two orders of magnitude with respect to the ones with the smallest coefficients (Figure 6). This clearly indicates that the observed nonlinear response is enhanced by being resonant with the ENZ wavelength; compared to that of the constituting materials, it is five times larger than the measured n_2 of gold and 10^4 times larger than that of TiO_2.

Electronic and thermal contributions to the nonlinear response

We use ultrashort pulses due to the low pulse energies needed to achieve irradiances high enough to observe nonlinear effects. This avoids the presence of intrapulse thermal effects; therefore, only the electronic contribution is in principle measured. It has been shown in [24] that the presence of linear and nonlinear

Table 2: Nonlinear properties (fit parameters for CA z-scan) of the multilayered stacks with d_m = 10 nm.

Sample	n_2 (×10^{-2} cm^2·GW^{-1})	β_+ (×10^4 cm·GW^{-1})	I_S^+ (GW·cm^{-2})	β_- (×10^3 cm·GW^{-1})	I_S^- (GW·cm^{-2})
ML740	0.53 ± 0.03	4.9 ± 0.3	1.37 ± 0.12	−1.32 ± 0.09	0.026 ± 0.005
ML760	0.21 ± 0.06	5.0 ± 0.5	1.26 ± 0.05	−1.47 ± 0.07	0.038 ± 0.004
ML780	3.04 ± 0.03	4.7 ± 0.1	1.13 ± 0.08	−1.26 ± 0.02	0.031 ± 0.011
ML800	10.3 ± 0.4	5.2 ± 0.2	0.980 ± 0.015	−0.88 ± 0.01	0.035 ± 0.005
ML820	6.9 ± 0.09	4.2 ± 0.4	0.986 ± 0.007	−0.72 ± 0.07	0.039 ± 0.005
ML840	0.51 ± 0.04	4.7 ± 0.2	0.973 ± 0.012	−0.99 ± 0.05	0.024 ± 0.003
ML860	0.064 ± 0.006	4.3 ± 0.1	0.994 ± 0.005	−0.82 ± 0.03	0.027 ± 0.009

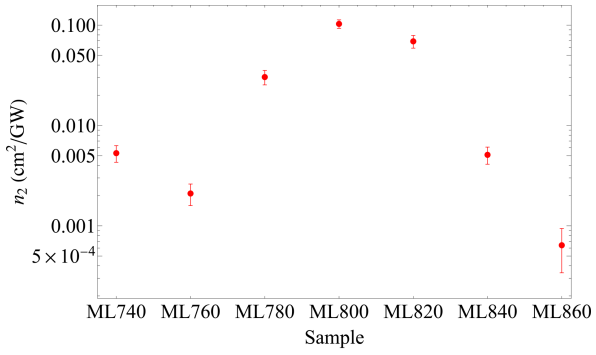

Figure 6: The nonlinear refractive index n_2 as a function of the ENZ point wavelength. We found a clear enhancement around 800 nm, as desired.

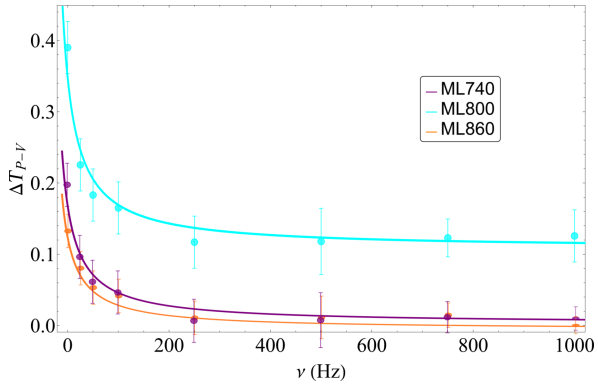

Figure 7: Peak-to-valley transmittance differences ΔT_{P-V} as a function of the chopper frequency for the samples ML740 (purple), ML800 (cyan), and ML860 (orange). The solid line is the fit using the equation provided in [32], following the procedure explained in [24]. When the chopper is turned off, we have the highest accumulated thermal effect; as the frequency rises, we see that the thermal effect gradually decreases until ΔT_{P-V} is constant. Hence, it can be assumed that the thermal effects were successfully suppressed.

absorption and the high pulse repetition rate intrinsic to the Ti:sapphire oscillators (around 100 MHz) may produce pulse-to-pulse temperature accumulation. This new effect will produce a contribution to the nonlinear refractive index of thermal origin. Given its thermal origin, this contribution will have a relatively long characteristic time. Almost every application exploits the electronic contribution of the nonlinear response; hence, we must study and define the nature of the response measured.

Using the modification of the z-scan technique proposed in [30], we studied the samples ML740, ML800, and ML860. Figure 7 shows the ΔT_{P-V} values extracted from the CA data at $I_0 = 1.09$ GW·cm^{-2} as a function of the chopper frequency. We obtained the fit using the equation provided in [32], following the procedure explained in [24]. We observe a maximum ΔT_{P-V} value for $\nu_{chopper} = 0$, that is, when the whole pulse train is applied to the sample and, hence, the thermal load is maximal. When the chopper frequency is increased, ΔT_{P-V} diminishes and quickly reaches a stable value for chopper frequencies above 300 Hz. Therefore, for these higher $\nu_{chopper}$ values, we only have the electronic contribution. From this, we obtain the nonlinear refractive index of the electronic contribution n_2^e; from the frequency $\nu_{chopper} \approx 0$, we obtain the value for both electronic and thermal contribution $n_2 = n_2^e + n_2^t$.

From Figure 7, we were able to differentiate the electronic and thermal contributions to the nonlinear response. In Table 3, we present the values with the corresponding nonlinear refractive indexes. We see that both contributions are positive, which is consistent with what we get without the chopper. We observe that, as expected, we have a thermal contribution to the nonlinear response. Regardless of this, the measured electronic contribution is significant. Compared to the nonlinear refractive index obtained from the normal z-scan technique, we do not observe any inconsistency with the values and order magnitude of the newly obtained nonlinear refractive indexes. We notice that the thermal contribution is around 70% of the nonlinear response for all three cases. This could mean that the pulse-to-pulse temperature accumulation occurs mainly in the gold layers, which have a fixed thickness in all three samples. We can also see that the electronic contribution to the nonlinear response follows the same trend as the nonlinear response measured with the full train of pulses; we obtain an enhancement in the ML800 sample of up to two orders of magnitude with respect to the other samples. Given the thermal contribu-

Table 3: Nonlinear properties (electronic and thermal contributions to the nonlinear refractive index) of the multilayered stacks with $d_m = 10$ nm.

Sample	n_2 (×10^{-2} cm^2·GW^{-1})	n_2^e (×10^{-2} cm^2·GW^{-1})	n_2^t (×10^{-2} cm^2·GW^{-1})	t_c (s)	D (×10^{-6} m^2·s^{-1})
ML740	0.53 ± 0.03	0.37 ± 0.04	0.18 ± 0.01	0.011 ± 0.003	2.8 ± 0.3
ML800	10.3 ± 0.4	6.7 ± 0.5	2.5 ± 0.3	0.013 ± 0.001	2.4 ± 0.2
ML860	0.064 ± 0.006	0.045 ± 0.005	0.019 ± 0.003	0.014 ± 0.002	2.2 ± 0.3

tion and the high repetition rate of the system, the material may be damaged or its properties may be changed due to heat accumulation. However, in repeated z-scan studies with the used peak irradiances, we did not see any damage, and repeating the experiment at the highest value gave the same signal each time.

In Table 3, we show the obtained characteristic thermal time $t_c(z) = \omega^2(z)/(4D)$, where $\omega(z)$ is the beam's waist and D is the thermal diffusivity. From this fit, we obtained times that are several orders of magnitude longer than the repetition rate of the pulses, which is consistent with the assumption of accumulated pulse-to-pulse thermal effects. From the characteristic thermal time t_c, we are able to obtain the thermal diffusivity D for these structures, which is closer to the titanium dioxide diffusivity $D = 1.35 \times 10^{-6}$ m^2·s^{-1} [33] than to that of gold $D = 1.17 \times 10^{-4}$ m^2·s^{-1} [34]. This can be because the gold/titanium dioxide ratio is 1:6, resulting in a thermal effect dominated by the thermal properties of titanium dioxide.

Conclusion

We were able to design and fabricate a multilayered system that presents hyperbolic dispersion. Ellipsometric data indicate that the ENZ points were slightly shifted towards longer wavelengths from those that they were designed for, but they remained near the desired region. Also, from the ellipsometric results, we can imply that, even though the gold layer was very thin, we were able to deposit a uniform layer instead of "island-like" layers that form for smaller thicknesses [28].

We studied both the absorptive and the refractive contribution to the nonlinear response of the fabricated samples, using the closed aperture z-scan technique with 100 fs pulses at 800 nm. The results show a fairly large enhancement of the nonlinearity of the sample with an ENZ point at 800 nm with a nonlinear refractive index $n_2 = 0.103$ cm^2·GW^{-1}. This value is orders of magnitude larger than those of the other samples, meaning that we obtained an enhancement of the nonlinear response at the desired wavelength. The thermal and electronic contributions to the response were resolved using a modified z-scan technique to yield $n_2^t = 0.067$ cm^2·GW^{-1} and $n_2^e = 0.024$ cm^2·GW^{-1}. Even though the thermal contribution dominates n_2, n_2^e is comparable to those of other ENZ materials reported, such as Ru/TiO_2 multilayers with $n_2 = 0.084$ cm^2·GW^{-1} [22], ITO with $n_2 = 0.11$ cm^2·GW^{-1} [35], AZO with $n_2 = 5.17 \times 10^{-3}$ cm^2·GW^{-1} [36], and a Au nanorod metamaterial with $n_2 = -0.024$ cm^2·GW^{-1} [37].

Acknowledgements

We thank M. A. Lopez-Alvarado for the preparation of the samples.

Funding

The authors would like to acknowledge the financial support by Secretaría de Ciencia, Humanidades, Tecnología e Inovación (SECIHTI) CF-2023-G-179 and the PhD scholarship given to F. A. Araiza-Sixtos (847770). Ministère de l'Enseignement supérieur, de la Recherche et de l'Innovation, France (ECOS Nord M19P01), and NANO-PHOT Ecole Universitaire de Recherche, France (ANR-EURE-0013). Allocations Doctorales Région Grand Est, France (Qsim). We conducted the calculations with the resources of the French regional Grand-Est HPC Center ROMEO.

Author Contributions

Fernando Arturo Araiza-Sixtos: conceptualization; data curation; formal analysis; investigation; methodology; software; validation; visualization; writing – original draft; writing – review & editing. Mauricio Gomez-Robles: investigation. Rafael Salas-Montiel: funding acquisition; project administration; resources; supervision; writing – review & editing. Raúl Rangel-Rojo: conceptualization; funding acquisition; project administration; resources; supervision; writing – original draft; writing – review & editing.

ORCID® iDs

Fernando Arturo Araiza-Sixtos - https://orcid.org/0000-0002-8713-3409
Mauricio Gomez-Robles - https://orcid.org/0000-0001-5589-7247
Rafael Salas-Montiel - https://orcid.org/0000-0002-9336-4019
Raúl Rangel-Rojo - https://orcid.org/0000-0001-5978-9489

Data Availability Statement

Additional research data generated and analyzed during this study is not shared.

References

1. Suresh, S.; Reshef, O.; Alam, M. Z.; Upham, J.; Karimi, M.; Boyd, R. W. *ACS Photonics* **2021,** *8,* 125–129. doi:10.1021/acsphotonics.0c01178
2. Alekseyev, L. V.; Podolskiy, V. A.; Narimanov, E. E. *Adv. OptoElectron.* **2012,** *2012,* 267564. doi:10.1155/2012/267564
3. Wang, Y.; Capretti, A.; Dal Negro, L. *Opt. Mater. Express* **2015,** *5,* 2415–2430. doi:10.1364/ome.5.002415
4. Shkondin, E.; Repän, T.; Aryaee Panah, M. E.; Lavrinenko, A. V.; Takayama, O. *ACS Appl. Nano Mater.* **2018,** *1,* 1212–1218. doi:10.1021/acsanm.7b00381
5. Suchowski, H.; O'Brien, K.; Wong, Z. J.; Salandrino, A.; Yin, X.; Zhang, X. *Science* **2013,** *342,* 1223–1226. doi:10.1126/science.1244303
6. Liu, Z.; Lee, H.; Xiong, Y.; Sun, C.; Zhang, X. *Science* **2007,** *315,* 1686. doi:10.1126/science.1137368
7. Subramania, G.; Fischer, A. J.; Luk, T. S. *Appl. Phys. Lett.* **2012,** *101,* 241107. doi:10.1063/1.4770517

8. Tumkur, T.; Zhu, G.; Black, P.; Barnakov, Y. A.; Bonner, C. E.; Noginov, M. A. *Appl. Phys. Lett.* **2011,** *99,* 151115. doi:10.1063/1.3631723
9. Krishnamoorthy, H. N. S.; Jacob, Z.; Narimanov, E.; Kretzschmar, I.; Menon, V. M. *Science* **2012,** *336,* 205–209. doi:10.1126/science.1219171
10. Yang, X.; Yao, J.; Rho, J.; Yin, X.; Zhang, X. *Nat. Photonics* **2012,** *6,* 450–454. doi:10.1038/nphoton.2012.124
11. Tumkur, T. U.; Gu, L.; Kitur, J. K.; Narimanov, E. E.; Noginov, M. A. *Appl. Phys. Lett.* **2012,** *100,* 161103. doi:10.1063/1.4703931
12. Rho, J.; Ye, Z.; Xiong, Y.; Yin, X.; Liu, Z.; Choi, H.; Bartal, G.; Zhang, X. *Nat. Commun.* **2010,** *1,* 143. doi:10.1038/ncomms1148
13. Kim, J.; Drachev, V. P.; Jacob, Z.; Naik, G. V.; Boltasseva, A.; Narimanov, E. E.; Shalaev, V. M. *Opt. Express* **2012,** *20,* 8100–8116. doi:10.1364/oe.20.008100
14. Mahmoodi, M.; Tavassoli, S. H.; Takayama, O.; Sukham, J.; Malureanu, R.; Lavrinenko, A. V. *Laser Photonics Rev.* **2019,** *13,* 1800253. doi:10.1002/lpor.201800253
15. Genchi, D.; Balasa, I.; Cesca, T.; Mattei, G. *Phys. Rev. Appl.* **2021,** *16,* 064020. doi:10.1103/physrevapplied.16.064020
16. Avrutsky, I.; Salakhutdinov, I.; Elser, J.; Podolskiy, V. *Phys. Rev. B* **2007,** *75,* 241402. doi:10.1103/physrevb.75.241402
17. Ramírez-Aragón, J.; López-Rayón, F.; Gómez-Robles, M.; Sosa-Sánchez, C. T.; Arroyo-Carrasco, M. L.; Salas-Montiel, R.; Téllez-Limón, R. *Micro Nanostruct.* **2024,** *196,* 207990. doi:10.1016/j.micrna.2024.207990
18. Abdulkareem, M.-u. A.; López-Rayón, F.; Sosa-Sánchez, C. T.; Bautista González, R. E.; Arroyo Carrasco, M. L.; Peña-Gomar, M.; Coello, V.; Téllez-Limón, R. *Nanomaterials* **2023,** *13,* 759. doi:10.3390/nano13040759
19. Santiago, K. C.; Mundle, R.; White, C.; Bahoura, M.; Pradhan, A. K. *AIP Adv.* **2018,** *8,* 035011. doi:10.1063/1.5024900
20. Hoffman, A. J.; Alekseyev, L.; Howard, S. S.; Franz, K. J.; Wasserman, D.; Podolskiy, V. A.; Narimanov, E. E.; Sivco, D. L.; Gmachl, C. *Nat. Mater.* **2007,** *6,* 946–950. doi:10.1038/nmat2033
21. Yao, J.; Liu, Z.; Liu, Y.; Wang, Y.; Sun, C.; Bartal, G.; Stacy, A. M.; Zhang, X. *Science* **2008,** *321,* 930. doi:10.1126/science.1157566
22. Araiza-Sixtos, F. A.; Solorio-Soto, F.; Lizarraga-Medina, E. G.; Tiznado, H.; Carriles-Jaimes, R.; Bueno-Escobedo, J. L.; Rangel-Rojo, R. *Opt. Mater.:X* **2024,** *22,* 100314. doi:10.1016/j.omx.2024.100314
23. Sheik-Bahae, M.; Said, A. A.; Wei, T.-H.; Hagan, D. J.; Van Stryland, E. W. *IEEE J. Quantum Electron.* **1990,** *26,* 760–769. doi:10.1109/3.53394
24. Hernández-Acosta, M. A.; Torres-Torres, C.; Oliver, A.; Rangel-Rojo, R. *Opt. Mater. (Amsterdam, Neth.)* **2024,** *155,* 115913. doi:10.1016/j.optmat.2024.115913
25. Rytov, S. M. *Sov. Phys. - JETP* **1956,** *29,* 605–616.
26. DeVore, J. R. *J. Opt. Soc. Am.* **1951,** *41,* 416–419. doi:10.1364/josa.41.000416
27. Johnson, P. B.; Christy, R. W. *Phys. Rev. B* **1972,** *6,* 4370–4379. doi:10.1103/physrevb.6.4370
28. Malureanu, R.; Lavrinenko, A. *Nanotechnol. Rev.* **2015,** *4,* 259–275. doi:10.1515/ntrev-2015-0021
29. Lepeshkin, N. N.; Schweinsberg, A.; Piredda, G.; Bennink, R. S.; Boyd, R. W. *Phys. Rev. Lett.* **2004,** *93,* 123902. doi:10.1103/physrevlett.93.123902
30. Can-Uc, B.; Rangel-Rojo, R.; Rodriguez-Fernandez, L.; Oliver, A. *Opt. Mater. Express* **2013,** *3,* 2012–2021. doi:10.1364/ome.3.002012
31. Cesca, T.; Calvelli, P.; Battaglin, G.; Mazzoldi, P.; Mattei, G. *Opt. Express* **2012,** *20,* 4537–4547. doi:10.1364/oe.20.004537
32. Falconieri, M. *J. Opt. A: Pure Appl. Opt.* **1999,** *1,* 662–667. doi:10.1088/1464-4258/1/6/302
33. Feng, X.; Wang, X.; Chen, X.; Yue, Y. *Acta Mater.* **2011,** *59,* 1934–1944. doi:10.1016/j.actamat.2010.11.059
34. Yeh, Y.; Wooten, F.; Huen, T. *Solid State Commun.* **1973,** *13,* 1845–1849. doi:10.1016/0038-1098(73)90742-4
35. Alam, M. Z.; De Leon, I.; Boyd, R. W. *Science* **2016,** *352,* 795–797. doi:10.1126/science.aae0330
36. Carnemolla, E. G.; Caspani, L.; DeVault, C.; Clerici, M.; Vezzoli, S.; Bruno, V.; Shalaev, V. M.; Faccio, D.; Boltasseva, A.; Ferrera, M. *Opt. Mater. Express* **2018,** *8,* 3392–3400. doi:10.1364/ome.8.003392
37. Neira, A. D.; Olivier, N.; Nasir, M. E.; Dickson, W.; Wurtz, G. A.; Zayats, A. V. *Nat. Commun.* **2015,** *6,* 7757. doi:10.1038/ncomms8757

License and Terms

BEILSTEIN JOURNAL OF NANOTECHNOLOGY

Durable antimicrobial activity of fabrics functionalized with zeolite ion-exchanged nanomaterials against *Staphylococcus aureus* and *Escherichia coli*

Perla Sánchez-López[1], Kendra Ramirez Acosta[1,2], Sergio Fuentes Moyado[1], Ruben Dario Cadena-Nava[1] and Elena Smolentseva[*1]

Full Research Paper

Open Access

Address:
[1]Universidad Nacional Autónoma de México, Centro de Nanociencias y Nanotecnología, Km. 107 Carretera Tijuana a Ensenada, C.P. 22860, Ensenada, Baja California, México and [2]Centro de Investigación Científica y de Educación Superior de Ensenada (CICESE), Carretera Ensenada-Tijuana, No. 3918, Zona Playitas, Ensenada 22860, México

Email:
Elena Smolentseva[*] - elena@ens.cnyn.unam.mx

* Corresponding author

Keywords:
antimicrobial activity; *Escherichia coli*; fabrics functionalization; ion exchange; nanomaterial; *Staphylococcus aureus*; zeolite

Beilstein J. Nanotechnol. **2026,** *17,* 262–274.
https://doi.org/10.3762/bjnano.17.18

Received: 24 July 2025
Accepted: 20 January 2026
Published: 06 February 2026

This article is part of the thematic issue "Symposium of Nanoscience and Nanomaterials 2024 (SNN 2024)".

Associate Editor: C. T. Yavuz

Abstract

Nanoparticle-based functionalization has emerged as an effective strategy to enhance the antimicrobial properties of textiles. In this study, silver (Ag^{+}), copper (Cu^{2+}), and zinc (Zn^{2+}) cations are ion-exchanged with Y-type zeolite (CBV-600) and subsequently applied to cotton fabrics using the pad–dry–cure method, with an acrylic resin serving as binder. The resulting functionalized fabrics, containing metal cation concentrations of 1.0–1.5 atom % are evaluated regarding their antimicrobial activity against *Staphylococcus aureus* (Gram-positive) and *Escherichia coli* (Gram-negative), as well as regarding their physicochemical and mechanical properties. Scanning electron microscopy confirms the uniform distribution and successful incorporation of nanomaterials onto the fabric surfaces. Antimicrobial tests reveal significant inhibition of bacterial growth, with silver-based materials demonstrating superior efficacy. Importantly, the antimicrobial effect persists after five washing cycles, demonstrating the durability of the functionalization. This method demonstrates a simple and industry-compatible approach for producing durable antimicrobial cotton fabrics.

Introduction

The development of nanotechnology has expanded into different areas of science, including physics, chemistry, biology, and medicine, over the past few decades [1,2]. Recently, nanoparticles (NPs), nanomaterials, and nanocomposites have been applied in various fields, including medicine and biotechnology, to reduce the recurrence of infections [3,4]. In this context,

nanotechnology and nanomaterials offer a new alternative to combat pathogens such as viruses and bacteria. Metal NPs have intrinsic manipulatable properties that make them useful in a wide variety of research fields, including biomedicine. Different types of NPs are currently explored for various biomedical applications, including disease prevention, diagnosis, and the improvement of antiviral drug delivery systems [5,6]. In some cases, the antimicrobial properties of NPs lead to creation of new "nano-antimicrobial" materials [7]. The mechanism by which nanoparticles act against viruses involves the interaction with the surface of the NPs, leading to adhesion and inactivation, thereby preventing the virion from entering the host cell. NPs release ions or transfer them to microorganisms, inducing oxidative stress. Given these possible mechanisms, viral microorganisms are unable to develop mutations for adaptation and are destroyed [8,9].

Recently, several types of NPs, including silver, copper, and zinc, have demonstrated great potential in antimicrobial applications due to their properties such as high specific surface area, safety for human use, multiple synthesis methods, and relatively low cost [4,10,11]. One of the most extensively studied nanomaterials in terms of antimicrobial properties is colloidal silver as its antimicrobial action affects various parts of microorganisms. In addition to silver, copper has attracted significant attention for its antimicrobial properties. It was officially recognized in 2008 by the United States Environmental Protection Agency (EPA) as the first metallic antimicrobial agent, highlighting its potential for broad-spectrum antibacterial applications [12]. Since then, copper has been extensively studied for its ability to inactivate a wide range of microorganisms. Today, both silver and copper are widely used in various medical and healthcare applications due to their effective antimicrobial activity.

For example, copper was found to be 99.9% efficient in inactivating microorganisms within the first two hours of contact [13]. The antimicrobial activity of copper alloys (61–95% Cu) against *E. coli* O157 was tested at different temperatures (4 and 22 °C) [14]. The highest antibacterial effect was observed at 22 °C, but only alloys containing 95% of Cu completely killed *E. coli*. Chitosan–copper nanoparticles exhibited high antibacterial activity against various bacterial strains, including methicillin-resistant *Staphylococcus aureus* (*S. aureus*), *Bacillus subtilis*, *Pseudomonas aeruginosa*, and *Salmonella choleraesuis* [15]. Some studies have shown that the size of Cu NPs plays a crucial role in their antimicrobial activity. For example, CuO NPs with a size of 4.8 nm demonstrated better antibacterial activity than larger particles (7.8 nm) [16]. The small Cu NPs have a greater capacity to penetrate the cell membrane [17,18].

Zinc oxide NPs are well known for their photocatalytic properties. Also, recent studies have demonstrated that ZnO possesses unique antibacterial, antimicrobial, and antifungal properties, making it effective against both Gram-positive and Gram-negative bacteria [19,20].

Recently, the application of nanotechnology has been extended to textiles. Fabrics functionalized with nanoparticles, also known as "smart textiles", possess a range of properties, including antistatic, UV-blocking, hydrophobic, electronic, thermoregulation, and antimicrobial effects [21-23]. One of the simplest way to incorporate nanomaterials into fabrics is by mimicking designs found in nature. It is well known that the leaves of some plants are water- or dust-repellent, and these repellent properties can be transferred to textiles by modifying the components involved in these mechanisms [24]. Among the physicochemical methods used for fabric functionalization with nanomaterials are coatings, electrospinning, assembling different components, fiber material composites, nanoscale fibers, and immersion in NPs solutions with a binder.

Nanoparticles such as Ag, Au, TiO_2, ZnO, Se, SiO_2, CuO, and Pt are widely used for textile functionalization [25]. Common methods for incorporating Ag and Cu NPs into cotton textiles involve treating the fibers at the end of the manufacturing process. Those methods require the use of previously prepared NPs, which are then bonded to the textile through chemical bonding or electrostatic interaction. The pad–dry–cure method is an effective alternative for applying nanoparticles to the surface of fabrics. In this process, crosslinking reactant, catalyst, softener, and other components are dried onto the fabric before the crosslinking reaction takes place during the curing stage [26-28]. Lateef et al. applied the pad–dry–cure method to functionalize commercial cotton and silk with Ag NPs using a self-cross-linking binder. The functionalized textiles were tested against *S. aureus*, *Escherichia coli* (*E. coli*), *Klebsiella pneumoniae*, *Klebsiella oxytoca*, *Proteus mirabilis*, and *Aspergillus niger*. It has been shown that at concentrations of 100 and 150 $\mu g \cdot mL^{-1}$, Ag NP-functionalized cotton and silk effectively inhibited the growth of the test isolates up to the fifth wash cycle [29]. Ag NPs deposited on the cotton fabrics via the pad–dry–cure process were tested for bactericidal activity against the Gram-positive *S. aureus* ATCC 25923 [30]. The results show that cotton fabric with concentrations of 10 and 20 ppm of Ag NPs exhibited strong bactericidal properties, reducing bacterial colonies by over 98%. Biogenic Ag NPs, obtained through fungal biosynthesis using extracellular filtrate of the epiphytic fungus *Bionectria ochroleuca* were incorporated into cotton and polyester fabrics using the pad–dry–cure method [28]. The silver-modified fabrics display antimicrobial activity

against *S. aureus*, *E. coli*, *Candida albicans*, *Candida glabrata*, and *Candida parapsilosis*.

Copper oxide nanoparticles were deposited on the cotton fabric in two steps: first, through microencapsulation using an ionic gelation method and exhaustion, followed by the pad–dry–cure method in the second step. The antibacterial properties of the coated fabric were then evaluated [31].

Zinc peroxide (ZnO_2) NPs synthesized via the sol–gel method were used to functionalize cotton textile fabrics through the pad–dry–cure method [32]. As shown in [33], ZnO NPs prepared through the sol–gel method were subsequently applied to the cotton fabric using the pad–dry–cure technique with dimethyloldihydroxyethyleneurea as a cross-linking agent. The results demonstrate good antibacterial activity against *S. aureus* and *E. coli* bacteria. The synthesis conditions, including concentration (1% and 2%), temperature (25 and 80 °C), and order of the ZnO NP application during the pad–dry–cure method were studied by Eskani and coworkers. Antibacterial activity of the treated fabrics was evaluated against *S. aureus* and *E. coli* [34].

Recently, the versatility of zeolite carriers for stabilizing silver–copper exchange zeolite microparticles demonstrating potential as durable antimicrobial agents for textile applications was highlighted [35].

Building on this growing body of research, our study focuses on the use of Ag, Cu, and Zn-exchanged Y-type zeolites, which offer high ion-exchange capacity and a well-defined framework structure that facilitate efficient antimicrobial ion delivery. By applying those nanomaterials to commercial cotton fabrics via the pad–dry–cure method, we aim to further explore the feasibility and effectiveness of zeolite-based antimicrobial treatment under conditions relevant to large-scale textile finishing. In the present work, the functionalization of textiles using the pad–dry–cure method with silver, copper, and zinc ions loaded on Y-zeolite (CBV-600) is demonstrated. The antimicrobial properties of impregnated textile samples were studied against *S. aureus* and *E. coli*, and their physicochemical and mechanical properties are discussed. The obtained results suggest that the synthesized materials can be applied as an effective alternative to inhibit and reduce the spread of different types of viruses and bacteria. Unlike our previous work, which focused on the antimicrobial performance of Ag- and Zn-loaded Y zeolite, the present study applies those nanomaterials, including Cu, to cotton fabrics via the pad–dry–cure method and evaluates the durability of their antimicrobial activity after fife washing cycles, representing a direct and practical extension of the prior findings.

Results and Discussion

Chemical composition

Prior to the fabric functionalization, the silver, copper, and zinc loadings in, respectively, Ag/CBV-600, Cu/CBV-600, and Zn/CBV-600 nanomaterials were analyzed by inductively coupled plasma optical emission spectroscopy (ICP-OES). The results confirmed silver, copper, and zinc contents of around 1.0–1.5 atom % [4]. Energy-dispersive X-ray spectroscopy (EDS) analysis performed on the functionalized fabrics in the present work confirmed the presence of silver (1.3 wt %), as well as copper and zinc (0.3 wt %) on the surface of textile (see Table 1 and Figure 1, right panel). The slight increase in silver content on the functionalized fabrics may be explained by the agglomeration of nanomaterials on the surface of fabrics and superficial nature of the EDS method. However, the content of copper and zinc in the functionalized textiles analyzed by EDS was nearly four times lower in comparison with Ag/CBV-600-bramante. This may be explained by non-homogeneous loading of nanomaterials on the textile, as also evidenced by SEM images. The Si/Al molar ratio for Y zeolite was 2.7, which coincided well with data provided by the supplier and measurements obtained through EDS and ICP-OES analysis. As discussed in our previous work [4], the ion exchange treatment did not induce any changes in the chemical composition of the zeolite structure, such as dealumination or disilation. No additional impurities in the samples were found.

SEM analysis

Figure 2 shows the micrographs of bramante fabric before and after its functionalization with 0.5 g of Ag/CBV-600, Cu/CBV-600, and Zn/CBV-600 nanomaterials using the pad–dry–cure method. As seen in Figure 2a, the original fabric did not show fiber degradation after washing prior to its functionalization. However, some foreign particles were observed, which may be attributed to contamination during handling (Figure 2a, right panel). These types of impurities are commonly present in fabrics, even after sterilization [28].

Once 0.5 g of nanomaterials (Ag/CBV-600 in Figure 2b, Cu/CBV-600 in Figure 2c, and Zn/CBV-600 in Figure 2d) were

Table 1: Contents of silver, copper, and zinc in the modified textile samples measured by EDS.

Sample	Metal loading, wt %					
	Si	Al	Ag	Zn	Cu	Si/Al
Ag/CBV-600-bramante	16.4	6.0	1.3	—	—	2.7
Cu/CBV-600-bramante	15.7	5.9	—	—	0.3	2.7
Zn/CBV-600-bramante	12.2	4.7	—	0.3	—	2.6

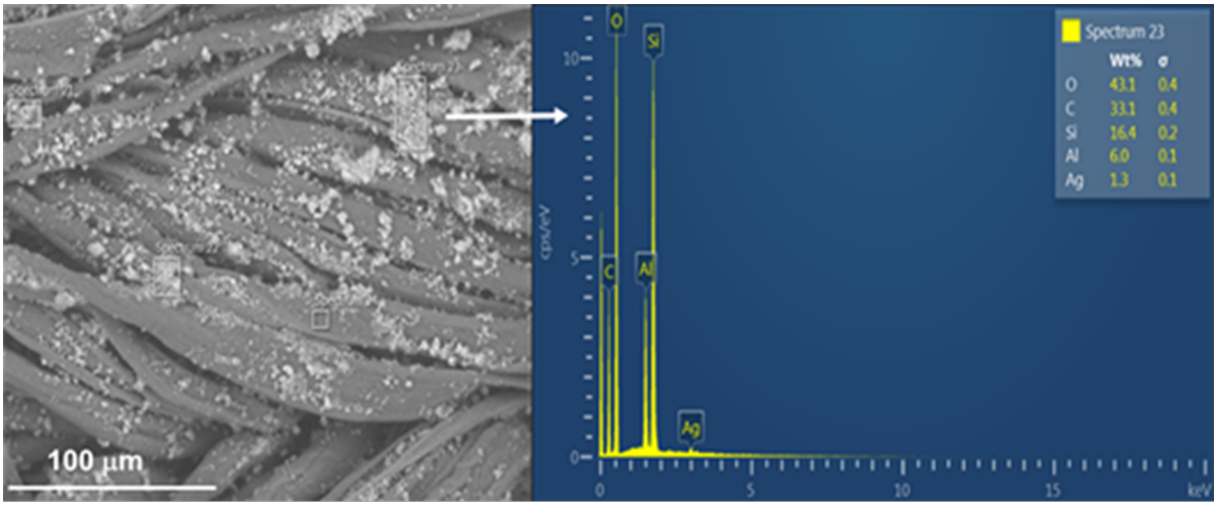

Figure 1: SEM micrographs of Ag/CBV-600-bramante (left) and its chemical analysis by EDS (right).

incorporated into the fabric, small, well-dispersed particles were observed on the textile surface. Panoramic micrographs of the functionalized fabrics showed varying degrees of nanomaterial aggregation: Ag/CBV-600 > Cu/CBV-600 > Zn/CBV-600. Large particles were observed for the bramante fabric with 0.5 g of Cu/CBV-600 (approximately 30 µm) (Figure 2c). However, better distribution of nanomaterials on the fabric surface was achieved for Ag/CBV-600 and Zn/CBV-600 (Figure 2b,d). Moreover, relatively small particles were found for Zn/CBV-600-bramante (Figure 2d) with uniform dispersion of nanomaterials on the fabric surface. Note, that the changes in the degree of aggregation may be attributed to the nature of the nanomaterial.

The functionalization of fabrics with acrylic resin as a binder allowed for the effective fixation of nanomaterials onto the fabrics. It is known that the high concentration of the binder could affect the antimicrobial activity of the fabrics [30]. Neither aggregation of the acrylic resin (10% *w*/*w*) nor degradation of the fibers after functionalization was observed for the prepared samples, demonstrating the optimal concentration (Figure 2). Therefore, it can be concluded that the proposed methodology, using acrylic resin at a 10% concentration, allowed for the effective incorporation of the nanomaterial, fixing it onto the fabrics without compromising the biocidal properties of functionalized textiles.

X-ray diffraction

XRD patterns of bramante fabrics, composed of 50% cotton and 50% polyester fibers, are shown in Figure 3. The bramante fabrics exhibited a typical cotton cellulose pattern, with three characteristic peaks at $2\theta \approx 14.7°$, 16.3°, and 22.4°, corresponding to the crystallographic planes (101), (101), and (002), respectively. Modification of the fabrics with nanomaterials led to an increase in the intensity of all peaks, while the position of the signals in XRD patterns remained unchanged (Figure 3). The later may be explained by the increase in crystallinity due to crosslinking with zeolite nanomaterials. A similar effect was observed in [36,37] for cotton fabrics cross-linked with dimethyloldihydroxyethyleneurea or treated with gallnut extract, respectively.

Antibacterial activity of functionalized fabrics

During the sunlight exposure assay, groups (A) and (C) of fabrics, corresponding to *E. coli* and *S. aureus*, respectively, were exposed to visible light at an intensity of 96.9 klux and UV-A/B radiation at 6704 $\mu W \cdot cm^{-2}$ under a glass microscope slide (Figure 4 and Table 2).

As seen in Figure 4, Ag/CBV-600-bramante showed strong antibacterial activity against *E. coli* (Figure 4Ac and 4Ah) and *S. aureus* (Figure 4Cc and 4Ch), as indicated by the lack of bacterial growth around the fabric. This effect was observed even when the fabrics were not exposed to sunlight and can be attributed to the well-known, strong antimicrobial properties of silver [38-41]. The susceptibility of bacteria to antimicrobial materials may depend on several factors, such as dose, humidity, and strain specificity [42,43]. Silver has been shown to exert a biocidal effect similar to that of copper against several *E. coli* and *S. aureus* strains using lower doses [43]. Likewise, surfaces coated with silver have exhibited lower minimum inhibitory concentrations (MICs) against *E. coli* and *S. aureus* strains compared to surfaces doped with copper and zinc [44]. Considering this, it is worth noting that the weight percentage

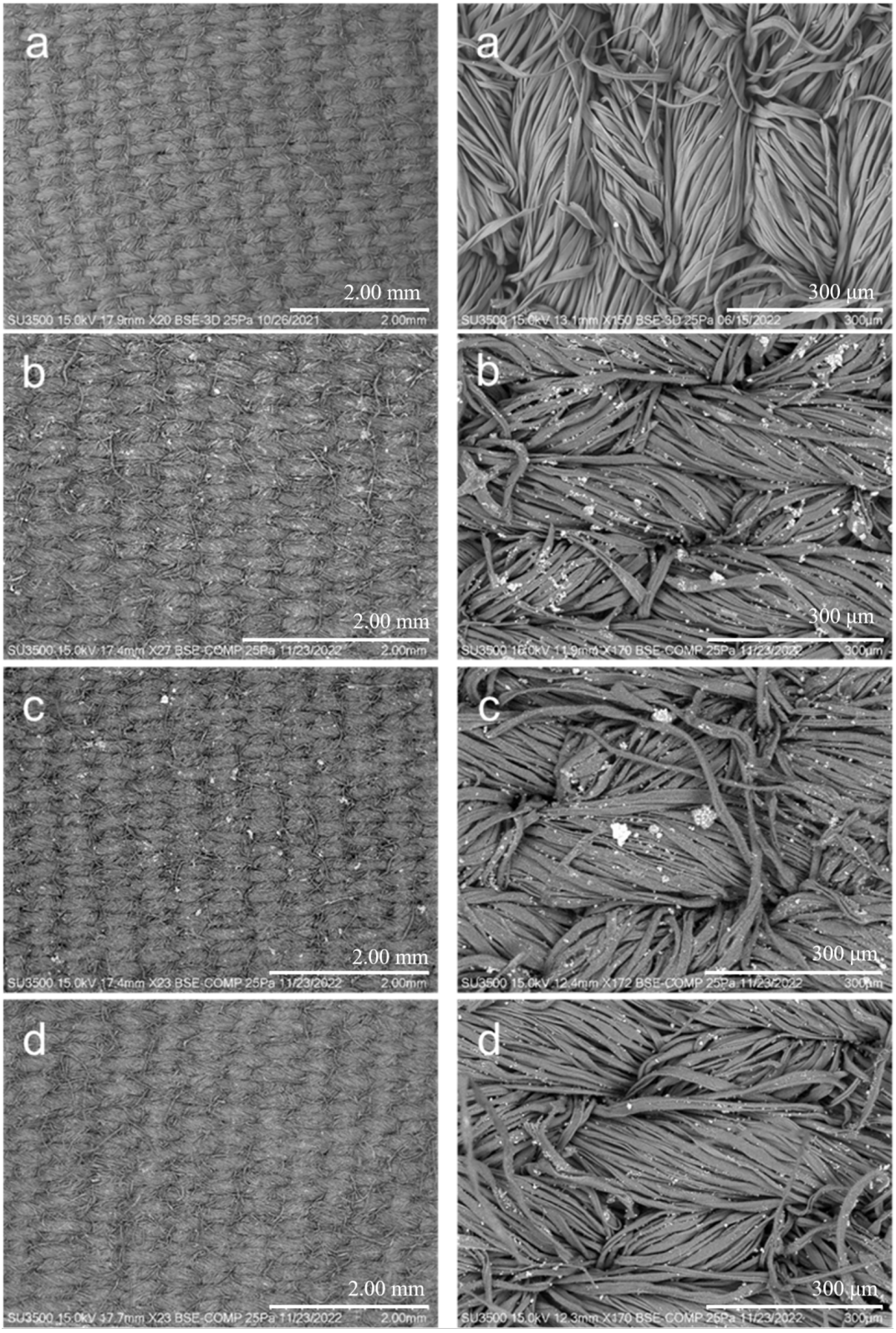

Figure 2: SEM micrographs of the samples. (Left column) Panoramic view and (right column) zoomed view. (a) Bramante fabric, (b) Ag/CBV-600-bramante, (c) Cu/CBV-600-bramante, and (d) Zn/CBV-600-bramante.

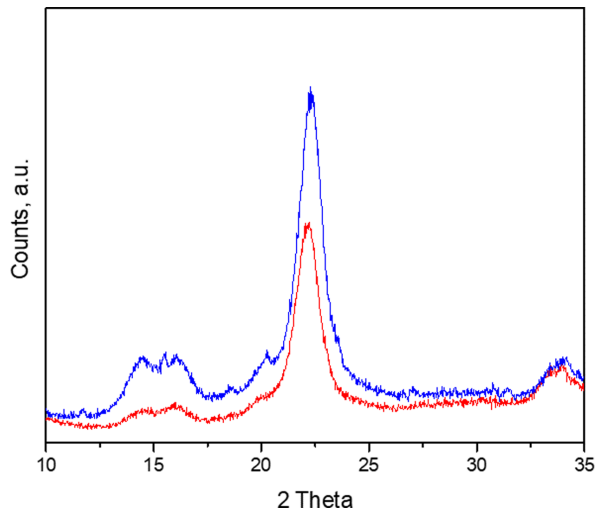

Figure 3: X-ray diffraction patterns of bramante fabric: nonmodified (red line) and modified with nanomaterial (blue line).

of Ag/CBV-600 in the fabrics is four times higher compared to Cu/CBV-600 and Zn/CBV-600 as shown in Table 1. This increase in the concentration of antimicrobial agent may also explain the difference in the antimicrobial activity observed compared to Cu/CBV-600 and Zn/CBV-600. If a greater weight content of Cu and Zn were to be obtained on functionalized fabrics, a similar antimicrobial effect to what is exhibited by Ag/CBV-600 might be achieved.

Although no direct comparison can be made between the effect of Ag/CBV-600-bramante with and without sunlight exposure, the impact of sunlight exposure on Ag/CBV-600-bramante was evident from the darkening of the fabrics that were exposed to sunlight (Figure 4Ah and Figure 4Ch). This suggests that the Ag^+ ions and small Ag NPs localized on the surface may undergo oxidation due to sunlight exposure. Cu/CBV-600 and Zn/CBV-600 nanomaterials exhibited a weaker antibacterial effect compared to AgCBV-600, particularly against *E. coli* (Figure 4Ad,i,e,j), and there was no significant difference between fabrics that were exposed to sunlight and those that were not. However, the biofilm thickness around these fabrics was smaller compared to the biofilm observed on the bacteria control groups with untreated fabric (Figure 4Aa,f). In this case, the antibacterial activity remained similar regardless of whether the fabrics were exposed to sunlight, as seen in Figure 4A. For *S. aureus*, the antibacterial activity of fabrics functionalized with Cu/CBV-600 and Zn/CBV-600 remained weaker compared to Ag/CBV-600. Additionally, sunlight-exposed fabrics functionalized with Cu/CBV-600-bramante and Zn/CBV-600-bramante (Figure 4B) did not show any blackening. However, sample Cu/CBV-600-bramante could inhibit *S. aureus* growth by up to 50% (Figure 4D) when exposed to sunlight. This represents a 20% increase in biocidal activity compared to Cu/CBV-600-bramante fabrics that were not exposed to sunlight, suggesting that the photocatalytic activity of Cu enhances its antibacterial efficacy. For fabrics with Zn/CBV-600-bramante, a minor increase in the inhibition of bacterial growth was also observed for *E. coli* following sunlight exposure.

Considering the effects observed on the fabrics exposed to sunlight, washed fabrics were exclusively tested under 60 min of sunlight exposure. A radiation level of 94.4 klux and UV-A/B radiation of 7.05 $mW{\cdot}cm^{-2}$ were registered. The antibacterial activity of fabrics after the fourth washing cycle is shown in Figure 5, along with the corresponding ANOVA results shown in Table 3. These fabrics were impregnated with *E. coli* or *S. aureus* and incubated on lysogeny broth (LB) agar plates for 20 h. The analysis of the growth radius around the fabrics shows that Ag/CBV-600-bramante fabrics inhibited bacterial growth by up to 95% (Figure 5A and Figure 5B). In contrast, Cu/CBV-600-bramante and Zn/CBV-600-bramante fabrics showed varying degrees of bacterial growth inhibition depending on the microorganism (Figure 5Ad,e and Figure 5Bd,e). Against *E. coli*, Cu/CBV-600-bramante fabrics inhibited bacterial growth by nearly 80%, while Zn/CBV-600-bramante fabrics achieved approximately 44% inhibition (Figure 5C). In contrast, the inhibitory effect of both Cu/CBV-600-bramante and Zn/CBV-600-bramante fabrics decreased against *S. aureus* after four cycles of washing. Bacterial growth was inhibited by 69% with Cu/CBV-600-bramante and by 16% with Zn/CBV-600-bramante. The stronger inhibition of Cu/CBV-600 compared to Zn/CBV-600 is consistent with results shown by Yao et al. [45], where Cu^{2+} zeolites showed higher inhibition of bacterial growth against *E. coli* and *S. aureus* compared to Zn^{2+} zeolites. The increased inhibition of *E. coli* and *S. aureus* using washed Cu/CBV-600-bramante may be attributed to the removal of excess material, which could lead to an increase in surface area and active sites [45]. Most importantly, these results demonstrate that the fabrics retain their antimicrobial activity even after four wash cycles. Such findings are significant for the potential applications of these fabrics in the manufacture of personal protective equipment.

SEM-EDS analysis of washed fabrics

To further evaluate the durability of the functionalized fabrics under practical conditions, the samples underwent repeated washing cycles, and their structural integrity and nanoparticles distribution were studied by SEM. Figure 6 shows the fabrics functionalized with the nanomaterials (Ag/CBV600-bramante, Cu/CBV600-bramante, and Zn/CBV600-bramante) after one, three, and five washing cycles. In all cases, the fabrics exhibited no fiber degradation after washing, and the presence of

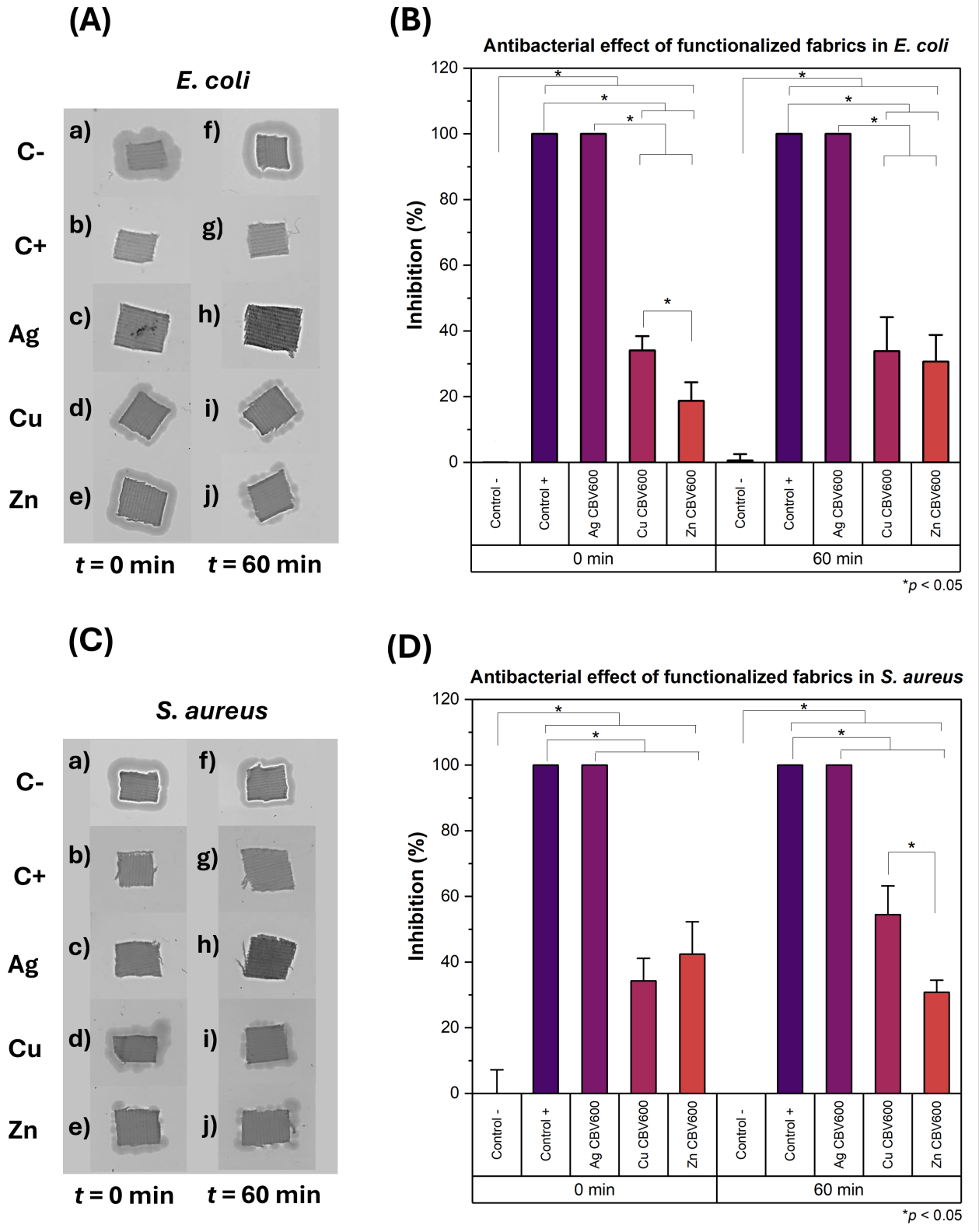

Figure 4: (A) *E. coli* growth on LB agar plates on fabrics exposed to 0 and 60 min of sunlight. (B) Inhibition of *E. coli* growth on fabrics after 0 and 60 min of exposure to sunlight. (C) *S. aureus* growth on LB agar plates on fabrics exposed to 0 and 60 min of sunlight. (D) Inhibition of *S. aureus* growth on fabrics after 0 and 60 min of exposure to sunlight. The asterisk (*) indicates $p < 0.05$.

Table 2: ANOVA results of antimicrobial effects of functionalized fabrics against *E. coli* and *S. aureus*.

Antimicrobial activity of functionalized fabrics against *E. coli*

	DF	Sum of squares	Mean square	F value	P value
materials	4	50105.21	12526.30	437.18	<0.0001
sunlight exposure	1	45.61	45.61	1.59	0.22
model	5	50150.82	10030.16	350.06	<0.0001
error	24	687.67	28.65	—	—
corrected total	29	50838.49	—	—	—

Antimicrobial activity of functionalized fabrics against *S. aureus*

	DF	Sum of squares	Mean square	F value	P value
materials	4	45116.36	11279.09	181.02	<0.0001
sunlight exposure	1	22.15	22.15	0.36	0.56
model	5	45138.51	9027.70	144.89	<0.0001
error	24	1495.37	62.31	—	—
corrected total	29	46633.89	—	—	—

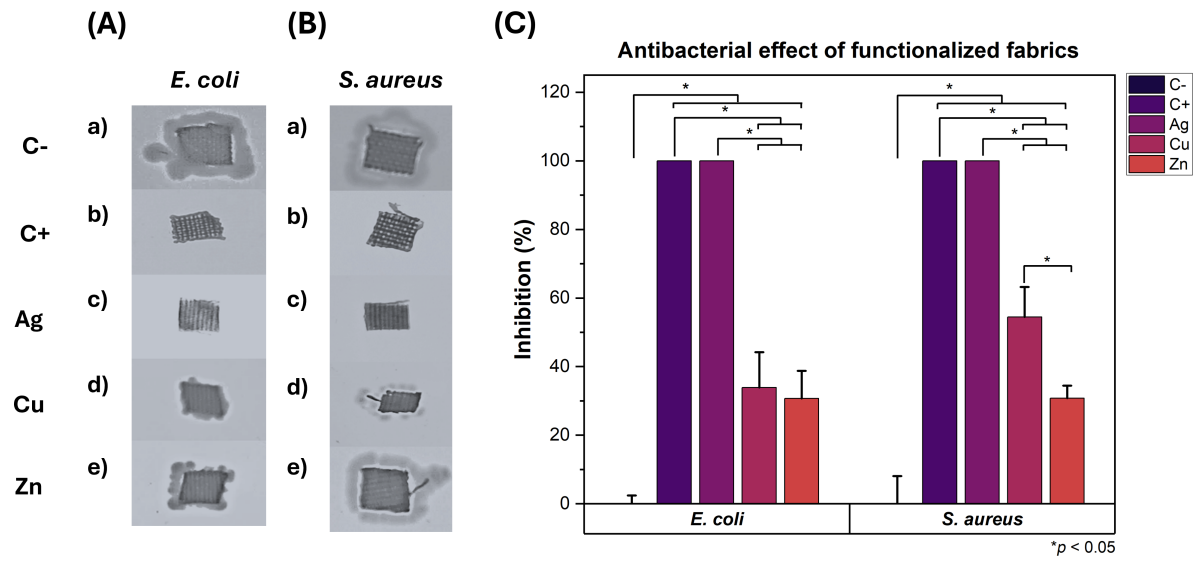

Figure 5: Antibacterial activity of fabrics after four wash cycles. Growth on LB agar plates of *E. coli* (A) and *S. aureus* (B) cultures after 20 h of incubation. Comparison of the inhibitory effect of fabrics impregnated with nanomaterials against *E. coli* and *S. aureus* (C). The asterisk (*) indicates $p < 0.05$.

nanoparticles was still observed. However, the micrographs revealed different degrees of nanomaterial aggregation after each washing cycle. SEM-EDS analysis detected Ag, Cu, and Zn only after the first washing cycle (Figure 7). However, the Ag, Cu, and Zn concentrations after three and five washing cycles might be below the detection limit of EDS (i.e., the phenomenon is related to the relatively low amount of nanomaterials used for fabric functionalization rather than to the complete removal of the nanomaterials). According to the literature [30], partial nanoparticle loss during washing is commonly reported, with slight leaching occurring after five to ten washing cycles. This loss of nanomaterial may affect its antimicrobial properties; however, the useful life of the textile with antimicrobial properties is extended. The persistent antimicrobial activity observed after five washing cycles further supports the strong adhesion and stability of the metal-loaded zeolites on the fabric surface. Based on those experiments, only minimal metal leaching during washing is expected.

Table 3: ANOVA results of antimicrobial effects of functionalized fabrics against *E. coli* and *S. aureus* after four wash cycles.

Antimicrobial activity of functionalized fabrics against *E. coli*					
	DF	Sum of squares	Mean square	F value	P value
materials	4	50105.21	12526.30	482.87	<0.0001
sunlight exposure	1	45.61	45.61	1.76	0.20
model	4	168.85	42.21	1.63	0.21
error	9	50319.67	5591.07	215.53	<0.0001
corrected total	20	518.82	25.94	—	—
Antimicrobial activity of functionalized fabrics against *S. aureus*					
	DF	Sum of squares	Mean square	F value	P value
materials	4	45116.36	11279.09	321.26	<0.0001
sunlight exposure	1	22.15	22.15	0.63	0.44
model	4	793.19	198.30	5.65	0.00329
error	9	45931.70	5103.52	145.36	<0.0001
corrected total	20	702.18	35.11	—	—

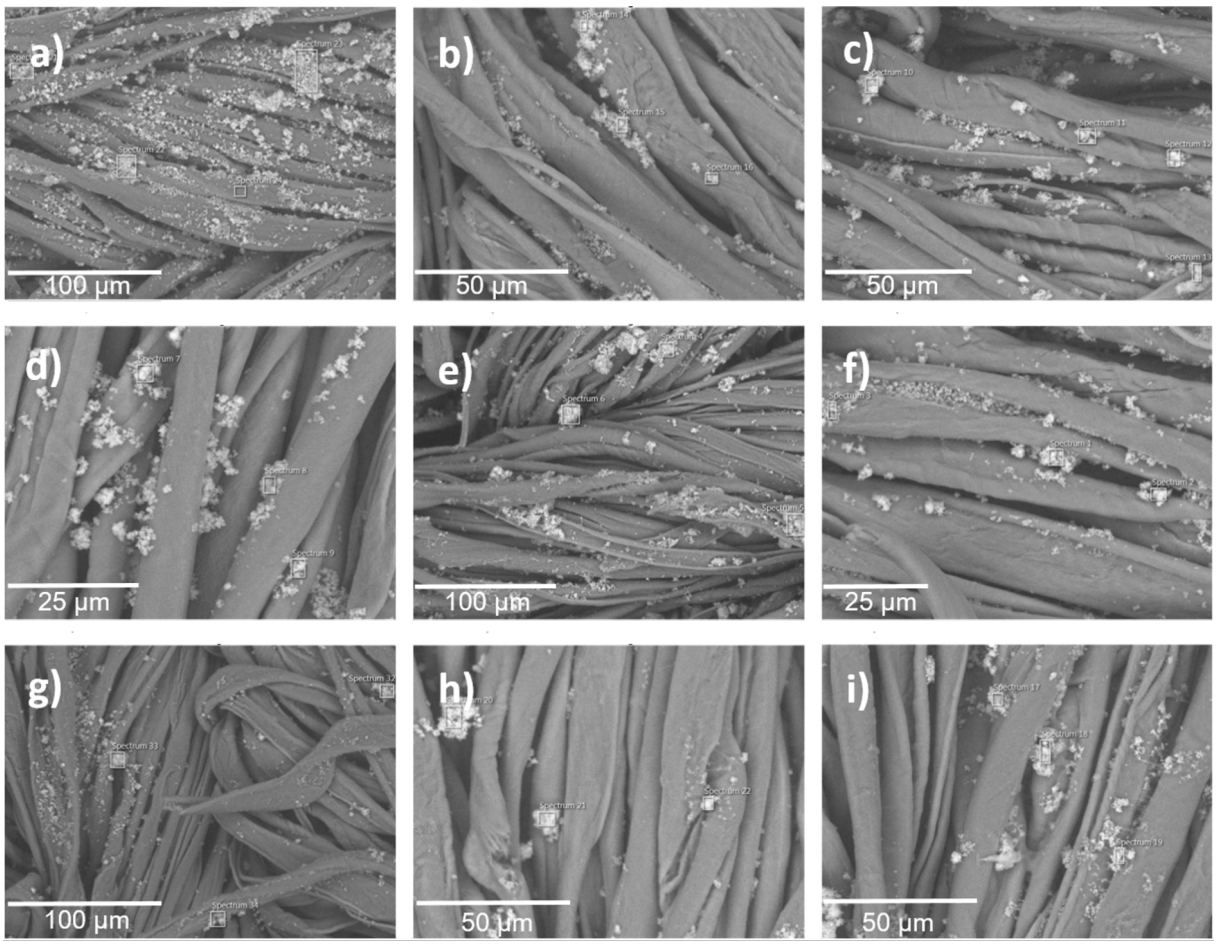

Figure 6: SEM micrographs of the samples after the first, third, and fifth washing cycles; (a–c) Ag/CBV600-bramante, (d–f) Cu/CBV600-bramante, and (g–i) Zn/CBV600-bramante.

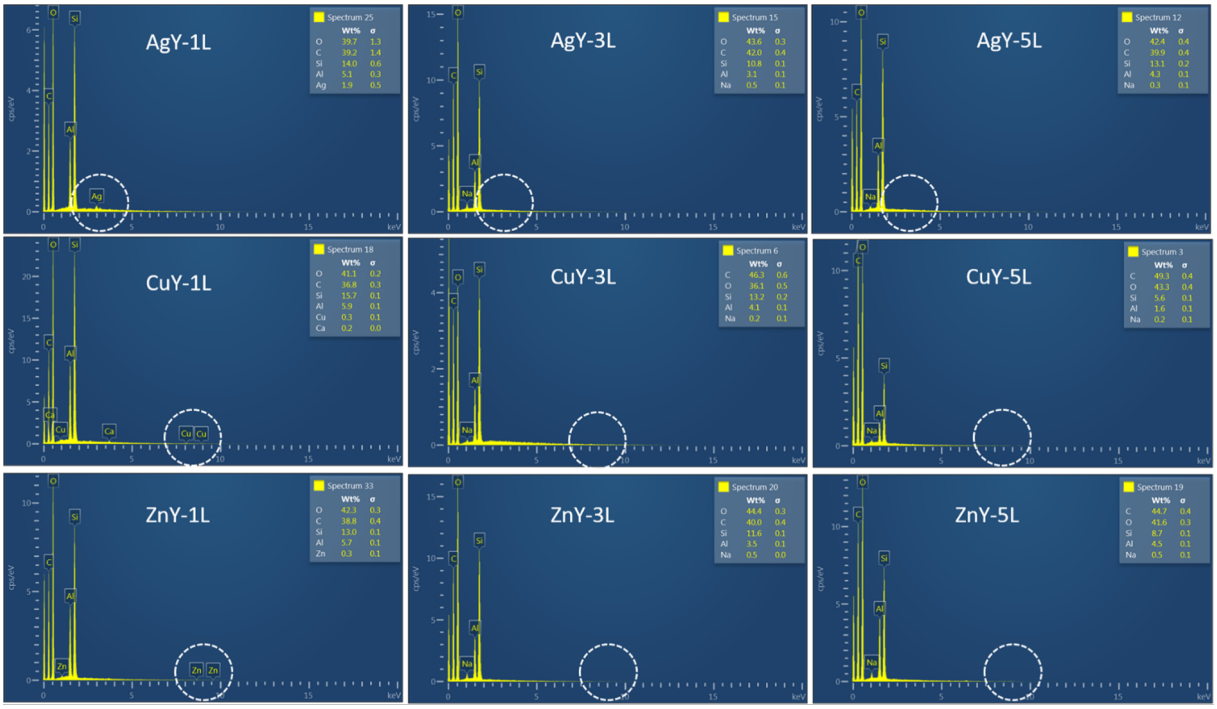

Figure 7: SEM-EDS analysis of bramante fabrics functionalized with Ag/CBV600, Cu/CBV600, and Zn/CBV600 after one, three, and five washing cycles.

Conclusion

This study successfully demonstrates the functionalization of cotton textiles using Ag^{+}, Cu^{2+}, and Zn^{2+} ions incorporated into Y-zeolite (CBV-600) via the pad–dry–cure method. The resulting nanostructured fabrics exhibited significant and durable antimicrobial activity against both *Staphylococcus aureus* (Gram-positive) and *Escherichia coli* (Gram-negative). Scanning electron microscopy confirmed the effective incorporation and uniform distribution of the nanomaterials on the fabric surface, facilitated by a 10% w/w acrylic resin binder. Among the tested materials, silver-based fabrics displayed the highest antibacterial efficacy, followed by copper and zinc, consistent with their known antimicrobial properties. Notably, the treated fabrics retained substantial biocidal activity even after multiple washing cycles, indicating the strong adhesion and stability of the zeolite-based nanomaterials. These findings highlight the potential of zeolite-supported metal ions as a scalable and effective approach for developing antimicrobial textiles with long-lasting performance. Such materials are promising candidates for use in healthcare, protective clothing, hygiene products, and other applications where microbial contamination poses a risk.

Experimental

Materials preparation

The pad–dry–cure method was used for fabric impregnation [30]. Prior to the experiment, the bramante fabrics containing 50% cotton and 50% polyester with a density of 150 threads (Parisina Company, Mexico) were washed with detergent (Alconox, Sigma Aldrich) and deionized water. Finally, the fabrics were dried at room temperature for one day. A 10% (*w*/*w*) acrylic resin (Acrylic binder 005, Royal Talens Company, Apeldoorn, Netherlands, chemical composition: 5-chloro-2-methyl-2*H*-isothiazol-3-one; 2-methyl-2*H*-isothiazol-3-one; 1,2-benzisothiazol-3(2*H*)-one) was used as a binding agent to immobilize the nanomaterials onto the fabrics. 100 mL of aqueous solution containing 0.5 g of M/CBV-600 (M = Ag, Cu, or Zn) suspension was prepared. Cut fabrics samples (5 cm^2) were immersed once in the prepared solution for 15 min under constant stirring until full wetting. Then, each sample was compressed between two rolling pins using a rolling machine (Marcato, Padova, Italy). Afterwards, the functionalized fabrics underwent a drying process at 90 °C for 10 min; finally, the samples were cured at 120 °C for 3 min. Both stages were carried out in a mechanical convection oven (no. MMTUF110X2, Memmert GmbH, Germany). Prior to drying and curing, the fabric was characterized without nanomaterials and without acrylic resin, as shown in Figure 2a. The fabrics were functionalized using the ion-exchanged zeolite-based Ag/CBV-600, Cu/CBV-600, and Zn/CBV-600 nanomaterials prepared previously in [4]. A detailed physicochemical characterization of these materials, including metal content, morphology, and structural properties was reported in [4].

Materials characterization

The morphology of the fabrics with and without NPs was analyzed by SEM. Images were acquired in a Hitachi SU3500 microscope operating at an accelerating voltage of 15 kV (Hitachi High-Tech Corp., Tokyo, Japan). The nanomaterial-containing fabric was placed on a metal grid with double-sided tape. For each sample, at least five representative images were captured. In order to analyze the grade of the washout of nanoparticles from the fabric, transmission electron microscopy (TEM) images were obtained using a JEOL JEM-2200FS (200 kV), and elemental analysis was performed using EDS.

The crystalline structure of the modified fabrics was determined by X-ray diffraction (XRD) in a Panalytical AERIS diffractometer using Cu Kα (λ = 1.54184 Å). The interval of XRD analysis was 2θ = 5–80°, with a step size of 0.01° and 1 s of measure time for each step.

The durability of the finish was assessed by washing the modified textile five times. The fabrics were washed using deionized water and the detergent Alconox. Mechanical action was applied using constant stirring at 5 rpm at 40 °C for 15 min per wash cycle, followed by drying at room temperature for 24 h between cycles. The antimicrobial properties of washed fabrics were evaluated after fourth washing cycle.

Antibacterial activity of functionalized fabrics

Antimicrobial activity experiments against *E. coli* and *S. aureus* were conducted using a custom protocol based on the zone of inhibition method (ISO 20645) for hydrophobic fabrics. The experiments were performed using textile squares of approximately 0.5 × 0.5 cm^2 of non-functionalized fabric (C− or negative control), fabric inoculated with 1 $mg{\cdot}mL^{-1}$ ampicillin (C+ or positive control), Ag/CBV600-bramante, Cu/CBV600-bramante, and Zn/CBV600-bramante. Bacteria cultures were prepared by growing them to a concentration of 10^8 $CFU{\cdot}mL^{-1}$. Then, the fabrics were inoculated with bacteria by immersing each textile square for 5 s in 1 mL of culture (4 $mL{\cdot}cm^{-2}$ of fabric). Afterwards, the fabrics were deposited on top of a glass microscope slide (Fisher Brand) and covered with a second glass slide. This setup helped to prevent environmental contamination while the fabrics were exposed to sunlight. Two sample groups were evaluated to determine if the photocatalytic activity of the materials enhanced antimicrobial activity: group A was not exposed to sunlight (t = 0 min), and group B was exposed to 60 min of UV-A/B radiation of sunlight (t = 60 min), which was measured using an URCERI light meter containing a UV-A/B detector. Afterwards, all fabrics were deposited onto LB agar plates and incubated at 37 °C. Bacterial growth was determined by taking photographs of the plates after 20 h of incubation and measuring the biofilm growth on the sides of the fabric. The experiment was repeated using Ag/CBV-600, Cu/CBV-600, and Zn/CBV-600 bramante fabrics that were washed four times to determine if the antimicrobial properties were retained after several wash cycles. The images of bacterial growth were analyzed using ImageJ to determine the growth thickness around the fabrics. All assays were performed using three biological replicates per condition and 20 measurements of growth thickness were taken per sample. The average of these measurements was used to compare between biological replicates.

Acknowledgements

The authors acknowledge Fabian Humberto Alonso and M. C. Pedro Casillas Figueroa for technical support. The image of the mask in the Graphical Abstract was created by Dacreativo via Pixabay (https://pixabay.com/). This content is not subject to CC BY 4.0.

Funding

This work was supported by DGAPA-PAPIIT (UNAM, Mexico) through the project IV-100124.

Author Contributions

Perla Sánchez-López: data curation; methodology; writing – original draft. Kendra Ramirez Acosta: data curation; methodology; writing – original draft. Sergio Fuentes Moyado: funding acquisition; project administration; resources; validation. Ruben Dario Cadena-Nava: data curation; methodology; visualization. Elena Smolentseva: conceptualization; formal analysis; investigation; supervision; visualization; writing – original draft; writing – review & editing.

ORCID® iDs

Perla Sánchez-López - https://orcid.org/0000-0001-5295-4269
Kendra Ramirez Acosta - https://orcid.org/0000-0003-2228-2435
Sergio Fuentes Moyado - https://orcid.org/0000-0002-9843-408X
Ruben Dario Cadena-Nava - https://orcid.org/0000-0001-8428-6701
Elena Smolentseva - https://orcid.org/0000-0003-2562-9094

Data Availability Statement

Data generated and analyzed during this study is available from the corresponding author upon reasonable request.

References

1. Nasrollahzadeh, M.; Sajadi, S. M.; Sajjadi, M.; Issaabadi, Z. Chapter 1 - An Introduction to Nanotechnology. In *An Introduction to Green Nanotechnology;* Nasrollahzadeh, M.; Sajadi, S. M.; Sajjadi, M.; Issaabadi, Z.; Atarod, M., Eds.; Interface Science and Technology, Vol. 28; Elsevier: London, U.K.; pp 1–27. doi:10.1016/b978-0-12-813586-0.00001-8
2. López-Cisneros, M.; Smolentseva, E.; Acosta, B.; Simakov, A. *Nanotechnology* **2021,** *32,* 425602. doi:10.1088/1361-6528/ac137c

3. Urnukhsaikhan, E.; Bold, B.-E.; Gunbileg, A.; Sukhbaatar, N.; Mishig-Ochir, T. *Sci. Rep.* **2021,** *11,* 21047. doi:10.1038/s41598-021-00520-2
4. Sánchez-López, P.; Hernández-Hernández, K. A.; Fuentes Moyado, S.; Cadena Nava, R. D.; Smolentseva, E. *ACS Omega* **2024,** *9,* 7554–7563. doi:10.1021/acsomega.3c06462
5. Herdiana, Y. *Heliyon* **2025,** *11,* e42739. doi:10.1016/j.heliyon.2025.e42739
6. Liang, L.; Ahamed, A.; Ge, L.; Fu, X.; Lisak, G. *ChemPlusChem* **2020,** *85,* 2105–2128. doi:10.1002/cplu.202000460
7. Beyth, N.; Houri-Haddad, Y.; Domb, A.; Khan, W.; Hazan, R. *Evidence-Based Complementary Altern. Med.* **2015,** *2015,* 246012. doi:10.1155/2015/246012
8. Yin, I. X.; Zhang, J.; Zhao, I. S.; Mei, M. L.; Li, Q.; Chu, C. H. *Int. J. Nanomed.* **2020,** *15,* 2555–2562. doi:10.2147/ijn.s246764
9. Raghupathi, K. R.; Koodali, R. T.; Manna, A. C. *Langmuir* **2011,** *27,* 4020–4028. doi:10.1021/la104825u
10. Wang, L.; Hu, C.; Shao, L. *Int. J. Nanomed.* **2017,** *12,* 1227–1249. doi:10.2147/ijn.s121956
11. Yılmaz, G. E.; Göktürk, I.; Ovezova, M.; Yılmaz, F.; Kılıç, S.; Denizli, A. *Hygiene* **2023,** *3,* 269–290. doi:10.3390/hygiene3030020
12. U.S. ENVIRONMENTAL PROTECTION AGENCY. NOTICE OF PESTICIDE Registration: Antimicrobial Copper Alloys - GroupV. 2008; https://www3.epa.gov/pesticides/chem_search/ppls/082012-00005-20080229.pdf (accessed Jan 26, 2026).
13. Prado, V. J.; Vidal, A. R.; Durán, T. C. *Revista Med. Chile* **2012,** *140,* 1325–1332. doi:10.4067/s0034-98872012001000014
14. Noyce, J. O.; Michels, H.; Keevil, C. W. *Appl. Environ. Microbiol.* **2006,** *72,* 4239–4244. doi:10.1128/aem.02532-05
15. Usman, M. S.; El Zowalaty, M. E.; Shameli, K.; Zainuddin, N.; Salama, M.; Ibrahim, N. A. *Int. J. Nanomed.* **2013,** *8,* 4467–4479. doi:10.2147/ijn.s50837
16. Thekkae Padil, V. V.; Černík, M. *Int. J. Nanomed.* **2013,** *8,* 889–898. doi:10.2147/ijn.s40599
17. Applerot, G.; Lellouche, J.; Lipovsky, A.; Nitzan, Y.; Lubart, R.; Gedanken, A.; Banin, E. *Small* **2012,** *8,* 3326–3337. doi:10.1002/smll.201200772
18. Azam, A.; Ahmed, A. S.; Oves, M.; Khan, M. S.; Memic, A. *Int. J. Nanomed.* **2012,** *7,* 3527–3535. doi:10.2147/ijn.s29020
19. Azizi-Lalabadi, M.; Ehsani, A.; Divband, B.; Alizadeh-Sani, M. *Sci. Rep.* **2019,** *9,* 17439. doi:10.1038/s41598-019-54025-0
20. Lallo da Silva, B.; Caetano, B. L.; Chiari-Andréo, B. G.; Pietro, R. C. L. R.; Chiavacci, L. A. *Colloids Surf., B* **2019,** *177,* 440–447. doi:10.1016/j.colsurfb.2019.02.013
21. Romagnoli, M. J.; Gonzalez, J. S.; Martinez, M. A.; Alvarez, V. A. Micro- and nanotechnology applied on eco-friendly smart textiles. In *Handbook of Nanomaterials and Nanocomposites for Energy and Environmental Applications;* Kharissova, O.; Martínez, L.; Kharisov, L., Eds.; Springer: Cham, Switzerland, 2020; pp 1–19. doi:10.1007/978-3-030-11155-7_58-1
22. Fang, Y.; Chen, G.; Bick, M.; Chen, J. *Chem. Soc. Rev.* **2021,** *50,* 9357–9374. doi:10.1039/d1cs00003a
23. Idumah, C. I. *J. Text. Inst.* **2021,** *112,* 2056–2076. doi:10.1080/00405000.2020.1858600
24. Singh, N. A. *Environ. Chem. Lett.* **2017,** *15,* 185–191. doi:10.1007/s10311-017-0612-8
25. Abou Elmaaty, T. M.; Elsisi, H.; Elsayad, G.; Elhadad, H.; Plutino, M. R. *Polymers (Basel, Switz.)* **2022,** *14,* 4273. doi:10.3390/polym14204273
26. Kittinaovarat, S. *J. Sci. Res., Chulalongkorn Univ.* **2006,** *31,* 2.
27. Wang, W.-Y.; Chiou, J.-C.; Yip, J.; Yung, K.-F.; Kan, C.-W. *Coatings* **2020,** *10,* 520. doi:10.3390/coatings10060520
28. Rodrigues, A. G.; Romano de Oliveira Gonçalves, P. J.; Ottoni, C. A.; de Cássia Ruiz, R.; Morgano, M. A.; de Araújo, W. L.; de Melo, I. S.; De Souza, A. O. *Biomed. Microdevices* **2019,** *21,* 56. doi:10.1007/s10544-019-0410-0
29. Aguda, O. N.; Lateef, A. *Environ. Technol. Innovation* **2021,** *24,* 102077. doi:10.1016/j.eti.2021.102077
30. Rojas-Lema, S. P.; Galeas-Hurtado, S. G.; Guerrero-Barragán, V. H. *Rev. Fac. Ing.* **2017,** *26,* 109–119. doi:10.19053/01211129.v26.n45.2017.6420
31. Anita, S.; Ramachandran, T.; Rajendran, R.; Koushik, C. V.; Mahalakshmi, M. *Text. Res. J.* **2011,** *81,* 1081–1088. doi:10.1177/0040517510397577
32. Uribe Valenzuela, C.; Roca Meneses, E.; Brañez Sánchez, M.; Álvarez Alayo, J.; Román Mendoza, L. E.; Torres, D. M.; Solís Veliz, J. L.; Gómez León, M. M. *Rev. Soc. Quim. Peru* **2016,** *82,* 216–231. doi:10.37761/rsqp.v82i2.126
33. Singh, A.; Chakraborty, J. N. *Res. J. Text. Apparel* **2023,** *27,* 141–156. doi:10.1108/rjta-11-2021-0130
34. Eskani, I. N.; Haerudin, A.; Setiawan, J.; Lestari, D. W.; Isnaini; Astuti, W. *IOP Conf. Ser.: Mater. Sci. Eng.* **2020,** *722,* 012029. doi:10.1088/1757-899x/722/1/012029
35. Sk, M. S.; Mia, R.; Hoque, E.; Ahmed, B.; Amin, M. J. I.; Kabir, S. M. M.; Mahmud, S. *Surf. Innovations* **2023,** *11,* 223–230. doi:10.1680/jsuin.22.00023
36. Parikh, D. V.; Thibodeaux, D. P.; Condon, B. *Text. Res. J.* **2007,** *77,* 612–616. doi:10.1177/0040517507081982
37. Hong, K. H. *Text. Res. J.* **2014,** *84,* 1138–1146. doi:10.1177/0040517513519007
38. Bruna, T.; Maldonado-Bravo, F.; Jara, P.; Caro, N. *Int. J. Mol. Sci.* **2021,** *22,* 7202. doi:10.3390/ijms22137202
39. Kalwar, K.; Shan, D. *Micro Nano Lett.* **2018,** *13,* 277–280. doi:10.1049/mnl.2017.0648
40. Maiti, S.; Krishnan, D.; Barman, G.; Ghosh, S. K.; Laha, J. K. *J. Anal. Sci. Technol.* **2014,** *5,* 40. doi:10.1186/s40543-014-0040-3
41. Pietrzak, K.; Gutarowska, B.; Machnowski, W.; Mikołajczyk, U. *Text. Res. J.* **2016,** *86,* 812–822. doi:10.1177/0040517515596933
42. Hobman, J. L.; Crossman, L. C. *J. Med. Microbiol.* **2015,** *64,* 471–497. doi:10.1099/jmm.0.023036-0
43. Ruparelia, J. P.; Chatterjee, A. K.; Duttagupta, S. P.; Mukherji, S. *Acta Biomater.* **2008,** *4,* 707–716. doi:10.1016/j.actbio.2007.11.006
44. Jaiswal, S.; McHale, P.; Duffy, B. *Colloids Surf., B* **2012,** *94,* 170–176. doi:10.1016/j.colsurfb.2012.01.035
45. Yao, G.; Lei, J.; Zhang, W.; Yu, C.; Sun, Z.; Zheng, S.; Komarneni, S. *Environ. Sci. Pollut. Res.* **2019,** *26,* 2782–2793. doi:10.1007/s11356-018-3750-z